NOVEL NONLINEAR TECHNIQUES FOR FEMTOSECOND PULSE GENERATION IN THE VISIBLE AND NEAR-INFRARED

Derryck T. Reid

A Thesis Submitted for the Degree of PhD
at the
University of St Andrews

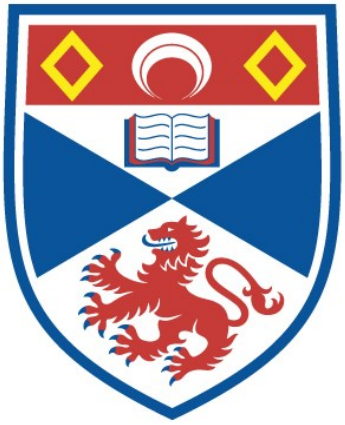

1995

Novel nonlinear techniques for femtosecond pulse generation in the visible and near-infrared

Thesis submitted for the degree of Doctor of Philosophy
to the University of St Andrews,

by,

Derryck T. Reid B. A.

J. F. Allen Physics Research Laboratories
Department of Physics and Astronomy
University of St Andrews
St Andrews
Fife KY16 9SS

December 1994

Declaration

I, Derryck Telford Reid, certify that this thesis has been composed by myself, that it is a record of my own work and that it has not been accepted in partial or complete fulfilment of any other degree or qualification.

I was admitted to the Faculty of Science of the University of St Andrews under Ordinance General Number 12 on 1st October 1991.

Signed Date 5.10.94

I hereby certify that the candidate has fulfilled the conditions of the Resolution and Regulations appropriate to the Degree of Ph.D.

Signature of supervisor Date

05.10.94

Copyright

In submitting this thesis to the University of St Andrews I understand that I am giving permission for it to be made available for use in accordance with the regulations of the University Library for the time being in force, subject to any copyright vested in the work not being affected thereby. I also understand that the title and abstract will be published and that a copy of the work may be made and supplied to any *bona fide* library or research worker.

To, Mum, Dad
and Gran,

Man has created new worlds - of language, of music, of poetry, of science; and the most important of these is the world of the moral demands, for equality, for freedom, and for helping the weak.

Sir Karl Popper,

The Open Society and Its Enemies, vol. 1, p 65

Abstract

The work presented in this thesis describes the design, configuration and operation of femtosecond optical parametric oscillators based on the materials $KTiOPO_4$ (KTP) and $RbTiOAsO_4$ (RTA) and pumped by a self-modelocked Ti:sapphire laser. The alignment of the pump laser is detailed and thermal effects in the Ti:sapphire rod are examined in the context of a general technique which optimises modelocked performance at any pump power.

A KTP-based femtosecond parametric oscillator is described which produces 400-fs-duration signal pulses at an average output power of 150 mW when operated in the absence of group-velocity dispersion-compensation. With intracavity dispersion-compensation, the oscillator produces 40-fs-duration pulses with an average power of 50 mW. Tuning is demonstrated from 1.12 - 1.25 μm in the signal wave and from 2.5 - 3.0 μm in the idler wave by changing only the pump-laser wavelength. Using a novel idler-feedback arrangement, reductions in the oscillation threshold and increases in the signal output power of 10 % are described. Soliton generation in the oscillator is achieved when the net cavity dispersion is positive and results show good agreement with theory.

An oscillator using RTA is demonstrated which achieves conversion efficiencies exceeding 30 % and has an operating threshold of only 50 mW. Average signal powers of 100 mW and 185 mW are extracted from the oscillators with and without dispersion-compensation respectively. The corresponding pulse durations are 67 fs and 980 fs and tunability in the signal and idler waves from 1.23 - 1.34 μm and 2.10 - 2.43 μm is demonstrated. Visible output from 620 - 660 nm is obtained by intracavity-doubling and powers of up to 170 mW are measured. These results suggest that RTA has a higher nonlinear coefficient than KTP.

Contents

1.1 Background

The generation of tunable ultrashort laser pulses in different regions of the optical spectrum is of great interest for many spectroscopic applications. These arise in photophysics, photochemistry, photobiology and optoelectronics. They range from time-domain study of molecular behaviour in response to photoexcitation [1] to the analysis of recombination dynamics in semiconductors [2]. The study of such processes requires optical pulses with femtosecond durations that are tunable over extended wavelength regions.

A variety of experiments exploit femtosecond pulses for the excitation of electronic or molecular transitions in a sample and then to probe the resulting relaxation behaviour. Such *pump-probe* techniques have been used in, for example, semiconductors to analyse electron-hole thermalisation dynamics through saturation absorption [3] and time-resolved luminescence spectroscopy [4]. Non-contact measurements of electrical signals in high-speed integrated circuits have been made using an electro-optic probe to modulate the amplitude of a femtosecond pulse [5] and similar techniques have allowed the characterisation of electrical pulses having fall times as short as 1.6 ps [6].

The applications of femtosecond pulses are not restricted to probing electronic behaviour. Femtosecond transition-state spectroscopy has been used to study the vibrational and rotational motion of diatomic molecules such as iodine [7, 8]. To investigate vibration, a femtosecond pump pulse was used to excite the iodine molecules to a bound electronic state in

which the molecular bond stretched and relaxed in a potential well. A second probe pulse then excited the molecules to a radiative state whose fluorescence provided a measure of the internuclear separation as a function of time. In another experiment studying the photofragmentation of the I-CN bond [9, 10], a femtosecond laser was tuned through the spectral range surrounding a resonant frequency of free CN. Time-resolved analysis of the fluorescence signal for different probe frequencies provided information about the timescale over which the bond-breaking process occurred.

From these examples alone it is clear that there are many applications which demand reliable sources of tunable femtosecond pulses. In the following section the established methods of generating femtosecond pulses in the visible and infrared are outlined and the inherent limitations of each of the methodologies are discussed.

1.2 Conventional tunable femtosecond sources

Until recently, existing high repetition-rate sources of femtosecond pulses fell into three main categories: modelocked dye lasers, vibronic lasers and colour-centre lasers. Using these sources, femtosecond pulses as short as 8.5 fs [11] have been generated directly from the ultraviolet to the mid-infrared and with average powers of up to several watts.

Dye Lasers

The demonstration in 1981 of a colliding-pulse-modelocked (CPM) dye laser [12] was the first example of a modelocked laser capable of producing pulses with durations less than 100 fs at a high-repetition-rate (~100 MHz). The CPM dye laser was a ring cavity containing an absorber

jet of 3,3'-diethyloxadicarbocyanide iodide (DODCI) in solution and a gain jet of rhodamine 6-G (Rh6G). In contrast to earlier passively modelocked lasers based on standing-wave configurations [13] the CPM laser operated with two or more counterpropagating pulses resonant in the ring cavity. When the counterpropagating pulses met in the thin DODCI jet the bleaching action of the absorber sharpened the leading edges of both pulses. Gain saturation in the Rh6G jet then reduced the pulse duration further by steepening the trailing edge of the pulses. The average output power of such dye lasers was limited to $\lesssim 10$ mW because the inclusion of a saturable absorber resulted in an operating threshold of several Watts. CPM lasers were only tunable over a narrow spectral range since the net bandwidth of the gain and absorber dyes was of the order of the bandwidth of the resonant femtosecond pulse. Operation across a limited range in the visible could be achieved by using different gain / absorber combinations [14 - 21] but complete tuning was never convincingly demonstrated for femtosecond pulses.

In the subsequent years, CPM dye lasers used in conjunction with amplifier systems for continuum generation enabled pulses tunable from 0.2 - 1.6 μm [22] to be produced at repetition rates up to 8 kHz [23]. Using difference-frequency generation between the amplified dye laser output and the continuum produced 480-fs pulses tunable from 1.7 - 4 μm and with peak powers as high as 10 kW [24]. These systems, although widely tunable, were limited by relatively low repetition-rates, weak continuum generation in the near-infrared and the availability of suitable dyes. In addition, amplifier-based systems typically produce ultrashort pulses whose duration and intensity vary within the Q-switched pulse envelope. For applications such as the analysis of multiple exponential decays in

ultrafast relaxation processes [25], a high-repetition-rate cw-modelocked source is desirable to obtain results with the highest signal-to-noise ratio.

Colour-centre Lasers

A new source of femtosecond pulses in the near-infrared was reported in 1984. The *soliton laser* [26, 27] was a synchronously-pumped KCl:Tl^0 (1) colour-centre laser tunable from 1.4 - 1.6 μm and modified to allow direct generation of pulses as short as 50 fs, substantially shorter than the 8 ps achieved in synchronously-pumped operation alone. Femtosecond operation was achieved by coupling a length of polarisation-preserving anomalously-dispersive fibre to the main laser cavity using a beamsplitter and retroreflector arrangement. The length of the optical path in the fibre arm was adjusted to be an integral multiple of the main cavity length. Short-pulse operation was originally attributed to bright solitonic generation in the fibre arm, but numerical modelling by Blow and Wood [28] showed that modelocking was enhanced even when the pulses returned from the fibre were temporally broadened, implying that solitonic effects were not necessary for femtosecond operation. This explanation was confirmed experimentally when 260 fs pulses were generated from a KCl:Tl colour centre laser modelocked using only normally dispersive fibre [29]. Pulses of 64-fs duration were subsequently produced from the same laser when erbium fibre, which exhibits enhanced nonlinearity, was used [30]. This coupled-cavity modelocking (CCM) behaviour was consistent with theories which emphasised the importance of interference between the pulse travelling in the master cavity and the self-phase-modulated pulse returned by the nonlinear fibre [31, 32]. The long upper-state lifetime of the laser-active centres in the KCl:Tl gain medium allowed particularly stable CCM operation but

modelocking of this kind was also successfully employed in an actively stabilised NaCl:OH^- colour-centre laser to produce 110-fs pulses [33]. A major application of modelocked colour-centre lasers was in the time-resolved characterisation of telecommunications optical fibres at 1.5 μm, a wavelength corresponding to the lowest loss window for silica fibres and a spectral region difficult to access using other sources. The need to maintain the colour-centre crystal at cryogenic temperatures restricted the availability of colour-centre lasers to research centres with access to a source of liquid nitrogen. Furthermore, the limited tuning range of femtosecond colour-centre lasers restricted their operation to the near-infrared. Clearly there remained an interest in finding more robust laser materials capable of sustaining femtosecond operation.

Vibronic Lasers

Solid-state vibronic materials are amongst the most recent laser media to have supported femtosecond modelocking. In contrast to narrow-line solid-state laser materials (eg. ruby, neodymium:YAG), vibronic media such as Ti:sapphire have vibrational sublevels which spread the electronic energy levels into broad bands thereby allowing laser transitions over a range of energies. This broad emission bandwidth is the feature of vibronic media which makes them attractive materials for femtosecond pulse generation. In addition, output powers of hundreds of milliwatts can be easily obtained from vibronic lasers at noise levels an order of magnitude lower than those of dye lasers because of the solid-state nature of the gain medium.

The forerunner of the femtosecond vibronic lasers in common use today was the CCM Ti:sapphire laser which was capable of producing 1.4-ps duration pulses [34]. Further work using a similar system generated

pulses as short as 90 fs by including compensation for group-velocity dispersion in both the master cavity and the fibre arm [35]. The complexity of this arrangement increased alignment-sensitivity and made the CCM Ti:sapphire laser less practical than the CCM colour-centre lasers which preceded it. Operation in the Ti:sapphire wavelength region of ≈ 800 nm was made more difficult than at longer wavelengths by the larger values of material group-velocity dispersion. The demonstration in 1990 of the self-modelocked Ti:sapphire laser [36] was a significant advance as it introduced a reliable solid-state widely-tunable femtosecond source requiring no modelocking elements except the gain medium itself. The mechanisms of self-modelocking involve configuring the laser cavity so that self-focusing in the gain medium favours modelocked operation over cw oscillation and are now well understood [37, 38]. Improvements in crystal fabrication and resonator design in the Ti:sapphire laser have resulted in lasers that can produce sub-150 fs pulses from 700 - 1053 nm [39, 40] with average output powers of up to 3 W and corresponding peak powers of ≈ 500 kW.

Self-modelocking has been demonstrated using vibronic media other than Ti:sapphire. In 1992 self-modelocking of Cr:LiSrAlF$_6$ (Cr:LiSAF) produced pulses as short as 50 fs at an average power of 200 mW from 800 - 920 nm using Ar-ion pumping at 476 nm [41]. This was followed in 1993 by the demonstration of a self-modelocked laser using Cr:forsterite pumped by a cw Nd:YAG laser which produced 48-fs pulses tunable from 1.21 - 1.26 μm at an average output power of 380 mW [42]. The wavelength coverage of femtosecond vibronic lasers was further extended in 1994 when the operation of a self-modelocked Cr^{4+}:YAG laser was reported [43]. Pumped by a cw Nd:YAG laser, the Cr^{4+}:YAG laser

produced 120-fs pulses tunable from 1.51 - 1.53 μm with an average output power of 360 mW.

The chart included as Fig. 1.1 shows the wavelength regions covered by femtosecond dye, colour-centre and vibronic lasers. It is obvious that large spectral regions, particularly in the near- to mid-infrared, still exist that are not readily covered by conventional femtosecond lasers. Modelocking of alternative vibronic media such as alexandrite and Co:MgF_2 may provide a partial solution but complete coverage could still only be achieved by using a variety of pump sources and laser media.

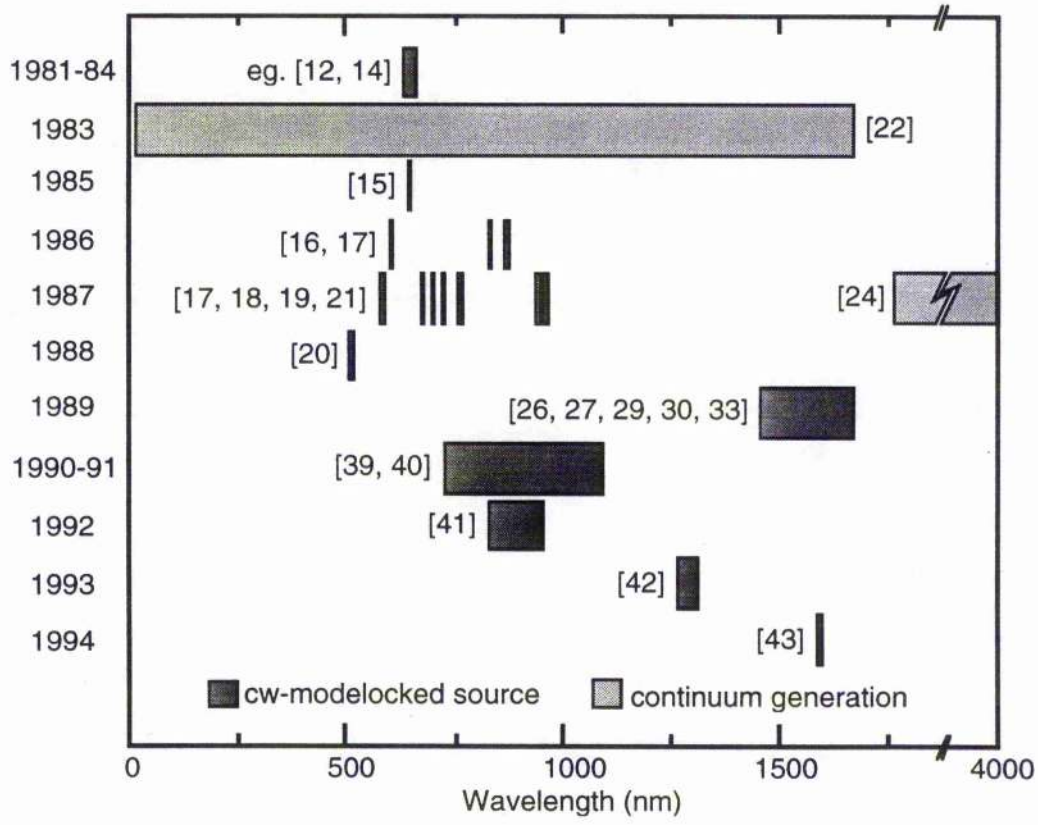

Figure 1.1 - Wavelengths in the visible and infrared available from conventional femtosecond sources.

A more satisfactory solution is to exploit the high peak output powers already available from self-modelocked vibronic lasers to efficiently generate new wavelengths using nonlinear frequency conversion techniques. In the following section a review of the progress in the development of synchronously-pumped femtosecond optical parametric oscillators towards providing continuous wavelength coverage in the visible and the near- to mid-infrared is presented.

1.3 Synchronously-pumped Optical Parametric Oscillators

The synchronously-pumped optical parametric oscillator (OPO) has for more than two decades been recognised as a highly effective alternative for the generation of ultrashort pulses in new wavelength regions. As early as 1972, Burneika and co-workers proposed a synchronously-pumped OPO configured so that the cavity lengths of the OPO and modelocked pump laser were equal [44]. In the same work, the researchers demonstrated an optical parametric amplifier (OPA) using KDP which was synchronously pumped by the second harmonic of a modelocked Nd:YAG laser. For many years, however, several factors limited the operation of picosecond OPOs to pulsed, doubly-resonant or amplified configurations. Continuous-wave-modelocked lasers providing adequately high intensity ($\approx$ 100 kW) were not available and pump sources were restricted to low repetition-rate Q-switched sources. The availability of suitable nonlinear crystals possessing sufficiently high damage-thresholds further hampered progress in OPO technology. In addition, the design of resonators with a high enough Q-factor was hindered by the lack of damage-resistant dielectric mirrors capable of high transmission at pump wavelengths and arbitrary output coupling at the OPO wavelengths.

For these reasons, the synchronously-pumped parametric oscillator has its origins in frequency-unstable doubly-resonant configurations such as the one demonstrated by Piskarskas and co-workers in 1988 [45]. This oscillator was pumped using the second harmonic of a cw-modelocked Nd:YAG laser and was based on $Ba_2NaNb_5O_{15}$. The OPO was pumped with pulses of 40-ps duration at a repetition frequency of 140 MHz and generated 37-ps pulses tunable from 0.96 - 1.19 μm with an average output power of 56 mW. The pump threshold power of only 28 mW was explained by the use of a long (l = 10 mm), highly nonlinear crystal configured in a resonator with feedback at both the signal and idler frequencies. This dual feedback was unfortunately detrimental as it resulted in the output spectrum of the OPO being characterised by a cluster structure caused by competition between the cavity modes of the signal and idler waves. Although the output of the doubly-resonant OPO is characterised by large amplitude and spectral instabilities, Ebrahimzadeh and co-workers exploited the low operating threshold associated with this configuration to demonstrate an all-solid-state oscillator based on $KTiOPO_4$ [46]. The OPO was pumped with 15-ps duration pulses from a frequency-doubled cw-modelocked diode-laser-pumped Nd:YLF laser and produced in total up to 40 mW of average power.

Doubly-resonant configurations using Q-switched pump sources have also been demonstrated. Piskarskas and co-workers used the frequency-doubled and compressed output of a Q-switched modelocked Nd:YAG to pump a doubly-resonant OPO based on $Ba_2NaNb_5O_{15}$ [47]. Tunability from 0.95 - 1.2 μm was achieved with the output pulses having durations as low as 3.5 ps and repetition rates of up to 3 kHz. Other doubly-resonant

Q-switched oscillators operating in the near-infrared have been demonstrated using MgO:$LiNbO_3$ [48] and LiB_3O_5 [49] and operating in the visible using β-BaB_2O_4 [50].

The poor stability of the doubly-resonant OPO limited its usefulness in the spectroscopic applications for which OPOs were being developed and was superseded by singly-resonant Q-switched picosecond oscillators such as the one first demonstrated by Bromley, Guy and Hanna [51]. Based on a crystal of KTP, their OPO produced 70-ps pulses tunable from 1.04 - 1.09 nm and exhibited conversion efficiencies of up to 30 %. A singly-resonant visible OPO was demonstrated by Burdulis and co-workers who used the third-harmonic of a Q-switched modelocked Nd:YAG laser to pump an oscillator based on β-BaB_2O_4 [52]. The 20-ps-duration output pulses were generated with conversion efficiencies of 30 % and were tunable in the wavelength range 406 - 3170 nm. Later work by Ebrahimzadeh, Hall and Ferguson used a frequency-doubled, modelocked, Q-switched diode-laser-pumped Nd:YLF laser to pump a singly-resonant oscillator based on LiB_3O_5 [53]. This temperature-tuned device was capable of continuous tuning from 664 - 2470 nm and displayed a conversion efficiency of 20 %. In common with the other singly-resonant devices reported, Ebrahimzadeh *et al* measured smooth frequency spectra which were entirely free of any mode-clustering effects. Similar results were also reported by Zhou and co-workers who used a frequency-doubled, modelocked, Q-switched Nd:YAG laser as the pump source for a temperature tuned LiB_3O_5 - based oscillator [54].

Q-switched singly-resonant systems, although displaying superior efficiency and frequency stability, also had inherent disadvantages. The duration and intensity of the picosecond pulses varied across the

Q-switched envelope and the low repetition-rate (≈ 1 Hz - 10 kHz) was not desirable for many applications requiring a high signal-to-noise ratio. Continuous-wave picosecond operation of a singly-resonant OPO was first reported by McCarthy and Hanna who used a frequency-doubled additive-pulse-modelocked diode-pumped Nd:YLF laser to pump a $KTiOPO_4$ - based oscillator [55]. The high-peak powers available from the 2.4-ps-duration pump pulses enabled this device to achieve a signal conversion efficiency of 16 % and transform-limited 1.5-ps pulses were produced with 42 mW of average power. Using a similar pump laser, Hall and co-workers demonstrated a singly-resonant picosecond OPO based on LiB_3O_5, tunable from 650 - 2650 nm and with an overall pump-conversion efficiency of > 50 % [56]. Another singly-resonant continuous-wave oscillator was reported by Chung and Siegman who used the 2.2-ps output pulses from a temporally-compressed cw-modelocked Nd:YAG laser to pump a $KTiOPO_4$ -based OPO [57]. The 2 - 3 ps-duration signal output pulses were produced at average powers of up to 240 mW corresponding to an overall conversion efficiency of 15 %. Finally, a self-modelocked Ti:sapphire laser producing 1.4-ps-duration pulses at an average power of 1.6 W was used by Nebel and co-workers as the pump source for a singly-resonant $KTiOPO_4$ - based OPO [58]. As much as 700 mW total power was produced in the two outputs of this device which were tunable in a wavelength range of 1.052 - 2.871 μm.

Work in synchronously-pumped OPOs had, for many years, relied on picosecond pump lasers as they represented the only sources capable of providing sufficiently large pulse energies. In 1989 Edelstein, Wachman and Tang became the first to demonstrate a high-repetition rate continuous-wave femtosecond OPO using an oscillator based on a thin crystal of $KTiOPO_4$ (KTP) and pumped at the intracavity focus of a dye

laser [59]. This singly-resonant OPO was broadly tunable from 820 - 920 nm and from 1.9 - 2.54 μm and produced 220-fs duration pulses at a repetition frequency of 100 MHz. The addition of intracavity optics compensating for group velocity dispersion effects allowed transform-limited pulses as short as 105 fs to be generated with tunability from 755 - 1040 nm and 1.5 - 3.2 μm being demonstrated [60, 61, 62, 63]. In 1990 an alternative method of producing femtosecond pulses from an OPO was demonstrated by Laenen, Graener and Laubereau who used 0.8-ps pulses from a modelocked Q-switched Nd:glass laser to pump a singly-resonant β-BaB_2O_4 - based OPO [64]. This system suffered from all of the disadvantages of Q-switched picosecond oscillators and typically produced pulses of duration 200 fs with an efficiency of 3 %.

The alignment and operation of the continuous-wave intracavity-pumped OPO required extraordinary extremes of precision and the low power output powers available from the CPM laser were not sufficient to pump an extracavity OPO directly. An important advance was made in 1992 when Mak, Fu and Van Driel demonstrated a femtosecond OPO pumped extracavity by the output of a hybridly modelocked dye laser operating at 645 nm [65]. Also based on KTP, their OPO was capable of generating 220-fs pulses at average signal output powers of 30 mW and was tunable from 1.2 - 1.39 μm. The extracavity pumped configuration allowed independent alignment of the laser and the OPO and was an important intermediary to the Ti:sapphire-pumped femtosecond OPO first demonstrated later in 1992 by Pelouch, Powers and Tang [66, 67]. This and similar OPOs [68, 69] used a KTP crystal cut for critical phase-matching (ie. designed for propagation not parallel to a crystal axis) and produced transform limited pulses as short as 57-fs with average signal powers of up to 340 mW.

As a result of the high average powers available from the self-modelocked Ti:sapphire pump laser, the femtosecond OPO displayed total pump conversion efficiencies of up 50 % and, when configured with high-reflectivity mirrors, average intracavity powers of more than 10 W could be achieved. These characteristics made the Ti:sapphire-pumped OPO an attractive means of producing tunable femtosecond pulses in the visible by using intracavity second-harmonic generation. In 1993 Ellingson and Tang successfully demonstrated an intracavity-frequency-doubled OPO based on KTP and pumped using a high power self-modelocked Ti:sapphire laser. By using angle-tuning they generated output pulses in the visible with durations as short as 95-fs and continuously tunable from 580 - 657 nm [70]. By configuring the OPO with mirrors that were highly-reflecting at the signal wavelength, average output powers as high as 240 mW were generated in the second-harmonic.

For technical reasons connected with their dye-laser origins, all of the Ti:sapphire-pumped femtosecond OPOs which had been demonstrated until 1993 were based on a critical phase-matching geometry using a noncollinear pumping scheme. A non-critical geometry (all waves propagating parallel to crystal axes) would clearly be advantageous as it this would maximise both the gain and the bandwidth available to the signal pulse and simultaneously allow collinear pumping. The first oscillator featuring a non-critical crystal geometry was demonstrated by Kafka, Watts and Pieterse using an LBO-based OPO [71]. By varying the temperature of the LBO crystal the output of their OPO was tunable from 1.3 - 1.5 μm and from 1.63 - 1.95 μm and non-transform-limited pulses as short as 40 fs were produced.

In the same year two femtosecond OPOs were reported which used a KTP crystal in a non-critical geometry. Nebel, Fallnich and Beigang presented a Ti:sapphire-pumped oscillator based on a 6mm-long crystal which was capable of producing 386-fs signal pulses tunable from 1.05 - 1.15 μm with an average output power of 300 mW [72]. Using a shorter crystal Reid, Dudley, Ebrahimzadeh and Sibbett generated transform-limited 40-fs signal pulses from 1.1 - 1.4 μm with average output powers of up to 50 mW [73, 74, 75, 76].

Most recently, as new nonlinear materials became available in 1993 and 1994 Ti:sapphire-pumped femtosecond OPOs were demonstrated based on KTA [77], CTA [78] and RTA [79 - 82], providing wavelength coverage over a wide spectral region including the visible [82]. Using a novel configuration Gale, Hache and Pavlov demonstrated a visible OPO pumped by the second harmonic of a self-modelocked Ti:sapphire laser which used βBBO to extracavity frequency double the pump laser and as the gain medium in the oscillator itself [83]. By employing difference frequency mixing between the pump laser and the output of the OPO femtosecond pulses in the mid-infrared were generated at microwatt power levels by these and other [84] researchers.

The schematic included as Fig. 1.2 shows the wavelength coverage provided directly by continuous-wave femtosecond OPOs reported to date. Clearly, rapid progress in the area of continuous-wave femtosecond OPOs has taken place in only a few years. New materials and new pump wavelengths will make possible the development of femtosecond OPOs capable of continuous tuning across wide spectral ranges including the visible and the 5 - 10 μm region. Table 1.1 (shown on the following pages)

provides a summary of the experiments involving continuous-wave femtosecond OPOs which have been reported in the literature to date.

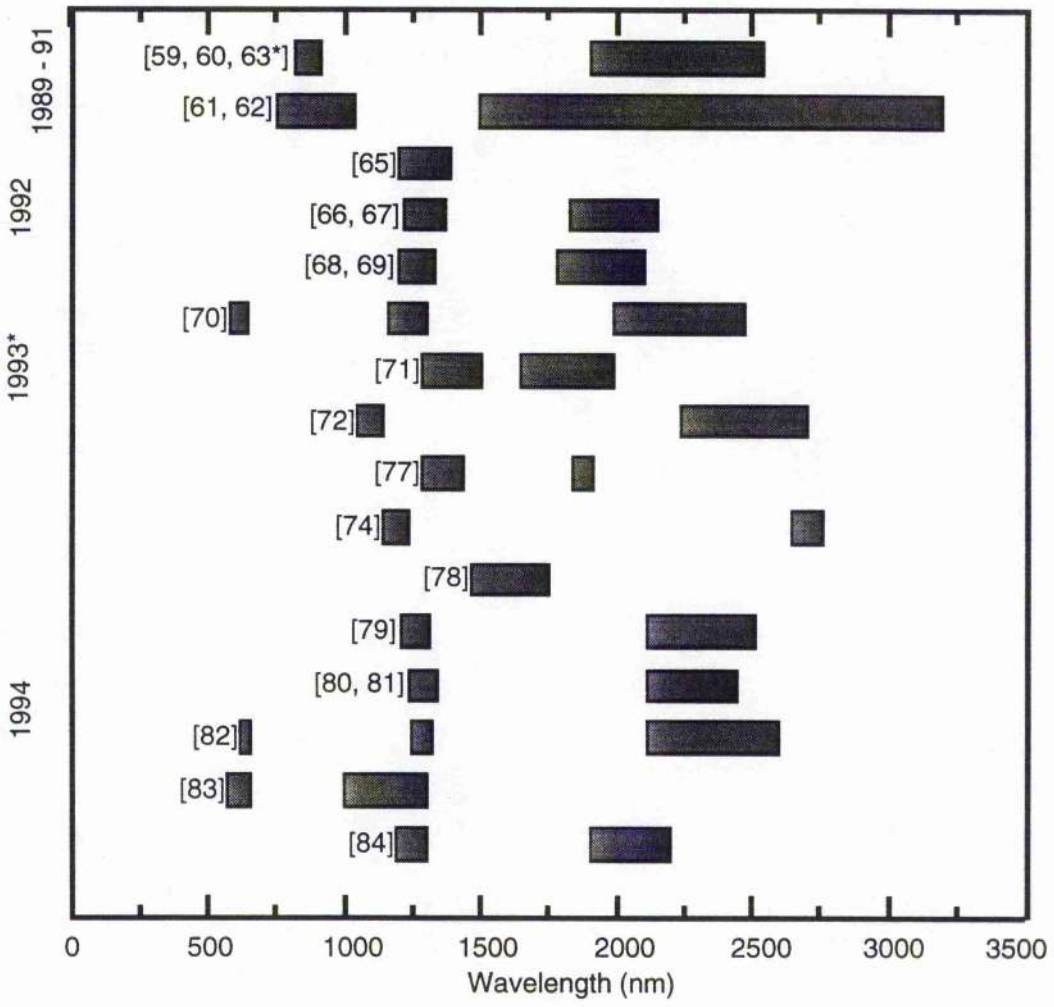

Figure 1.2 *Wavelengths in the visible and infrared generated directly by continuous-wave femtosecond optical parametric oscillators.*

When the work presented in this thesis was begun, the only femtosecond optical parametric oscillator to have already been demonstrated was the intracavity-pumped system reported by Edelstein *et al* [59]. This device required precision alignment and the output powers were extremely low. The then recently-demonstrated self-modelocked

Ti:sapphire laser had yet to be used as a pump source for an OPO and its operation was not well understood. The motivation behind the work presented here was to demonstrate a reliable system delivering reasonably high output powers and free of the restrictions of dye-laser operation.

1.4 Conclusions

In the following chapter the configuration and design will be discussed of the self-modelocked Ti:sapphire laser used as a pump source for the optical parametric oscillators described in later chapters. Chapter 3 will address in detail the design considerations of importance in the construction of a femtosecond optical parametric oscillator and will include a discussion of the choice of nonlinear crystal used as the parametric gain medium. In Chapter 4 results will be presented from a Ti:sapphire-pumped OPO based on the nonlinear material KTP and a discussion of the temporal and spectral output characteristics of the OPO under various operating conditions will be given. A study of soliton propagation in the OPO will be described and operation using a variety of signal and idler cavity geometries will also be included. The work presented in Chapter 5 will describe the configuration of a Ti:sapphire-pumped OPO using the nonlinear material RTA and will also detail the extension of the OPO output into the visible using intracavity frequency-doubling. Finally, in Chapter 6, the work presented in this thesis will be summarised and the implications for future initiatives in the area of femtosecond OPOs will be outlined.

Table 1.1. Summary of cw-femtosecond optical parametric oscillator experiments reported to date.

Pump Laser	*Crystal*	*Tuning*	*Output Power (signal)*	*Efficiency (signal)*	$\Delta\tau_{min}$	*Ref.*
R6G / DODCI CPM Dye λ_0= 620nm	KTP t =1.4mm θ=47° ϕ=0° Noncollinear o→eo	820 - 920nm 1.90 - 2.54μm	2 mW	Intracavity pumped	220 fs	[59]
R6G / DODCI CPM Dye λ_0= 620nm	KTP t =1.4mm θ=47° ϕ=0° Noncollinear o→eo	820 - 920nm 1.90 - 2.54μm	2 mW	Intracavity pumped	105 fs	[60]
R6G / DODCI CPM Dye λ_0= 620nm	KTP t =1.4mm θ=47° ϕ=0° Noncollinear o→eo	755 - 1040nm 1.50 - 3.2μm	2 mW	Intracavity pumped	105 fs	[61]
R6G / DODCI CPM Dye λ_0= 620nm	KTP t =1.4mm θ=53° ϕ=0° Noncollinear o→eo	755 - 1040nm 1.50 - 3.20μm	2 mW	Intracavity pumped	120 fs	[62]
Hybrid Dye λ_0= 645nm	KTP t =1.5mm Noncollinear o→eo	1.2 - 1.34μm 1.24 - 1.39μm	30 mW	10.7%	220 fs	[65]
Ti:sapphire λ_0 = 790nm	KTP t =1.15mm θ=47.5° ϕ=0° Noncollinear o→eo	1.22 - 1.37μm 1.82 - 2.15μm	215 mW	17.2%	75 fs	[66]
Ti:sapphire λ_0 = 765nm	KTP t =1.5mm θ=67° ϕ=0° Noncollinear o→eo	1.2 - 1.34μm 1.78 - 2.1μm	100 mW	16.7%	103 fs	[69]
Ti:sapphire λ_0 = 790nm	KTP t =1.5mm θ=67° ϕ=0° Noncollinear o→eo	1.2 - 1.34μm 1.78 - 2.1μm	185 mW	23.1%	62 fs	[68]
Ti:sapphire λ_0 = 790nm	KTP t =1.15mm θ=47.5° ϕ=0° Noncollinear o→eo	1.22 - 1.37μm 1.82 - 2.15μm	340 mW	13.6%	57 fs	[67]
R6G / DODCI CPM Dye λ_0= 620nm	KTP t =1.4mm θ=47° ϕ=0° Noncollinear o→eo	820 - 920nm 1.9 - 2.54μm	2 mW	Intracavity pumped	100 fs	[63]

Table 1.1. cont'd, Summary of cw-femtosecond optical parametric oscillator experiments reported to date.

Pump Laser	*Crystal*	*Tuning*	*Output Power (signal)*	*Efficiency (signal)*	$\Delta\tau_{min}$	*Ref.*
Ti:sapphire λ_0 = 790nm	KTP t =1.5mm θ=45° ϕ=0° Noncollinear o→eo 47μm βBBO oo→e	580 - 657nm* 1.16 - 1.314μm 1.98 - 2.4μm	240 mW* OPO HR	11.4%*	95 fs * 120 fs	[70]
Ti:sapphire λ_0 = 780nm	LBO θ=90° ϕ=0° Collinear e→oe	1.3 - 1.5μm 1.63 - 1.95μm	250 mW	12.5%	40 fs	[71]
Ti:sapphire λ_0 = 785nm	KTP t =6.0mm θ=0° ϕ=0° Collinear e→oe	1.05 - 1.15μm 2.24 - 2.7μm	300 mW	30%	386 fs	[72]
Ti:sapphire λ_0 = 780nm	KTA t =1.47mm θ=50° ϕ=0° Noncollinear o→eo	1.29 - 1.44μm 1.83 - 1.91μm	75 mW	7.5%	85 fs	[77]
Ti:sapphire λ_0 = 830nm	KTP t =1.5mm θ=90° ϕ=0° Collinear o→eo	1.1 - 1.4μm 2.30 - 3.38μm	135 mW	15 %	40 fs	[74, 73, 75, 76]
Ti:sapphire λ_0 = 790nm	CTA t =1.0mm θ=90° ϕ=0° Collinear o→eo	1.46 - 1.74μm	100 mW	9.1%	64 fs	[78]
Ti:sapphire λ_0 = 800nm	RTA θ=53° ϕ=0° Noncollinear o→eo	1.2 - 1.31μm 2.1 - 2.5μm	100 mW	6.7 %	85 fs	[79]
Ti:sapphire λ= 785 - 855nm	RTA t =2.0mm θ=90° ϕ=0° Collinear o→eo	1.23 - 1.34 μm 2.1 - 2.43 μm	185 mW	21 %	67 fs	[80, 81]
Ti:sapphire λ= 780 - 880nm	RTA t =2.0mm θ=90° ϕ=0° Collinear o→eo βBBO t =200μm oo→e	620 - 660 nm* 1.24 - 1.32 μm 2.1 - 2.59μm	170 mW* OPO HR	15.5%*	60 fs *	[82]
SHG Ti:sapphire λ_0 = 410nm	βBBO t =2.0mm θ=32° Noncollinear e→oo	575 - 660nm 1.0 –1.3 μm	120 mW	13.3 %	59 fs	[83]
Ti:sapphire λ_0 = 780nm	LBO θ=90° ϕ=0° Collinear e→oe	1.18 - 1.3μm 1.9 - 2.2μm (2.6 - 4.3 μm)	450 mW - (50 μW)	22.5 % - (0.0025 %)	65 fs (180 fs)	[84]

* *Second harmonic of the resonant signal wave*

References

1. See for example, M. Nisoli, A. Cybo-Ottone, S. De Silvestri, V. Magni, R. Tubino, S. Luzzati, A. Musco and D. Commoretto, Solid State Communications, **86**, 583 (1993)

2. See for example, A. Tomita, J. Shah, J. E. Cunningham, S. M. Goodnick, P. Lugli and S. L. Chuang, Physical Review B **48**, 5708 (1993)

3. W. -Z. Lin, R. W. Schoenlein, J. G. Fujimoto and E, P. Ippen, IEEE J. Quantum Electron. **24**, 267 (1988)

4. J. Shah, B. Deveaud, T. C. Damen, W. -T. Tsang, A. C. Gossard and P. Lugli, Phys. Rev. Lett. **59**, 222 (1987)

5. J. A. Valdamis, Electron. Lett. **23**, 1308 (1987)

6. C. J. Madden, R. A. Marsland, M. J. W. Rodwell and D. M. Bloom, Appl. Phys. Lett. **54**, 1019 (1989)

7. M. Dantus, R. M. Bowman and A. H. Zewail, Nature **343**, 737 (1990)

8. M. Gruebele and A. Zewail in: *Physics Today*, p24 May 1990

9. M. Dantus, M. J. Rosker and A. H. Zewail, J. chem. Phys. **87**, 2395 (1987)

10. M. J. Rosker, M. Dantus and A. H. Zewail, J. chem. Phys. **89**, 6113; 6128 (1988)

11. J. Zhou, G. Taft, C. Shi, H. C. Kapteyn and M. M. Murnane, Paper MA2 in: Ultrafast Phenomena **8**, 4 (1994)

12. R. L. Fork, B. I. Greene and C. V. Shank, Appl. Phys. Lett. **38**, 671 (1981)

13. E. P. Ippen, C. V. Shank and A. Dienes, Appl. Phys. Lett. **21**, 348 (1972)

14. H. Vanherzeele, R. Torti and J.-C. Diels, Appl. Opt. **23**, 4182 (1984)

15. M. C. Nuss, R. Leonhardt and W. Zinth, Opt. Lett. **10**, 559 (1985)

16. M. D. Dawson, T. F. Boggess, D. W. Garvey and A. L. Smirl, Opt. Comm. **60**, 79 (1986)

17. J. Dobler, H. H. Shultz and W. Zinth, Opt. Comm. **57**, 407 (1986)

18. M. D. Dawson, T. F. Boggess and A. L. Smirl, Opt. Lett. **12**, 254 (1987)

19. M. D. Dawson, T. F. Boggess and A. L. Smirl, IEEE J. Q. El. Lett.

20. P. M. W. French and J. R. Taylor, Opt. Lett. **13**, 470 (1988)

21. M. D. Dawson, T. F. Boggess and A. L. Smirl, Opt. Lett. **12**, 590 (1987)

22. R. L. Fork, C. V. Shank, C. Hirlimann, R. Yen and W. J. Tomlinson, Opt. Lett. **8**, 1 (1983)

23. W. H. Knox, M. C. Downer, R. L. Fork and C. V. Shank, Opt. Lett. **9**, 552 (1984)

24. D. S. Moore and S. C. Schmidt, Opt. Lett. **12**, 480 (1987)

References continued,

25. A. Migus, A. Antonetti, J. Etchepare, D. Hulin and A. Orszag, Journal of the Optical Society of America B **2**, 584 (1985)

26. L. F. Mollenauer and R. H. Stolen, Opt. Lett. **9**, 13 (1984)

27. F. M. Mitschke and L. F. Mollenauer, Opt. Lett. **12**, 407 (1987)

28. K. J. Blow and D. Wood, J. Opt. Soc. Am. B **5**, 629 (1988)

29. P. N. Kean, X. Zhu, D. W. Crust, R. S. Grant, N. Langford and W. Sibbett, Opt. Lett. **14**, 39 (1989)

30. X. Zhu, P. N. Kean and W. Sibbett, Opt. Lett. **14**, 1192 (1989)

31. J. Mark, L. Y. Liu, K. L. Hall, H. A. Haus and E. P. Ippen, Opt. Lett. **14**, 48 (1989)

32. F. Ouellette and M. Piché, Opt. Comm. **60**, 99 (1986)

33. G. T. Kennedy, R. S. grant, W. E. Sleat and W. Sibbett, Opt. Lett. **18**, 208 (1993)

34. J. Goodberlet, J. Wang, J. G. Fujimoto and P. A. Schulz, Opt. Lett. **14**, 1125 (1989)

35. D. E. Spence and W. Sibbett, J. Opt. Soc. Am. B **8**, 2053 (1991)

36. D. E. Spence, P. N. Kean and W. Sibbett, Opt. Lett. **16**, 42 (1991)

37. R. E. Bridges, R. W. Boyd and G. P. Agrawal, Opt. Lett. **18**, 2026 (1993)

38. G. Cerullo, S. De Silvestri, V. Magni and L. Pallaro, Opt. Lett. **19**, 807 (1994)

39. For example, the *Spectra Physics Tsunami* laser

40. J. D. Kafka, M. L. Watts and J. -W. Pieterse, IEEE J. Quant. Electron. **28**, 2151 (1992)

41. J. M. Evans, D. E. Spence, W. Sibbett, B. H. T. Chai and A. Miller, Opt. Lett. **17**, 1447 (1992)

42. A. Sennaroglu, C. R. Pollock and H. Nathel, Opt. Lett. **18**, 826 (1993)

43. A. Sennaroglu, C. R. Pollock and H. Nathel, Opt. Lett. **19**, 390 (1994)

44. K. Burneika, M. Ignatavicius, V. Kabelka, A. Piskarskas and A. Stabinis, IEEE J. Q. Electron. **QE-8**, 574 (1972)

45. A. Piskarskas, V. Smil'gyavichyus and A. Umbrasas, Sov. J. Quant. Electron. **18**, 155 (1988)

46. M. Ebrahimzadeh, G. P. A. Malcolm and A. I. Ferguson, Opt. Lett. **17**, 183 (1992)

47. A. S. Piskarskas, V. Smil'gyavichyus, A. Umbrasas, J. P. Juodisius, A. S. L. Gomes and J. R. Taylor, Opt. Lett. **14**, 557 (1989)

48. G. T. Maker and A. I. Ferguson, Appl. Phys. Lett. **56**, 1614 (1990)

References continued,

49. M. Ebrahimzadeh, G. J. Hall and A. I. Ferguson, Appl. Phys. Lett. **60**, 1421 (1992)

50. A. Piskarskas, V. Smilgevicius, A. Umbrasas, A. Fix and R. Wallenstein, Opt. Comm. **77**, 335 (1990)

51. L. J. Bromley, A. Guy and D. C. Hanna, Opt. Comm. **70**, 350 (1989)

52. S. Burdulis, R. Grigonis, A. Piskarskas, G. Sinkevicius, V. Sirutkaitis, A. Fix, J. Nolting and R. Wallenstein, Opt. Comm. **74**, 398 (1990)

53. M. Ebrahimzadeh, G. J. Hall and A. I. Ferguson, Opt. Lett. **17**, 652 (1992)

54. H. Zhou, J. Zhang, T. Chen, C. Chen and Y. R. Shen, Appl. Phys. Lett. **62**, 1457 (1993)

55. M. J. McCarthy and D. C. Hanna, Opt. Lett. **17**, 402 (1992)

56. G. J. Hall, M. Ebrahimzadeh, A. Robertson, G. P. A. Malcolm and A. I. Ferguson, J. Opt. Soc. Am. B **10**, 2168 (1993)

57. J. Chung and A. E. Siegman, J. Opt. Soc. Am. B **10**, 2201 (1993)

58. A. Nebel, C. Fallnich, R. Beigang and R. Wallenstein, J. Opt. Soc. Am. B **10**, 2195 (1993)

59. D. C. Edelstein, E. S. Wachman and C. L. Tang, Appl. Phys. Lett. **54**, 1728 (1989)

60. E. S. Wachman, W. S. Pelouch and C. L. Tang, J. Appl. Phys. **70**, 1893 (1991)

61. C. L. Tang, E. S. Wachman and W. S. Pelouch, Paper CFM5 CLEO (1991)

62. E. S. Wachman, D. C. Edelstein and C. L. Tang, Opt. Lett. **15**, 136 (1990)

63. J. A. Moon, IEEE J. of Q. El. **29**,265 (1993)

64. R. Laenen, H. Graener and A. Laubereau, Opt. Lett. **15**, 971 (1990)

65. G. Mak, Q. Fu and H. M. van Driel, Appl. phys. Lett. **60**, 542 (1992)

66. W. S. Pelouch, P. E. Powers and C. L. Tang, Paper CPD14-1/27, CLEO (1992)

67. W. S. Pelouch, P. E. Powers and C. L. Tang, Opt. Lett. **17**, 1070 (1992)

68. Q. Fu, G. Mak and H. M. van Driel, Opt. Lett. **17**, 1006 (1992)

69. Q. Fu, G. Mak and H. M. van Driel, Paper CWD1 CLEO (1992)

70. R. J. Ellingson and C. L. Tang, Opt. Lett. **18**, 438 (1993)

71. J. D. Kafka, M. L. Watts and J. W. Pieterse, Paper CPD 32-1/68 CLEO (1993)

72. A. Nebel, C. Fallnich and R. Beigang, Paper JWB5 CLEO (1993)

73. D. T. Reid, J. M. Dudley, M. Ebrahimzadeh and W. Sibbett, Paper 107 in the Technical Digest of the Eleventh UK National Quantum Electronics Conference, Belfast (1993)

References continued,

74. J. M. Dudley, D. T. Reid, M. Ebrahimzadeh and W. Sibbett, Opt. Comm. **104**, 419 (1994)

75. D. T. Reid, J. M. Dudley, M. Ebrahimzadeh and W. Sibbett, J. Mod. Opt. **41**, 1231 (1994)

76. D. T. Reid, J. M. Dudley, M. Ebrahimzadeh and W. Sibbett, Opt. Lett. **19**, 825 (1994)

77. P. E. Powers, S. Ramakrishna and C. L. Tang, Opt. Lett. **18**, 1171 (1993)

78. P. E. Powers, C. L. Tang and L. K. Cheng, Opt. Lett. **19**, 37 (1994)

79. P. E. Powers, C. L. Tang and L. K. Cheng, Paper CWM4 in: Conference on Lasers and Electro-Optics **8**, 251 (1994)

80. D. T. Reid, M. Ebrahimzadeh and W. Sibbett, Postdeadline paper CPD 1.3 in: Postdeadline technical digest of the European Conference on Lasers and Electro-Optics p 5 (1994)

81. D. T. Reid, M. Ebrahimzadeh and W. Sibbett, Opt. Lett. **19** accepted (1994)

82. D. T. Reid, M. Ebrahimzadeh and W. Sibbett, J. Opt. Soc. Am. B., submitted (1994)

83. G. M. Gale, F. Hache and L. I. Pavlov, Paper WC1 in: Ultrafast Phenomena **7**, 333 (1994); Paper CThI2 in: Conference on Lasers and Electro-Optics **8**, 318 (1994); T. J. Driscoll, G. M. Gale and F. Hache, Opt. Comm. **110**, 638 (1994)

84. J. D. Kafka, M. L. Watts and J. W. Pieterse, Paper CWI6 in: Conference on Lasers and Electro-Optics **8**, 237 (1994)

2.1 Introduction

The self-modelocked Ti:sapphire laser described briefly in *Chapter 1* has, in only a few years, become the standard laboratory source of high-average-power cw-modelocked femtosecond pulses in the far-red and near-infrared. In this chapter, a detailed description is given of the self-modelocked Ti:sapphire laser used as the pump source for the experimental femtosecond optical parametric oscillators (OPOs) described later in this thesis. A discussion of the techniques used to measure the temporal and spectral characteristics of the modelocked output of the laser is also included. The chapter begins with a review of linear and nonlinear pulse propagation in transparent optical media which introduces many of the effects referred to in the discussion of the pump laser.

2.2 Optical pulse propagation in linear and nonlinear media

The understanding of the propagation and interaction of optical pulses in linearly and nonlinearly dispersive systems is of great importance in the design of modelocked lasers, frequency-conversion systems and other technologies such as optical fibre communications. This section begins by examining the effects of material dispersion on the shape and velocity of a pulse propagating in a system displaying a linear response to an electric field. Phenomena such as spectral broadening and self-focusing are described later in a discussion of propagation in nonlinear systems.

Pulse propagation in linear systems

When a polarised electric field, E , interacts with an atomic medium, a corresponding polarisation, P, is induced as the atomic nuclei shift towards the direction of the applied field and the electrons move in the oppposite direction. The frequency-dependent response of the system is characterised by the atomic susceptibility, $\chi(\omega)$, which is a complex quantity relating the applied and polarisation fields by,

$$P(\omega) = \chi(\omega)\,\varepsilon_o\,E(\omega) \tag{1}$$

where ε_o is the dielectric permeability of free space. The real part of $\chi(\omega)$ corresponds to a frequency-dependent phase relation between the applied field and the induced polarisation and is used to define the refractive index as,

$$n(\omega) = \sqrt{1 + \chi'(\omega)}\ . \tag{2}$$

In contrast, the imaginary component describes absorption of the applied field due to atomic resonances in the medium. The frequency dependence of the refractive index is known as *dispersion* and has a number of consequences for the propagation of optical pulses having a finite frequency bandwidth.

It is well known that Fourier transforming a Gaussian envelope function in time results in a Gaussian envelope in frequency. Similarly, a modelocked pulse of finite duration has a spectrum containing a range of frequencies (or covering a band of wavelengths). The duration of the shortest pulse which can be supported by a particular frequency bandwidth is described by the *time-bandwidth product* ($\Delta\nu\Delta\tau$) which has a unique value for specific pulse envelope shapes. For Gaussian pulses $\Delta\nu\Delta\tau$

≈ 0.44 when $\Delta\nu$ and $\Delta\tau$ are measured at the pulse intensity full-width half-maximum (FWHM) positions.

Figure 2.1 illustrates the time-varying amplitudes and the power spectra of two Gaussian pulses of identical durations. The pulse shown in Fig. 2.1(a) and (b) has a time-bandwidth product of 0.44 and is therefore *transform-limited* . The time-bandwidth product of the second pulse shown in (c) and (d) is ≈ 4.4 indicating that this pulse is *chirped* ie. has a time-varying instantaneous frequency. A pulse of duration ≈ 10 times shorter could therefore be supported by the available bandwidth.

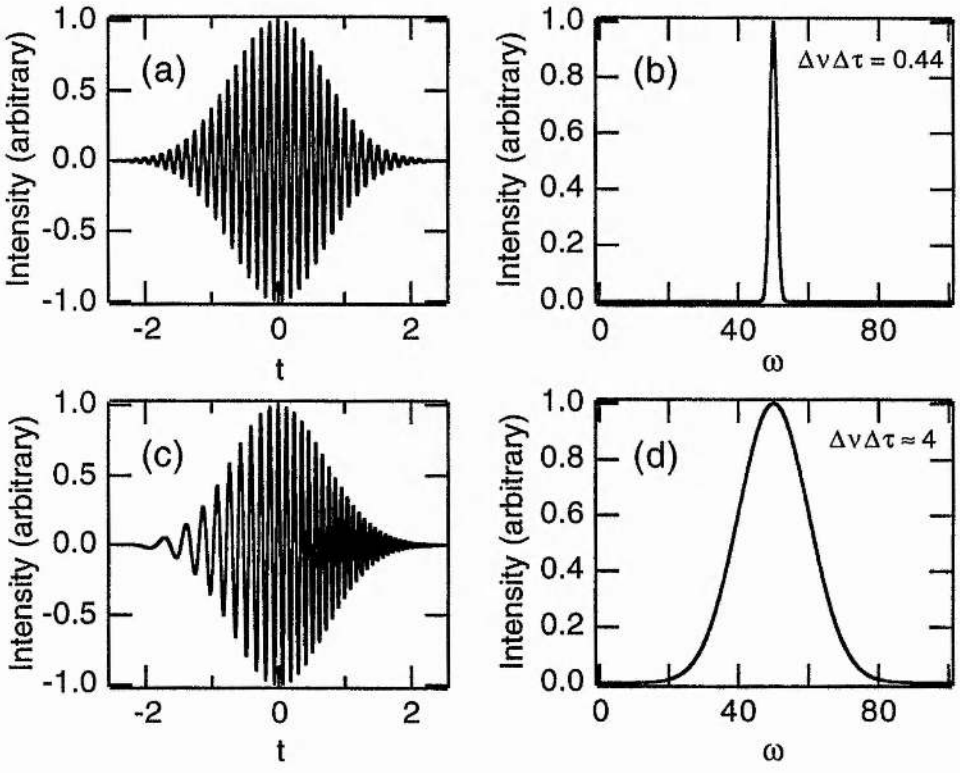

Figure 2.1 Amplitude and spectrum of an unchirped Gaussian pulse (a, b) and of a pulse with linear chirp (c, d)

In a dispersive system, each frequency component within a pulse travels at a unique phase velocity given by ω/k where k $(=2\pi n(\omega)/\lambda_o)$ is the wavenumber inside the medium. Pulse broadening occurs as faster components extend the leading edge of the pulse envelope while slower components retard the trailing edge. The instantaneous velocity of the centre of the pulse envelope is known as the *group velocity* and is given by,

$$v_g = 1 / \left(\frac{dk}{d\omega}\right)_{\omega=\omega_0} . \tag{3}$$

For a pulse to propagate without dispersive broadening, all parts of the pulse envelope must travel with the same velocity. *Group velocity dispersion* (GVD) describes the change in the pulseshape due to different regions of the envelope propagating with different group velocities and is given by,

$$\text{GVD} = \left(\frac{d^2k}{d\omega^2}\right)_{\omega=\omega_0} . \tag{4}$$

Group-velocity dispersion in optical systems is often responsible for broadening pulses to durations greater than the transform limit by introducing a linear phase change or chirp across the pulse. The sign of GVD is positive for wavelengths below ~1.5 μm in most materials and becomes increasingly negative for longer wavelengths. In solid-state modelocked lasers such as the Ti:sapphire it is the gain medium itself which contributes the greatest positive dispersion in the laser resonator. Other intracavity elements such as an acousto-optic modelocker, prisms and mirrors also contribute positive dispersion. To obtain the shortest pulses from the laser the net cavity group-velocity dispersion must be close to zero. A practical method for providing adjustable negative GVD in laser cavities was suggested by Fork, Martinez and Gordon [1] who showed that suitably positioned pairs of prisms could provide negative group-velocity dispersion even when the material dispersion of the prisms

themselves was positive. The prisms are oriented for minimum deviation and at Brewster's angle as illustrated in Fig. 2.2.

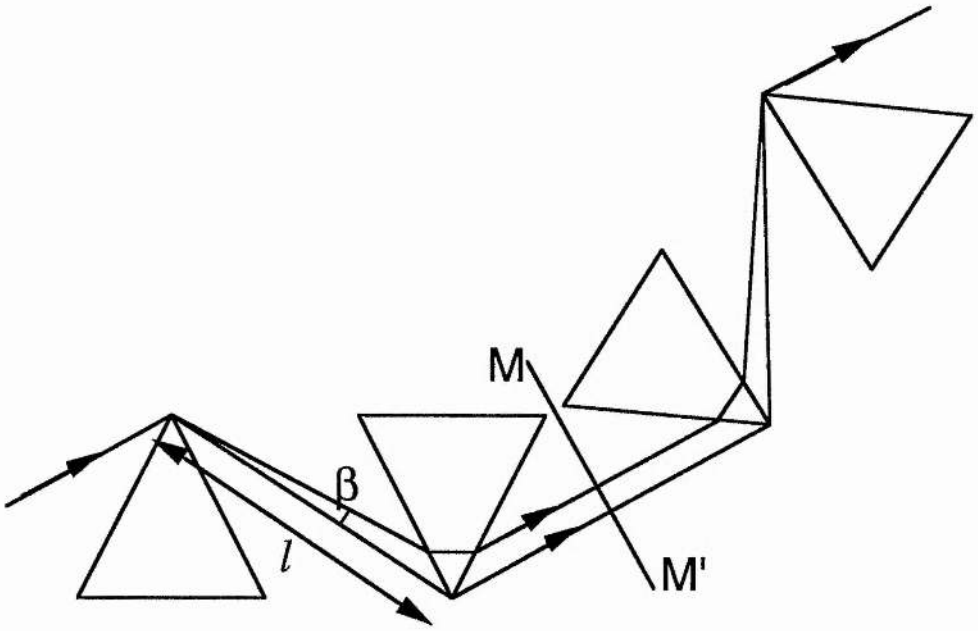

Figure 2.2 Four-prism sequence having negative group-velocity dispersion. (taken from ref. [1])

Continuous adjustment of dispersion from negative through zero can be achieved by translating individual prisms to vary the amount of intracavity glass. The group-velocity dispersion of the prism arrangement is described in terms of the second derivative of the optical path, P, with respect to the free-space wavelength. As a function of prism separation l, material dispersion $n(\lambda)$ and the ray divergence after the first prism β, the dispersion is given by,

$$\frac{d^2P}{d\lambda^2} = 4l \left\{ \left[\frac{d^2n}{d\lambda^2} + \left(2n - \frac{1}{n^3}\right)\left(\frac{dn}{d\lambda}\right)^2 \right] \sin\beta - 2\left(\frac{dn}{d\lambda}\right)^2 \cos\beta \right\} \qquad (5)$$

The positive material dispersion associated with an intracavity element of thickness t and index n is given by,

$$\frac{d^2P}{d\lambda^2} = t\left(\frac{d^2n}{d\lambda^2}\right). \tag{6}$$

Using these expressions the net group-velocity dispersion can be evaluated for a particular laser cavity allowing resonators for femtosecond pulses to be designed which contribute minimally to pulse-broadening. The application of this technique in the configuration of the Ti:sapphire pump laser will be detailed later in this chapter.

The discussion included here has dealt only with the effects and correction of group-velocity dispersion associated with the second derivative of phase with respect to frequency or *second-order dispersion*. Compensation for third-order dispersion has recently been demonstrated in self-modelocked Ti:sapphire lasers by careful selection of prism materials [2, 3, 4] or by using specially coated dielectric mirrors [5] and has allowed the generation of sub-20 fs pulses to become widespread.

Pulse propagation in nonlinear systems

In the linear systems discussed already, the propagation of an electromagnetic wave in a material resulted in a polarisation directly proportional to the instantaneous electric field strength of the wave. If the wave amplitude is sufficiently intense then the polarisation response of the medium may become nonlinear with respect to the applied field. The polarisation can be written as a power series expansion in the applied field:

$$P(\omega) = \chi_{(1)}\varepsilon_o E + \chi_{(2)}\varepsilon_o E^2 + \chi_{(3)}\varepsilon_o E^3 + \ldots, \tag{7}$$

where $\chi_{(1)}$ is the linear susceptibility introduced earlier and $\chi_{(2)}$ and $\chi_{(3)}$ are frequency-dependent nonlinear susceptibilities responsible for phenomena such as harmonic generation and the intensity-dependent

behaviour of the refractive index, respectively. Frequency conversion and pulse-shaping effects relying on $\chi_{(2)}$ will be described in depth in Chapter 3. The remaining discussion concerns nonlinear effects arising from the $\chi_{(3)}$ term in the polarisation and the consequences of these effects on a pulse propagating in the presence of linear dispersion.

If the total susceptibility is defined as $\boldsymbol{P} / \varepsilon_0 \boldsymbol{E}$, then it is easy to show that the refractive index has a nonlinear dependence on field strength described by,

$$n = n_0 + n_2 E^2 \qquad \text{where, } n_2 \approx \frac{\chi_{(3)}}{2n_0} . \tag{8}$$

The nonlinear refractive index n_2 can be exploited in a *Kerr cell modulator* where a high-voltage electric signal is applied to a material with a large third-order susceptibility to modulate the refractive index seen by an optical wave. Using this technique, either phase or amplitude modulation of the wave can be achieved.

The field associated with an intense optical wave can itself be capable of modulating the refractive index of a medium, resulting in an intensity dependence of the refractive index known as the *Kerr effect*. One important consequence of this effect is the phenomena of *self-focusing* where an intense beam induces a weak positive lens in the optical medium. This is understood by considering the phase velocity of the wavefront as it propagates through the medium as illustrated in Figure 2.3. The centre of the beam, which is most intense, sees the highest index of refraction causing the centre of the wavefront to be retarded more than the edges and focusing results.

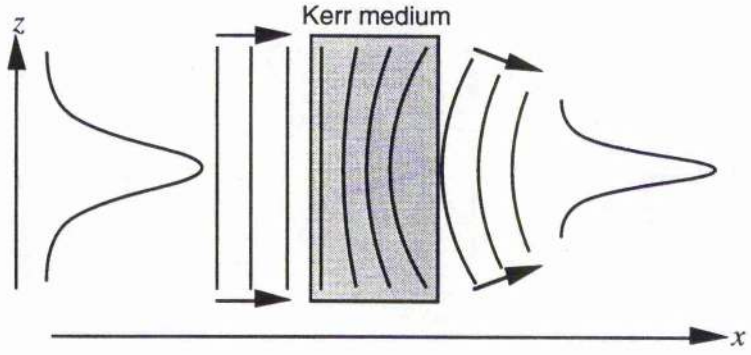

Figure 2.3 Self-focusing of an intense beam due to the optical Kerr effect

The optical Kerr effect can modify an optical signal not only spatially, but also in the time domain. *Self-phase-modulation* (SPM) occurs in optical pulses when the centre of the pulse experiences a larger refractive index variation or phase-shift than the leading or trailing edges. The instantaneous phase shift of the pulse in propagating through a length l of an optical medium will be,

$$\phi(t) = -\frac{2\pi n(t) l}{\lambda}, \tag{9}$$

which results in an instantaneous frequency chirp described by,

$$\frac{d\phi}{dt} = -\frac{2\pi n_2 l}{\lambda}\frac{dI}{dt} \tag{10}$$

This chirp is not linearly distributed across the pulse since it is proportional to the rate of change of the pulse intensity as illustrated in Figure 2.4.

Self-phase-modulation broadens the frequency bandwidth of the pulse by increasing the frequency on the trailing (high-frequency) edge and lowering the frequency on the leading (low-frequency) edge. In the presence of positive group-velocity dispersion the pulse will broaden very rapidly as the difference in frequency between the leading and trailing

edges is increased. In a medium possessing negative group-velocity dispersion, a pulse chirped by SPM is compressed since lower frequency components travel slower and higher frequencies faster. This retards the leading edge of the pulse and accelerates the trailing edge. The resulting duration can be significantly shorter than that of the original unchirped pulse since SPM can substantially expand the pulse frequency bandwidth.

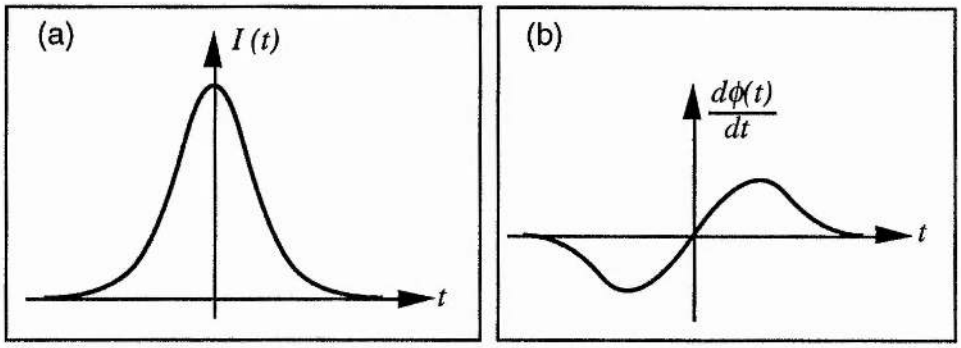

Figure 2.4 Pulse intensity envelope (a) and subsequent frequency chirp resulting from self-phase-modulation (b)

As modelocked lasers are systems in which the resonant pulse can experience both SPM and negative GVD the resulting equilibrium is of importance in the understanding of the factors determining the output pulse duration of the laser. Solution of the *nonlinear Schrödinger equation* provides a quantitative method of analysing pulse propagation through a nonlinear dispersive optical medium. Written in a differential form the nonlinear Schrödinger equation is,

$$\left[\frac{\partial}{\partial z} + k'\frac{\partial}{\partial t} - j\frac{k''}{2}\frac{\partial^2}{\partial t^2} + j\frac{\beta_2 |E^2|}{2}\right]E(z,t) = 0, \qquad (11)$$

where k' and k'' are the first and second derivatives of k with respect to ω. The terms in k' and k'' represent group velocity and group-velocity dispersion respectively and β_2 is a term describing the optical Kerr effect in the medium.

Two solutions of the nonlinear Schrödinger equation are of particular interest in the study of optical pulse propagation. A pulse propagating in a medium with positive dispersion will be described by a *dispersive* solution of the equation and will broaden as it travels through a medium. An intense pulse may simultaneously aquire substantial frequency chirp and, on leaving the medium, can be compressed to shorter than its original duration using a suitable dispersive element such as a grating pair. At low pulse intensities dispersive broadening can also occur when the medium is negatively dispersive but, in the case of a pulse of sufficiently high intensity, self-phase-modulation can result in steady compression of the centre of the pulse. In this way an equilibrium is reached where nonlinear effects concur with linear dispersion to produce a pulse whose shape does not vary as the pulse propagates. This *non-dispersive* solution of the nonlinear Schrödinger equation is an example of a first-order *soliton* and corresponds to a pulse having a $\mathrm{sech}^2(t)$ intensity profile. In a dispersion-compensated modelocked laser such as the self-modelocked Ti:sapphire the pulse evolution is often referred to as *solitonlike* since the pulse shape is determined by the combined effects of SPM in the gain medium and linear dispersion in the rest of the resonator. The pulse cannot however be generally referred to as a soliton because the effects of SPM and GVD are localized and not distributed throughout the whole cavity.

Higher-order soliton solutions of the nonlinear Schrödinger equation can also exist. Instead of a constant temporal and spectral profile the duration and bandwidth of these pulses varies periodically at a rate described by the *soliton frequency* . Figure 2.5 illustrates the temporal evolution of a third-order soliton over a time equal to one soliton period.

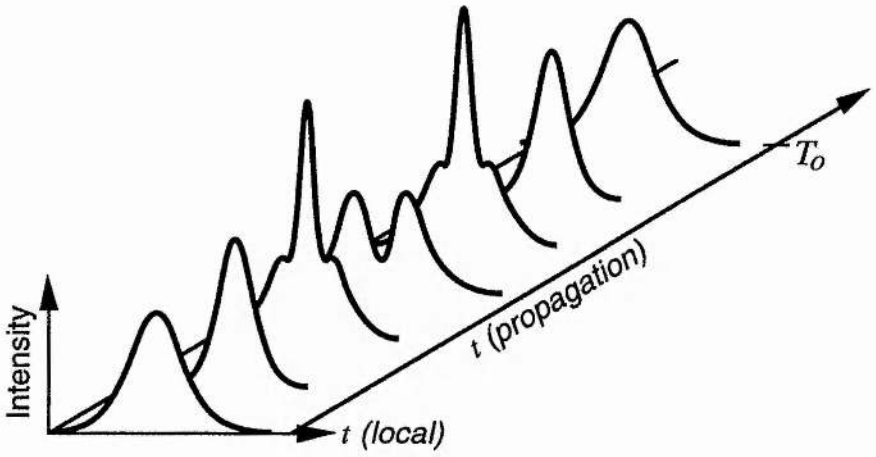

Figure 2.5 *Temporal evolution of a third-order soliton over the soliton period*

Periodic pulse breakup and restoration at the soliton frequency has been observed experimentally in negatively dispersive optical fibres [6] and similar behaviour in a femtosecond optical parametric oscillator is described in detail in Chapter 4 of this thesis.

2.3 The Ti:sapphire gain medium

In common with many other solid-state laser media, Ti:sapphire ($Ti:Al_2O_3$) is a uniaxial crystal consisting of a transparent solid host (Al_2O_3) doped with a small percentage of impurity ions (Ti^{3+}). The host material, sapphire, exists as an octahedral crystal with six O^{2-} ions lying adjacent to each Al^{3+} site. The structure of $Ti:Al_2O_3$, where Ti^{3+} ions are substituted for Al^{3+} ions at a small percentage (~0.1 %) of sites, is illustrated by Figure 2.6.

Ti:sapphire crystals are commonly grown by the Czochralski method using an iridium crucible initially prepared with TiO_2 and Al_2O_3 in solid

form [7]. Growth takes place in an atmosphere of nitrogen gas and is initiated by touching an oriented sapphire crystal onto the top of the melt.

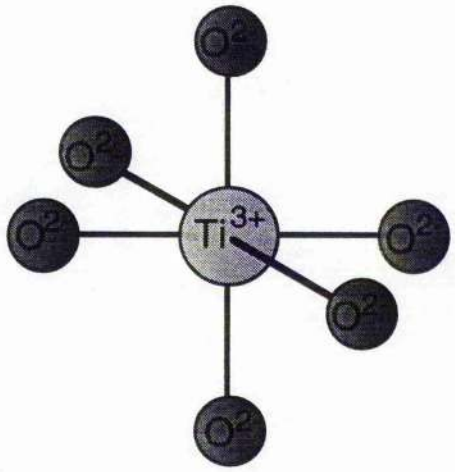

Figure 2.6 *Octahedral arrangement of O^{2-} ions around the laser-active Ti^{3+} ion in Ti:Al_2O_3*

Above a temperature of 1750°C, Ti^{3+} ions are formed as Ti_2O_3 by a dissociation reaction described as,

$$2TiO_2 \rightarrow Ti_2O_3 + \frac{1}{2}O_2. \qquad (12)$$

When a temperature of 2050°C is reached the liquid Ti_2O_3 then mixes with the molten Al_2O_3 present and, by drawing the sapphire seed crystal at a rate of 0.5 cm/h, good quality Ti:sapphire crystals as long as 30 cm and with doping concentrations as high as 0.1 % can be obtained after anealing.

Laser action in Ti:sapphire was first reported in 1982 [8] and was attributed to the presence of the Ti^{3+} ion. In isolation the Ti^{3+} ion has an electronic configuration of $1s^2 2s^2 2p^6 3s^2 3p^6 3d^1$. However, within the Al_2O_3 lattice, the strong cubic field from the O^{2-} ions surrounding an octahedral site splits the energy levels into triply degenerate $^2T_2$ ground state and a

doubly degenerate ^2E excited state [9] as illustrated in Fig. 2.7. Furthermore, the field associated with the trigonal arrangement of Al^{3+} ions splits the ground $^2T_2$ state into two levels and the lower of these is split into a further two levels by the spin-orbit interaction.

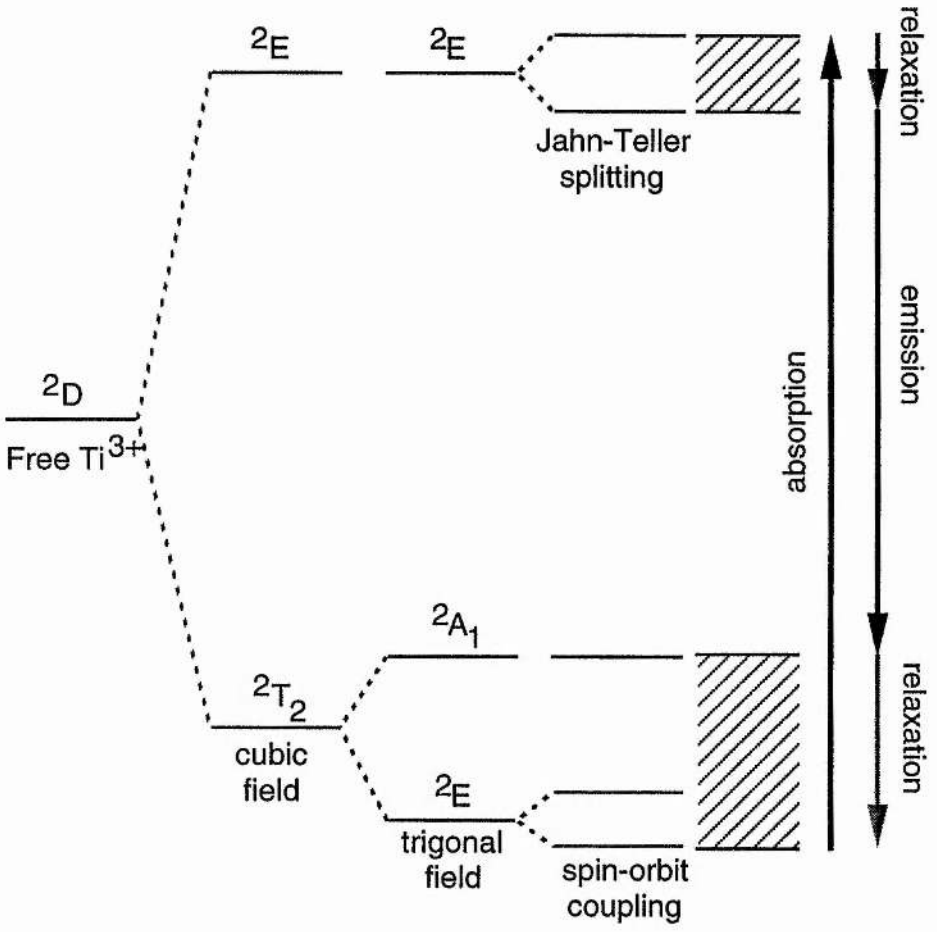

Figure 2.7 Energy level diagram of the laser transition in Ti:Al_2O_3

Absorption from the ground $^2T_2$ state to the ^2E excited state occurs in the visible around a wavelength of 500 nm and is characterised by a dual-peaked spectrum caused by Jahn-Teller splitting. Fluorescence from the $^2T_2$ to ^2E transition occurs from 600 - 1100 nm and has been measured to have a lifetime of 3.15 μs [10]. The absorption and fluorescence spectra measured by Moulton [10] for polarisations parallel (π) and orthogonal (σ) to the crystal *c* -axis are reproduced in Fig. 2.8.

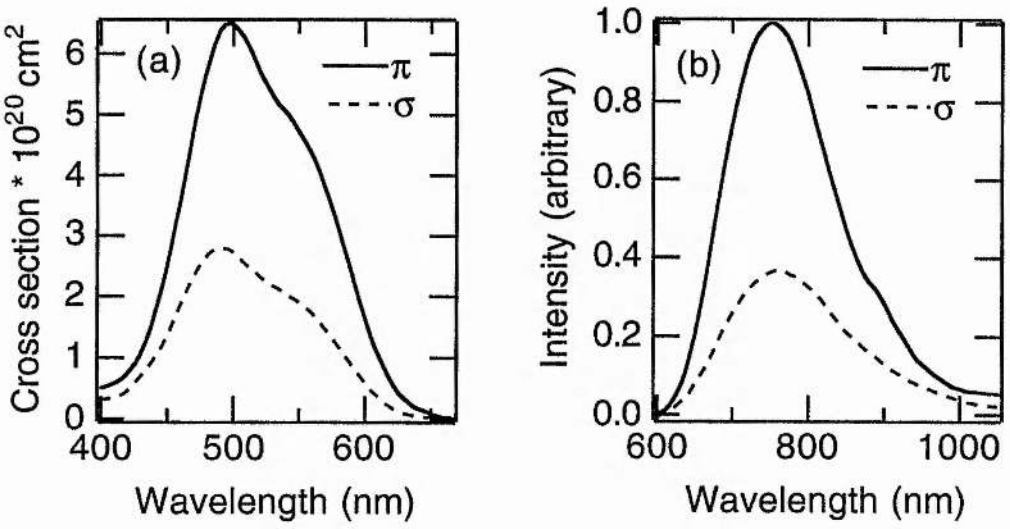

Figure 2.8 *Polarised absorption (a) and fluorescence (b) spectra for the $^2T_2$ to ^2E transition in Ti:Al_2O_3 (taken from Ref. 10)*

The short excited-state lifetime for Ti:sapphire limits the type of pump sources which can be used to continuous-wave, short-pulse or Q-switched lasers. Flashlamp pumping is not possible unless special short-pulse flashlamps are used. The lifetime is too long to allow synchronous pumping and any modulation of the pump will only have a small effect on the gain. The cross-section for stimulated emission is large (~3 x 10^{-19} cm^2) which allows crystal lengths as short as a few millimetres to be used. Gain in Ti:sapphire can be reduced by a weak but broad residual absorption maximising at around 800 nm caused by the existence of Ti^{3+}-Ti^{4+} ion pairs. A figure of merit can therefore be defined for a particular crystal as the peak Ti^{3+} absorption at 490 nm divided by the peak residual absorption at 850 nm. In recent years improved growth methods have raised the maximum achievable figure of merit for Ti:sapphire from 100 to as much as 1000. Table 2.1 contains a summary of the typical spectroscopic and material properties of Ti:sapphire.

Table 2.1 Typical material and spectroscopic properties of Ti:Al_2O_3

Property	*Value*
Crystal unit cell	Hexagonal a = 4.758Åc = 12.991 Å
Thermal conductivity, κ	0.34 W cm $^{-1}$K $^{-1}$
Refractive index (λ = 800 nm)	n = 1.760
Thermal refractive index, $\frac{dn}{dT}$	1.2 x 10 $^{-6}$ K^{-1}
Nonlinear refractive index, n_2	3 x 10 $^{-19}$ cm ^{2} W $^{-1}$
Fluorescence lifetime, τ	3.15 µs
Gain cross-section, σ_{gain}	3 x 10 $^{-19}$ cm ^{2}
Absorption cross-section, σ_{abs}	3 - 6.5 x 10 $^{-20}$ cm ^{2}
Figure of merit	200

2.4 The self-modelocked Ti:sapphire laser

Since the original demonstration by Spence, Kean and Sibbett [11] of a Ti:sapphire laser capable of directly producing 60-fs pulses without any obvious intracavity modelocking element, the technique of *self-modelocking* has been widely used to generate femtosecond pulses in a variety of solid-state lasers. Using this technique high-average-power pulses as short as 11 fs have been produced from a Ti:sapphire laser [4, 5]. In this section the principles of self-modelocking will be outlined together with a brief review of a number of different implementations which have been demonstrated to date.

Self-modelocking

Soon after the first demonstration of self-modelocking it was suggested [12] that, in the femtosecond Ti:sapphire laser, the peak intracavity powers of several hundred kilowatts were capable of inducing self-focusing effects at the beam waist in the Ti:sapphire rod. This self-focusing or *Kerr-lensing* effect would be absent when the laser was not modelocked with the result that the cw cavity mode would be different from that of the modelocked laser, in agreement with experimental observations [11]. Judicious positioning of intracavity elements such as apertures, slits or even prisms could therefore discriminate against the cw cavity mode resulting in higher gain for modelocked operation. Even without any "hard aperture" in the resonator, self-modelocking could result in an increase in gain if the cavity was configured so that, on modelocking, the mode change led to increased overlap with the pump beam in the gain medium. Theoretical and experimental investigations [13, 14] have shown that, with an optimised cavity configuration, the size of the cw and modelocked transverse modes may differ by as much as 50 % and stable modelocking has been demonstrated using suitably positioned intracavity apertures in agreement with theory.

The mechanism of self-modelocking is passive and has been compared to the action of a fast saturable absorber which symmetrically steepens the leading and trailing edges of the pulse. Self-modelocking is not generally self-starting and requires external initiation in the form of a primitive picosecond pulse or a noise-spike. Occasional self-starting behaviour was observed in the self-modelocked laser reported by Spence et al [11] who attributed modelocking to the interaction of the fundamental and higher order transverse modes in the resonator. Recent work by Cerullo and co-workers [14] has demonstrated a self-modelocked Ti:sapphire laser based

on a resonator design which exploits mode-perturbations to initiate modelocking. Self-modelocking has also been successfully initiated by using a moving mirror in an external coupled cavity to perturb the modes in the main resonator [15, 16, 17]. Regenerative modelocking using an acousto-optic modulator has been used to generated picosecond pulses with peak powers sufficient to initiate either picosecond or femtosecond self-modelocked operation [18, 19]. Other starting mechanisms have relied on wavelength dependent techniques such as using a coloured glass filter [20], a saturable absorber dye [21] or an external coupled-cavity containing a nonlinear reflector [22]. Less elegant methods including tapping a cavity mirror or "table-banging" have also proved effective. Table 2.2 provides a summary of some of the starting mechanisms used to initiate self-modelocking in Ti:sapphire lasers.

Table 2.2 Starting-mechanisms employed in self-modelocked Ti:sapphire lasers

Method	*Comments*	*Reference*
Mode-beating	Original reported Ti:sapphire laser	[11]
Moving mirror	In linear cavities, feedback from external cavity can destroy modelocking	[15, 16, 17]
Acousto-optic modulation	Initiates fs or ps operation	[18]
Glass Filter	Wavelength-dependent	[20]
Dye saturable absorber	Wavelength-dependent Not solid-state	[21]
Nonlinear reflector	Wavelength-dependent	[22]
Table-banging	Operator-intensive	[11]

Configuration of the Ti:sapphire pump laser

The self-modelocked Ti:sapphire laser used as the pump source for the femtosecond optical parametric oscillators described in the following chapters was modified from a continuous-wave (cw) *Spectra-Physics 3900S* laser. In its original form this laser was configured as a horizontally-polarised four-mirror resonator with a cavity length of approximately 0.8 m. The Ti:sapphire gain medium was a 20-mm-long Brewster-angled rod cut for propagation along the *a*-axis and with the *c*-axis parallel to the plane of incidence of the Brewster faces. This crystal geometry achieved the highest gain since light polarised parallel to the *c*-axis experiences a larger emission cross-section than the orthogonal polarisation. The figure of merit of the rod was approximately 200. The cavity mirrors surrounding the Ti:sapphire rod were broadband coatings which were highly-reflecting (HR) for wavelengths from 750 - 900 nm and were deposited on 15-mm-diameter substrates with curvatures of r = -100 mm. Both of the remaining resonator mirrors were plane; one was an HR coating similar to those described already and the other was an output coupler centred at 850 nm and with a transmission of 3.5 %. The laser was pumped with all lines (λ = 488 - 514.5 nm) of an Ar-ion laser operating in a TEM 00 transverse mode and pump light was coupled into the resonator through one of the curved mirrors using a focusing mirror of curvature r = 228 mm. The pump light was polarised along the *c*-axis of the Ti:sapphire rod as this polarisation corresponds to the maximum absorption cross-section in the gain medium. To provide bandwidth limitation a three-plate birefringent filter (BRF) was included in the cw Ti:sapphire laser.

Conversion to a self-modelocked laser required the BRF to be removed and the cavity to be extended to a length of approximately 1.8 m to allow an 82 MHz acousto-optic modelocker to be included. The modelocker was

driven *regeneratively* ie. at the exact cavity frequency, by detecting and then amplifying the cavity mode-beating. The drive frequency for the modulator was derived by filtering then frequency dividing this signal. Other necessary modifications included the addition of group-velocity dispersion compensation using a Brewster-angled sequence of four intracavity SF10 glass prisms and adjustment of the focusing mirrors surrounding the Ti:sapphire rod. The schematic displayed in Figure 2.9 illustrates the cavity arrangement of the laser when configured for self-modelocking.

The apex separation of the prisms used for dispersion compensation was chosen to allow a net negative cavity dispersion of between ≈ 500 - 1000 fs^2 in accordance with the experimental requirements for minimum duration, solitonlike pulse propagation [23].

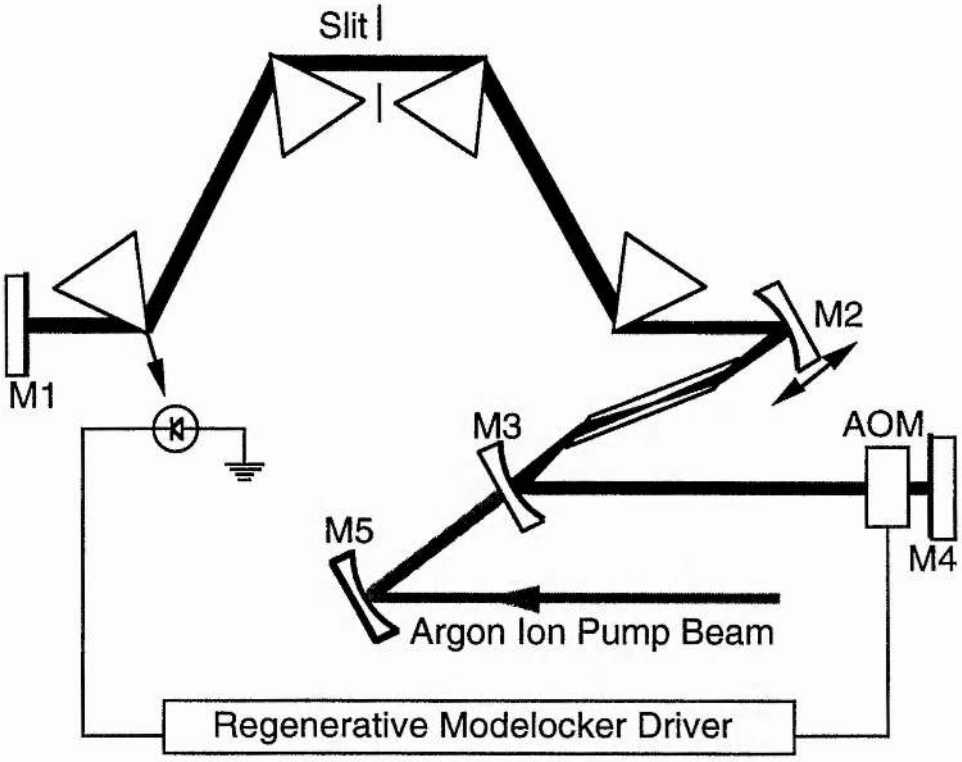

Figure 2.9 Cavity configuration of the self-modelocked Ti:sapphire laser

The apex-separation of each of the two prism-pairs used was 30 cm and allowed the laser to operate with approximately 4 mm of intracavity glass per prism. The various contributions to group-velocity dispersion in the laser are listed for a wavelength of 800 nm in Table 2.3, illustrating that the major source of positive dispersion in the cavity is the SF10 prism material itself.

Table 2.3 Cavity elements significantly contributing to dispersion in the Ti:sapphire laser at λ = 800 nm

Cavity element	*Group-velocity dispersion* $(d^2\phi/d\omega^2)$
Ti:sapphire rod, l = 20 mm	+ 580 fs^2
Quartz acousto-optic modelocker, t = 10 mm	+ 360 fs^2
4 x SF10 prism tips, 4 mm glass per prism	+ 2550 fs^2
2 x SF10 prism-pairs, apex separation 300 mm	- 4010 fs^2
Total	*- 520 fs^2*

With the resonator arranged for net negative dispersion as described, the laser was configured for self-modelocked operation by correctly adjusting the distance from the Ti:sapphire rod to each of the curved cavity focusing mirrors. The alignment technique used was similar to that described by Lemoff and Barty [24] and exploited the change in transverse mode between cw and self-modelocked operation. Firstly, the focusing mirror M3 (see Fig. 2.9) was adjusted to collimate the intracavity beam onto the end mirror M4. With the plane mirrors M1 and M4 optimised for maximum cw output power the remaining focusing mirror M2 was then translated until the far-field output of the laser had the form of the TEM 02 transverse mode reproduced in Fig. 2.10(a). Self-modelocked operation

could then be easily initiated by tapping a cavity mirror or by switching on the regenerative modelocker. The far-field transverse mode of the self-modelocked laser was TEM 00 and is reproduced as Fig. 2.10(b).

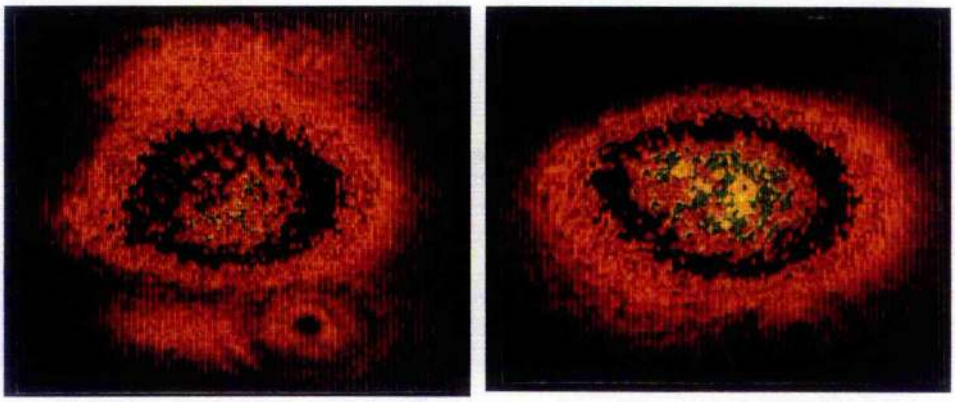

Figure 2.10 *Far-field transverse modes of the output of the Ti:sapphire laser when operating cw (a) and self-modelocked (b).*

Changing the power of the Ar-ion pump laser altered the position of mirror M2 which resulted in a TEM 02 transverse mode. This behaviour can be understood to be the result of a pump-power-dependent thermal lens in the Ti:sapphire rod. In an experiment examining this effect, the pump power was varied from 7.0 - 10.5 W and a TEM 02 transverse cavity mode maintained by adjusting the position of the focusing mirror.

The results, shown in Figure 2.11, indicate a linear relationship between mirror position and pump power with a translation of 120 μm/W being necessary to correct for changes in pump power.

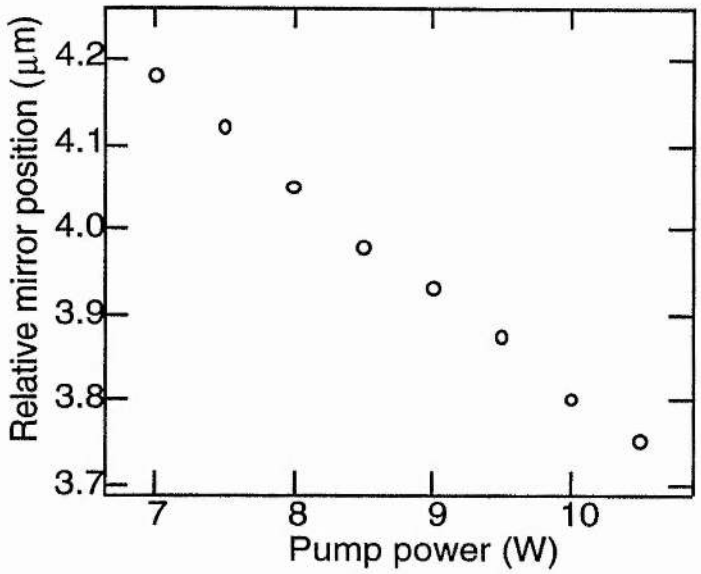

Figure 2.11 *Focusing mirror positions resulting in a TEM 02 output from the Ti:sapphire laser for various pump powers*

For a constant pump power, self-modelocking could be obtained across a range of positions of the focusing mirror but the "TEM 02" position always corresponded to the configuration capable of producing the highest average powers while remaining modelocked. In a supplementary experiment the pump power remained constant and the focusing mirror was translated across a range including the TEM 02 position. By defining the *modelocking efficiency* as the maximum average modelocked power / maximum cw power, the optimum position of the focusing mirror was determined. Graphs of modelocking efficiency measured at pump powers of 7 W and 10 W (Figure 2.12) both maximised at the mirror position corresponding to the TEM 02 transverse mode. Higher order transverse modes were observed in the cw output for other mirror positions and the corresponding self-modelocked outputs were also not generally TEM 00.

Work is currently ongoing to develop a theoretical model of thermal lensing in the Ti:sapphire rod which is consistent with the results

presented here. A proper undertanding of thermal effects in vibronic gain media will be of continuing importance in the design of all-solid-state diode-pumped systems, particularly those based on Cr:LiSAF which has an even higher pump absorption cross-section than Ti:sapphire.

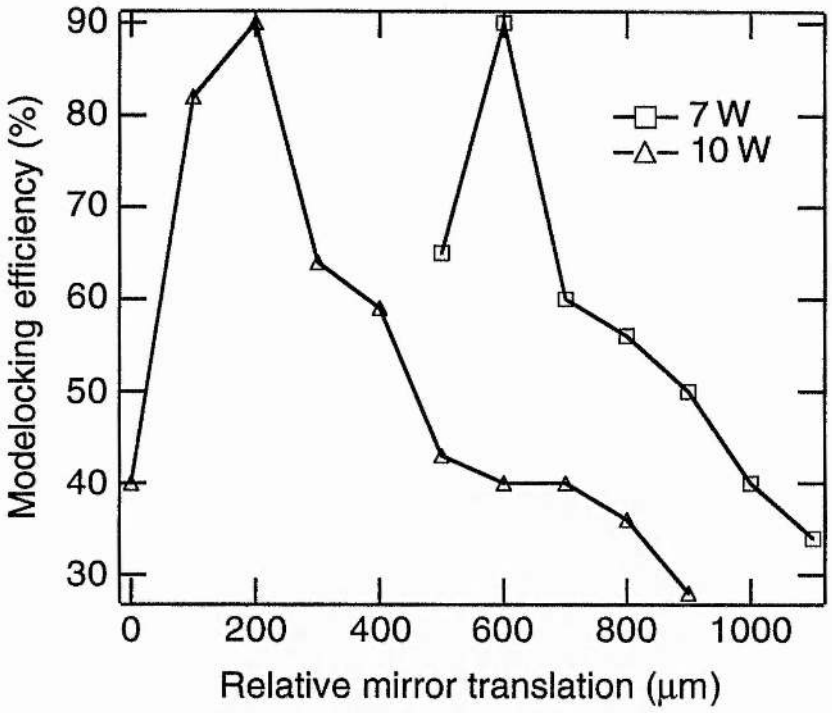

Figure 2.12 Modelocking efficiency for various focusing mirror positions at pump powers of 7 W (a) and 10 W (b)

The results presented in Figure 2.12 demonstrate that the alignment technique described earlier is a reproducable and effective method of configuring the Ti:sapphire laser for optimum self-modelocked performance. When the prism sequence was aligned correctly the laser typically remained self-modelocked for several hours even with the regenerative modelocker turned off. The inclusion of a variable horizontal slit immediately before the M4 end mirror further improved the stability of the modelocking. It is thought that this was a result of discrimination against the vertical TEM 02 cw mode by the horizontal aperture.

Configured in this way, it was found that if modelocking was interupted the average output power in cw oscillation would be ≈ 50 % lower. Once modelocked, narrowing the horizontal aperture often led to a reduction in the duration and an increase in the peak power of the output pulses. This behaviour is consistent with the proposal that a peak-power-dependent Kerr-lens is responsible for determining the transverse cavity mode in self-modelocked operation.

The application of the Ti:sapphire laser as a pump source for optical parametric oscillators demanded a configuration capable of delivering several hundred milliwatts of average output power. With a pump power of 10 W from the Ar-ion laser the typical average output power when self-modelocked was appoximately 1 W. A proportion of this was required for diagnostic purposes to monitor the output pulses and a further fraction was lost at steering and isolator optics. For this reason the laser was configured for optimum operation at the higher pump power of 15 W. Using a 20 % output coupler as much as 1.9 W was generated in the self-modelocked output and the laser was self-starting. The useful power output from the laser in typical operation was approximately 1 W across the tuning range determined by the cavity optics of 780 - 880 nm.

2.5 Measurement of ultrashort optical pulses

For many experiments involving ultrashort pulses it is important to have accurate spectral and temporal information describing the pulse profiles. In photoexcitation experiments, if the frequency bandwidth of the pulse is too large then more than one species may be excited. Similarly, in studies of relaxation dynamics, an accurate measurement of the pulse duration is often required for correct interpretation of the results.

Current methods of pulse measurement can provide information about the intensity of the pulse using either a scanning monochromator to record $I(\nu)$ or an *intensity autocorrelation* to infer $I(t)$. Information about the phase $\phi(t)$ of the pulse can be partially obtained from an *interferometric autocorrelation* which is capable of indicating the presence of chirp. Recently, a novel technique known as frequency-resolved optical gating (FROG) has been shown experimentally to provide complete intensity and phase information [25] although this technique is not yet in widespread use. In this section, laboratory techniques allowing measurement of pulses in the time and frequency domains are described and representative examples of the output from the Ti:sapphire pump laser are included.

Time-domain measurements - the autocorrelation function

The *fringe resolved* or interferometric autocorrelation function offers a quantitative means of determining the duration of a pulse and a qualitative measure of the amount of chirp present. It works by splitting the pulse, $E(t)$, into two replicas which are then recombined with a variable relative delay, τ, in a nonlinear medium phase-matched for second-harmonic generation (SHG) medium. The resulting signal is given by,

$$g_2(\tau) = \frac{\int_{-\infty}^{+\infty} | [E(t) + E(t - \tau)]^2 |^2 \, dt}{\int_{-\infty}^{+\infty} E(t)^4 \, dt}, \qquad (13)$$

The laboratory arrangement used in the measurement of pulses from the Ti:sapphire laser is illustrated in Figure 2.13. A beamsplitter divided the original pulse in two. The reflected pulse travelled to a stationary retroreflector and the transmitted pulse to a moving retroreflector mounted on the cone of a 50 W loudspeaker. The loudspeaker provided the necessary variable delay and was driven by a large amplitude, low frequency signal which was also used for triggering purposes. The retroreflectors were adjusted to recombine the two beams inside a crystal of βBBO cut for SHG and the frequency-doubled light was detected using a visible photomultiplier tube (PMT). The output from the PMT was used to display the interferometric autocorrelation, $g_2(\tau)$, or, by using a suitable smoothing capacitance, the time-averaged intensity autocorrelation, $< g_2(\tau) >$.

The FWHM duration of the pulse intensity is related to the FWHM width of the pulse autocorrelation by a conversion factor that depends on the pulse shape and the type of autocorrelation recorded.

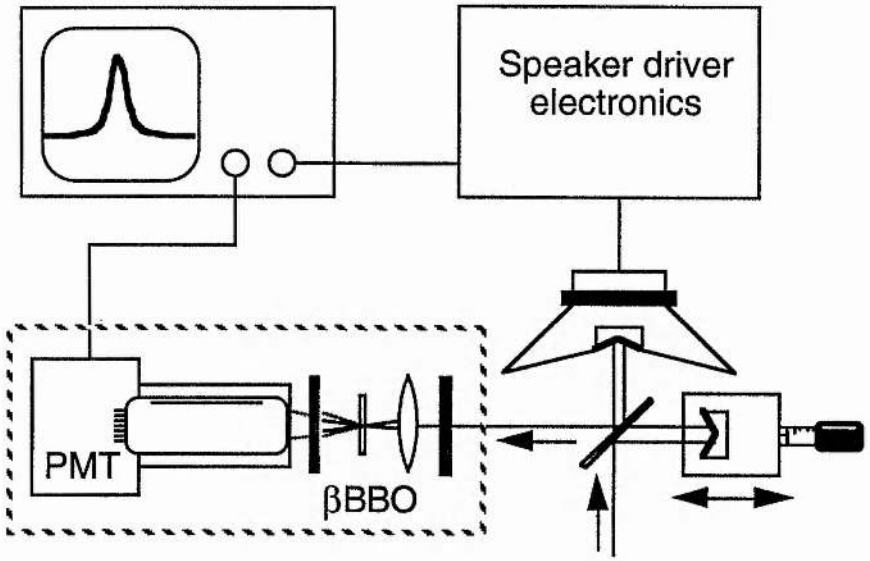

Figure 2.13 Laboratory implementation of interferometric autocorrelator

A summary of the appropriate conversion factors for pulses with $\text{sech}^2(t)$ and e^{-t^2} (= Gaussian) intensity profiles is given in Table 2.4 together with the time-bandwidth product of the transform-limited pulseshape.

Table 2.4 Diagnostic values for pulses with $\text{sech}^2(t)$ and Gaussian intensity profiles.

Intensity Profile	$\Delta\tau_{g_2(t)}/\Delta\tau_p$	$\Delta\tau_{<g_2(t)>}/\Delta\tau_p$	$\Delta\nu_p\Delta\tau_p$
e^{-t^2}	1.697	1.414	0.441
$\text{sech}^2(t)$	1.897	1.543	0.315

An interferometric and intensity autocorrelation of the output of the Ti:sapphire pump laser operating at a wavelength of 830 nm are reproduced in Figure 2.14. The interferometric autocorrelation (Figure 2.14a) shows an 8:1 signal ratio between the baseline and the maximum which indicates complete modelocking in the absence of an intense cw

background or noise spike components. For the same reasons, the intensity autocorrelation (Figure 2.14b) has the characteristic 3:1 ratio between the baseline and the maximum.

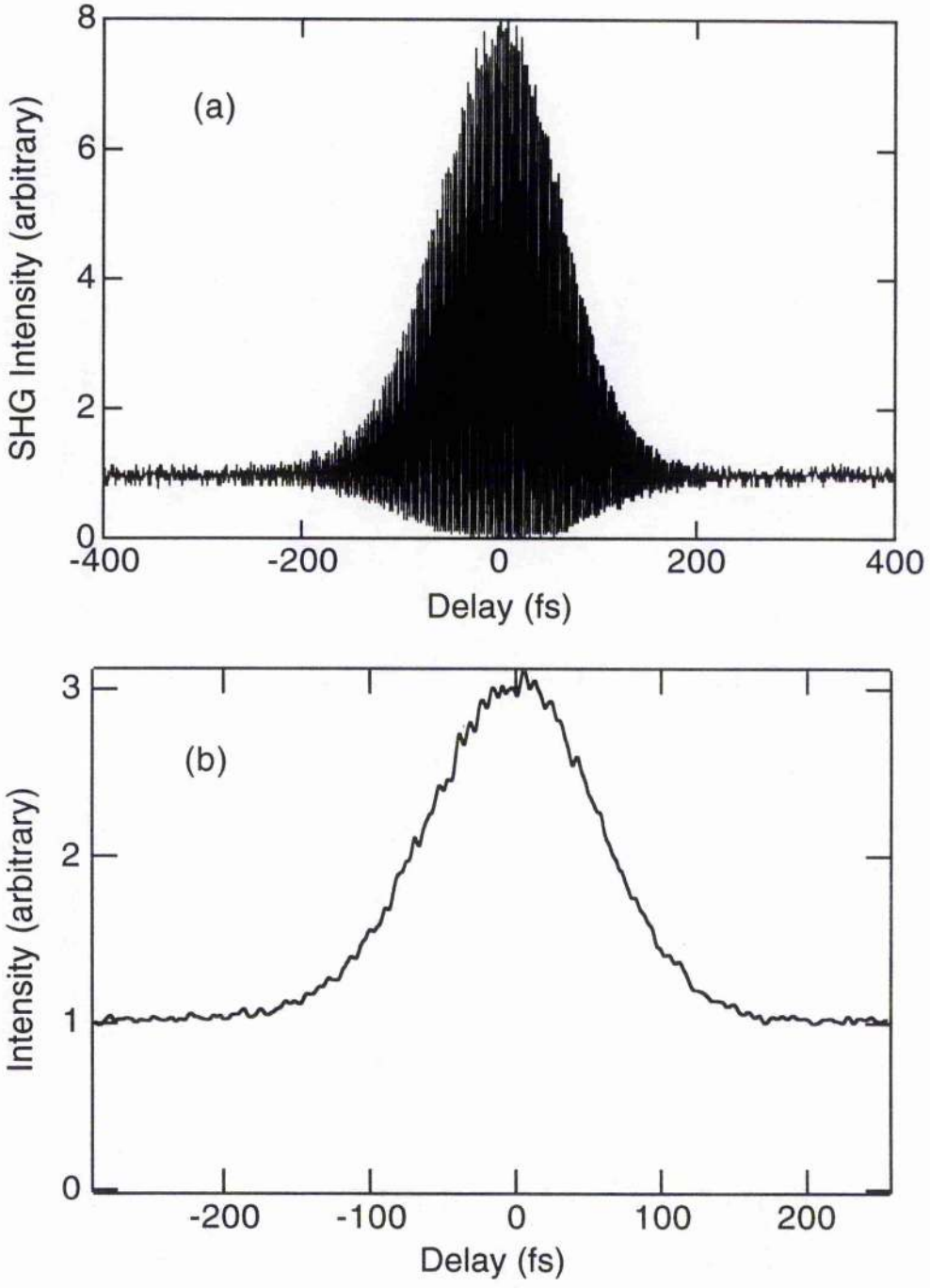

Figure 2.14 Interferometric (a) and intensity (b) autocorrelation profiles of the output pulses from the self-modelocked Ti:sapphire laser

Pulse duration measurements derived using the interferometric autocorrelation may be inaccurate since the autocorrelation is sensitive to even modest amounts of frequency chirp which manifests itself as a broad pedestal. For this reason the intensity autocorrelation was used for all pulse duration measurements. Assuming a $\mathrm{sech}^2(t)$ pulse intensity profile (consistent with solitonlike pulse propagation) and using the conversion factors listed in Table 2.4 the pulse duration was measured to be 85 fs. The duration inferred from the interferometric autocorrelation was also 85 fs, implying that the pulses were free of chirp.

Frequency-domain measurements

The spectral characteristics of a modelocked laser can be determined by measurements at either optical frequencies or radio frequencies corresponding to investigation of the spectral bandwidth of the pulse or examination of the repetition frequency of the laser. Together with pulse-duration measurements, the former can give an estimation of the amount of chirp present within each pulse in the modelocked output. The latter can give details of the *phase noise* or *timing jitter* of the modelocked pulse sequence and provides information about the stability of the laser.

Measurements of the pulse intensity spectrum, $I(\nu)$, were made using a fibre-coupled *optical spectrum analyser* (OSA) which is essentially a digitally-calibrated, scanning monochromator. The OSA recorded the power spectrum of the pulse which is described mathematically by,

$$I(\nu) = E(\nu)\,E^{*}(\nu), \tag{14}$$

where $E(\nu)$ is the Fourier transform of $E(t)$ and $E^{*}(\nu)$ represents the complex conjugate of $E(\nu)$. The resolution of the OSA was approximately 0.1 nm. A representative spectrum of the output of the self-modelocked

Ti:sapphire laser recorded using the OSA and corresponding to the autocorrelation data included earlier is displayed in Figure 2.15. The measured bandwidth of 9 nm implies a time-bandwidth product of 0.33, confirming that the pulses from the pump laser are nearly transform-limited.

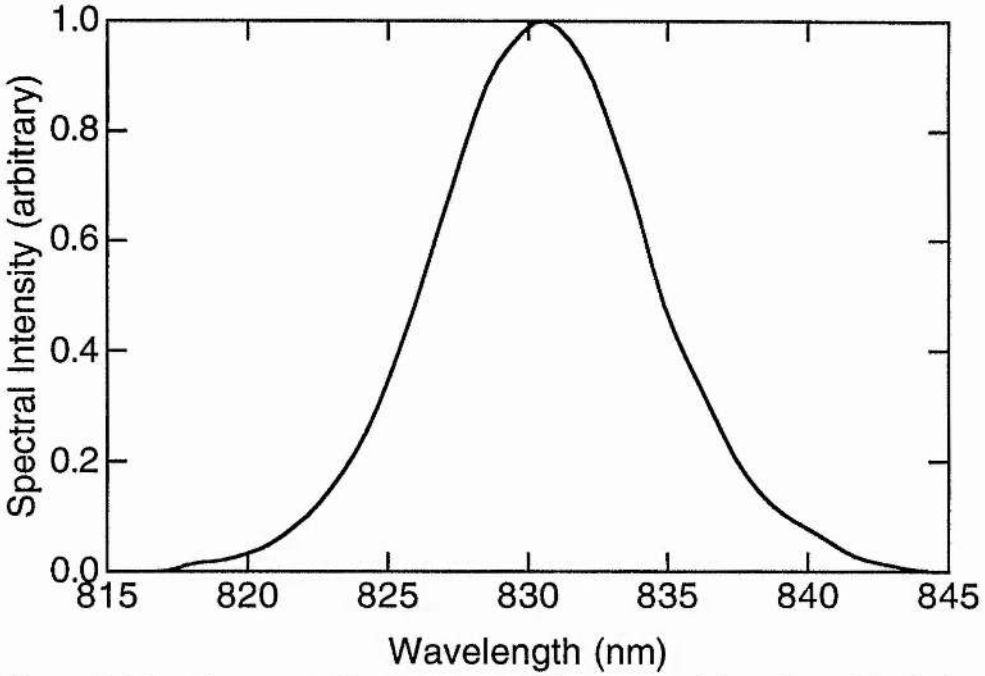

Figure 2.15 Representative spectrum of the output of the self-modelocked Ti:sapphire pump laser

Phase noise

Phase noise or timing jitter is a form of random noise found in all electronic or optical oscillators and, in modelocked lasers, results in an uncertainty in the pulse repetition time. Although the error in the roundtrip time is small ($\approx 10^{-22}$ s), the exact time at which a future pulse will follow cannot be predicted exactly. Timing jitter can also be interpreted as a dephasing of the pulse repetition frequency. In the Ti:sapphire laser, major sources of phase noise are acoustic vibrations ($\approx$ 1 - 100 Hz), variations of the refractive index of Ti:sapphire rod due to mains voltage ripple on the Ar-ion pump laser ($\approx$ 50 Hz) and electronic noise in

the modelocker driver. Measurement of the phase noise of the laser indicates its suitability for applications where a source of well synchronised pulses is needed, eg. streak-camera resolution measurement.

Useful measurement requires a formalism treating the pulses in both the time and frequency domains. A perfectly modelocked laser (ie. no phase or amplitude noise) produces identical pulses at a repetition rate of one pulse every T seconds. In the frequency domain, the largest contribution to the output power exists at the fundamental frequency and lower contributions at higher harmonics as illustrated in Figure 2.16.

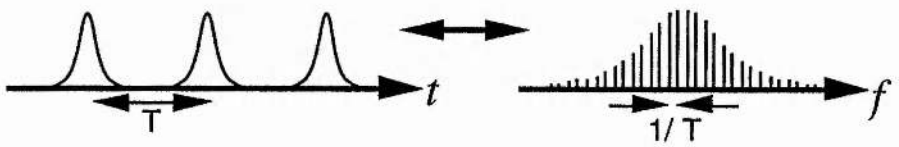

Figure 2.16 The output pulse sequence and corresponding frequency components of a perfectly modelocked laser

The pulse sequence can be described in the time domain as,

$$F_o(t) = \sum F(t+nT) = F(t) \times \sum \delta(t+nT) \qquad (15)$$

and in the frequency domain as,

$$F_o(f) = F(f) \times \frac{1}{T} \sum \delta(f+\frac{n}{T}) \qquad (16)$$

A real modelocked laser, however, displays fluctuations in amplitude and roundtrip time and these can be included as an amplitude function, A(t), and a jitter function, J(t) = $\delta T/T$, where δT is the deviation in the roundtrip time due to phase noise. In the time domain the pulse sequence is now described by,

$$F_o(t) = [1 + A(t)] \times \sum F(t + nT + J(t)T) \qquad (17)$$

The power spectrum of the pulse sequence can be derived and is given by,

$$P_o(f) = |F_o(f)|^2$$

$$= \frac{1}{T^2} |F_o(f)|^2 \left[\sum \delta(f + \frac{n}{T}) + \sum P_A(f + \frac{n}{T}) + (2\pi T)^2 \sum n^2 P_J(f + \frac{n}{T}) \right] \quad \text{—(18)}$$

The phase noise term, $n^2 P_J(f + \frac{n}{T})$, dominates at higher harmonics because of the n^2 dependence. By comparing the spectrum of a pulse sequence centred at the fundamental repetition frequency with a spectrum centred at a higher harmonic ($n > 1$) we can extract the power spectrum of the phase noise itself, $P_J(f)$. Shown below as Figure 2.17 are representative power spectra of the fundamental and the tenth harmonic of the Ti:sapphire laser output pulse sequence.

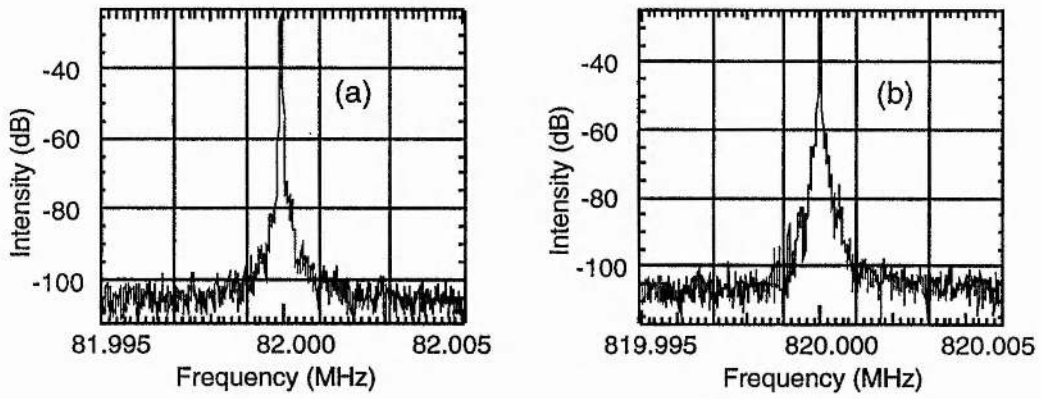

Figure 2.17 Power spectra of the pulse train on a dB scale and centred at the fundamental frequency (a) and at the tenth harmonic (b).

On a logarithmic scale $P_J(f)$ obeys a $1/f$ law with diminishing contributions at higher frequencies. This is easily understood since high frequencies correspond only to short time intervals over which the arrival time of a subsequent pulse can be predicted accurately because $\sum \delta T$ is small.

For any oscillator, $P_J(f)$ can be deduced from the spectra of the fundamental and harmonic pulse sequences. Figure 2.18 presents a representative example of the single sideband power spectrum of the phase noise measured on the output of the Ti:sapphire laser. The function was derived from the fundamental and the 10th harmonic spectra of the pulse sequence.

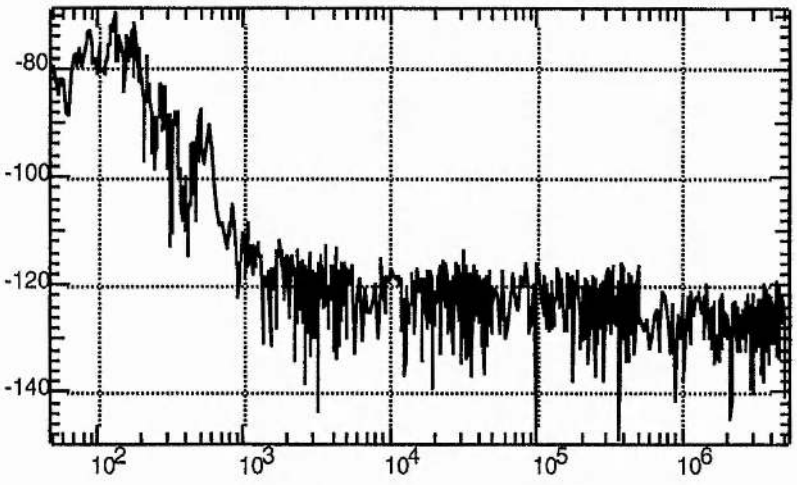

Figure 2.18 Single sideband power spectrum of the phase noise of the Ti:sapphire laser recorded on a dB scale.

Detailed measurements of phase noise allow different modelocking methods, and laser sources to be compared. The suitability of a laser for an application requiring regular high-repetition-rate pulses is determined effectively using phase noise techniques. Further measurements of the phase noise of a Ti:sapphire-pumped femtosecond optical parametric oscillator are described later in Chapter 4.

Amplitude Noise

Amplitude noise (represented by $A(t)$ in the formalism presented earlier) was also present on the output of the Ti:sapphire laser and was recorded by monitoring the output pulse sequence on a 50Ω-input-impedance oscilloscope using a fast (≈ 1 GHz bandwidth) silicon

photodiode. Estimated intensity fluctuations of no more than 1 % were measured on the self-modelocked output when the oscilloscope was adjusted to a slow (10 ms) timebase. An oscillogram showing the output pulse sequence is displayed below in Figure 2.19. Results presented later in Chapter 4 describe a comparison between the amplitude noise present on a femtosecond OPO and the intensity fluctuations of the pump laser.

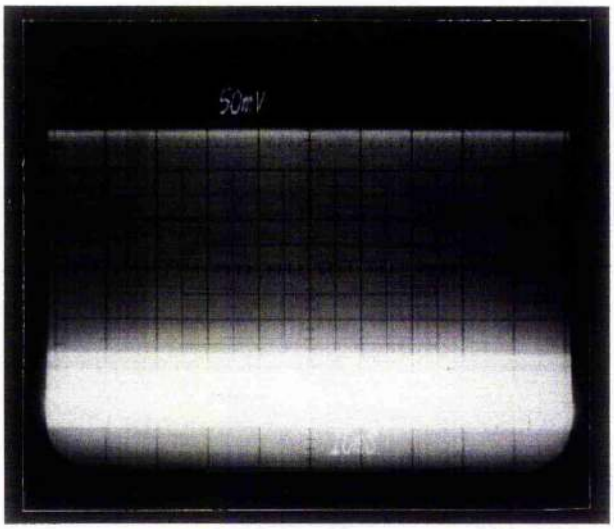

Figure 2.19 *Oscillogram showing the amplitude noise on the output pulse sequence from the self-modelocked Ti:sapphire laser*

2.6 Conclusions

In this chapter a detailed description has been presented of the configuration, design and performance of the self-modelocked Ti:sapphire laser used as a pump source for the optical parametric oscillators described in subsequent chapters. In typical operation the laser has demonstrated an average useful power output of over 1 W in the form of 85-fs pulses completely free of any background cw-component or multiple pulsing effects. Continuous tuning of the laser across a range, determined by the cavity optics, from 780 - 880 nm has been achieved at these power

levels. The importance of the pump-induced thermal lens in the Ti:sapphire gain medium has been discussed in detail and a general alignment procedure has been described which optimises modelocked performance at any given pump power. In addition, a variety of effects determining pulse propagation in optical media have been introduced. In Chapter 3 the factors critical to the design of a femtosecond optical parametric oscillator will be discussed in detail and will include limiting criteria imposed by some of the pulse propagation effects already presented in this chapter.

References

1. R. L. Fork, O. E. Martinez and J. P. Gordon, Opt. Lett. **9**, 150 (1984)

2. C. P. Huang, H. C. Kapteyn, J. W. McIntosh and M. M. Murnane, Opt. Lett. **17**, 139 (1992)

3. C. P. Huang, M. T. Asaki, S. Backus, M. M. Murnane, H. C. Kapteyn and H. Nathel, Opt. Lett. **17**, 1289 (1992)

4. M. T. Asaki, C. -P. Huang, D. Garvey, J. Zhou, H. C. Kapteyn and M. M. Murnane, Opt. Lett. **18**, 977 (1993)

5. A. Stingl, C. Spielmann, F. Krausz and R, Szipöcs, Opt. Lett. **19**, 204 (1994)

6. R. H. Stolen, L. F. Mollenauer and W. J. Tomlinson, Opt. Lett. **8**, 186 (1983)

7. P. Lacovara, L. Esterowitz and M. Kokta, IEEE J. Quant. Electron. **21**, 1614 (1985)

8. P. F. Moulton, Twelfth International Quantum Electronics Conference, Munich (1982)

9. E. D. Nelson, J. Y. Wong and A. L. Schawlow, Phys. Rev. **156**, 298 (1967)

10. P. F. Moulton, J. Opt. Soc. Am. B. **3**, 125 (1986)

11. D. E. Spence, P. N. Kean and W. Sibbett, Opt. Lett. **16**, 42 (1991)

12. M. Piché, N. McCarthy and F. Salin, Paper MB8 in the Optical Society of America Annual Meeting 1990, Boston, Massachussetts

13. R. E. Bridges, R. W. Boyd and G. P. Agrawal, Opt. Lett. **18**, 2026 (1993)

14. G. Cerullo, S. De Silvestri , V. Magni and L. Pallaro, Opt. Lett. **19**, 807 (1994)

15. N. H. Rizvi, P. M. W. French and J. R. Taylor, Opt. Lett. **17**, 279 (1992)

16. Y. M. Liu, K. W. Sun, P. R. Prucnal and S. A. Lyon, Opt. Lett. **17**, 1219 (1992)

17. W. S. Pelouch, P. E. Powers and C. L. Tang, Opt. Lett. **17**, 1581 (1992)

18. D. E. Spence, J. M. Evans, W. E. Sleat and W. Sibbett, Opt. Lett. **16**, 1762 (1991)

19. Kafka et al IEEE 2151 (1992)

20. N. Sarukura, Y. Ishida, T. Yanagawa and H. Nakano, Appl. Phys. Lett. **57**, 229 (1990)

21. N. Sarukura, Y. Ishida and H. Nakano, Opt. Lett. **16**, 153 (1991)

22. U. Keller, G. W. 'tHooft, W. H. Knox and J. E. Cunningham, Opt. Lett, **16**, 1022 (1991)

References continued

23. J. D. Kafka, M. L. Watts and J. -W. J. Pieterse, IEEE J. Quant. Electron. **28**, 2151 (1992)

24. B. E. Lemoff and C. P. J. Barty, Opt. Lett. **17**, 1367 (1992)

25. D. J. Kane and R. Trebino, Opt. Lett. **18**, 823 (1993)

3.1 Introduction

In the previous chapters, a review of the progress in the development of femtosecond optical parametric oscillators (OPOs) was outlined and a description of pulse propagation in linear and nonlinear media was presented. The design considerations of a femtosecond OPO encompass many of the issues already introduced in the discussion of the self-modelocked Ti:sapphire laser in *Chapter 2* and also require detailed calculations in determining the choice of an appropri

ate nonlinear crystal. This chapter begins with a discussion of the theory concerning the parametric interaction between electromagnetic waves and includes a general treatment of how the optimum crystal geometry can be determined for a particular parametric process. The application of this theory is then described in the design of a femtosecond parametric oscillator.

3.2 The nonlinear polarisation

In Chapter 2 the polarisation response of a transparent medium to an applied field was described by the power series expansion:

$$P = \chi_{(1)}\varepsilon_o E + \chi_{(2)}\varepsilon_o E^2 + \chi_{(3)}\varepsilon_o E^3 + \ldots, \qquad (1)$$

where $\chi_{(1)}$ is the linear susceptibility introduced earlier and $\chi_{(2)}$ and $\chi_{(3)}$ are frequency-dependent nonlinear susceptibilities describing the quadratic and cubic dependence of the polarisation on the applied field. Effects arising from $\chi_{(1)}$ and $\chi_{(3)}$ have already been dealt with in the previous chapter. This section will concentrate on nonlinear frequency conversion exploiting the $\chi_{(2)}$ susceptibility term in the polarisation.

To illustrate how the term in $\chi_{(2)}$ can result in second harmonic and other frequencies, we can consider the effect on a nonlinear medium of the applied field,

$$E = E_1 \cos(k_1 x - \omega_1 t) + E_2 \cos(k_2 x - \omega_2 t) \qquad (2)$$

which results from mixing two waves of frequencies ω_1 and ω_2. The nonlinear component of the polarisation, $P^{(2)}$, is proportional to $\chi_{(2)}E^2$ and so has terms in $\cos 2\omega_1 t$ and $\cos 2\omega_2 t$ which correspond to the second harmonics of the original frequencies. Also present are terms proportional to $\cos 2(\omega_1 - \omega_2)t$ and $\cos 2(\omega_1 + \omega_2)t$ which describe difference-frequency and sum-frequency generation respectively. Nonlinear effects relying on $\chi_{(2)}$ are only observed in *noncentrosymmetric* media (materials not possessing a centre of symmetry). In *centrosymmetric* media (see Figure 3.1a) symmetry considerations require that the magnitude of the polarisation induced by an applied field $+E$ is equal to that resulting from a field $-E$. In noncentrosymmetric materials however the magnitude of the induced polarisation depends on the sign of the applied field (see Figure 3.1b).

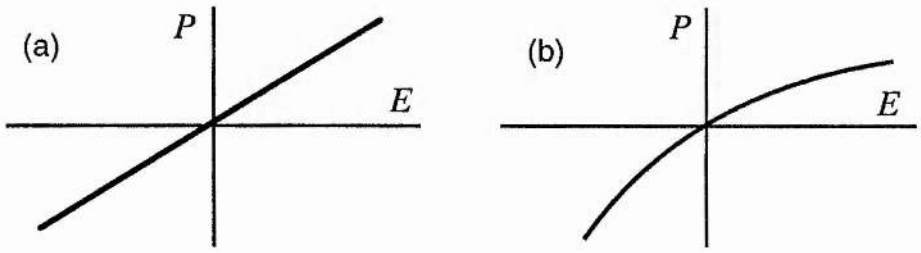

Figure 3.1 Dependence on applied field of the induced polarisation in a centrosymmetric (a) and noncentrosymmetric (b) medium

In the presence of an electromagnetic wave the resulting polarisation in a centrosymmetric material follows the applied field as illustrated in Figures 3.2a-d. The form of the induced polarisation in a noncentrosymmetric medium is depicted in Figures 3.2e-h and is different for positive and negative components in the applied field.

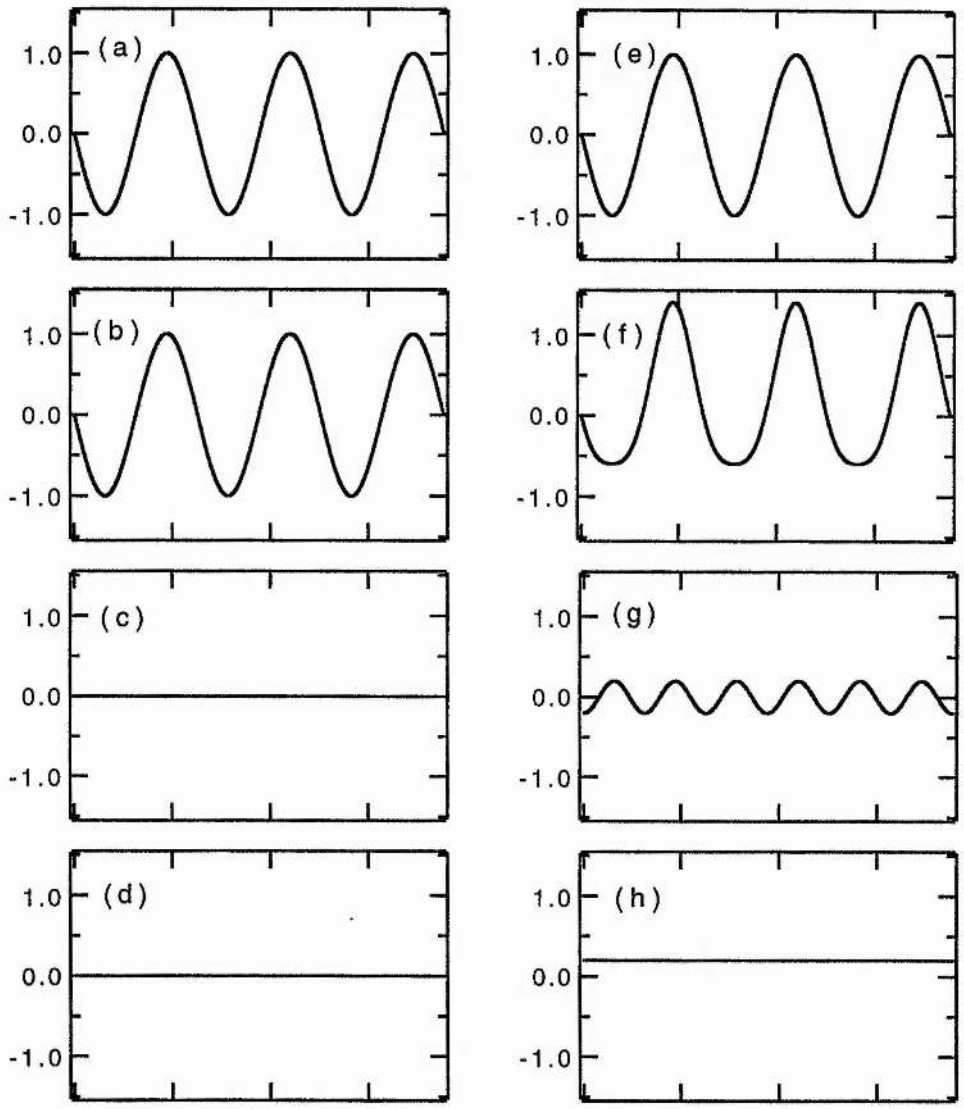

Figure 3.2 Driving field and resulting polarisation response, second-harmonic component and dc-component in a centrosymmetric (a - d) and a noncentrosymmetric (e - h) medium

3.3 The coupled-wave equations

In a nonlinear interaction between three travelling waves of different frequencies, how will each of their associated fields evolve as the waves propagate through the medium? To answer this question it is first necessary to obtain an expression relating the internal electric (vector) field in a medium **E** resulting from a driving polarisation **P**.

Maxwell's equations, which have the form,

$$\nabla \times \mathbf{E} = -\frac{\partial \mathbf{B}}{\partial t}, \qquad \text{and} \qquad \nabla \times \mathbf{H} = \frac{\partial \mathbf{D}}{\partial t} + \mathbf{J} \tag{3}$$

can be used together with the relations,

$$\mathbf{D} = \varepsilon_o \mathbf{E} + \mathbf{P} \qquad \mathbf{J} = \sigma \mathbf{E} \qquad \mathbf{B} = \mu_o \mathbf{H} \tag{4}$$

to derive a wave equation,

$$\nabla^2 \mathbf{E} - \mu_o \sigma \frac{\partial \mathbf{E}}{\partial t} - \mu_o \varepsilon_o \frac{\partial^2 \mathbf{E}}{\partial t^2} = \mu_o \frac{\partial^2 \mathbf{P}}{\partial t^2}. \tag{5}$$

When the fields are restricted to propagation in one dimension as described by the complex expressions,

$$\mathbf{E}(z, t) = \frac{1}{2}[\, E(z, \omega) \exp j(\mathbf{k}\cdot\mathbf{z} - \omega t) + E^*(z, \omega) \exp j(\mathbf{k}\cdot\mathbf{z} + \omega t)\,] \tag{6a}$$

$$\mathbf{P}(z, t) = \frac{1}{2}[\, P(z, \omega) \exp j(\mathbf{k}\cdot\mathbf{z} - \omega t) + P^*(z, \omega) \exp j(\mathbf{k}\cdot\mathbf{z} + \omega t)\,] \tag{6b}$$

and, under the assumption of a slow variation of the complex field envelope with distance, the wave equation becomes,

$$\frac{\partial \mathbf{E}}{\partial z} + \alpha \mathbf{E} + \frac{1}{c}\frac{\partial \mathbf{E}}{\partial t} = \frac{i \mu_o c \omega}{2n} \mathbf{P} \tag{7}$$

where $\alpha = \mu_o \sigma c/2$ is the electric field loss coefficient. In the frequency domain, the nonlinear polarisations of three interacting waves, related by

$\omega_1 + \omega_2 = \omega_3$, can be expressed using the definitions of Equations (6a) and (6b) to give,

$$\begin{aligned} P(\omega_1) &= 2\, d_{eff}\, \varepsilon_o\, E(\omega_3)\, E^*(\omega_2) \\ P(\omega_2) &= 2\, d_{eff}\, \varepsilon_o\, E(\omega_3)\, E^*(\omega_1) \\ P(\omega_3) &= 2\, d_{eff}\, \varepsilon_o\, E(\omega_1)\, E(\omega_2)\,. \end{aligned} \tag{8}$$

These polarisation terms can be substituted into Equation (7) to derive three coupled equations which can be used to describe any steady-state three-wave nonlinear interaction,

$$\frac{dE_1}{dz} + \alpha_1 E_1 = j\,\kappa_1 E_3 E_2^*\, e^{j\,\Delta\mathbf{k}\cdot\mathbf{z}} \tag{9a}$$

$$\frac{dE_2}{dz} + \alpha_2 E_2 = j\,\kappa_2 E_3 E_1^*\, e^{j\,\Delta\mathbf{k}\cdot\mathbf{z}} \tag{9b}$$

$$\frac{dE_3}{dz} + \alpha_3 E_3 = j\,\kappa_3 E_1 E_2\, e^{-j\,\Delta\mathbf{k}\cdot\mathbf{z}} \tag{9c}$$

where E_j is used to abbreviate $E(\omega_j)$ and,

$$\begin{aligned} \kappa_i &= \frac{\omega_i\, d_{eff}\, \varepsilon_o}{n_i\, c}\,, & \alpha_i &= \mu_o\, \sigma_i\, c/2\,, \\ \omega_3 &= \omega_1 + \omega_2\,, & \mathbf{k}_3 &= \mathbf{k}_1 + \mathbf{k}_2 + \Delta\mathbf{k}\,. \end{aligned} \tag{10}$$

The coupled-wave equations describe the phase relationships governing the direction of energy flow between any three interacting waves. These are specific to the particular mixing process and, if not correctly satisfied, can describe damping of the fields instead of energy transfer. The necessary phase relations between the fields for sum, difference and parametric interactions are listed in Table 3.1.

Table 3.1 Phase relations satisfied by various three-wave mixing processes

Process	*Phase Relations*
Sum frequency mixing $\omega_1 + \omega_2 \rightarrow \omega_3$	$\phi_1 = \pi/2 + \phi_3 - \phi_2$ $\phi_3 = \pi/2 + \phi_1 + \phi_2$
Difference frequency mixing $\omega_3 - \omega_2 \rightarrow \omega_1$	$\phi_1 = \pi/2 + \phi_3 + \phi_2$ $\phi_2 = \pi/2 + \phi_3 - \phi_1$
Parametric amplification $\omega_3 \rightarrow \omega_1 + \omega_2$	$\phi_1 = \pi/2 + \phi_3 - \phi_2$ $\phi_2 = \pi/2 + \phi_3 - \phi_1$ $\phi_3 = \pi/2 + \phi_1 + \phi_2$

Under the appropriate boundary conditions, the coupled wave equations can be used to predict several characteristic features of nonlinear interactions. One of the most important of these is known as *phase-matching*. A perfectly phase-matched interaction has $\Delta\mathbf{k} = 0$ but incomplete phase-matching reduces the amplitude efficiency of a nonlinear process according to a phase synchronism factor *sinc* $(\Delta kl\ /2)$ where l is the length of the nonlinear medium and Δk is the magnitude of $\Delta\mathbf{k}$. In practice, imperfect phase-matching arises from either angular or spectral mismatch between the interacting waves with each other. A more detailed discussion of phase-matching in crystalline media is included in Section 3.4.

Results of applying the coupled wave analysis to the case of phase-matched *sum-frequency-mixing* (SFM), where an intense pump field at ω_2 mixes with an input at ω_1 to produce a wave at ω_3, show that the input wave can be converted fully into the output over a finite interaction length

in the nonlinear medium. For lengths exceeding this however, the field at ω_3 begins to reconvert to the input at ω_1.

In the case of phase-matched *difference-frequency-mixing* (DFM), in which an intense pump field at ω_3 mixes with an input at ω_1 to give an output at ω_2, the coupled wave equations show that both the input wave and the generated wave can experience gain. This is unlike the results of SFM where the output field increased only by depletion of the input wave and implies that an amplifier or oscillator can be constructed which is based on difference generation. Oscillation using this principle is discussed further in Section 3.7.

3.4 Phase-matching in crystalline materials

In any nonlinear frequency-conversion process, the efficiency can be limited by the frequency-dependence of the refractive index. For example, in the case of second-harmonic generation, the fundamental and the frequency-doubled light are initially in phase. However, the two wavelengths travel with different phase velocities determined by the dispersion of the material and, at some later time, the frequency-doubled light generated by the fundamental will be out of phase with the existing second-harmonic and destructive interference will result. Therefore, in this situation, maximum second-harmonic output can only be extracted over a certain length of material, known as the *coherence length*. To maximise conversion efficiency using all of the nonlinear medium available, it is advantageous if the polarisation axes of the waves can be chosen so that the birefringence of the material allows each wave to travel in phase with the others. Many materials have nonlinear susceptibilities which can couple energy from a wave of one polarisation to a wave of the orthogonal

polarisation, allowing efficient generation and phase-matching to be achieved simultaneously.

It is often useful to know which directions within a crystal can support phase-matching for a particular nonlinear process. In a three-wave interaction, energy-conservation and phase-matching require that,

$$\omega_3 = \omega_1 + \omega_2 \qquad \text{and,} \quad \mathbf{k}_3 = \mathbf{k}_1 + \mathbf{k}_2 \,, \tag{11}$$

which, for collinear interactions, is equivalent to,

$$\frac{1}{\lambda_3} = \frac{1}{\lambda_1} + \frac{1}{\lambda_2} \qquad \text{and,} \quad \frac{n_3}{\lambda_3} = \frac{n_1}{\lambda_1} + \frac{n_2}{\lambda_2} \,, \tag{12}$$

where all the wavelengths take their free-space values.

The calculation of the crystal directions which support phase-matching therefore requires the refractive indices associated with a given direction to be computed. In a biaxial crystal, the refractive index experienced by a wave polarised along (θ, ϕ) is described by an ellipse known as the index ellipsoid (illustrated in Figure 3.3) which, in its general form, is given by the transcendental equation [1],

$$\frac{\sin^2\theta\cos^2\phi}{n_i^{-2} - n_{1_i}^{-2}} + \frac{\sin^2\theta\sin^2\phi}{n_i^{-2} - n_{2_i}^{-2}} + \frac{\cos^2\theta}{n_i^{-2} - n_{3_i}^{-2}} = 0 \tag{13}$$

The general solution of Equation (13) requires an iterative method, so it is often more convenient to restrict the calculation of phase-matching to principal planes formed by the optical axes. This not only simplifies the mathematics but is useful since the effective nonlinear coefficient often maximises in at least one principal plane. The refractive indices associated with propagation in the principal planes are listed below in Table 3.2.

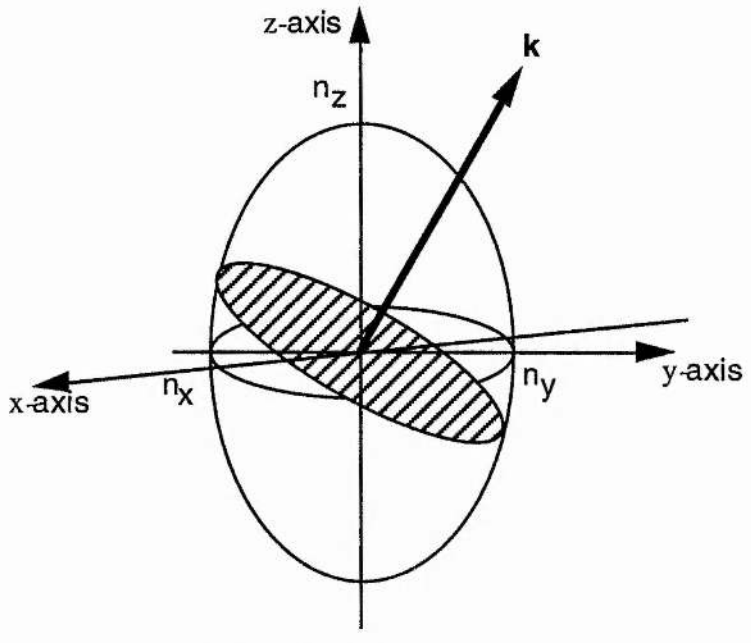

Figure 3.3 The index ellipsoid

Table 3.2 Form of the refractive indices associated with a wave propagating in a principal optical plane. $n_{//}$ and $n_{\perp}$ are the indices parallel and normal to the plane respectively.

Principal plane	*Propagation direction (//k)*	$n_{\perp}$	$n_{//}$
12	(90°, ϕ)	n_3	$\left(\frac{\sin^2\phi}{n_1^2} + \frac{\cos^2\phi}{n_2^2}\right)^{-1/2}$
13	(θ, 0°)	n_2	$\left(\frac{\sin^2\theta}{n_3^2} + \frac{\cos^2\theta}{n_1^2}\right)^{-1/2}$
23	(θ, 90°)	n_1	$\left(\frac{\sin^2\theta}{n_3^2} + \frac{\cos^2\theta}{n_2^2}\right)^{-1/2}$

For a general three-wave interaction where $\omega_3 = \omega_1 + \omega_2$, the process is described as *Type I* when the polarisations of ω_1 and ω_2 are parallel and *Type II* when the polarisations are orthogonal. In parametric generation, the expressions given above can be used to determine the unique

wavelengths which are phase-matched for a chosen propagation direction and pump wavelength. This technique can be used to plot "phase-matching curves" of wavelength against propagation angle, examples of which are included in Chapters 4 and 5 for KTP and RTA. Alternatively, for processes such as second-harmonic generation, it can be more important to determine the angular locus over which phase-matching occurs. If the angular behaviour of the effective nonlinear coefficient is also known, it then becomes easy to identify the optimum crystal orientation.

3.5 Nonlinear susceptibility and effective nonlinear coefficients

Tensor description of nonlinear interactions

The example illustrated in Figure 3.2 described a scalar relationship between polarisation and applied field. In general however the field components in many different directions determine the polarisation response along any one direction. For this reason, a full description requires the nonlinear polarisation and the applied field to be related by the three-dimensional nonlinear susceptibility tensor $\mathbf{d}_{ijk}^{(2)}$ such that,

$$P_i(t) = \sum_{ijk} 2\, d_{ijk}^{(2)}\ \varepsilon_o\, E_j(t)\, E_k(t)\ . \qquad (14)$$

Since interchanging the order of E_j and E_k in the above equation can have no physical meaning it follows that $d_{ijk} = d_{ikj}$. The tensor $\mathbf{d}_{ijk}$ can therefore be simplified to a 3 x 6 matrix, $\mathbf{d}_{il}$ where the subscript l replaces the subscripts jk according to the convention (known as the *piezoelectric contraction*) where,

$$\begin{array}{lll} 11 \rightarrow 1 & 22 \rightarrow 2 & 33 \rightarrow 3 \\ 23 = 32 \rightarrow 4 & 13 = 31 \rightarrow 5 & 12 = 21 \rightarrow 6. \end{array} \tag{15}$$

The interaction of two electromagnetic waves in a nonlinear medium is therefore described by a two-dimensional tensor $\mathbf{d}_{il}$ which is unique to the material. However, not all the components of this tensor are independent of each other. *Kleinman's conjecture* [2] states that if the polarisation is a single-valued function of electric field (for example, in a lossless medium) then no physical significance can be attached to the order of the field components E_j, E_k and E_l. All the d_{ijk} coefficients that are related by a rearrangement of the subscripts are therefore equal. Applied together with the symmetry relation, Kleinman symmetry reduces the number of independent components of $\mathbf{d}_{il}$ to ten, so that,

$$\mathbf{d}_{il} = \begin{pmatrix} d_{11} & d_{12} & d_{13} & d_{14} & d_{15} & d_{16} \\ d_{16} & d_{22} & d_{23} & d_{24} & d_{14} & d_{12} \\ d_{15} & d_{24} & d_{33} & d_{23} & d_{13} & d_{14} \end{pmatrix} \tag{16}$$

Values for some or all of the d_{il} components can be obtained experimentally for transparent nonlinear materials using a variety of techniques [3, 4]. Further discussion of the nonlinear susceptibility is included later in a description of the calculation of the effective nonlinear coefficient for any nonlinear interaction in a crystal medium.

Frames of reference

A major source of ambiguity in the calculation and reporting of crystallographic information in nonlinear optics results from confusion over the relationships between the various co-ordinate frames

encountered in the description of different quantities. Particular difficulty arises in determining the behaviour of biaxial crystals in the orthorhombic *mm2* crystal class due to differences between the literature and standardised reporting designations such as those proposed in IEEE / ANSI-Std. 176-1987 [5]. Table 3.3 lists the axes and class designations common in the literature together with the IEEE / ANSI designations for some common orthorhombic crystals. In this table, the smallest, mid-sized and largest unit cell parameters are designated by S , M and L and crystals are described as being positive or negative biaxial according to whether the angle between the z-axis and the optic axis is less than or greater than 45°. The frames of reference listed are those of the piezoelectric axes *{XYZ}*, the crystallographic axes *{abc}*, the optical axes *{xyz}* and the polar axes *{123}* . In the IEEE / ANSI recommendations the crystallographic axes *{abc}*, which describe the unit cell, are assigned in size order by the convention $c_o < a_o < b_o$ and the optical axes *{xyz}* are chosen so that $n_z > n_y > n_x$. The piezoelectric axes *{XYZ}* , in which the nonlinear susceptibility tensor is defined, are chosen according to the direction of the polar axis (the rotation axis *not* lying perpendicular to a mirror plane). By definition the X-axis is parallel to the shorter non-polar axis and the Z-axis is parallel to the polar axis itself. The Y-axis is chosen to make *{XYZ}* a right-handed frame. Spherical polar co-ordinates used to describe wave directions inside the crystal are defined in the *{123}* frame where *3* is the spherical-polar axis ($\theta = 0$) and *1* is the azimuthal axis ($\phi = 0$). For positive biaxial crystals the *{123}* frame is equivalent to *{xyz}* with *1=x, 2=y and 3=z* while negative biaxial crystals have *1=y, 2=z and 3=x.*

Table 3.3 IEEE/ANSI-Std. 176-1987 and commonly used literature axis and class designations of selected orthorhombic crystals (taken from Ref. [6])

Crystal	*Type*	*IEEE/ANSI*			*Class*	*Literature*			*Class*	*Differences*
		M	*L*	*S*		*M*	*L*	*S*		
KTP	+ve	Z	Y	X	2mm	Z	X	Y	mm2	a, b, c,X, Y; d_{31}, d_{32} reversed from IEEE / ANSI (same for d_{31}, d_{32})
		a	b	-c		c	a	b		
		z	x	-y		z	x	y		
		3	1	2		3	1	2		
RTA	+ve	Z	Y	X	2mm	Z	X	Y	mm2	a, b, c,X, Y; d_{31}, d_{32} reversed from IEEE / ANSI (same for d_{31}, d_{32})
		a	b	-c		c	a	b		
		z	x	-y		z	x	y		
		3	1	2		3	1	2		
LBO	-ve	X	Y	Z	mm2	Y	X	Z	mm2	a, b,X, Y, 1, 2, 3; d_{31}, d_{32} reversed from IEEE / ANSI (same for d_{31}, d_{32})
		a	b	c		b	a	c		
		z	x	y		z	x	-y		
		2	3	1		3	1	2		
$KNbO_3$	-ve	Y	Z	X	m2m	X	Z	Y	mm2	b, c,X, Y, 1, 2, 3; d_{31}, d_{32} reversed from IEEE / ANSI (same for d_{31}, d_{32})
		a	b	c		a	c	b		
		-y	x	z		y	x	z		
		1	3	2		2	1	3		

Calculation of the effective nonlinear coefficient

The conversion efficiency of a nonlinear process is depends directly on the value of the effective nonlinear coefficient, d_{eff}, which is a function of the material nonlinear coefficients d_{il} and the **E**-field polarisation directions. The interaction of two applied fields $\mathbf{E}_j$ and $\mathbf{E}_k$ induces a second-order polarisation field $\mathbf{P}_i$ given by,

$$P_i = \hat{a}_i \; d_{ijk} \; \hat{a}_j \hat{a}_k \; E_j E_k \; = \; d_{eff} E_j E_k \,, \tag{17}$$

where $\hat{a}_i$, $\hat{a}_j$ and $\hat{a}_k$ are the unit vectors of $\mathbf{P}_i$, $\mathbf{E}_j$ and $\mathbf{E}_k$ and $\mathbf{d}_{ijk}$ is the second-order polarisation tensor of the nonlinear material. The effective nonlinear coefficient can therefore be expressed as,

$$d_{eff} = \hat{a}_i \; d_{ijk} \; \hat{a}_j \hat{a}_k \,. \tag{18}$$

A wave propagating inside a crystal will decompose into two orthogonal polarisation components, a slow ray e_1 and a fast ray e_2. The corresponding electric displacement vectors, $\mathbf{D}^{e1}(\omega_i)$ and $\mathbf{D}^{e2}(\omega_i)$, are perpendicular to the propagation direction $\mathbf{k}(\theta,\phi)$ and have unit vectors $\hat{b}^{e1}$ and $\hat{b}^{e2}$ given by,

$$\hat{b}^{e1} = \begin{pmatrix} -\cos\theta\cos\phi\cos\delta_i + \sin\phi\sin\delta_i \\ -\cos\theta\sin\phi\cos\delta_i - \cos\phi\sin\delta_i \\ +\sin\theta\cos\delta_i \end{pmatrix} = \begin{pmatrix} b_1^{e1} \\ b_2^{e1} \\ b_3^{e1} \end{pmatrix} \tag{19a}$$

$$\hat{b}^{e2} = \begin{pmatrix} -\cos\theta\cos\phi\sin\delta_i - \sin\phi\cos\delta_i \\ -\cos\theta\sin\phi\sin\delta_i + \cos\phi\cos\delta_i \\ +\sin\theta\sin\delta_i \end{pmatrix} = \begin{pmatrix} b_1^{e2} \\ b_2^{e2} \\ b_3^{e2} \end{pmatrix} \tag{19b}$$

where δ_i is the polarisation angle which for positive biaxial crystals is given by [6],

$$\tan 2\delta_i^{+} = \frac{\sin 2\phi\cos\theta}{\sin^2\phi - \cos^2\theta\cos^2\phi + \cot^2\Omega_i\sin^2\theta} \tag{20}$$

and which for negative biaxial crystals is,

$$\tan 2\delta_i^{-} = \frac{-\sin 2\phi\cos\theta}{\cos^2\phi - \cos^2\theta\sin^2\phi + \tan^2\Omega_i\sin^2\theta} \tag{21}$$

The optic axes lie at angles of $\pm\Omega_i$ to the z-axis where Ω_i is given by,

$$\Omega_i = \pm\arcsin\left(\frac{n_z(\omega_i)}{n_y(\omega_i)}\sqrt{\frac{n_y^2(\omega_i) - n_x^2(\omega_i)}{n_z^2(\omega_i) - n_x^2(\omega_i)}}\right) \tag{22}$$

Electric field **E** and displacement **D** are related in a principal-axis system by,

$$\begin{pmatrix} E_1 \\ E_2 \\ E_3 \end{pmatrix} = \begin{pmatrix} 1/n_1^2 & 0 & 0 \\ 0 & 1/n_2^2 & 0 \\ 0 & 0 & 1/n_3^2 \end{pmatrix} \begin{pmatrix} D_1 \\ D_2 \\ D_3 \end{pmatrix} \tag{23}$$

The electric fields for the two polarisation components are therefore,

$$\mathbf{E}^{e1}(\omega_i) = \left(\frac{(b_1^{e1})^2}{n_1^4(\omega_i)} + \frac{(b_2^{e1})^2}{n_2^4(\omega_i)} + \frac{(b_3^{e1})^2}{n_3^4(\omega_i)} \right)^{1/2} \mathbf{D}^{e1}(\omega_i) = \mathbf{P}(\omega_i)\ \mathbf{D}^{e1}(\omega_i) \tag{24a}$$

$$\mathbf{E}^{e2}(\omega_i) = \left(\frac{(b_1^{e2})^2}{n_1^4(\omega_i)} + \frac{(b_2^{e2})^2}{n_2^4(\omega_i)} + \frac{(b_3^{e2})^2}{n_3^4(\omega_i)} \right)^{1/2} \mathbf{D}^{e2}(\omega_i) = \mathbf{Q}(\omega_i)\ \mathbf{D}^{e2}(\omega_i) \tag{24b}$$

The unit vectors of electric field which are needed to calculate d_{eff} can be expressed as,

$$\hat{a}^{e1} = \frac{1}{\mathbf{P}(\omega_i)} \begin{pmatrix} b_1^{e1} / n_1^2(\omega_i) \\ b_2^{e1} / n_2^2(\omega_i) \\ b_3^{e1} / n_3^2(\omega_i) \end{pmatrix} = \begin{pmatrix} a_1^{e1} \\ a_2^{e1} \\ a_3^{e1} \end{pmatrix} \tag{25a}$$

$$\hat{a}^{e2} = \frac{1}{\mathbf{Q}(\omega_i)} \begin{pmatrix} b_1^{e2} / n_1^2(\omega_i) \\ b_2^{e2} / n_2^2(\omega_i) \\ b_3^{e2} / n_3^2(\omega_i) \end{pmatrix} = \begin{pmatrix} a_1^{e2} \\ a_2^{e2} \\ a_3^{e2} \end{pmatrix} \tag{25b}$$

For mixing between two waves of parallel polarisation (*Type I* interaction) the E^2 column tensors are,

$$\hat{a}^{e1} \cdot \hat{a}^{e1} = \begin{pmatrix} a_1^{e1} a_1^{e1} \\ a_2^{e1} a_2^{e1} \\ a_3^{e1} a_3^{e1} \\ 2a_2^{e1} a_3^{e1} \\ 2a_1^{e1} a_3^{e1} \\ 2a_1^{e1} a_2^{e1} \end{pmatrix} = \begin{pmatrix} A_{11} \\ A_{12} \\ A_{13} \\ A_{14} \\ A_{15} \\ A_{16} \end{pmatrix}^{+} \tag{26a}$$

$$\hat{a}^{e2} \cdot \hat{a}^{e2} = \begin{pmatrix} a_1^{e2} a_1^{e2} \\ a_2^{e2} a_2^{e2} \\ a_3^{e2} a_3^{e2} \\ 2a_2^{e2} a_3^{e2} \\ 2a_1^{e2} a_3^{e2} \\ 2a_1^{e2} a_2^{e2} \end{pmatrix} = \begin{pmatrix} A_{11} \\ A_{12} \\ A_{13} \\ A_{14} \\ A_{15} \\ A_{16} \end{pmatrix}^{-} \tag{26b}$$

and for orthogonally polarised waves (*Type II* interaction) the $\mathbf{E}^2$ column tensor is,

$$\hat{a}^{e1} \cdot \hat{a}^{e2} = \begin{pmatrix} a_1^{e1} a_1^{e2} \\ a_2^{e1} a_2^{e2} \\ a_3^{e1} a_3^{e2} \\ a_2^{e1} a_3^{e2} + a_3^{e1} a_2^{e2} \\ a_1^{e1} a_3^{e2} + a_3^{e1} a_1^{e2} \\ a_1^{e1} a_2^{e2} + a_2^{e1} a_1^{e2} \end{pmatrix} = \begin{pmatrix} A_{21} \\ A_{22} \\ A_{23} \\ A_{24} \\ A_{25} \\ A_{26} \end{pmatrix} \tag{27}$$

Substituting the above results into the general definition for d_{eff} gives expressions for the effective nonlinear coefficients for both Type I and Type II interactions.

In positive biaxial crystals, Type I parametric conversion is phase-matched by $e_2 \rightarrow e_1, e_1$ while Type II interactions require $e_2 \rightarrow e_2, e_1$ so,

$$d_{eff}^{+}(I) = \begin{pmatrix} a_1^{e2} \\ a_2^{e2} \\ a_3^{e2} \end{pmatrix} d_{ijk} \begin{pmatrix} A_{11} \\ A_{12} \\ A_{13} \\ A_{14} \\ A_{15} \\ A_{16} \end{pmatrix}^{+} \tag{28a}$$

$$d_{eff}^{+}(II) = \begin{pmatrix} a_1^{e2} \\ a_2^{e2} \\ a_3^{e2} \end{pmatrix} d_{ijk} \begin{pmatrix} A_{21} \\ A_{22} \\ A_{23} \\ A_{24} \\ A_{25} \\ A_{26} \end{pmatrix}. \tag{28b}$$

Negative biaxial crystals require $e_1 \rightarrow e_2$, e_2 to satisfy type I phase-matching while type II processes phase-match as $e_1 \rightarrow e_1$, e_2 with the result that,

$$d_{eff}^{-}(I) = \begin{pmatrix} a_1^{e1} \\ a_2^{e1} \\ a_3^{e1} \end{pmatrix} d_{ijk} \begin{pmatrix} A_{11} \\ A_{12} \\ A_{13} \\ A_{14} \\ A_{15} \\ A_{16} \end{pmatrix}^{-} \tag{29a}$$

$$d_{eff}^{-}(II) = \begin{pmatrix} a_1^{e1} \\ a_2^{e1} \\ a_3^{e1} \end{pmatrix} d_{ijk} \begin{pmatrix} A_{21} \\ A_{22} \\ A_{23} \\ A_{24} \\ A_{25} \\ A_{26} \end{pmatrix}. \tag{29b}$$

Values of the nonlinear coefficients d_{il} are normally quoted in the *{XYZ}* frame and need to be converted to the *{123}* frame in which θ and ϕ are defined. For crystals possessing orthorhombic symmetry or higher this can be achieved by a permutation of the indices of d_{ijk} and in general any two frames can be related by a sequence of rotations using tensor

operators [6]. An example of the calculation of d_{eff} for Type II parametric generation in KTP is illustrated in Chapter 4.

3.6 Calculation of optimum parameters in three-wave mixing processes in crystalline nonlinear media

In a nonlinear process, the energy conversion efficiency depends on a variety of parameters. The importance of phase-matching to achieve $\Delta k = 0$ has already been outlined in the previous section as has the role of the nonlinear susceptibility d_{il} which is responsible for coupling energy between interacting waves. Another important effect observed in birefringent media is *Poynting-vector walkoff* which is the difference between the wavefront direction (**k** - vector) and the ray direction (**s** - vector). This limits efficiency by reducing the spatial overlap between the interacting waves. Finally, the finite spectral bandwidths of the interacting waves result in a certain amount of imperfect phase-matching in any process. This can be described in terms of a limited bandwidth for a particular interaction. This section describes in detail how the importance of the effects outlined above can be determined quantitatively. All of the analysis is presented for the general case of a biaxial crystal (ie. $n_x \neq n_y \neq n_z$) although the results are equally valid in the uniaxial limit.

Poynting-vector walkoff

In a nonlinear crystal, the *walkoff angle* is defined as the angle between the wave-vector **k** and the Poynting vector **s**. and is therefore also the angle between the electric field vector **E** and the displacement vector **D**. In a biaxial crystal, a ray propagating in any direction except along an optical axis will "walkoff" from the wavevector direction as illustrated in Figure 3.4. The wavevector lies normal to surfaces of constant phase while

the Poynting vector is the direction of ray propagation or energy flow. The walkoff angle can be calculated using the results of the previous section which include expressions for vectors parallel to **D** and **E**.

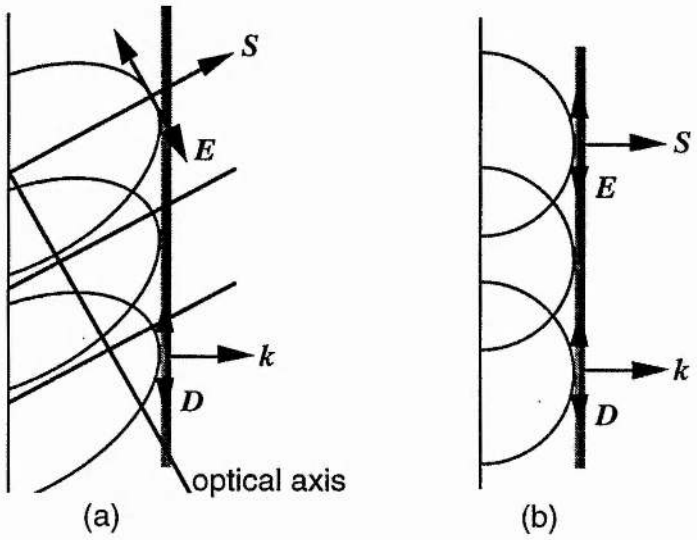

Figure 3.4 Off-axis propagation of wavelets in a birefringent (a) and an isotropic (b) material

The unit vectors parallel to **D** and **E** were given by $\hat{b}$ and $\hat{a}$ respectively. The walkoff angle α can be obtained for any wave from the dot product $\hat{a} \cdot \hat{b}$ where,

$$\alpha = \arccos\ (\hat{a} \cdot \hat{b})\,. \tag{30}$$

Walkoff amongst the rays in a three-wave interaction can affect conversion efficiency if, at some point, the rays fail to overlap sufficiently [7] and, in severe cases, can lead to aperturing of a beam whose diameter is comparable to the crystal cross-section. For these reasons it is often favourable in a three-wave interaction to avoid walkoff problems by choosing a *noncritical* crystal geometry in which all rays propagate along an optical axis. The more general *critical* phase-matching geometry, where

one or more beams propagate along directions not aligned with any optical axis, are however subject to walkoff problems. In this situation, efficiency can still be optimised if a crystal cut is chosen in which the three waves interact noncollinearly so that the rays *walkon* to each other as they travel through the crystal [8]. In this case, the overlap of the interacting beams increases with propagation and efficiency is not so severely affected.

Spectral bandwidth and acceptance angles

It was mentioned earlier that the efficiency of any nonlinear process depends on the mismatch between the wavevectors of the interacting waves according to the power conversion factor $sinc^2\ (\Delta kl/2)$. A useful criterion for the maximum allowable wavevector mismatch is given by,

$$\Delta k = \pm \pi / l \tag{31}$$

which corresponds to an efficiency of ≈ 40 % of the maximum attainable. For a three-wave interaction the efficiency depends on the directions and the magnitudes of the wavevectors involved (see Figure 3.5) and the mismatch is given by,

$$\begin{aligned} \Delta k &= | \mathbf{k}_1 \pm \mathbf{k}_2 - \mathbf{k}_3 | \\ &= k_1 \cos \varphi_3 \pm k_2 \cos (\varphi_2 - \varphi_3) - k_3 \end{aligned} \tag{32}$$

Clearly there is a maximum variation of any parameter (eg. wavelength, internal angle, temperature etc.) ΔX that can be accommodated while $|\Delta k| \leq \pi/l$. This is described by the first order Taylor expansion,

$$\Delta k = \Delta k_o + \frac{\partial \Delta k}{\partial \Delta X} \Delta X = \pm \frac{\pi}{l} \tag{33}$$

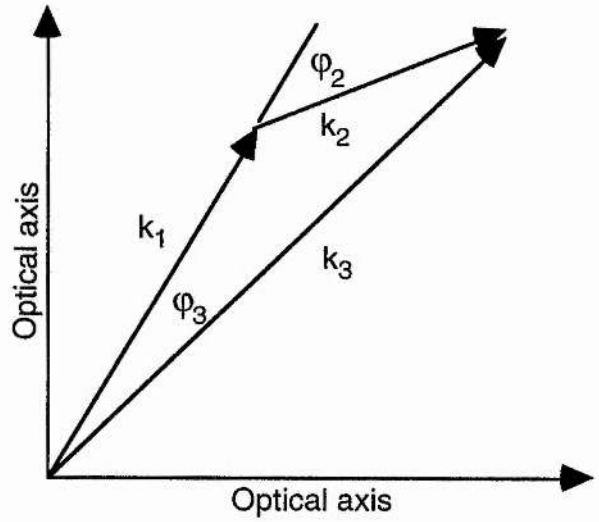

Figure 3.5 Wavevector diagram defining the relative angles between interacting waves

Treatment to second order is described in detail by Barnes and Corcoran [9] and enables special cases in which the first order term is small to be analysed accurately. When the interacting waves are nominally phase-matched at line centre (ie. $\Delta k_o = 0$) the full spectral bandwidth is given by $2\Delta\lambda_2$ where,

$$\Delta\lambda_2 =$$

$$\left[2l \left(\pm \frac{\partial n_2}{\partial \lambda_2} \cos(\varphi_2 \mp \varphi_3) \frac{1}{\lambda_2} \mp \frac{\partial n_3}{\partial \lambda_3} \frac{\lambda_3}{\lambda_2^2} \mp n_2 \cos(\varphi_2 \mp \varphi_3) \frac{1}{\lambda_2^2} \pm n_2 \frac{1}{\lambda_2^2} \right) \right]^{-1} \quad \text{—— (34)}$$

and the plus and minus signs correspond to sum and difference frequency-mixing processes $\omega_3 = \omega_1 \pm \omega_2$. If the Sellemeier equations are known for a particular nonlinear crystal then the phase-matching bandwidth can be calculated for any combination of wavelengths. One result, that longer crystals have smaller phase-matching bandwidths

restricts the length of crystal which can be used in the frequency conversion of broad-bandwidth ultrashort pulses. This is considered further in Section 3.8

The maximum angular variation can be calculated in a similar way to the spectral bandwidth and is derived to terms in the second order in Reference [9]. An important case occurs for non-critical phase-matching where all the waves interact collinearly along a principal optical axis. Here, the first order term in the Taylor series expansion about constant θ or ϕ vanishes and the angular acceptance ($\Delta\theta$ or $\Delta\phi$) increases substantially.

3.7 Optical parametric oscillation

A *parametric oscillator* exploits difference frequency mixing to convert energy from a powerful high-frequency pump wave at ω_3 into outputs with frequencies ω_1 and ω_2 (conventionally known as the *signal* and the *idler* waves). By configuring the nonlinear medium within a high-finesse resonator, feedback can be supplied at one or both of the lower frequencies and a *singly-resonant* or *doubly-resonant* oscillator is formed. Figure 3.6 shows a schematic representation of the resonator of an optical parametric oscillator.

Oscillation occurs when the roundtrip gain experienced by the resonant wave(s) exceeds the net cavity losses. The gain is highest in the doubly-resonant oscillator (DRO) where both of the generated waves experience minimal loss and, consequently, the threshold pump intensity required to reach oscillation is much lower than in the singly-resonant oscillator (SRO). DRO operation requires that both the waves are properly

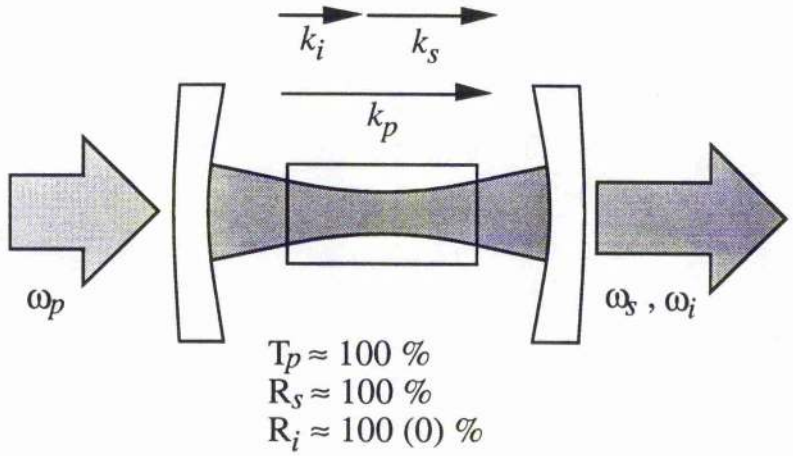

Figure 3.6 *Schematic representation of a singly (doubly) resonant optical parametric oscillator.*

resonated which places a severe constraint on the length of the resonator since only certain lengths are equal to an integral number of both signal and idler modes. Excessive variation in the resonator length or in the pump frequency leads to instabilities in the threshold condition causing intensity fluctuations in the output of a DRO. For these reasons, singly-resonant operation is often preferred because of the more stable output even though much higher pump powers are necessary. Calculation of the gain of a singly-resonant oscillator will be described in detail in the following section.

The superior stability of the singly-resonant oscillator makes it the more attractive device for applications requiring narrow linewidth or high wavelength stability. The higher oscillation threshold requires peak pump intensities which generally are only available from pulsed laser systems. Quasi-continuous-wave operation within the duration of a Q-switched pulse envelope is one method of achieving singly-resonant operation. Another is to use a modelocked pump source and configure the signal wave resonator to be synchronous with the pump laser pulse repetition

period. This arrangement ensures that the amplified signal pulse always returns to the gain crystal at the same time as the subsequent pump pulse. Gain is confined to a temporal window corresponding to the duration of the overlap between the pump and the signal pulses in the nonlinear crystal.

3.8 Design considerations for a synchronously-pumped, singly-resonant, femtosecond OPO

This section introduces the essential requirements necessary to realise optimum operation from an optical parametric oscillator synchronously-pumped by the output of a cw-modelocked femtosecond laser. The choice of nonlinear material and estimation of the pump-power oscillation threshold are discussed and the importance of the resonator design including focusing and output coupling considerations is illustrated. In addition, effects influencing the output pulse durations from the OPO are reviewed.

Nonlinear material

In deciding the appropriate nonlinear crystal to use for an OPO, a number of considerations must be taken into account. Even before any of the nonlinear or dispersive properties of the crystal are considered, there are issues such as optical transparency, optical and thermal damage and chemical stability that must be evaluated.

Considering first the optical transparency of the material, if either the signal or idler output from the OPO is a wavelength in the infrared then many nonlinear crystals may not be fully transparent. Table 3.4 lists the optical transparency of a number of common nonlinear materials, many of which exhibit cutoff frequencies in the near-infrared. Absorption at the

resonant wavelength will reduce the efficiency of the OPO while energy absorbed at the non-resonant wavelength may heat or damage the crystal.

Table 3.4 Optical transparency of common nonlinear materials

Nonlinear material	*Optical transparency*	*Reference*
β-BBO	*198 nm - 2.6 μm*	[10]
LBO	*160 nm - 2.6 μm*	[11]
KTP	*350 nm - 4.5 μm*	[12]
RTA	*350 nm - 5.3 μm*	[13]
$KNbO_3$	*400 nm - 4.5 μm*	[14]

While even cw light absorbed outside the transparency window of a material may cause damage due to heating effects, the high intensities of modelocked or Q-switched pulses can result in optical damage at any wavelength. The incident power density of light required to damage a nonlinear crystal will depend on several factors including wavelength, pulse duration and pulse energy. Damage thresholds can only be compared when this information is taken into account.

The damage threshold of a material is commonly determined by focusing a Q-switched nanosecond pulse of known energy into a sample which is then inspected for damage using interference techniques. Typically, pulses with longer durations can cause optical damage more readily. Observations of low repetition rate picosecond and cw-femtosecond OPO experiments have reported no damage to KTP crystals pumped with MW-peak-power pulses in prolonged use [15, 16]. In a study of βBBO [17] the one-shot damage threshold was found to be as high as 13.5 GW/cm^2 for a 1 ns - duration pulse at a wavelength of 1064 nm. In a

separate investigation the damage threshold of βBBO due to a 100fs red pulse was reported to be as high as 1 TW/cm^2 [18]. Comparison of these results can provide an order-of-magnitude estimate of the damage thresholds of common nonlinear materials at femtosecond pulse durations, a summary of which is given in Table 3.5.

Table 3.5 Damage intensity thresholds at ns and fs pulse durations for common nonlinear materials

Material	*1 ns pulse damage threshold (GW/cm^2)*	*100 fs pulse damage threshold (TW/cm^2)*	*Reference*
LBO	18.9†	1.8*	[19]
KTP	15	1.1*	[20]
BBO	13.5	1.0	[17, 18]

**Inferred values* †*Pulse duration 1.3 ns*

Finally, for most applications requiring prolonged use of a crystal, the chemical stability of the material is important. Some nonlinear materials such as KDP are hygroscopic and require to be kept in a moisture-free environment. Others crystals, for example $KNbO_3$, can spontaneously form microscopic single-crystal domains within the bulk material which can compromise phase-matching in an OPO. Other mechanical details of the material such as the thermo-elastic coefficient may be of interest if phase-matching requires that the crystal is maintained at a high temperature eg. Type I non-critically phase-matched LBO-based oscillators.

Optimum focusing in an optical parametric oscillator

For an OPO to reach steady state oscillation the single pass gain of the nonlinear crystal must exceed the roundtrip losses of the resonator. It is

important therefore to accurately estimate the pump-power threshold for oscillation and to correctly match the pump and cavity mode focusing to minimise threshold.

There have been several theoretical studies of how parametric gain depends on pump focusing. The effect of focusing on parametric upconversion [21], singly-resonant [22] and doubly-resonant oscillators [23] have all been considered. Guha and Falk [24] give a general analysis of threshold pump intensity for singly and doubly-resonant OPO's. For an SRO they derive an expression for the pump power threshold P_{th} as a function of a focusing factor h_s and of the three frequencies involved where,

$$P_{th}=\frac{\varepsilon_S\, n_s\, n_i\, n_p\, c^3\, (k_s + k_p)}{128\, \omega_S\, \omega_i\, \chi^2\, \pi^2\, l\, h_s\, k_s\, k_p} \tag{35}$$

and,
$$\chi \ \ (esu\ units) \ = \frac{3 \times 10^4}{2\pi} d_{eff} \ \ (SI\ units). \tag{36}$$

Two dimensionless quantities used in Equation (35) are ε_s which is the fractional roundtrip cavity loss and h_s which is a factor describing the efficiency of the parametric interaction with focusing. All other variables are in S.I. units and l is the crystal length.

The focusing factor h_s depends on wavelength, crystal length, walkoff angle and the confocal parameters of the beams which are defined as,

$$b \ = \frac{2\pi w_o^2}{\lambda}\ , \tag{37}$$

where w_o is the radius of the beam waist formed in the crystal. Guha and Falk provide plots of h_s which are derived numerically. Figure 3.7a reproduces the dependence on the signal focusing of h_s when the confocal

parameter of the pump is equal to the crystal length. In Figure 3.7b h_s is shown for equal pump and signal confocal parameters.

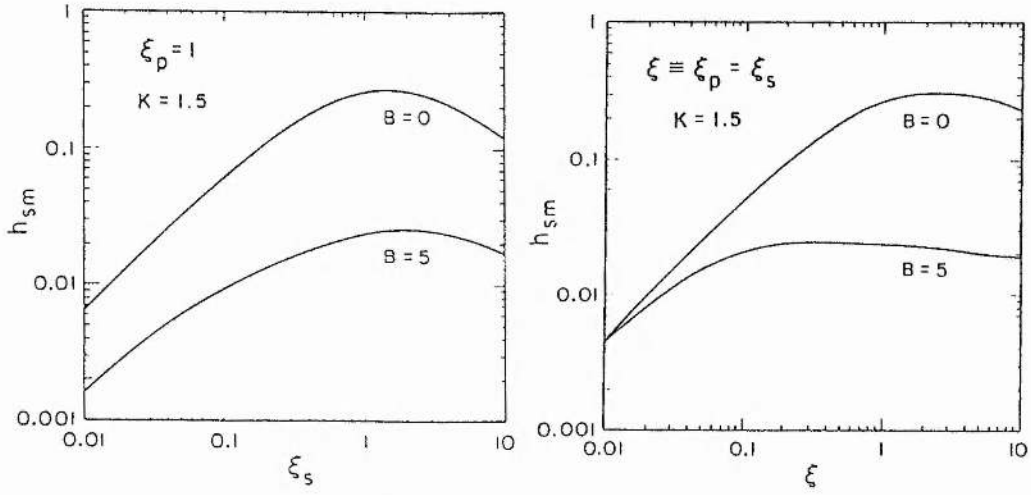

Figure 3.7 Dependence of the focusing factor h_s on the signal focusing on the signal confocal parameter when the pump confocal parameter equals the crystal length (a) and the signal confocal parameter (b).

These results show that, in the absence of walkoff and when the confocal parameters of the pump and signal waves are equal, h_s maximises at ≈ 0.25 for optimum focusing. This situation occurs when the confocal parameters of the pump and resonant waves ($b_s = b_p$) are smaller than the length of the nonlinear crystal such that $l = 2.7b_s = 2.7b_p$. It is often difficult experimentally to achieve focusing as tight as $l = 2.7b$ and, in this situation, h_s maximises for unequal pump and signal confocal parameters where $b_s > b_p$. Values of h_s for unequal confocal parameters are also given by Guha and Falk.

When the analysis outlined above is applied to an OPO pumped by a modelocked laser, the power threshold obtained is equal to the mean power delivered by the modelocked pulse. This can be expressed as an average power if the pulse duration and repetition frequency of the pump

laser are known. Using this method, the calculation of the expected threshold power of a Ti:sapphire-pumped femtosecond OPO using KTP is described in Chapter 4. From Equation (35) it is clear that (within the limit imposed by the acceptance bandwidth) the threshold power depends inversely on the crystal length, implying that longer crystals are of benefit in reducing the power necessary for oscillation.

Resonator design

Steady-state oscillation of a synchronously-pumped femtosecond OPO requires the cavity lengths of the OPO and the pump laser to be interferometrically matched. Any small mismatch between the cavity repetition periods of the pump laser and the OPO has the effect of modifying the signal wavelength of the OPO. This occurs because the pulse transit time through the OPO cavity is frequency dependent with the result that a change in wavelength of a few tens of nanometres is sufficient to compensate a cavity length mismatch of a few microns.

Analysis of the coupled-wave equations in the limit of no idler feedback shows that, for a cw singly-resonant OPO, 100 % signal-photon-conversion efficiency (ie. no backconversion from the signal wave to the pump) occurs for a pump power $(\pi/2)^2$ times above threshold [25]. Numerical simulation of a singly-resonant synchronously-pumped OPO, taking into account dispersive-broadening effects and bandwidth control, has also shown that maximum efficiency corresponds to pumping at approximately twice threshold [26]. These results imply that, for maximum signal extraction, the output coupling of the OPO resonator should be chosen so that the threshold power corresponds to approximately half of the available pump power. Better stability is also expected for pump powers a few times above threshold since the length

mismatch between the pump and OPO cavities becomes less critical further above threshold.

The geometry of the OPO cavity must allow variable length adjustment and be capable of providing intracrystal mode sizes with $w_0 \approx 20$ μm. This is necessary to achieve suitably high intensities for low-threshold operation and, at the same time, to provide adequate mode-matching for crystals of practical length. Three or four-mirror resonators readily satisfy these requirements and can take the form of either standing-wave or ring cavities. If the ellipticity of the output mode is of importance then a cavity configuration should be chosen which can provide compensation for astigmatism. Dunn and Ferguson [27] have shown that a three-mirror V cavity containing a Brewster-angled crystal can only compensate for astigmatism in the collimated arm of the resonator and not inside the crystal. However, they also demonstrate that a four-mirror Z, X or ring cavity using a Brewster crystal can simultaneously provide astigmatism compensation inside and outside the crystal. Although a Brewster-angled geometry can give complete astigmatism compensation, an antireflection-coated crystal used at normal incidence is often preferable because of the easier alignment and angle-tuning it provides. In this case the resonator fold-angle is kept small to minimise aberrations caused by astigmatism. In addition, a Brewster-geometry only allows efficient pumping if the resonant wave and the pump have parallel polarisations and doubly-resonant operation is therefore not a possibility.

The roundtrip loss of the resonator is also important since cavities whose loss coefficients are equivalent for laser gain media are not necessarily of equal loss when used with a phase-matched gain medium. In an OPO configured for single-pass pumping, phase-matching

requirements mean that the pulse only experiences gain when travelling in one direction through the nonlinear crystal. The standing-wave resonator with the smallest roundtrip loss is therefore the three-mirror V cavity since each "gain pass" through the crystal corresponds to only four mirror reflections and four crystal surfaces. In contrast, the Z and X cavities each incur six mirror reflections and four crystal surfaces for each gain pass through the nonlinear medium. The four-mirror-ring cavity has the lowest roundtrip loss with only four reflections and two crystal surfaces for each gain pass. Alignment considerations may however rule out this configuration.

Pulse duration in a synchronously-pumped OPO

Design parameters of particular interest in the construction of a femtosecond parametric oscillator include spatial walkoff, spectral bandwidth and group-velocity walkaway between the pump, signal and idler pulses. These effects can reduce gain and increase the duration of the output pulses from the oscillator.

The resonant signal pulse in the cavity of a synchronously-pumped femtosecond OPO is subject to many of the pulse-broadening effects that are apparent in modelocked lasers such as second and third-order group-velocity dispersion, bandwidth limitation, self-phase-modulation and gain saturation. Additionally, other effects unique to parametric devices can influence the duration of the output pulses from an OPO. Pump depletion, group-velocity walkaway, phase-matching bandwidth and nonlinear parametric gain are competing effects often with magnitudes comparable to those already mentioned.

At least two detailed theoretical studies of pulse evolution in a synchronously-pumped OPO have been carried out and both proceed by numerically solving the coupled-wave equations described earlier. Becker *et al* [28] have considered only the degenerate case of Type I phase-matching where the signal and idler waves are indistinguishable. Cheung and Liu however [26], have solved for the general case of non-degenerate signal and idler wavelengths in a singly-resonant oscillator. Both studies conclude that the duration of the pump pulse imposes a fundamental limit on the width of the signal pulse. In both cases, pump depletion is the dominant effect determining the signal pulse duration. The further above threshold the OPO is operated then the more severe the pump depletion will be. The intensity-dependent parametric gain broadens the pump pulses because it depletes the centre of the pulse more strongly than the wings. In turn, this broader pump envelope determines the shape of the amplified signal pulse. The shortest pulses are therefore obtained when the OPO is operated just above threshold. In the degenerate case, where $\Delta\tau_p$ represents the pump pulse duration, output pulses as short as 0.25 $\Delta\tau_p$ are predicted. In the more general, non-degenerate analysis, the theoretical limit on the signal pulse duration is found to be 0.4 $\Delta\tau_p$. Neither study includes bandwidth broadening of either the pump or the signal pulse due to self-phase-modulation so, experimentally, shorter pulse durations may be possible.

In their non-degenerate analysis, Cheung and Liu demonstrate that the shape of the pulse envelope from an synchronously-pumped OPO will generally be asymmetric [26]. If the cavity roundtrip time of the OPO is not exactly matched to the pump repetition rate then the returning signal pulse will interact with either the leading or trailing edge of the pump pulse depending on whether the OPO cavity frequency is higher or lower

than that of the pump laser. Even when the repetition rates are exactly matched, the difference in the group velocities of the pump and signal pulses (*walkaway*) will result in asymmetric pump depletion and, consequently, an asymmetric signal envelope. Time-varying phase relations between the pump and the generated waves are also responsible for the asymmetry of the signal pulse. Expressed in a travelling-wave form, the coupled-wave equations include a phase term involving the first derivative of signal field with time. This term therefore takes a different sign for the rising and falling edge of the pulse and so each edge sees a unique phase-mismatch with respect to the centre of the pump pulse. The result is that the leading edge of the signal pulse is favoured and sees more gain than the trailing edge.

Group-velocity *walkaway* between the pump, signal and idler pulses is not only involved in making the signal pulse asymmetrical but also introduces broadening and reduces the gain of the OPO by affecting the temporal overlap of the three waves. Walkaway between the signal and the pump reduces their interaction and affects the signal field gain directly. The pump - idler walkaway however, only affects the signal indirectly through the resulting pump - idler mixing (the signal pulse could still experience gain in the initial absence of any idler radiation). In choosing a nonlinear material and a particular crystal cut it is therefore important to calculate the difference in pump and signal pulse transit times through the crystal. If this significantly exceeds the duration of either pulse then the efficiency of the interaction is likely to be reduced. To allow comparison between various materials and internal propagation directions, it is usual to calculate the difference in pulse arrival times after propagation through one millimetre of material. Expressed in units of *fs/mm* , this is given by,

$$\Delta t = \frac{1}{v_{g1}} - \frac{1}{v_{g2}}, \quad \text{where,} \tag{38a}$$

$$v_{gi} = \frac{c}{n - \lambda_i (dn/d\lambda_i)}, \tag{38b}$$

$n(\lambda)$ is the refractive index response of the material, and all velocities are measured in units of *mm/fs* . Typical values, in many materials, are approximately 100 fs/mm between the pump and the signal wave so, used in femtosecond OPOs, crystals with lengths in excess of one or two millimetres provide no additional benefit. If the waves have the same polarisation and the medium is positively dispersive then the signal pulse will lead the pump pulse. In this situation, the idler pulse may either lead or lag the pump since it propagates at a group velocity determined by a separate polarisation axis within the medium. Some materials eg. LBO possess very favourable phase-matching and birefringence qualities which allow pump and signal pulses to travel with minimal relative walkaway.

Second and third order group-velocity dispersion will also affect the duration of the resonant pulse in the OPO. After propagating through a length z of a dispersive medium, an initially transform-limited Gaussian pulse of duration $\Delta\tau_o$ will broaden through second-order dispersion to a duration given by,

$$\Delta\tau = \Delta\tau_o \sqrt{\left(1 + \left(\frac{z}{z_D}\right)^2\right)} \tag{39}$$

where the *dispersion distance*, defined as the length of the medium over which the pulse broadens by $\sqrt{2}$, is given by,

$$z_D = \frac{\Delta\tau_o^2}{4 \ln 2} \left(\frac{d^2k}{d\omega^2}\right)^{-1} \tag{40}$$

Typical dispersion distances for a 100-fs duration-pulse are ≈ 1 cm. In the absence of dispersion compensation, the duration of the output signal pulse can be estimated from the width of the pump pulse if the roundtrip loss of the OPO resonator is known. For example, if the cavity losses are ≈ 1 % then the average photon lifetime of the signal pulse in the resonator, before extraction through output coupling, can be considered to be ≈ 100 roundtrips. The pulse therefore travels through the nonlinear medium ≈ 200 times so the total propagation distance is $200t$, where t is the thickness of the nonlinear crystal. Equations (39) and (40) can then be used to estimate the final duration of the output pulse.

Operating the OPO using an intracavity prism sequence configured as described in Chapter 2 can however fully compensate for second-order dispersion in the resonator. Pulse broadening due to third-order group-velocity dispersion has been discussed by Asaki *et al* [29] who predict a square-root dependence of pulse duration on third-order dispersion,

$$\Delta\tau \propto \sqrt{\frac{d^3\phi}{d\omega^3}} \tag{41}$$

but, at wavelengths in the visible and near-infrared, this term is usually only significant for pulse durations under around 50 fs.

Another more fundamental limit on the pulse duration is imposed by the finite phase-matching bandwidth of the crystal. A 100-fs-duration $sech^2(t)$ pulse centred at a wavelength of 1μm has a frequency spectrum FWHM bandwidth of 10.7 nm. Efficiently frequency conversion therefore requires a crystal phasematching bandwidth of at least 10 nm. For many materials this limits the length of the nonlinear crystal to no more than 4 or 5 mm. Long crystals therefore cannot be used in femtosecond parametric

oscillators and consequently, only crystals with a high effective nonlinear coefficient can provide enough gain for efficient operation.

Both of the limits on crystal length outlined above, namely walkaway and phase-matching bandwidth, only apply to femtosecond oscillators. Longer crystals have been used successfully in picosecond systems such as the one demonstrated by Nebel *et al* using KTP [30] and the LBO-based device reported by Ebrahimzadeh *et al* [31]. Higher single-pass gain is, however, not necessarily obtained in these systems since the intracavity peak powers are much lower.

3.9 Conclusions

This chapter has outlined the theory of nonlinear interactions in crystalline media and has provided a background for a discussion of the necessary design criteria relevant to the efficient operation of a femtosecond optical parametric oscillator. In the following chapter a characterisation of a KTP-based parametric oscillator pumped by a self-modelocked femtosecond Ti:sapphire laser will be described. The application of many of the design principles detailed in Chapter 3 will also be illustrated.

References

1. J. Yao, W. Sheng and W. Shi, J. Opt. Soc. Am. B. **9**, 891 (1992)

2. D. A. Kleinman, Phys. Rev. **126**, 1977 (1962)

3. M. M. Choy and R. L. Byer, Phys. Rev. B. **14**, 1693 (1976)

4. S. K. Kurtz, J. Jerphagnon and M. M. Choy, "Nonlinear dielectric susceptibilities," in Landolt-Bornstein, Numerical Data and Fundamental Relationships in Science and Technology, New Series, Group III, Crystals and Solid State Physics (Berlin: Springer) **11**, 671 (1979)

5. "IEEE standards on piezoelectricity," IEEE / ANSI Std. 176-1987, Chapter 3, "Crystallography applied to piezoelectric crystals", pp15 - 28, A. W. Warner, D. Berlincourt, A. H. Meitzler and H. F. Tierson

6. D. A. Roberts, IEEE J. Quant.. Electron. **28**, 2057 (1992)

7. S. Singh in: Handbook of Laser Science and Technology (Ed., M. J. Weber) **3**,Part 1, Section 1.1 (1986)

8. E. S. Wachman, W. S. Pelouch and C. L. Tang, J. Appl. Phys. **70**, 1893 (1991)

9. N. P. Barnes and V. J. Corcoran, Appl. Opt. **15**, 696 (1976)

10. K. Kato, IEEE J. of Quant. Electron. **22**, 1013 (1986)

11. C. Chen, Y. Wu, A. Jiang, B. Wu, G. You, R. Li and S. Lin, J. Opt. Soc. Am. B. **6**, 616 (1989)

12. F. C. Zumsteg, J. D. Bierlein and T. E. Gier, J. Appl. Phys. **47**, 4980 (1976)

13. R. A. Stolzenberger, D. N. Loiacono and J. Rottenberg, Paper CFF2 in: Conference on Lasers and Electro-Optics **8**, 415 (1994)

14. D. Eimerl, Ferroelectrics **72**, 95 (1987)

15. L. J. Bromley, A. Guy and D. C. Hanna, Opt. Comm. **70**, 350 (1989)

16. D. C. Edelstein, E. S. Wachman and C. L. Tang, Appl. Phys. Lett. **54**, 1728 (1989)

17. D. Eimerl, L. Davis, S. Velsko, E. K. Graham and A. Zalkin, J. Appl. Phys. **62**, 1968 (1987)

18. T. R. Zhang, H. R. Choo, and M. C. Downer, Appl. Opt. **29**, 3927 (1990)

19. Trade literature, F. C. Castech Corporation

20. T. Y. Fan, C. E. Huang, B. Q. u, R. C. Eckardt, Y. X. Fan, R. L. Byer, and R. S. Feigelson, Appl. Opt. **26**, 2390 (1987)

21. S. Guha and, J. Falk, J. Appl. Phys. **51**, 50 (1979)

22. R. Fischer, C. Tran-ba, and L. W. Wieczorek, Sov. J. Quantum Electron. **7**, 1455 (1978)

References continued,

23. G. D. Boyd and, D. A. Kleinman, J. Appl. Phys. **39**, 3597 (1968)

24. S. Guha, F. Wu, and J. Falk, IEEE J. Quant. Electron. **18**, 907 (1982)

25. S. T. Yang, R. C. Eckardt and R. L. Byer, J. Opt. Soc. Am. B. **10**, 1684 (1993)

26. E. C. Cheung and J. M. Liu, J. Opt. Soc. Am. B. **7**, 1385 (1990)

27. M. H. Dunn and A. I. Ferguson, Opt. Comm. **20**, 214 (1977)

28. M. F. Becker, D. J. Kuizenga, D. W. Phillion and A. E. Siegman, J. Appl. Phys. **45**, 3996 (1974)

29. M. T. Asaki, C.-P. Hunag, D. Garvey, J. Zhou, H. C. Kapteyn and M. M. Murnane, Opt. Lett. **18**, 977 (1993)

30. A. Nebel, C. Fallnich, R. Beigang and R. Wallenstein, J. Opt. Soc. Am. B. **10**, 2195 (1993)

31. M. Ebrahimzadeh, S. French, A. Miller and W. Sibbett, Opt. Lett. (submitted)

4.1 Introduction

In the preceding chapter, the design criteria appropriate to the operation of a synchronously-pumped femtosecond optical parametric oscillator (OPO) were outlined. The application of these principles in the construction of a KTP-based parametric oscillator pumped by the femtosecond output of a self-modelocked Ti:sapphire laser will now be described in this chapter.

The experimental configuration of the OPO, with and without intracavity dispersion compensation, is detailed and includes a discussion of the alignment procedures used and the choice of resonator optics. A thorough characterisation of the signal output from the OPO is described including details of pulse durations, spectral bandwidths, tunability and output powers. Results of amplitude and phase noise measurements of the signal pulse sequence are included and, additionally, various non-phasematched processes occuring in the OPO are detailed. A numerical model of the effects of self-phase-modulation in the OPO is presented which gives good agreement with experiment. In addition, solitonic operation of the OPO is demonstrated and quantitative results consistent with theory developed for fibres are presented. The chapter begins with a detailed description of the crystal used in the oscillator and reviews the material and nonlinear properties of a KTP crystal which are significant in a parametric oscillator implementation.

4.2 KTP crystal

This section will begin by reviewing the material and optical properties of $KTiOPO_4$ (KTP) including its crystal structure and mechanical qualities. An outline of the calculation of the effective nonlinear coefficient is included to illustrate how the choice of crystal orientation used for the OPO was made. Angle and wavelength tuning curves for this geometry are presented along with the derivation of the oscillation threshold for the OPO.

Structural and optical properties of KTP

$KTiOPO_4$ (KTP) is a relatively new nonlinear material [1] which belongs to the category of compounds which are described by the chemical formula $MTiOXO_4$ where M can be K, Rb, Tl, NH_4 or Cs and X can be P or As. All of the compounds are isomorphs belonging to the orthorhombic point group $mm2$ and the space group $Pna2_1$. The high nonlinearity of KTP makes it an attractive material for many frequency-conversion applications. These nonlinearities result from the noncentrosymmetric structure which is characterised by chains of TiO_6 octahedra, linked at two corners, and separated by PO_4 tetrahedra [2]. Alternately long and short Ti-O bonds recur along these chains and result in distortion of the TiO_6 octahedra which is responsible for the large nonlinear and electro-optic coefficients observed. The K ion is weakly bonded to both the Ti octahedra and the P tetrahedra and sits between these at a high-coordination-number site.

Large, single crystals of KTP are readily grown using either hydrothermal [3] or flux [4, 5] growth techniques. In the hydrothermal method, the crystal is grown from a seed and nutrient solution maintained

for a period of weeks at high temperature (≈ 600 °C) and pressure (≈ 25000 psi). The equipment restrictions for high-pressure operation limit the size of crystals which can be fabricated using this technique to approximately 20 mm x 20 mm x 60 mm. The flux growth procedure works by maintaining a seed KTP crystal and a flux solution (potassium phosphate) at a constant temperature between 700 - 1000 °C and then allowing crystallisation from the melt to occur on cooling. This method has the advantage of operating at atmospheric pressure and therefore does not require sophisticated autoclave equipment. Consequently, larger crystals can be grown by the flux method and sizes up to 60 mm x 55 mm x 30 mm have been obtained.

A problem of ferroelectric domain formation occurs in both hydrothermal [6] and flux [7] grown crystals with domain walls forming parallel to crystallographic planes. As hydrothermal growth occurs at temperatures well below the Curie temperature for KTP (938 °C), single-domain crystals are generally obtained if a single-domain seed is used. However, the higher temperatures associated with flux growth make single-domain crystal growth more difficult to guarantee.

Other minor differences (eg. in electrical conductivity) exist between hydrothermally and flux grown KTP because of specific impurities and defects introduced by the individual fabrication methods. When the damage thresholds of crystals derived by the two techniques were compared, evidence was found which suggested that hydrothermal KTP was more resistant to damage than the flux grown material [2]. Bulk damage is observed in KTP as grey-track formation and has been linked to the thermal effects of catastrophic self-focusing in high power laser applications [8].

Refractive index measurements have been reported for both flux grown [9, 10] and hydrothermally-grown [11] KTP crystals and used to derive Sellemeier equations valid from the ultraviolet to the mid-infrared. The transmission spectrum of $RbTiOPO_4$ (reproduced in Figure 4.1) is given by Zumsteg *et al* [1] and illustrates a sharp water absorption at around 2.8 μm probably caused by stretching of an *O-H* bond. The broad absorption around 3.8 μm is also attributed to *O-H* stretching while absorption due to the PO_4 and TiO_6 groups is responsible for the long-wavelength cutoff beyond ≈ 4.5 μm. The mid-infrared transmission of KTP is similar since the K / Rb ion does not contribute to the long-wavelength absorption.

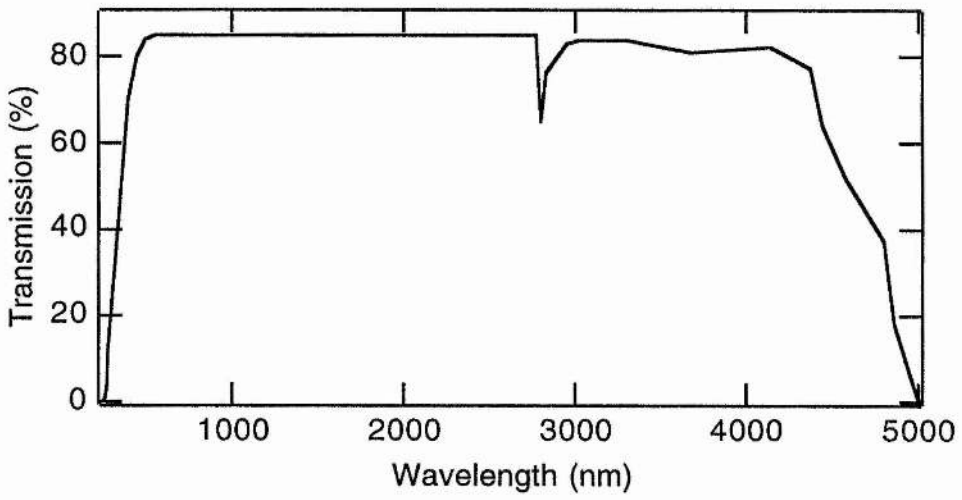

Figure 4.1 Transmission spectrum of $RbTiOPO_4$ (taken from Ref. [1])

Values for the nonlinear optical coefficients of KTP have been reported by several research groups. In more recent evaluations based on measurements of frequency-doubling efficiency [10, 12, 13], the values found appeared much lower than those determined by the Maker fringe method used in earlier characterisations [1]. This discrepancy would

explain the lower than expected second-harmonic efficiencies reported for frequency-doubling [14, 15]. The most up-to-date values, expressed in the {XYZ} frame, are given in Table 4.1 and Kleinman symmetry is used to identify $d_{15} = d_{31}$ and $d_{24} = d_{32}$.

Table 4.1 Summary of structural and optical properties of KTP

Property	*Value*	*Ref.*
Crystal class	Orthorhombic, point group $2mm$ space group $Pna2_1$	[1]
Unit cell parameters	a = 10.616 Å, b = 12.814 Å, c = 6.404	[2]
Refractive index (λ = 1.064 μm)	n_x = 1.740, n_y = 1.748, n_z = 1.830, (positive biaxial)	[11]
Nonlinear refractive index, n_2	3.1 x 10^{-15} cm^2 W^{-1}	[16]
Transmission	350 nm - 4.5 μm	[1]
Damage threshold	150 MW / cm^2	[1]
Nonlinear optical coefficients	$d_{15(31)}$ = 3.6 pm/V $d_{24(32)}$ = 2.0 pm/V d_{33} = 8.3 pm/V	[10, 12, 13]

Orientation and specifications of the OPO KTP crystal

It is clear from the values of the nonlinear coefficients that, in KTP, d_{15} can produce the strongest (phasematched) nonlinear coupling between two fields. Although d_{33} is larger it only couples power between parallel waves which cannot be phase-matched using material birefringence. By expanding the tensor notation and using the relationships between reference frames listed in Table 3.2, this coefficient can be written as,

$$d_{15} = d_{113} = d_{131} = d_{311}$$
$$= d_{XXZ} = d_{XZX} = d_{ZXX}$$
$$= d_{yyz} = d_{yzy} = d_{zyy} \ .$$

The maximum coupling is therefore obtained between fields polarised along the optical y and z axes, implying that Type II phasematching along the x-axis would give the most efficient frequency conversion.

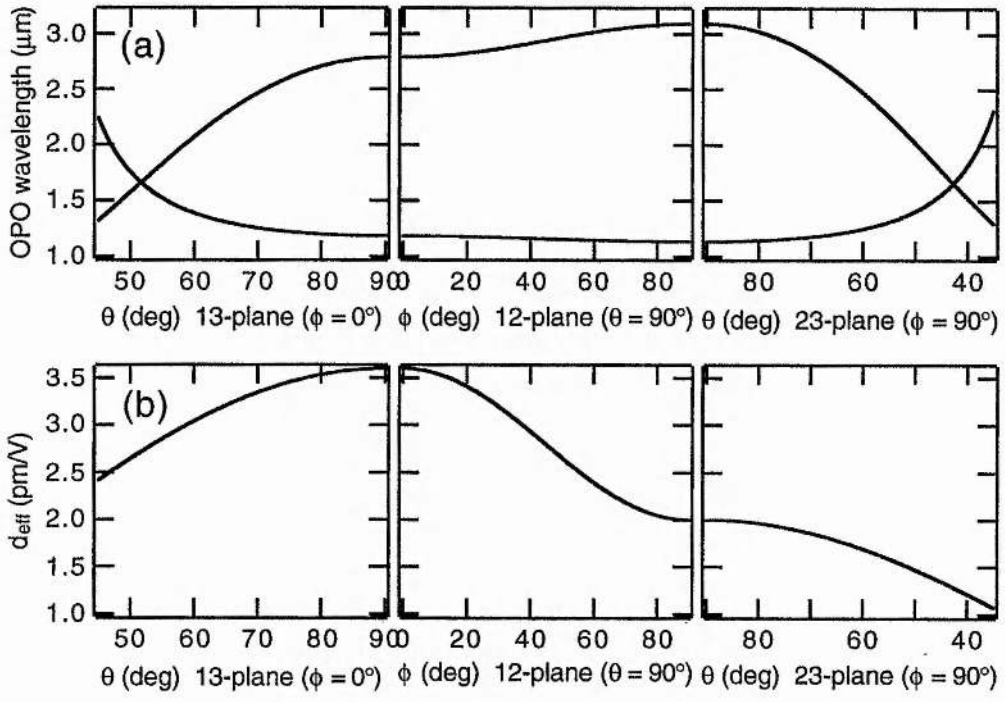

Figure 4.2 Phase-matching curves (a) and effective nonlinear coefficient (b) in the principal optical planes for a Type II parametric interaction in hydrothermal KTP with a pump wavelength of 830 nm. Refractive index data used in calculations are from Ref. [11].

The graphs displayed in Figure 4.2 show the calculated (collinear) phase-matching curves and effective nonlinear coeffcients in the principle optical planes for a Type II OPO interaction in KTP at a pump wavelength of 830 nm. This pump wavelength was of particular interest because it corresponds to the centre of the Ti:sapphire tuning range. The results confirm that the effective nonlinear coefficient for a Type II parametric

interaction maximises for propagation along the x-axis and the tuning curves demonstrate that phasematching is possible.

The crystal orientation chosen for the OPO was for propagation along the x-axis with the pump and signal waves parallel to the y-axis and the idler polarised along the z-axis. As well as optimising gain, this cut avoids problems of Poynting vector walkoff because it uses a collinear non-critical phase-matching geometry. Additionally, angular acceptance is also maximised by this cut, allowing tighter focusing to be used. The expected tuning for pump wavelengths from 700 - 1000 nm is shown in Figure 4.3.

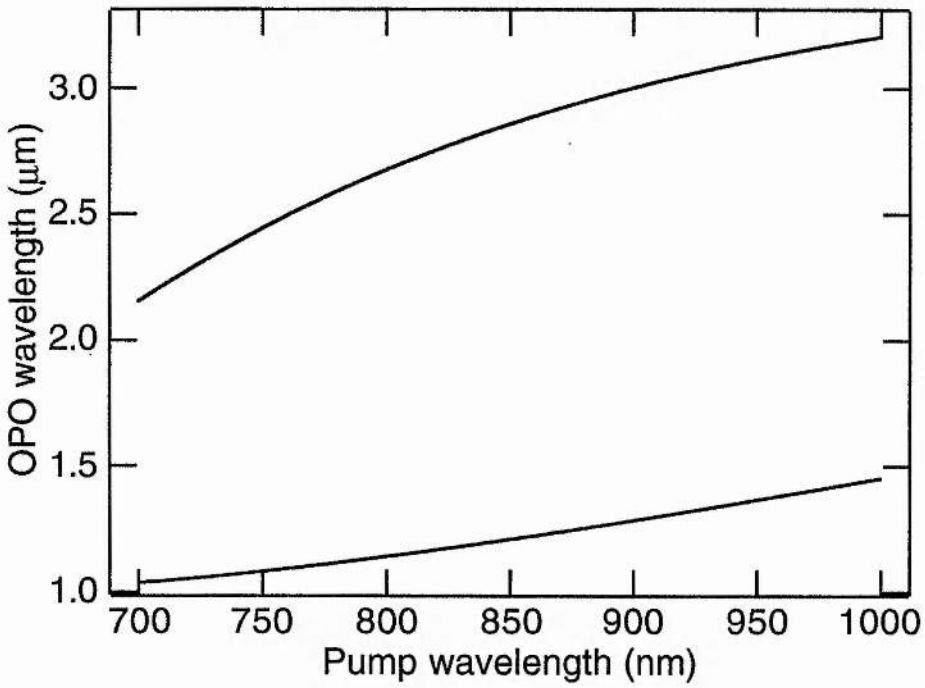

Figure 4.3 Pump wavelength tuning for noncritically phase-matched Type II parametric generation along the x-axis in KTP

The oscillation threshold for a singly-resonant OPO phase-matched along the x-axis can be calculated if cavity losses are assumed. Following the analysis presented in Chapter 3, and assuming a roundtrip loss of 2 %

for the signal wave, the estimated threshold for a 1-mm crystal is 90 mW when pumped with 100-fs-duration $\text{sech}^2(t)$ pulses. This figure does not take into account any reduction in efficiency due to pulse walkaway or phase-variations between the waves resulting from nonlinear dispersion. In view of these considerations, and allowing for a margin of error (measurements of material nonlinear coefficients can be inaccurate to as much as ± 20 %), a crystal of length 1.5 mm was considered to offer sufficient gain. The crystal was cut for phase-matching at normal incidence and both faces had an aperture of 5 mm x 5 mm

The signal phase-matching bandwidth associated with a 1.5-mm KTP crystal oriented as described is approximately 34 nm when pumped at a wavelength of 830 nm. This bandwidth is capable of supporting transform-limited 45-fs-duration $\text{sech}^2(t)$ signal pulses. Clearly, a crystal of this length does not place any restrictions on femtosecond operation.

The remaining question concerning the chosen orientation of the KTP crystal is the values of group-velocity walkaway between pump, signal and idler pulses. At a pump wavelength of 830 nm and over a length of 1 mm, the signal pulse leads the pump pulse by ≈ 100 fs. The idler pulse travels slowest and lags the pump by ≈ 200 fs. Pulse walkaway lengths are therefore similar to the crystal length, implying that most of the crystal can contribute to gain.

To minimise loss in the OPO resonator, the crystal faces were anti-reflection (AR) coated with a single layer MgF_2 quarter-wave coating for maximum transmission (T > 99.9 %) centred at the signal phase-matching wavelength of 1180 nm. High transmission (T > 95 %) was also specified at the pump wavelength of 830 nm but no special coating requirement was

included at the 2.8 μm idler wavelength. A summary of the complete OPO crystal details is included as Table 4.2.

Table 4.2 Summary of the specifications of the OPO KTP crystal at a pump wavelength of 830 nm

Parameter (λ_p = 830 nm)	*Value*
Phase-matching orientation	Collinear non-critical phase-matching for propagation // x-axis: p // y-axis, s // y-axis, i // z-axis
Dimensions	1.5 mm (t) x 5 mm (w) x 5 mm(h)
Signal and idler wavelengths	λ_s = 1.18 μm, λ_i = 2.8 μm
Anti-reflection coatings	T > 99.9 % @ λ = 1.18 μm T > 95 % @ λ = 830 nm
Effective nonlinear coefficient	d_{eff} = 3.6 pm/V
Signal phase-matching bandwidth	$\Delta\lambda_s$ = 34 nm
Group-velocity walkaway	p-s 100 fs/mm (*signal* leads) p-i 200 fs/mm (*idler* lags)

4.3 Configuration of the KTP-based femtosecond OPO without dispersion compensation

The remainder of this chapter details the configuration and operation of a singly-resonant femtosecond OPO based on the KTP crystal geometry already described. The results presented in this section describe the operation of the OPO configured without dispersion compensation and include detailed analysis of the temporal and spectral output pulse characteristics and tunability. In particular, numerical modelling concerning the effects of intracavity SPM on the signal output pulses from the uncompensated resonator is described.

Experimental arrangement of the uncompensated OPO

A schematic of the cavity arrangement used for the OPO is displayed in Figure 4.4. The basic three-mirror, standing-wave resonator consisted of two concave high-reflectivity mirrors (r = 10 cm) and a plane high-reflectivity mirror or output coupler. The cavity fold angle was minimised to reduce astigmatism and the cavity length was synchronous with that of the pump laser. Pump light was focused using a 50 mm focal length lens to a 17 μm spot radius inside the KTP crystal through one of the curved mirrors. An optical isolator was used to prevent optical feedback (caused by reflections at the crystal surface) from compromising the modelocking in the pump laser. A half-wave plate was inserted after the output isolator to rotate the transmitted light back to its original horizontal polarisation. The single-stack curved mirrors, which were deposited on 25-mm-diameter plano-concave BK7 glass substrates, were highly reflecting (R > 99.7 %) for wavelengths from 1.1 - 1.3 μm and were highly transmitting (T > 95 %) at the pump wavelength. The plane output coupler had a transmission of 1.5 % centred at a wavelength of 1.2 μm and was deposited on a 12.5-mm diameter CaF_2 substrate.

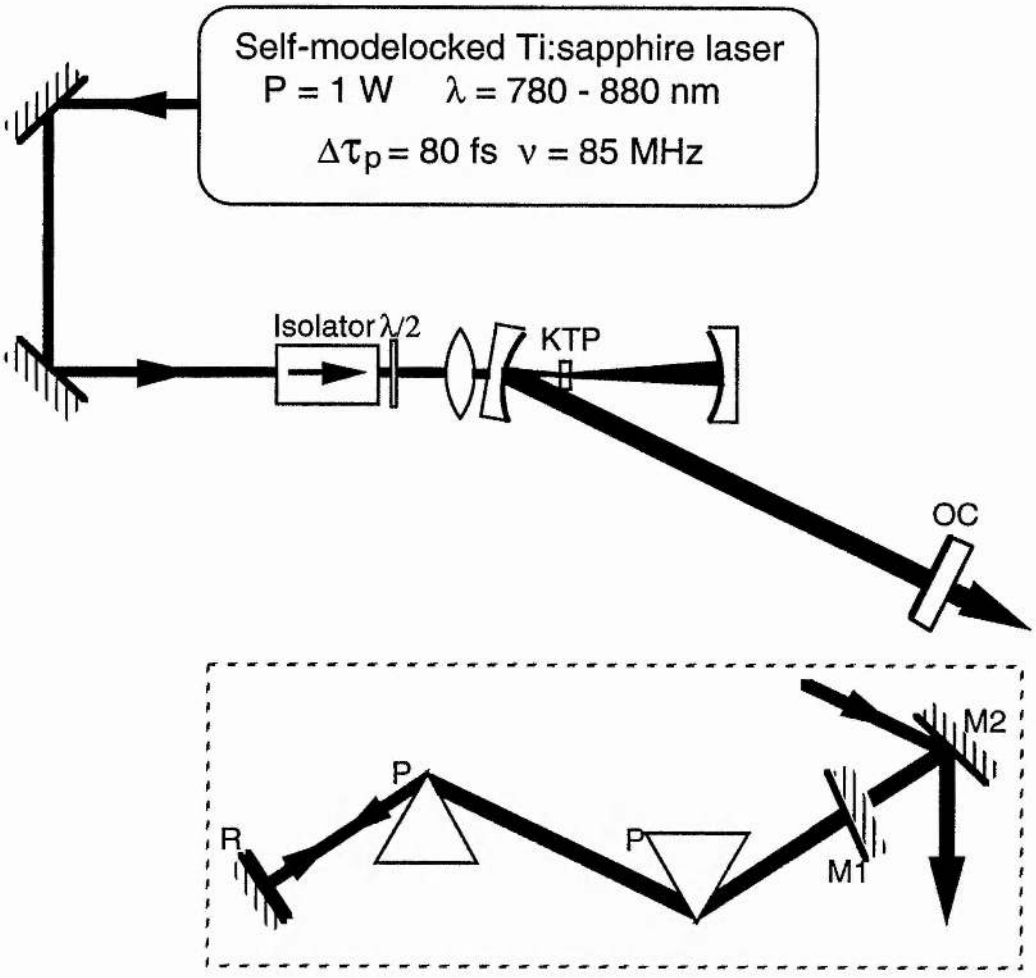

Figure 4.4 *Cavity configurations of the uncompensated OPO including extracavity dispersion compensation (inset).*

The KTP crystal was held in position using a two-piece perspex mount (depicted in Figure 4.5) which clamped the edges of the crystal. Thin strips of self-amalgamating PTFE tape were used to cushion the edges of the crystal where contact was made with the mount. Angular and translational control over the crystal orientation was provided by a combination of three translation stages and a three-axis prism-table.

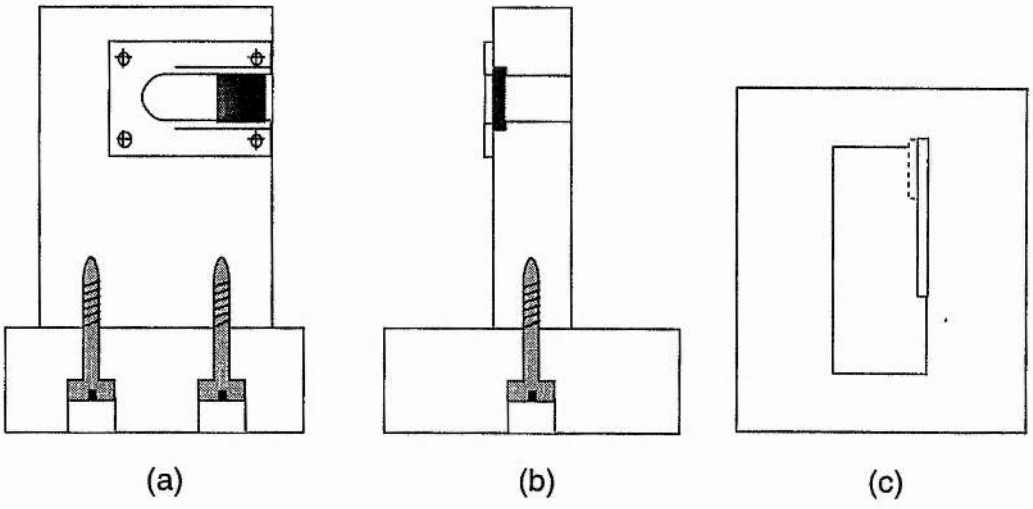

Figure 4.5 *Side (a, b) and top (c) views of the KTP-crystal mount*

Oscillator alignment

Alignment of the femtosecond OPO was made difficult by the lack of spontaneous emission from the nonlinear crystal and by the cavity length tolerances imposed by synchronous pumping. The first Ti:sapphire-pumped femtosecond OPO reported was aligned using a low noise germanium diode and phase-sensitive detector to monitor the single-pass parametric fluorescence generated in the KTP crystal [17]. Our alignment technique exploits the collinear pumping geometry and uses the several milliwatts of blue light which is produced in the KTP crystal through non-phasematched second-harmonic generation of the pump. Using the three-mirror resonator shown in Figure 4.4, the crystal was positioned close to the centre of the calculated stability range and was adjusted to retroreflect the pump beam. The power in the frequency-doubled pump was then maximised by translating the focusing lens and the cavity mirrors were adjusted to collimate the light on the output coupler. Fine mirror adjustment allowed the pump and second-harmonic beams to be traced around the cavity and overlapped. Oscillation was observed when the

period of the cavity was made synchronous with that of the pump laser by translating the output coupler.

Output characteristics of the KTP femtosecond OPO

With a pump power of 1 W and in the absence of dispersion compensation the parametric oscillator produced average powers of up to 150 mW in the signal beam. Oscillation was observed for average pump powers as low as 230 mW measured at the focusing lens. Difficulties of collection and collimation prevented the power in the idler beam from being determined directly but the ratio of photon energies implies that ≈ 50 - 100 mW was generated at 2.8 μm. The OPO output was contained in a TEM 00 mode and was essentially independent of the pump mode. Parametric oscillation in a TEM 00 mode was observed even with a TEM 01 pump mode although the reduced spatial overlap between the pump and signal resulted in lower output powers. Intensity and interferometric autocorrelation techniques were used to measure pulse durations and to obtain information about frequency chirp in the pulses. A digital optical spectrum analyser was used to monitor the spectral composition of the pulses.

Results from the OPO when operated without any dispersion compensation are reproduced in Figure 4.5. The measured intensity autocorrelation (Figure 4.6a) implies a pulse duration of 400 fs. The interferometric autocorrelation (Figure 4.6b) and the pulse spectrum (Figure 4.7) indicate that the pulses are highly chirped and the corresponding duration-bandwidth product is around 5. The twin-peaked structure of the pulse spectrum is a characteristic signature of self-phase-modulation (SPM), implying that the origin of the frequency chirp on the signal pulses is SPM arising inside the KTP crystal at the cavity focus. The

combination of self-phase modulated spectral broadening and intracavity group velocity dispersion (GVD) broadens the resonant signal pulses to a duration much longer than that of the original pump pulse. The broadening due to linear GVD alone can be estimated by using the method outlined in Chapter 3. At a wavelength of 1.18 μm, the signal dispersion distance in KTP is 3.7 cm. With output coupling of 1.5 %, the average signal pulse lifetime in the cavity is ≈ 67 roundtrips, corresponding to propagation through ≈ 20 cm of KTP. Assuming that the initial signal pulse width is limited by the pump pulse duration of 85 fs, then a Gaussian output pulse of duration 470 fs would be expected.

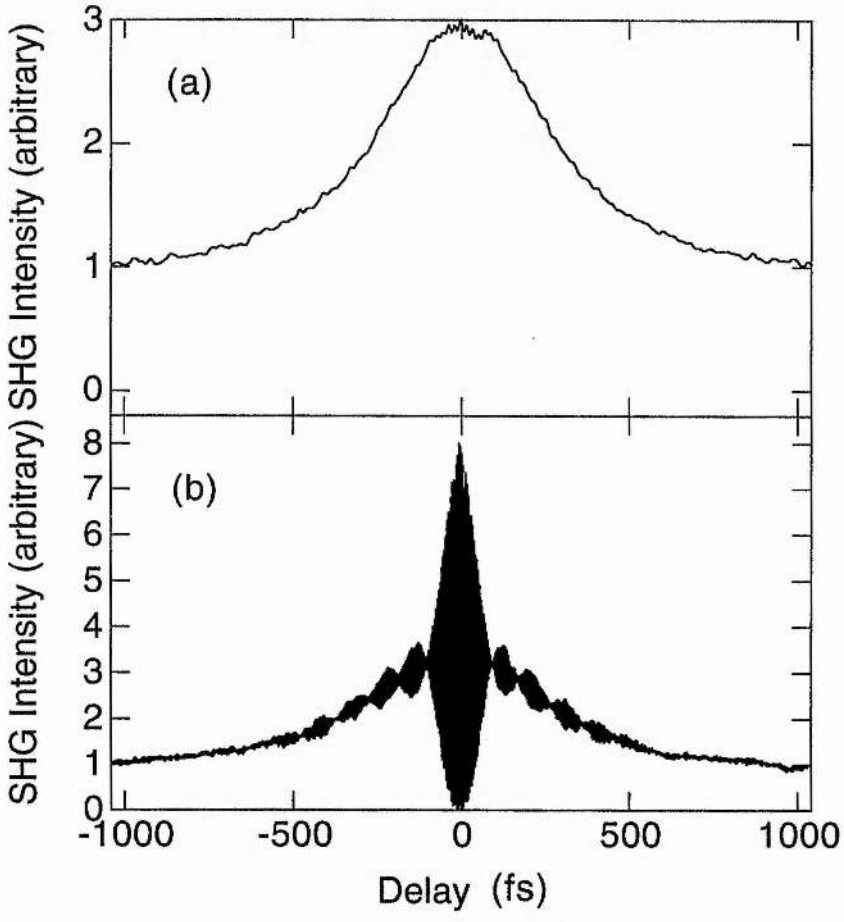

Figure 4.6 Intensity (a) and interferometric (b) autocorrelation of the output from the uncompensated OPO

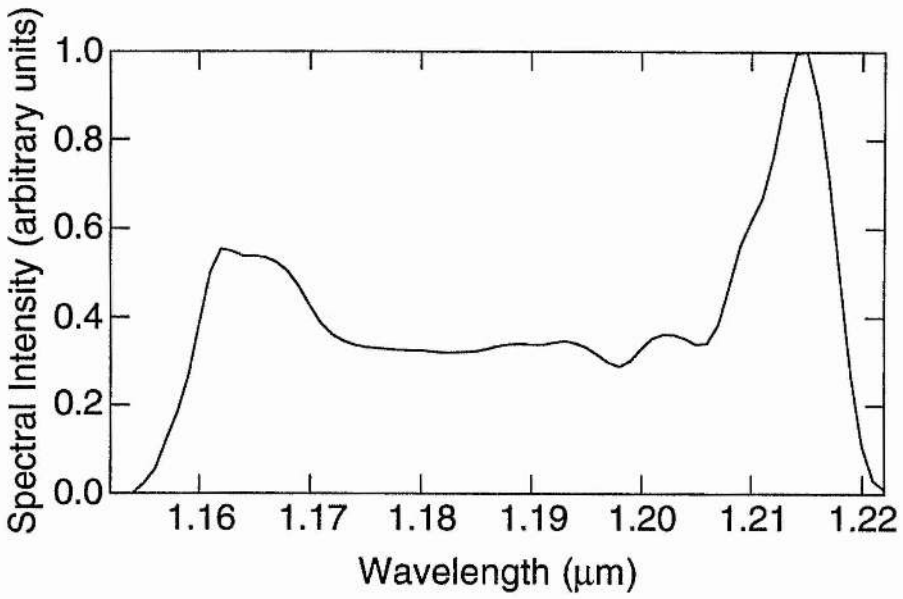

Figure 4.7 Spectrum of the signal output of the uncompensated OPO

Wavelength tuning of the KTP femtosecond OPO

With Ti:sapphire pump tuning the OPO signal wavelength is potentially tunable from 1.0 - 1.4 μm and the idler from 2.2 - 3.1 μm. Experimental results, limited by the reflectivity of the mirrors, are reproduced in Figure 4.8 and demonstrate pump tuning of the signal from 1.12 - 1.25 μm and of the idler from 2.5 - 3.0 μm along with a theoretical curve predicted from Sellemeier data for KTP [2]. The OPO can also be tuned by changing the crystal angle but for non-critical phase-matching angle tuning is less rapid than pump tuning and also involves modifying the alignment of the OPO.

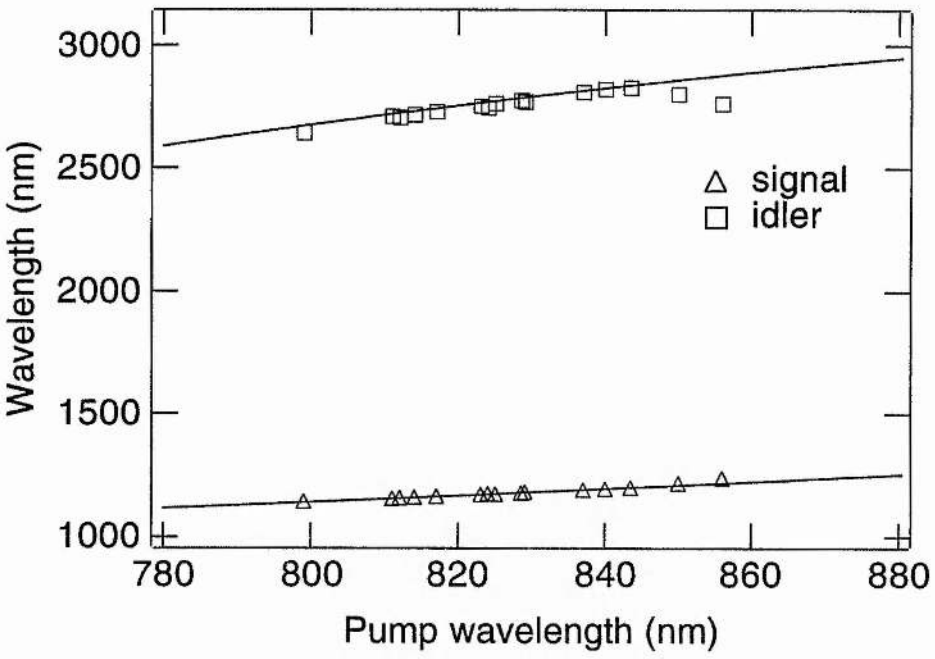

Figure 4.8 *Experimental (symbols) and predicted (solid line) pump tuning of the KTP femtosecond OPO*

Under special circumstances, when the cavity dispersion permits soliton generation, the OPO is capable of generating signal wavelengths as long as 1.4 μm without the need for pump tuning beyond 840 nm. Results detailing this behaviour are included later in this chapter.

Self-phase-modulation in the uncompensated OPO

The fringe-resolved autocorrelation profiles together with spectral data indicate that, in the absence of dispersion compensation, pulses produced by the OPO are highly chirped. This chirp can be attributed primarily to self-phase-modulation (SPM) occurring in the focal region of the KTP crystal which results from a phase shift induced by the intensity-dependent refractive index of the material. The pulse broadening observed arises from the combined effects of SPM and group velocity dispersion (GVD) of the signal pulse as it makes multiple passes of the OPO cavity.

An estimation of the amount of SPM occurring in the KTP crystal can be made from a calculation of the peak nonlinear phase shift ϕ_{MAX} given by [18],

$$\phi_{MAX} = \frac{2\pi}{\lambda} n_2 I_o L \ . \tag{1}$$

With cavity losses of 1.5%, the average photon lifetime of the signal in the OPO resonator is about 67 roundtrips. Taking n_2 for KTP to be 3.1×10^{-15} cm^2 W^{-1} [16], a net phase shift of π radians will be accumulated in the cavity lifetime with intensities of the order of 1 GW cm^{-2}. Typical intracavity intensities are of the order of tens of GW cm^{-2} and so significant SPM should be expected.

A simple model can be used to predict qualitatively the features of the pulse autocorrelation profiles and spectra attributed to SPM. Consider a Gaussian pulse with carrier frequency and intensity pulse duration (FWHM) $\Delta\tau$. The electric field amplitude is given by,

$$E_o(t) = \exp(-2\ln 2 t^2 / \Delta\tau^2) \exp(i \omega_o t) \tag{2}$$

with corresponding intensity,

$$I(t) = E_o^*(t) E_o(t) \tag{3}$$

In the presence of a nonlinear phase shift across the pulse the resultant field envelope becomes,

$$E(t) = E_o(t) \exp[i \phi_{NL}(t)]. \tag{4}$$

where the nonlinear phase shift $\phi_{NL}(t)$ is given by,

$$\phi_{NL}(t) = I(t)\,\phi_{MAX}, \tag{5}$$

and the maximum phase shift ϕ_{MAX} is given by equation (1). This model allows the effect of SPM on the pulse envelope to be calculated for any value of maximum phase shift experienced by the pulse. The fringe resolved autocorrelation function and power spectrum of the pulse can easily be generated using the formulæ given in Chapter 2. The results of the modelling are shown in Figure 4.9 for a variety of different values of the maximum SPM phase shift using an initial Gaussian pulse of intensity fwhm $\Delta\tau$ = 400 fs.

It is well known that the effect of SPM in the frequency domain is to introduce substantial spectral broadening along with a double-peaked spectrum. However, in the time domain, SPM in isolation is not capable of modifying the pulse intensity envelope - this requires material dispersion as well. The results of the numerical modelling indicate that the nonlinear phase shift manifests itself as a modulation in the wings of the interferometric autocorrelation. Physically, this modulation can be treated as a beat note between the two most intense spectral components in the pulse. It can be seen from Figure 4.9 that the number of minima in the interferometric autocorrelation profile correlates well with the maximum nonlinear phase shift experienced by the pulse. This allows an empirical estimate to be made of the maximum phase shift present on the signal output pulses from the OPO. For N minima, the phase shift (to within $\pi/2$) is given by,

$$\phi_{MAX} \approx \frac{N\pi}{2} \tag{6}$$

Experimentally, although a prominent pedestal is observed on the OPO pulse autocorrelation trace at all levels of intracavity power, a strong

modulation is only observed at intracavity power levels less than 20 $GWcm^{-2}$. This is to be expected because as the SPM phase shift increases with intracavity power, the modulation frequency will increase and be more difficult to resolve in the autocorrelation function. The results shown in Figures 4.6 and 4.7 were obtained with an estimated intracavity intensity in the KTP crystal of 5 GW cm^{-2} corresponding to a maximum phase shift, calculated using equation (1), of $\phi_{MAX} = 16$ radians $= 5.1\pi$. This is in good agreement with the phase shift $\phi_{MAX} \sim 5\pi$ expected based on the observed number of 10 minima in the experimental autocorrelation function.

Several other features of the experimental results can be also explained with a simple qualitative consideration of the effects of SPM and GVD in the OPO cavity. The observed spectrum in Figure 4.7 is strongly asymmetric, unlike those predicted from the simple model, but it has been shown that asymmetric pulse spectra from SPM are generated when the propagating pulse is itself asymmetric [18]. The parametric pulse shaping results of Cheung and Liu [19] discussed in the previous chapter imply that the leading edge of the pulse (red-shifted by SPM) sees more gain than the (blue-shifted) trailing edge. Red-shifted components would therefore dominate the pulse spectrum. in agreement with experimental observations.

The modulation of the autocorrelation function predicted by the simple SPM model is stronger than that which is experimentally observed. Furthermore, the model also predicts a deep spectral modulation which is not clearly resolved in the measured pulse spectrum. This loss of contrast suggests that there are additional field dephasing processes occurring in the OPO cavity, most likely arising from the effects of dispersion and

group-velocity walkaway in the KTP crystal. A more detailed model, based on the nonlinear Schrödinger equation, would be required to explain these effects more quantitatively.

4.4 OPO with extracavity dispersion compensation

Extracavity dispersion compensation of the signal output from the uncompensated OPO has been implemented using a pair of SF14 prisms separated by 90 cm and used in a double-pass configuration as illustrated by Figure 4.4 (inset). Intensity and interferometric autocorrelation profiles of the pulses after optimal extracavity dispersion compensation are included as Figure 4.10. The pulse duration deduced from the intensity autocorrelation of Figure 4.10a is 90 fs but the residual pedestal on the interferometric autocorrelation in Figure 4.10b indicates that some uncompensated nonlinear chirp still remains. The inability to completely remove the chirp on the signal pulses is a limitation of this scheme for extracavity dispersion compensation [20].

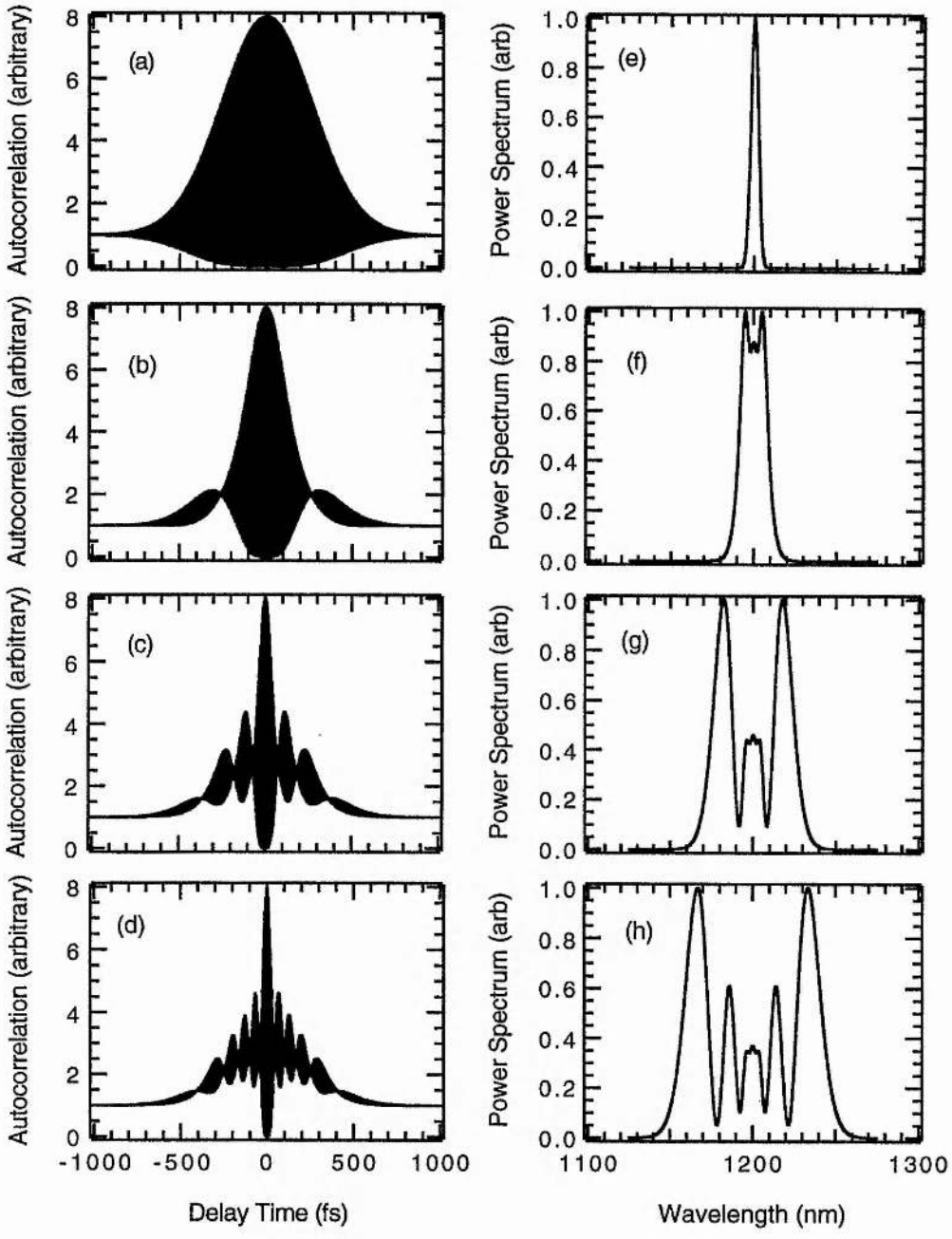

Figure 4.9 Numerical results showing the effects of SPM on the interferometric autocorrelation and the spectrum of an initially unchirped Gaussian pulse of FWHM duration 400 fs. For peak nonlinear phase-shifts of 0, π, 3π, 5π, the interferometric autocorrelations are shown in (a) - (d) respectively, while the corresponding spectra are illustrated in (e) - (h) respectively.

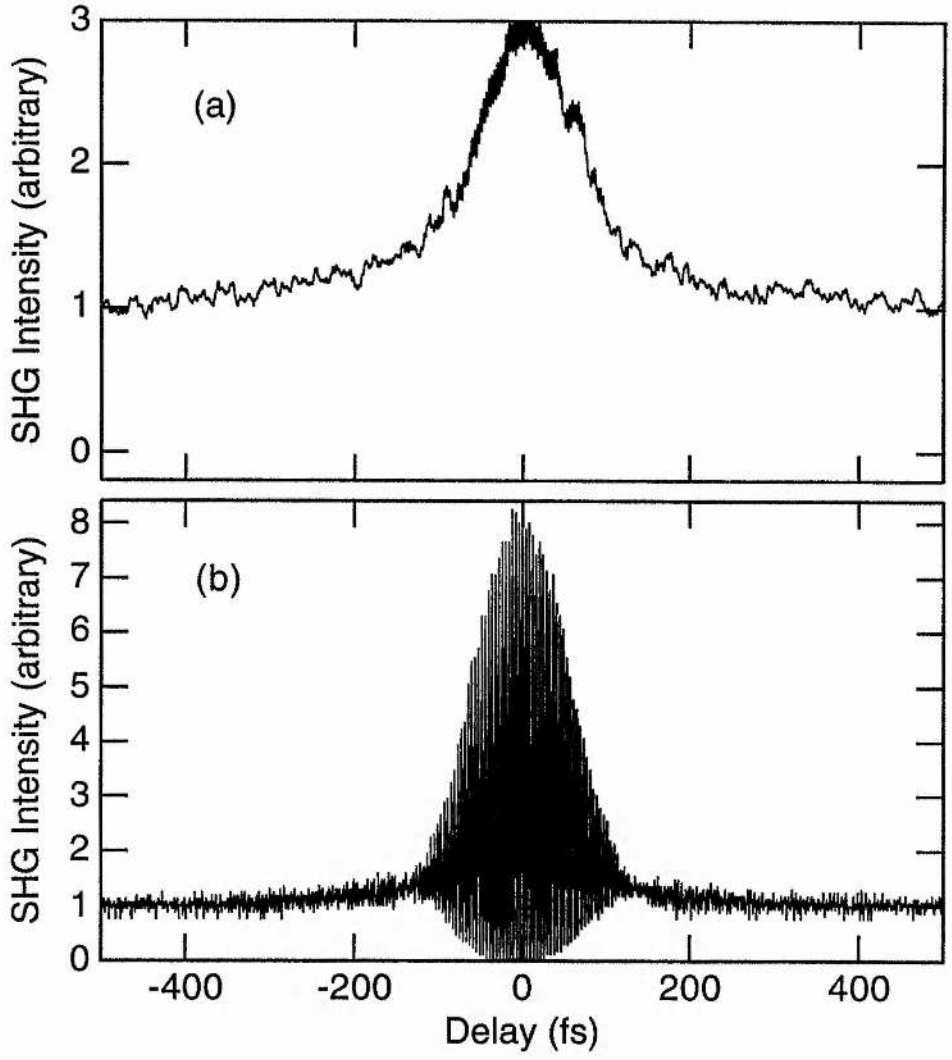

Figure 4.10 Intensity (a) and interferometric (b) autocorrelation profiles of the signal output of the OPO after extracavity dispersion compensation

4.5 OPO with intracavity dispersion compensation

Intracavity dispersion compensation has also been implemented in the OPO. In this section, time and frequency-domain measurements are presented for signal pulses from the dispersion-compensated oscillator. A comparison of various cavity configurations is described including a scheme demonstrating reduced-threshold operation of the OPO by utilising feedback at the idler wavelength. Measurements of the OPO amplitude and phase noise are detailed and these provide insights into the

stability of the femtosecond parametric oscillator. Behaviour unique to the femtosecond OPO, including several non-phase-matched parametric processes and cavity length dependent tuning effects is also discussed. Finally, detailed evidence is presented in support of soliton formation in the dispersion-compensated OPO and is related to theory based on the nonlinear Schrödinger equation.

Configuration of the dispersion-compensated OPO

To obtain the shortest pulses from the parametric oscillator it is necessary to fully utilise the increased bandwidth produced by self-phase modulation in the crystal. Intracavity dispersion compensation permits the chirp introduced onto the pulse in a single pass of the cavity to be removed before it becomes large enough to dominate the kinetics of pulse evolution in the OPO. By configuring the cavity as illustrated in Figure 4.11 to include a pair of intracavity SF14 prisms (apex-separation 24 cm) it was possible to routinely generate transform-limited pulses with durations as short as 40 fs.

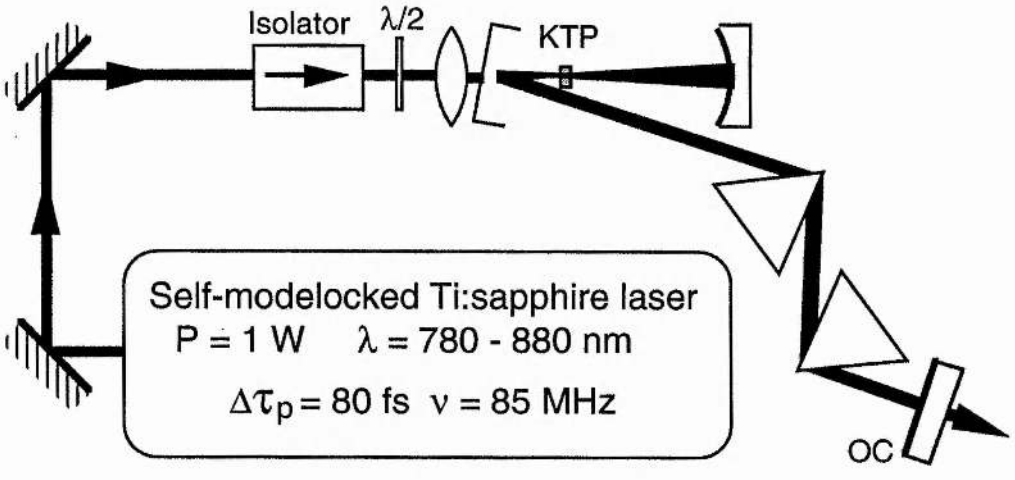

Figure 4.11 Cavity schematic of the OPO with intracavity dispersion compensation

Representative temporal and spectral measurements of the output signal pulses are reproduced in Figure 4.12. The duration of these pulses measured from the intensity autocorrelation data in Figure 4.12a was 39 fs. Inspection of the interferometric autocorrelation in Figure 4.12b and the pulse spectrum in Figure 4.12c implies that the pulses are chirp free, and their duration-bandwidth product of 0.33 ($\text{sech}^2(t)$ intensity profile assumed) is close to the Fourier-transform limit. The average output power from the intracavity dispersion compensated OPO was typically ≈ 50 mW, corresponding to peak output powers of ≈ 15 kW. A small increase in the oscillation threshold to approximately 300 mW was observed due to the insertion of the prism pair. Although the prisms used were not cut for Brewster incidence at 1.2 μm (they were originally specified at a wavelength of 1.5 μm), prism losses are unlikely to be entirely responsible for the reduction in output power. Reduced temporal overlap between pump and the shorter-duration signal pulse in the compensated OPO will increase the oscillation threshold. Another explanation may be that imperfections in the cut of the KTP crystal rotate the polarisation of the signal wave and, consequently, increase loss at each of the eight Brewster surfaces encountered by the pulse during one cavity roundtrip.

The theoretical study of pulse behaviour in a synchronously-pumped OPO by Cheung and Liu [19] which was discussed in the previous chapter does not include the effect of SPM on the output pulse duration. In the femtosecond regime the high intracavity peak powers demand that the effects of both SPM and GVD are included in a complete treatment [21]. The pulse evolution in the dispersion-compensated OPO operating with net negative cavity dispersion is *solitonlike* in that the duration is determined by the balance between

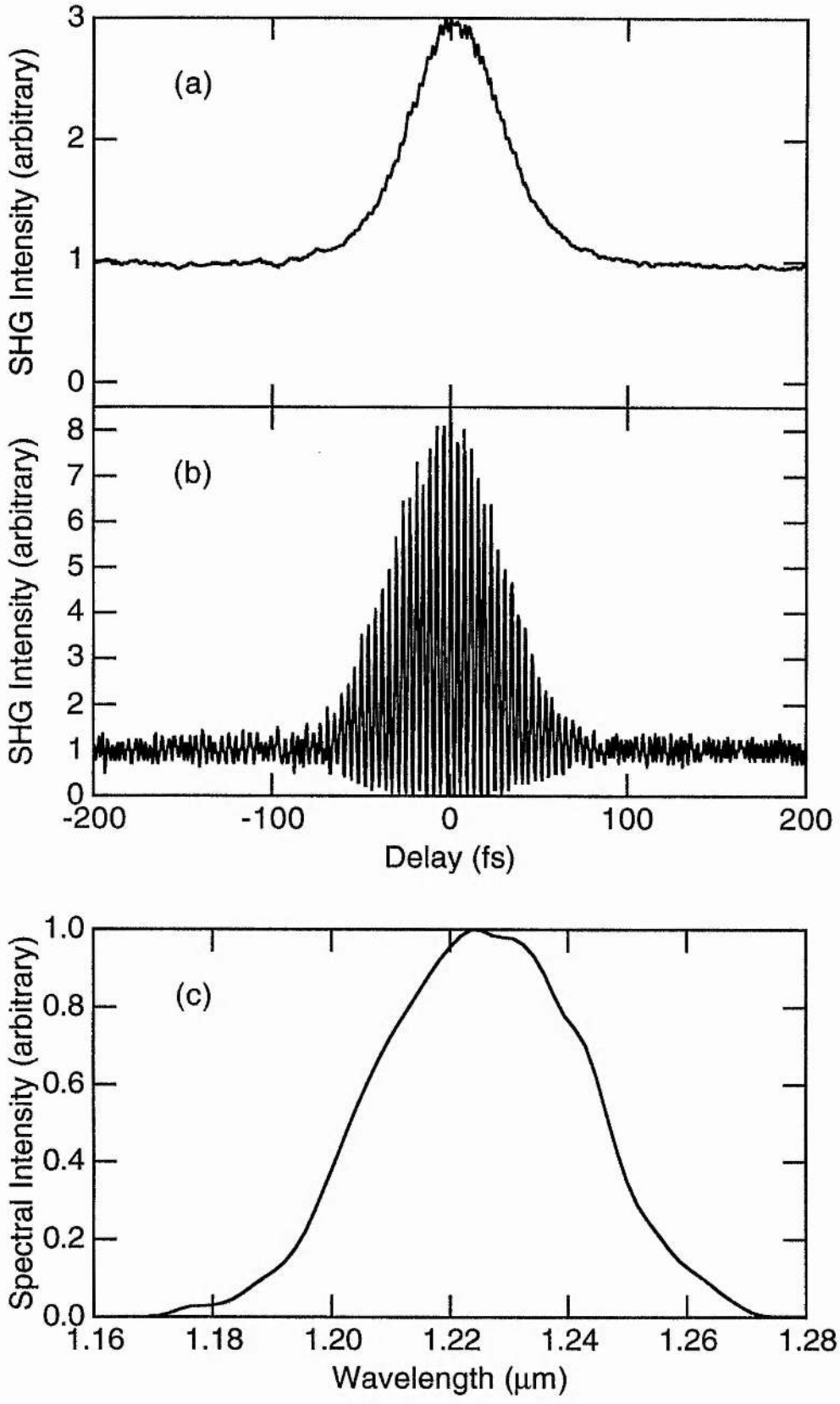

Figure 4.12 *Intensity (a) and interferometric (b) autocorrelation profiles and spectrum (c) of the signal output pulse from the OPO operated with intracavity dispersion compensation.*

SPM and GVD. These effects were investigated as a function of the net cavity dispersion by varying the position of one of the SF14 glass prisms. The results of this study are illustrated in Figure 4.13.

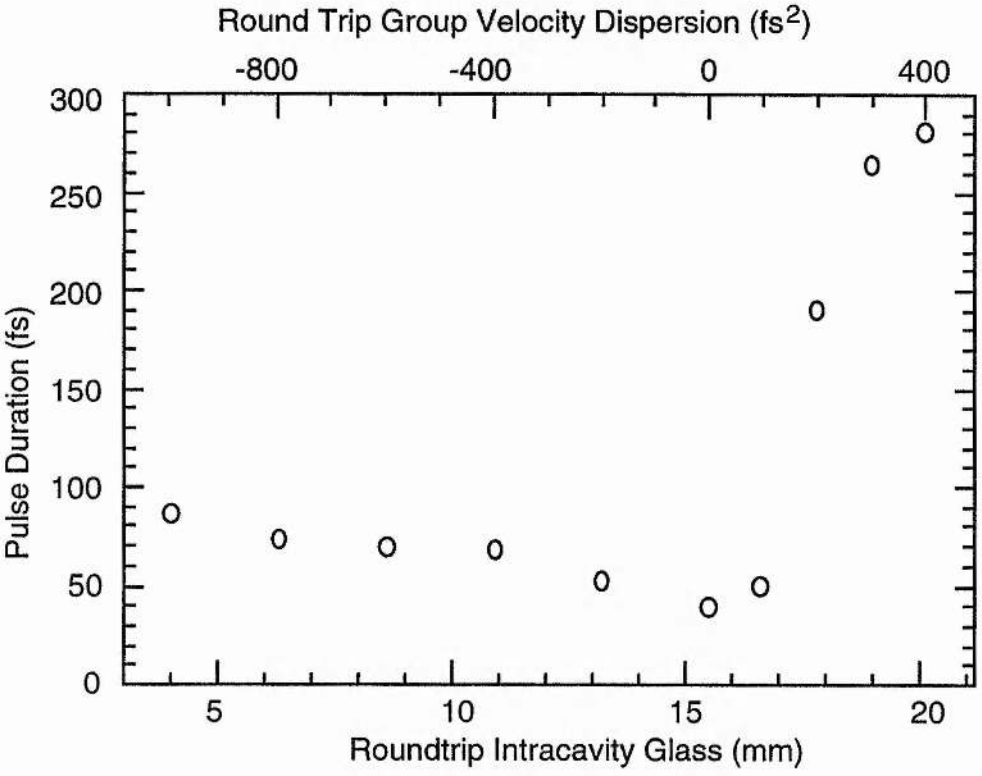

Figure 4.13 Dependence of the signal output pulse duration on the amount of intracavity glass in the cavity of the dispersion compensated OPO

The amount of intracavity glass can be converted to an equivalent value of GVD expressed in units of fs^2 . In this study the zero GVD point (as included in Figure 4.13) has been identified with the amount of intracavity glass corresponding to the minimum pulse duration. Although the point of minimum pulse duration can be shown, in the presence of SPM, to correspond to slightly negative values of GVD [22], this approximation is useful in distinguishing the chirp-free pulses observed in the negative GVD regime from the chirped pulses in the positive GVD region. Clearly, in the negative GVD regime the pulse duration only rises

slowly as the magnitude of the dispersion increases. In contrast, when the cavity dispersion is positive, the pulse duration increases rapidly for increasing values of GVD. These results are similar to those observed in previous studies of modelocked lasers [23, 24] and are in agreement with theoretical predictions for behaviour in lasers where SPM and GVD co-operate to determine the pulse evolution [22].

Optimum OPO cavity geometry

The results displayed in Table 4.3 detail OPO performance for several standing-wave cavity geometries on the basis of pump-power conversion efficiencies and output pulse durations. The highest conversion efficiency was obtained in resonators where both the pump and signal modes were focused to a beam waist of radius approximately 18 μm, corresponding to confocal parameters of 3.8 mm and 3.0 mm respectively. Tighter focusing may have enabled even higher efficiencies to be obtained (as would be expected from optimum focusing calculations) but practical considerations restricted the focal length of the cavity optics which could be used. The effective pump focal length f given in Table 4.3 represents the combined effect of the focusing lens and a cavity mirror of radius of curvature r.

The *X*-cavity differs from the other arrangements described. The details of the alignment technique used, although relying on overlapping the roundtrip cavity reflections, differed slightly from that described earlier. The minimum pulse duration was always found to be longer than in the *V*-cavity. It is thought that third-order dispersion in the *X*-cavity associated with the two additional mirror reflections per roundtrip was most probably responsible for this lower limit.

Table 4.3 Standing-wave cavity configurations of the KTP-based OPO and their effect on performance.

Configuration	w_o (s)	w_o (p)	$P_{threshold}$	P_{sig}/P_{pump}	$\Delta\tau_p$ (comp)
V-cavity f = 67 mm r = -100 mm	18 μm	17 μm	230 mW	21 %	400 fs (39 fs)
V-cavity f = 100 mm r = -150 mm	27 μm	25 μm	500 mW	17 %	600 fs (38 fs)
V-cavity f = 133 mm r = -200 mm	37 μm	34 μm	280 mW	15 %	-
X-cavity f = 67 mm r = -100 mm	16 μm	17 μm	240 mW	21 %	400 fs (56 fs)

Dispersion-compensated OPO with idler-feedback

The femtosecond OPOs reported in the literature so far have been singly-resonant devices requiring typical pump powers of around 200 mW to reach threshold [17]. The route to a compact femtosecond source offering high wallplug efficiency will rely on passive modelocking of gain media such as Cr:LiSAF which can be excited directly using high power laser diodes operating in the near-infrared [25]. The development of a low-threshold femtosecond OPO to complement the modest output powers available from diode-pumped devices may employ feedback of either the pump or the idler wave to achieve a reduction in threshold. Preliminary experiments carried out with the KTP OPO have demonstrated that

feedback of the idler wave can reduce the operating threshold and increase the output power of the OPO.

Using a dichroic polarising beamsplitter (T > 90 % @ 2.8 μm / R > 99.7 % @ 1.2 μm) the signal and idler pulses were allowed to propagate in separate dispersion-compensated cavities (see Figure 4.14) giving individual control over cavity length and dispersion for each wave. The horizontally-polarised idler cavity contained two prisms made of monocrystalline germanium [26] and two infrasil prisms. The combination of these allowed the net cavity dispersion experienced by the idler wave to be adjusted through zero. The signal cavity contained two SF14 glass prisms of apex separation 24 cm as described earlier but, in this configuration, the signal was vertically polarised and so a vertical prism sequence was used.

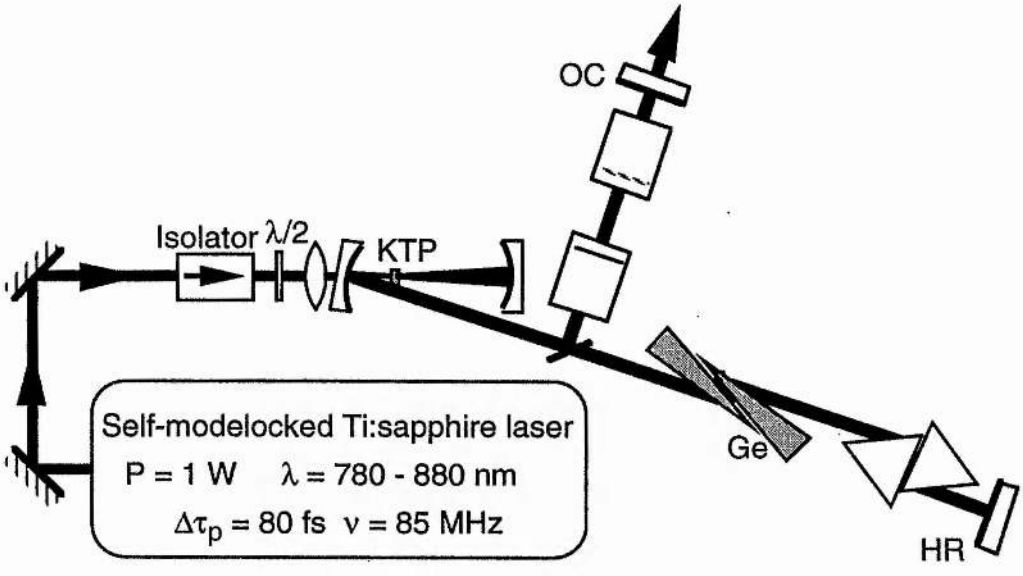

Figure 4.14 Cavity configuration of the dispersion-compensated OPO with idler feedback

When the signal wave was already resonant, bringing the idler cavity into near synchronism resulted in gain or depletion of the signal intensity

of around 10 % as illustrated in Figure 4.15. The corresponding reduction in threshold power was approximately 10 %. If the idler cavity was blocked and the pump power reduced until oscillation stopped, then unblocking the idler cavity was sufficient to recover oscillation.

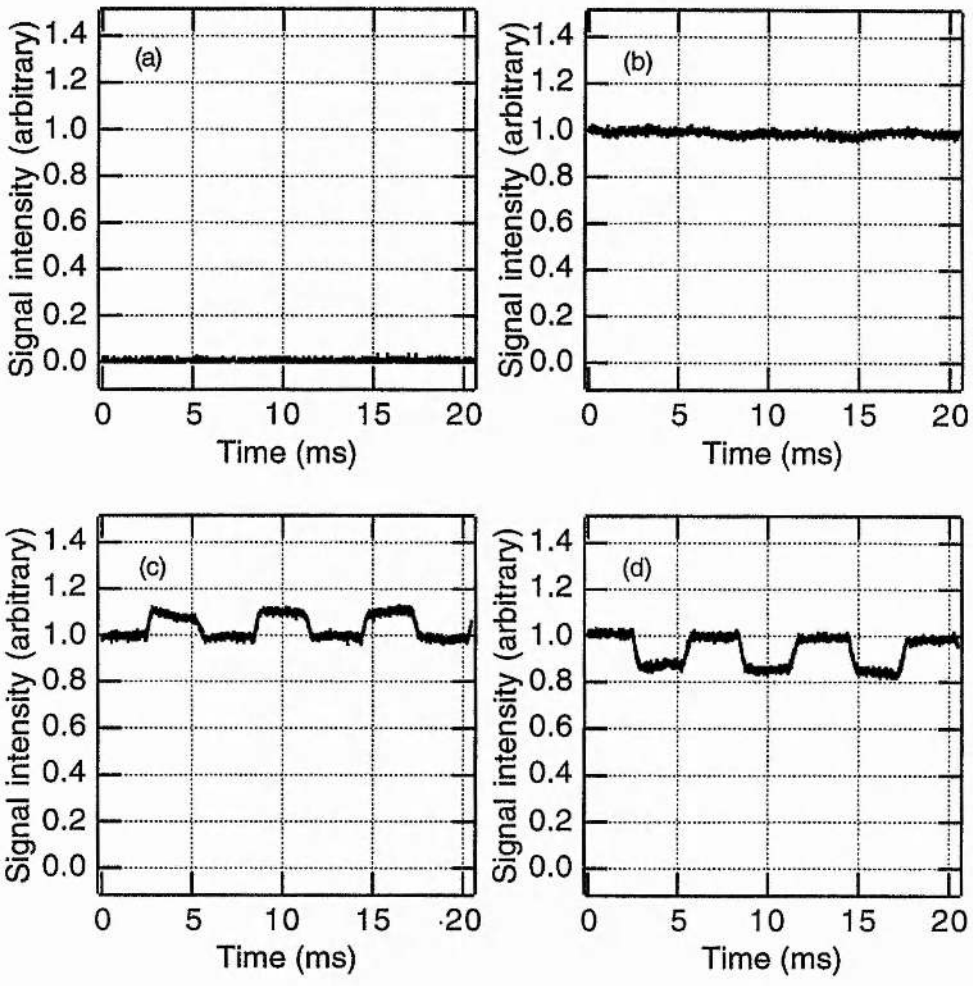

Figure 4.15 Intensity of the signal pulses from the KTP-based OPO with idler feedback. No oscillation (a), signal resonant and idler cavity blocked (b), signal resonant with idler cavity chopped and adjusted for gain (c) and signal resonant with idler cavity chopped and adjusted for depletion (d).

A change in the idler cavity length of approximately 500 nm separated the position of signal gain from the position of signal depletion. The modest increase in signal power can be attributed to the high roundtrip loss at the idler wavelength of the dielectric optical coatings used in the

cavity and also to the effects of walkaway between the idler and the signal pulses in the KTP crystal. For these reasons the system does not behave as if it is genuinely doubly-resonant. Future work using a crystal with smaller walkaway such as LBO should achieve significant improvements in gain when used in a truly doubly-resonant configuration. In a system with small signal - idler walkaway, additional benefits such as increased control over signal pulse shape and duration should also be realisable.

Amplitude noise measurements

The KTP femtosecond OPO is an extremely robust device requiring no alignment on a day-to-day basis except for minor cavity length adjustment. Furthermore, when aligned correctly, oscillation persists for several hours at a time without any form of active stabilisation. The amplitude noise present on the outputs of both the parametric oscillator and the pump laser was compared and typical oscillograms are shown in Figure 4.16. Although intensity fluctuations on the pump Ti:sapphire laser are typically less than 1 %, in the absence of dispersion compensation the output of the OPO is relatively noisy, exhibiting amplitude fluctuations of around 10 %. The addition of dispersion compensation and the associated increase in spectral control reduces this figure to around 4 %. This is consistent with earlier experimental and theoretical studies [24, 27] which indicated that inadequate spectral control in lasers where SPM and GVD are significant can result in a relatively unstable output. Similar considerations are therefore likely

(a)

(b)

(c)

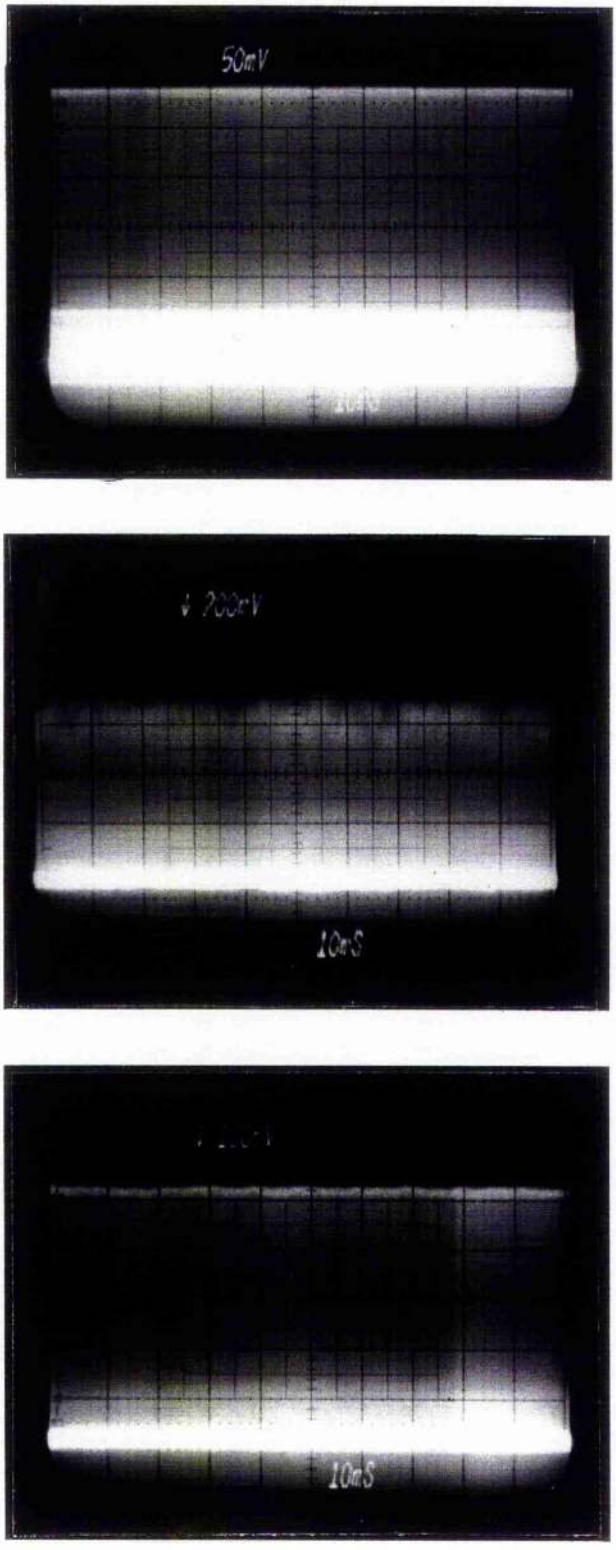

Figure 4.16 Oscillograms showing the amplitude noise of the self-mode-locked Ti:sapphire pump laser (a), the OPO without dispersion compensation (b) and the OPO with intracavity dispersion compensation (c). The timebase is 10 msec/division in each case.

to apply to the output of the OPO since SPM is a dominant effect in the cavity. The amplitude noise figures measured for the OPO should be expected to exceed those of the pump laser given the nonlinear nature of the parametric amplification process. Amplitude stabilisation can be implemented to reduce the intensity fluctuations present on the OPO output which can be caused by vibration, air currents or thermal effects.The original technique used exploited the shift in output pulse wavelength arising from a change in cavity length [28]. Wavelength tuning of this kind occurs when a cavity length change results in a loss of synchronism with the pump laser. In response the centre wavelength of the resonant signal pulse shifts and the ensuing change in group velocity delay in the KTP crystal brings the OPO back into synchronism with the pump laser and maximises gain. When the net cavity GVD is negative, longer wavelength pulses travel with slower group velocities such that a reduction in cavity length increases the output wavelength of the OPO.

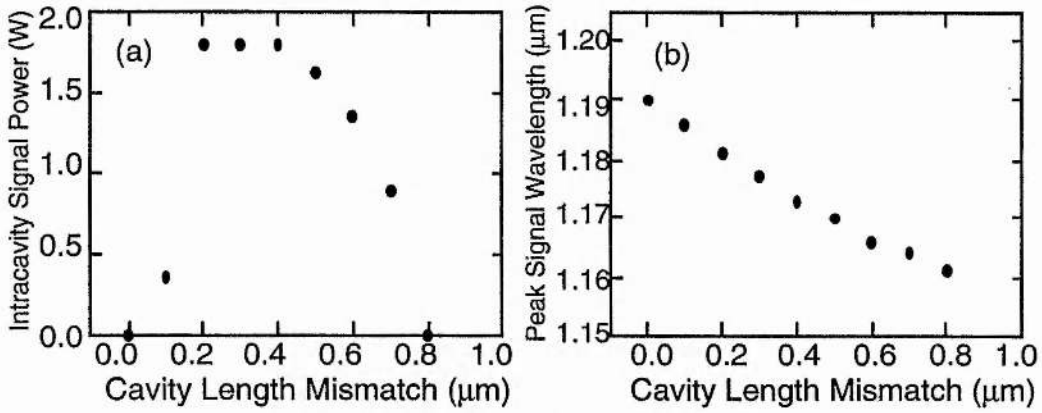

Figure 4.17 Variation of signal intensity (a) and wavelength (b) with changes in OPO cavity length. Increasing mismatch corresponds to longer cavity lengths.

Cavity-length tuning in the dispersion-compensated OPO is shown in Figure 4.17 together with the variation in signal intensity across a length

adjustment of ≈ 1 μm. The variation of wavelength with cavity length was linear and corresponds to a rate of 35 nm/μm. Oscillation was observed to occur within a cavity length adjustment of 0.8 μm but higher cavity tolerances were observed when the OPO was operated further above threshold.

Phase-noise measurements

Using techniques described elsewhere [29, 30], measurements were made of the phase noise of the signal output of the OPO and typical results are listed together with the phase noise of the pump laser in Table 4.4. The phase noise performance in the 50 - 500 Hz frequency range provides the most useful comparison between OPO and the pump laser because this frequency band corresponds to timing jitter fluctuations on millisecond timescales and provides a good indicator of longer term pulse stability. In the absence of dispersion compensation the phase noise of the OPO is considerably worse than that of the pump laser. This observation is consistent with the large intensity fluctuations apparent in this configuration and is attributed to the lack of spectral control in the cavity. The results when the OPO is operated with dispersion compensation are perhaps unexpected since the phase-noise characteristics measured in this configuration are consistently better than those of the pump laser. The improvement in phase noise can be attributed to a combination of synchronous pumping and the lack of a population lifetime in the gain process. Timing jitter present on the pump laser will not couple efficiently into the OPO since any mismatch in arrival time between the pump and signal pulses at the nonlinear crystal will result in reduced gain and cannot be transferred to the amplified signal pulse. Phase noise in the OPO can, however, exceed that of the pump laser when the resonant signal pulse has a duration much greater than the pump pulse. In this situation

the arrival time of the pump pulse at the crystal is less critical and timing jitter in the pump pulse sequence will be communicated to the signal pulse.

Table 4.4 Measured phase noise characteristics of the pump Ti:sapphire laser and the OPO operated with and without intracavity dispersion compensation.

Frequency Band	*R M S Timing Jitter*		
	Self-modelocked Ti:S pump laser	*OPO - no dispersion compensation*	*OPO - intracavity dispersion compensation*
50 - 500 Hz	12.0 ps	41.8 ps	3.6 ps
500 Hz - 5 kHz	1.7 ps	2.4 ps	0.70 ps
5 - 50 kHz	< 0.62 ps *	< 1.4 ps *	< 1.0 ps *

* *Instrumental noise meant that it was only possible to obtain an upper limit on the phase noise measurements in the highest frequency band (5kHz-50kHz).*

Our observations suggest that the amplitude and phase noise in the OPO are independent of each other. This implies that control of the OPO cavity length by active stabilisation, although improving the amplitude noise characteristics, may not serve to directly improve the phase noise.

Non-phase-matched interactions in the compensated OPO

The intracavity peak power of the dispersion compensated OPO is close to 1 MW and is therefore capable of generating directly observable sequences of pulses in the visible via non-phase-matched processes that would normally be too inefficient to be observed through parametric oscillation. We have observed a total of five non-phase-matched interactions in addition to the production of the signal and idler pulse sequences and these are listed in Table 4.5.

Table 4.5 Nonlinear interactions and corresponding average intracavity powers in the compensated OPO

Wavelength (nm)	*Description of Nonlinear Interaction*		*Average Intracavity Power*
400	$\omega = \omega_s + \omega_s + \omega_s$	$o + o + o \rightarrow o$	$< 1\ \mu W$
415	$\omega = \omega_p + \omega_p$	$o + o \rightarrow e$	1 mW
490	$\omega = \omega_s + \omega_p$	$o + o \rightarrow o$	1 mW
600	$\omega = \omega_s + \omega_s$	$o + o \rightarrow e$	10 μW
635	$\omega = \omega_i + \omega_p$	$e + o \rightarrow o$	$< 1\mu W$
1200	$\omega_s = \omega_p - \omega_i$	$o + e \rightarrow o$	3. 5 W
2690	$\omega_i = \omega_p - \omega_s$	$o + o \rightarrow e$	30 mW

The dominant processes involve sum-frequency mixing between the single-pass signal and the pump light to generate blue light at 490 nm and single-pass frequency doubling of the pump light producing a wavelength of 415 nm. The photograph reproduced as Figure 4.18 illustrates the amount of sum-frequency light generated at 490 nm.

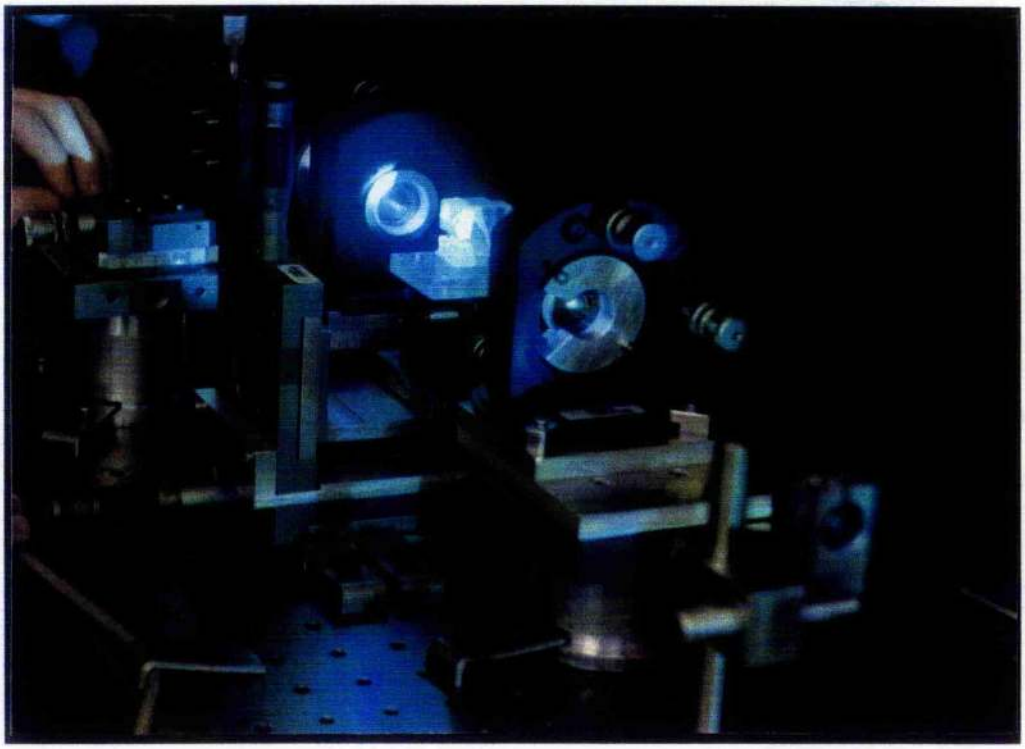

Figure 4.18 *The KTP femtosecond OPO in operation. The blue light is generated by pump-signal sum-frequency-mixing*

The other processes observed are the second and third harmonic generation of the signal which generate pulses at 600 nm and 400 nm respectively and sum-frequency mixing between the single-pass idler and the pump light that produces light at 635 nm. The spectral bandwidths of the light generated at 490 nm and 600 nm are sufficient to support pulses of sub-100 fsec duration. The addition of a second intracavity nonlinear crystal cut for efficient sum-frequency mixing or second-harmonic generation would therefore provide femtosecond pulses with tunability in the visible.

Soliton formation in the femtosecond OPO

High-order soliton formation in a femtosecond laser was first reported in a colliding-pulse-modelocked dye laser operating at 620 nm when $N = 3$ solitons were observed [31]. Such results were consistent with theoretical predictions for dispersive optical fibres which showed that pulses capable of propagating without dispersive broadening could exist when an appropriate balance between self-phase-modulation (SPM) and group-velocity-dispersion (GVD) was established [32]. Soliton formation in a modelocked laser can be expected to manifest itself in both the temporal and spectral characteristics of the laser output. Consequently, pulse breakup and restoration at the soliton frequency has been observed as an amplitude modulation of the modelocked pulse sequence [31]. Furthermore, the simultaneous production of solitonic and dispersive waves displaces the pulse spectrum towards the region of anomalous GVD and spectral splitting around the point of zero dispersion has been reported [33].

The necessary conditions for soliton formation which combine sufficient self-phase-modulation with variable group-velocity-dispersion can be satisfied in a femtosecond OPO. In normal operation substantial SPM and GVD experienced by a pulse in the nonlinear crystal is compensated by the intracavity prism-pair. However, when the intracavity GVD is made slightly positive, the spectrum of the pulse splits and shifts towards longer wavelengths. This behaviour is accompanied by a periodic amplitude modulation on the pulse sequence at a frequency in the 0.5 MHz to 2.2 MHz range.

The spectral and temporal characteristics of the output of the OPO as a function of the amount of intracavity GVD was investigated by adjusting

one of the SF14 prisms. Pulse spectra and corresponding autocorrelations were recorded for a range of positive cavity dispersion values and the pulse duration was observed to vary with dispersion as shown in Figure 4.19. The point of zero dispersion has been normalised to the maximum amount of intracavity glass that allowed the formation of transform-limited pulses.

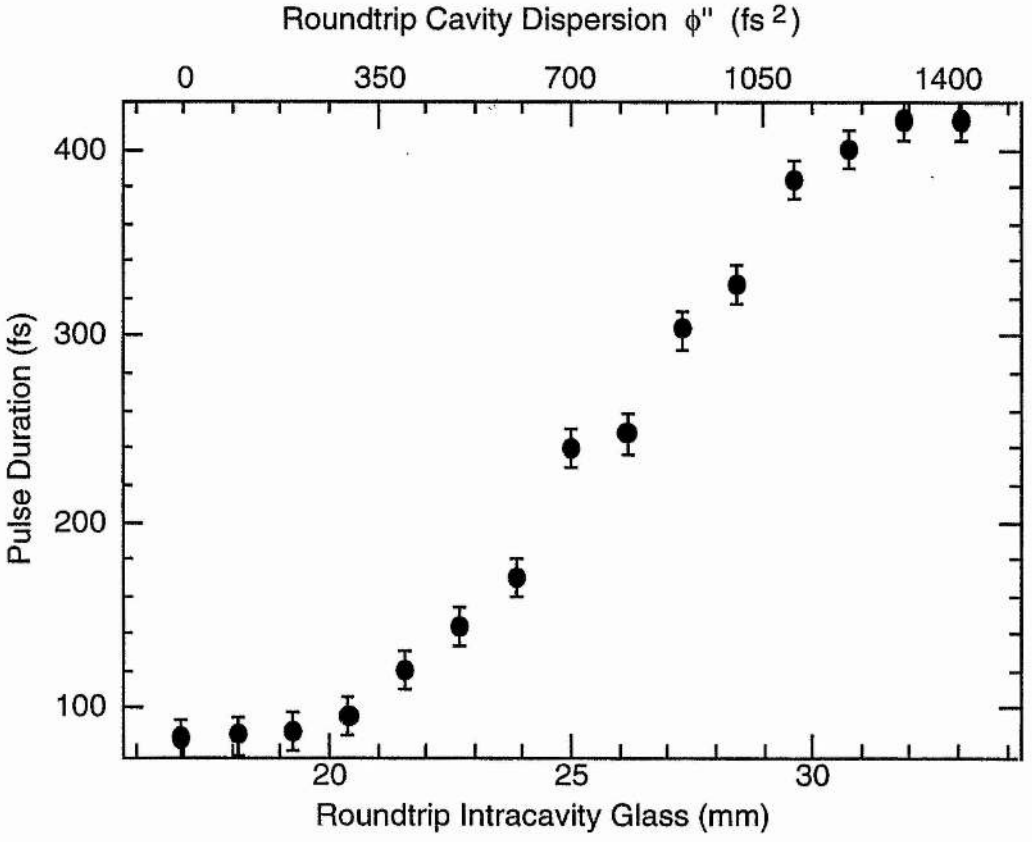

Figure 4.19 Dependence of the pulse duration on the amount of intracavity glass introduced in the dispersion compensated OPO. The upper axis indicates the equivalent cavity dispersion in fs² (see text)

The pulse spectrum at zero GVD is depicted in Figure 4.20a. Increasing the positive cavity dispersion by a small amount to +100 fs² resulted in the generation of a second spectral component at a wavelength which is 80 nm longer than the original as illustrated in Figure 4.20b. The maximum wavelength shift shown in Figure 4.20c occurred for a cavity dispersion of

+700 fs^2. The two spectral components produced were separated by 70 nm and the peak wavelength was displaced by 70 nm from the position occupied at zero cavity dispersion. An additional increase of 100 fs^2 in the dispersion inhibited longer wavelength generation and the corresponding spectrum is reproduced as Figure 4.20d. Further increasing the cavity dispersion lead ultimately to the formation of pulses having the spectrum of Figure 4.20e which is characteristic of the OPO when it is operated in the absence of any dispersion compensation.

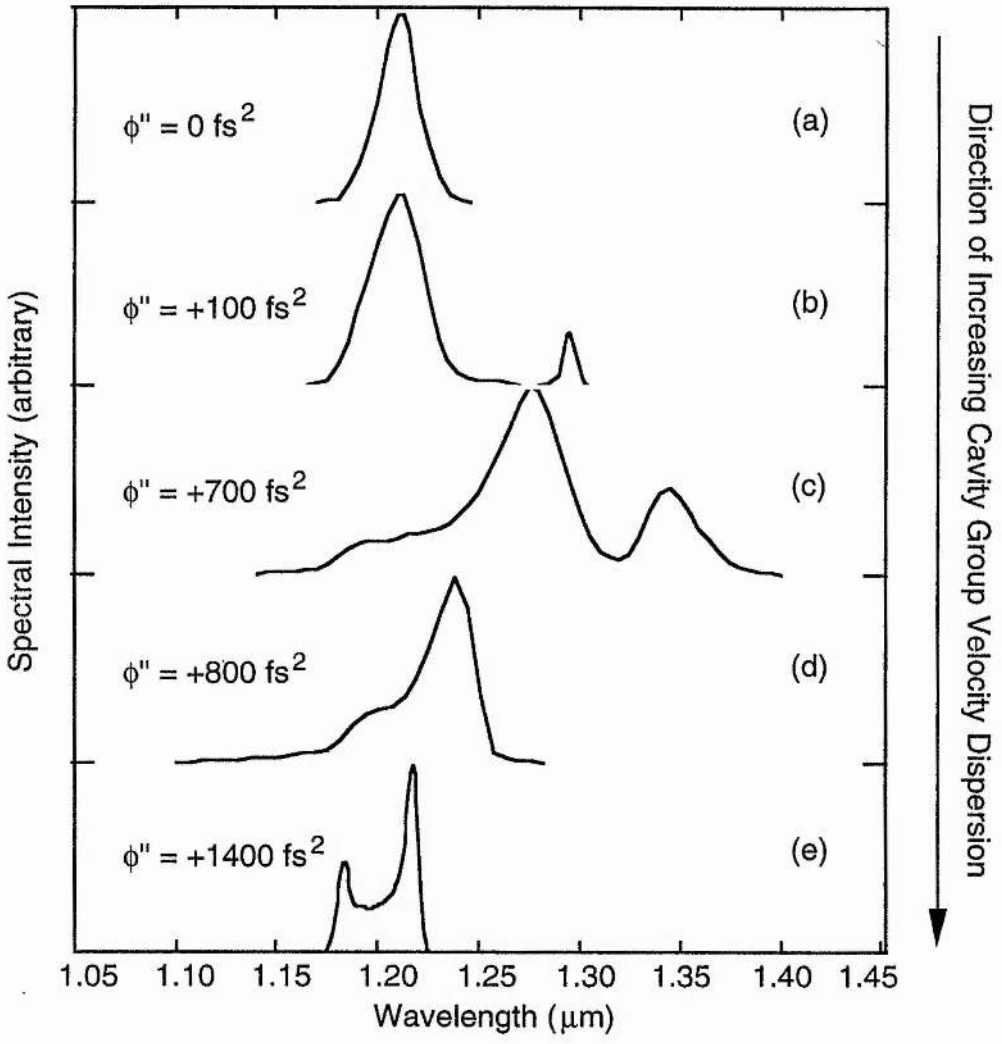

Figure 4.20 Spectral data for the signal output of the dispersion compensated OPO operated with positive cavity dispersion.

A maximum operating wavelength was observed, above which the signal output spontaneously shifted to longer wavelengths. For the particular configuration of the OPO that was used, this wavelength was approximately 1320 nm and corresponded to the position where the dispersive component of the pulse separated from the solitonic component. This spectral splitting was first predicted by Wai *et al* [34] using a model developed for pulse propagation in optical fibres at 1300 nm. Identifying the critical wavelength of the OPO with the zero dispersion point of the fibre model allows the experimental data to be related quantitatively to the theory.

In the model, a condition necessary for soliton propagation is presented in terms of the wavelength shift, $\Delta\lambda$, towards the anomalous regime, requiring that,

$$\Delta\lambda > 6\,(\text{nm})\,(\text{ps}) / \Delta\tau_p\ , \qquad (7)$$

where $\Delta\tau_p$ is the duration of the soliton pulse in picoseconds. In the OPO, the pulse duration of 240 fs measured at the position of maximum wavelength shift sets a lower limit of 25 nm for $\Delta\lambda$ for this condition. At the point where longer wavelength generation became evident pulses of duration 88 fs were monitored and this would require $\Delta\lambda > 68$ nm for soliton propagation. This is close to the 80 nm shift measured experimentally.

A further prediction of the model is that the solitonic and dispersive components of the spectrum are found to be displaced by different amounts from the critical frequency. The dispersive part is expected to

experience 1.7 times the spectral displacement of the soliton. The spectrum of Figure 4.20c displays a ratio of the displacements of frequency in the dispersive wave to that of the soliton of 1.6 which is again in good agreement with the model.

In the configuration described above we observed that the RF spectrum of the output of the OPO exhibited strong sidebands at 2.0 MHz. This observation of a periodic intensity variation in the pulse train can be related to dispersion using an expression derived by Salin *et al* [31] which gives the soliton frequency f_o as a function of the cavity dispersion ϕ'' and the cavity roundtrip period T :

$$f_o = 2\phi'' / 0.322\,\pi\,\Delta\tau_p^2\,T \qquad (8)$$

Applying this formula in the situation of maximum wavelength shift where $\Delta\tau_p = 240$ fs, $\phi'' = 700$ fs^2 and the cavity repetition period is 11.8 ns, the predicted soliton frequency of 2.0 MHz agrees closely with experimental observation. This frequency, which corresponds to around 40 cavity roundtrips, is considerably higher than the tens of kHz (ie. several thousand roundtrips) observed in CPM dye lasers [31, 33]. The difference arises because the KTP crystal used in the OPO contributes substantially higher phase modulation and dispersion during each cavity roundtrip than the jets used in dye lasers.

Further evidence for soliton formation in the OPO is provided by the observation of triple-peaked intensity autocorrelation profiles which were observed at a wavelength of 1180 nm and with an intracavity dispersion of 320 fs^2. The evolution of a second or third order soliton (N = 2, 3) is characterised by a periodic twofold temporal splitting of the pulse. This behaviour results in a characteristic triple-peaked autocorrelation profile

as first observed for high-order soliton propagation in optical fibres [35]. In contrast to the experience of soliton production in CPM dye lasers the OPO showed a large degree of instability and the character of the autocorrelation profile changed rapidly between solitonic and dispersive modes. We attribute this behaviour to a combination of the sensitivity of soliton formation to wavelength and fluctuations in OPO centre wavelength incurred by small changes in cavity length [36]. A typical autocorrelation profile, which contains information covering approximately 10,000 cavity roundtrips, is depicted in Figure 4.21. An accompanying oscillogram showing the intensity modulation of the output of the OPO is given in Figure 4.22. The modulation frequency of 550 kHz is consistent with a pulse of duration around 300 fs under the corresponding dispersive conditions.

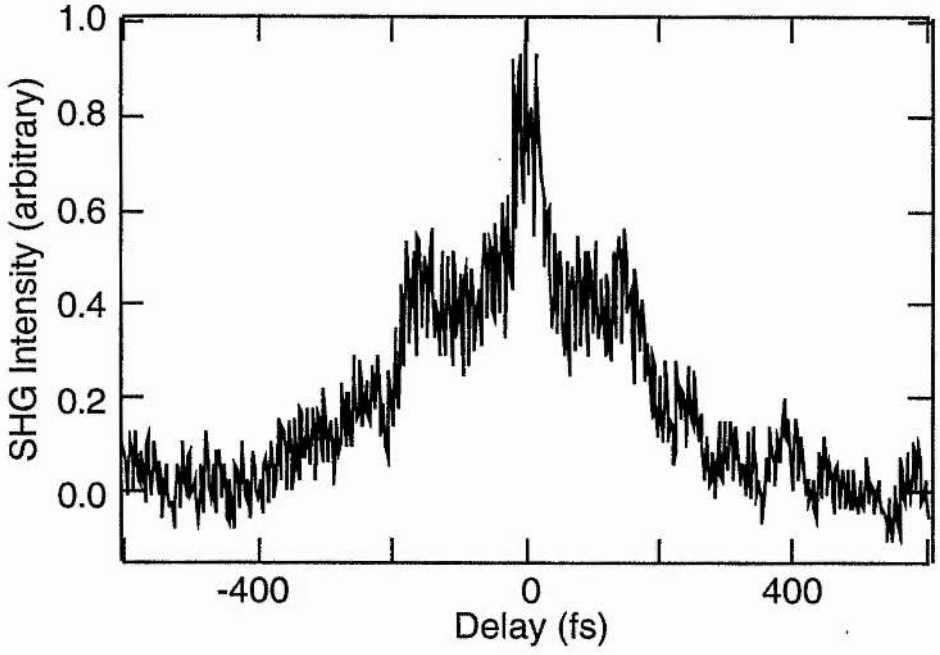

Figure 4.21 Intensity autocorrelation profile of the signal output of the OPO at a wavelength of 1180 nm exhibiting the three fold splitting that is characteristic of a solitonic pulse

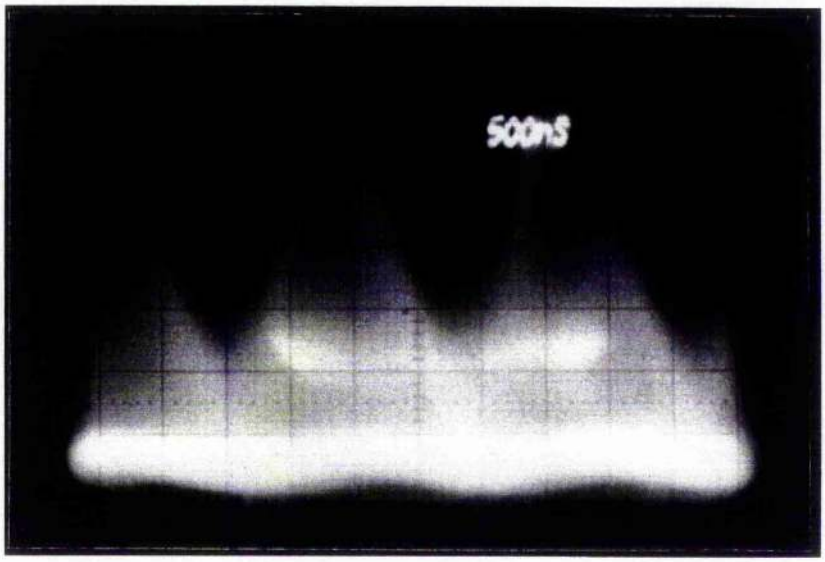

Figure 4.22 Oscillogram showing intensity modulation of the signal output pulse sequence from the OPO.

The pulse spectrum corresponding to the autocorrelation of Figure 4.21 and reproduced as Figure 4.23a did not exhibit the spectral splitting observed at longer wavelengths. In order to test whether the solitonic component of the spectrum was embedded in a strong dispersive component, an intracavity aperture was inserted into the shorter wavelength edge of the dispersed beam . The effect of the aperture was to discriminate against shorter wavelength production and the resulting spectrum is shown in Figure 4.23b. This double-peaked spectrum exhibited a critical wavelength of 1183 nm in this configuration and the ratio of the displacements of frequency in the dispersive wave to that of the soliton is 1.8 which is consistent with the results taken at longer wavelengths. Autocorrelation profiles obtained with the aperture in place were similar to that shown in Figure 4.21.

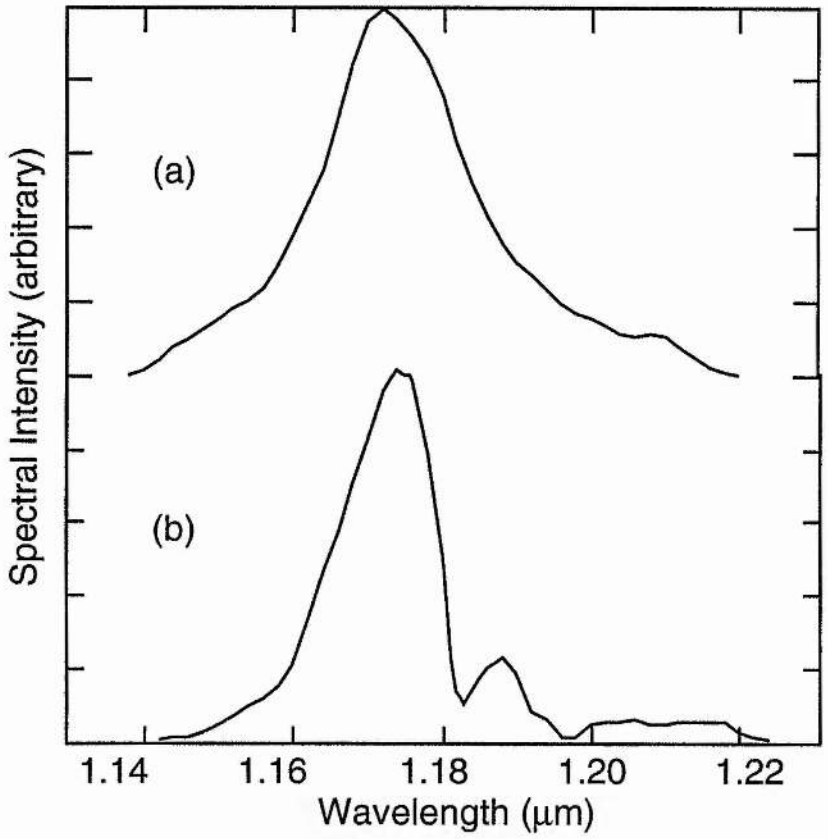

Figure 4.23 Optical spectra of the OPO (a) without an intracavity aperture and (b) with a long wavelength pass aperture

Although the recorded autocorrelation profiles of the signal output of the femtosecond OPO are consistent with higher-order $N = 2, 3$ soliton propagation, time-resolved pulse measurements within the soliton period similar to those discussed in ref. [31] would be required to establish the exact order. However, the quantitative agreement with theory derived from the nonlinear Schrödinger equation offers sufficient evidence to support the assertion that soliton formation occurs within the OPO.

4.6 Conclusions

In this chapter, results have been presented from a Ti:sapphire-pumped KTP-based femtosecond optical parametric oscillator. Without dispersion compensation the signal output pulses were highly chirped and uncompensated self-phase modulation and group-velocity dispersion were demonstrated to be the dominant pulse-shaping effects in the cavity. The addition of intracavity dispersion compensation allowed transform-limited pulses with durations as short as 40 fs to be produced. The performance of various resonator configurations have been compared and, using a novel idler-feedback scheme, threshold reductions of ≈ 10 % have been achieved. A study of the stability of the OPO has been described and, while OPO amplitude noise is consistently poorer than that of the pump laser, timing jitter figures have been measured which were consistently better than those of the pump. Several non-phase-matched processes occurring in the OPO have been reported and their implications for a visible femtosecond source considered. Evidence supporting soliton formation in the OPO has been presented and found to be in good quantitative agreement with existing theory.

With new materials and improvements to cavity design the femtosecond OPO represents an extremely attractive source of ultrashort pulses having tunability in the visible to mid-infrared spectral regions. In Chapter 5 the operation of a femtosecond OPO based on the new crystal $RbTiOAsO_4$ is described. By using intracavity second-harmonic generation this RTA parametric oscillator is capable of efficiently generating ultrashort pulses having tunability in both the visible and infrared.

References

1. F. C. Zumsteg, J. D. Bierlein and T. D. Gier, J. Appl. Phys. **47**, 4980 (1976)

2. J. D. Bierlein and H. Vanherzeele, J. Opt. Soc. Am. B. **6**, 622 (1989)

3. R. A. Laudise, R. J. Cava and A. J. Caporaso, J. Crys. Growth **74**, 275 (1986)

4. J. C. Jacco, G. M. Loiacono, M. Jaso, G. Mizell and B. Greenberg, J. Crys. Growth **70**, 484 (1984)

5. P. F. Bordui, J. C. Jacco, G. M. Loiacono, R. A. Stolzenberger and J. J. Zola, J. Crys. Growth **84**, 403 (1987)

6. J. D. Bierlein and F. Ahmed, Appl. Phys. Lett. **51**, 1322 (1987)

7. G. M. Loiacono and R. A. Stolzenberger,Appl. Phys. Lett. **53**, 1498 (1988)

8. T. A. Driscoll, H. J. Hoffman, R. E. Stone and P. E. Perkins, J. Opt. Soc. Am. B. **3**, 683 (1986)

9. T.-Y. Fan, C. E. Huang, B. Q. Hu, R. C. Eckardt, Y. X. Fan, R. L. Byer and R. S. Feigelson, Appl. Opt. **26**, 2390 (1987)

10. K. Kato, IEEE J. Quant. Electron. **27**, 1137 (1991)

11. H. Vanherzeele, J. D. Bierlein and F. C. Zumsteg, Appl. Opt. **27**, 3314 (1988)

12. R. C. Eckardt, H. Masuda, Y. X. Fan and R. L. Byer, IEEE J. Quant. Electron. **26**, 922 (1990)

13. D. A. Roberts, IEEE J. Quant. Electron **28**, 2057 (1992)

14. W. P. Risk, R. N. Payne, W. Lenth, C. Harder and H. Meier, Appl. Phys. Lett. **55**, 1179 (1989)

15. J. C. Baumert, F. M. Schellenberg, W. Lenth, W. P. Risk and C. C. Bjorklund, Appl. Phys. Lett. **51**, 2192 (1987)

16. M. Sheik-Bahae, D. C. Hutchings, D. J. Hagan and E. W. van Stryland,IEEE J. Quant. Electron. **27**,296 (1991)

17. W. S. Pelouch, P. E. Powers and C. L. Tang, Opt. Lett. **17**, 1070 (1992)

18. R. H. Stolen and C. Lin, Phys. Rev. A. **17**, 1448 (1978)

19. E. C. Cheung and J. M. Liu, J. Opt. Soc. Am. B. **7**, 1385 (1990)

20. J.-C. M. Diels, J. J. Fontaine, I. McMichael and F. Simoni, Appl. Opt. **24**, 1270 (1985)

21. J. A. Moon, IEEE J. Quant. Electron. **29**, 265 (1993)

22. H. A. Haus, J. G. Fujimoto and E. P. Ippen, J. Opt. Soc. Am. B **8**, 2068 (1991)

23. A. Finch, G, Chen, W. Sleat and W. Sibbett, J. Mod. Opt. **35**, 345 (1988)

References continued,

24. H. Avramopoulos, P. M. W. French, G. H. C. New, M. M. Opalinska, J. R. Taylor and J. A. R. Williams, Opt. Comm. **76**, 229 (1990)

25. D. Kopf, K. J. Weingarten, L. Brovelli, M. Kamp and U. Keller, Postdeadline Paper CPD22 in: Conference on Lasers and Electro-Optics 8 (1994)

26. Germanium prisms were fabricated by Pilkington Optronics PLC, St. Asaph, Wales, UK.

27. W. L. Nighan, T. Gong and P. M. Fauchet, IEEE J, Quant. Electron. **25**, 2476 (1989)

28. E. S. Wachman, D. C. Edelstein and C. L. Tang, Optics Letters **15**, 136 (1990)

29. D. R. Walker, D. W. Crust, W. E. Sleat and W. Sibbett, IEEE Journal of Quantum Electronics **28**, 289 (1992)

30. D. von der Linde, Applied Physics B **39**, 201 (1986)

31. F. Salin, P.Grangier, G. Roger and A. Brun, Physical Review Letters **56**, 1132 (1986)

32. A. Hasegawa and F. Tappert, Applied Physics Letters **23**, 142 (1973)

33. F. W. Wise, I. A. Walmsley and C. L. Tang, Optics Letters **13**, 129 (1988)

34. P. K. A. Wai, C. R. Menyuk. H. H. Chen and Y. C. Lee, Optics Letters **12**, 628 (1987)

35. L. F. Mollenauer, R. H. Stolen and J. P. Gordon, Physical Review Letters **45**, 1095 (1980)

36. D. C. Edelstein, E. S. Wachman and C. L. Tang, Applied Physics Letters **54**, 1728 (1989)

5.1 Introduction

In Chapter 4, a characterisation was presented of a femtosecond optical parametric oscillator (OPO) based on the material KTP. The structural isomorphs of KTP, namely $KTiOAsO_4$ (KTA) [1, 2], $CsTiOAsO_4$ (CTA) [3], $RbTiOPO_4$ (RTP) [4] and $RbTiOAsO_4$ (RTA) [5], have recently become available as optical-quality crystals and offer versatile phase-matching and high nonlinear coefficients. The work in this chapter describes the design, configuration and operation of a femtosecond OPO using the material RTA and pumped by a self-modelocked Ti:sapphire laser. Detailed results are presented describing the signal output pulses from both the dispersion-compensated and uncompensated OPO including details of average power, durations and tunability. Low-threshold operation is highlighted and conversion efficiencies of greater than 30 % are demonstrated. Using intracavity frequency-doubling in β-BBO the output of the OPO has been extended to provide tunability in the visible. A complete characterisation of this system is included, detailing conversion efficiencies, pulse durations and average powers. The chapter begins with a review of the titanyl arsenates and presents comparisons with KTP.

5.2 RTA and the titanyl arsenates

Structure and preparation of RTA

RTA belongs to the family of KTP isomorphs already introduced in Chapter 4 and described by the general formula $M^{+}TiOM^{5+}O_4$ where, M^{+} = K, Rb, Cs, Tl or NH_4 and M^{5+} = P or As.

Growth of RTA is carried out using the high-temperature flux method in a way similar to that already described for KTP (§ 4.2). An explicit account of the growth method was first given by Han and co-workers [5]. The starting materials Rb_2CO_3, H_3AsO_4 and TiO_2 and were used to prepare a flux solution of Rb_2O-As_2O_3-TiO_2. A seed crystal was then suspended in this solution and growth proceeded over a period of five weeks while the temperature was reduced gradually from 850 - 730 °C. The RTA crystals produced by this method had typical dimensions of 30 × 15 × 15 mm.

The structure of all the isomorphs is orthorhombic and has been detailed in Chapter 4. The unit cell sizes of the isomorphs increase with increasing atomic number of the M^+ ion due to the larger ionic radius. The crystal lattice parameters of RTA are given later in Table 5.1.

Linear and nonlinear optical properties

Unlike KTP, which has reduced transmission at 3.4 μm and 4.3 μm resulting from absorption that can be attributed to the phosphate group [6], the titanyl arsenates possess optical transparency extending further into the infrared to the 5.3 μm region. A transmission spectrum of RTA is included as Figure 5.1 and illustrates that the absorption which occurs at 2.8 μm in KTP due to *O-H* bonds is not present in RTA.

The linearly dispersive optical properties of the arsenate isomorphs are different from those of KTP. Details of the principal refractive indices of RTA are included in Table 5.1. The birefringence (n_z - n_x) of the isomorphs decreases with increasing atomic number of the M^+ ion [7] and consequently their phase-matching properties are different. This behaviour makes the titanyl arsenates very attractive crystals for

parametric generation and frequency-conversion applications. The variation in phase-matching has already been exploited in the development of a hybrid crystal, based on the KTP isomorphs, which is phase-matchable for 1064 nm frequency-doubling along a principal optical axis (ie. non-critical phase-matching) [7]. Such a material elliminates walkoff problems associated with critical phase-matching in KTP and therefore allows longer crystals to be used to generate second-harmonic light at high efficiency.

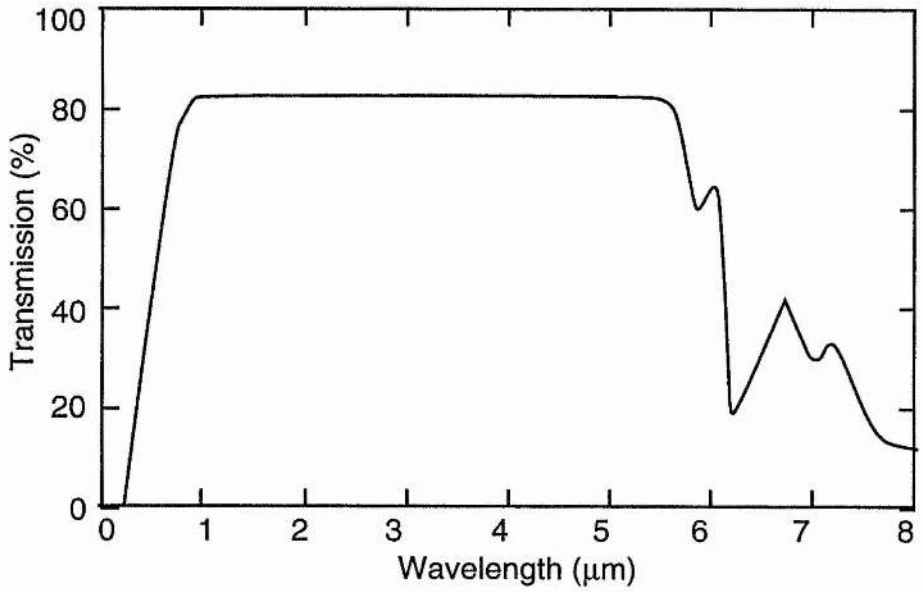

Figure 5.1 Transmission spectrum of RTA (reproduced from ref. [5])

Phase-matching calculations based on Sellemeier equations for the arsenates [6] show that an OPO pumped by a typical Ti:sapphire laser (ie. single mirror set, tunable from ≈ 750 - 900 nm) can cover most of the 1.0 - 3.0 μm spectral region using only non-critically phase-matched RTA and CTA. The predicted tuning ranges for non-critically phase-matched Ti:sapphire-pumped OPOs using various KTP isomorphs is summarised in Fig. 5.2.

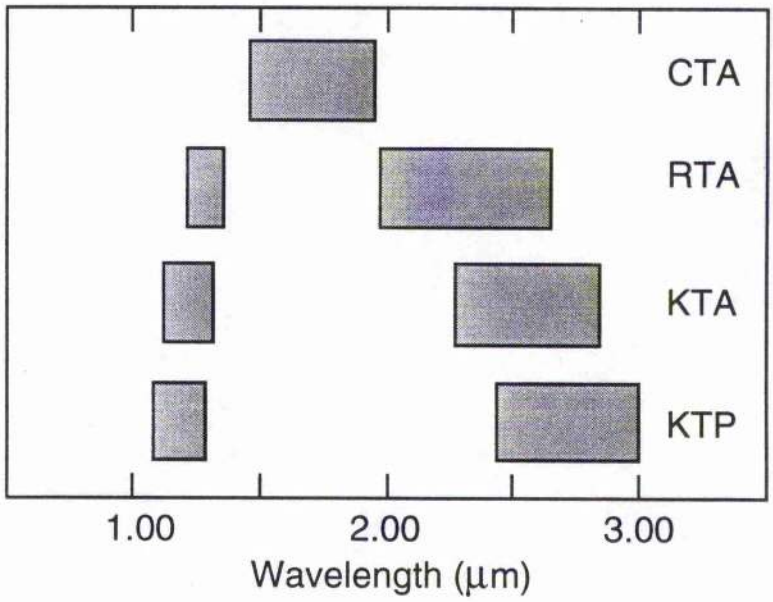

Figure 5.2 Wavelengths generated by Ti:sapphire-pumped OPOs phase-matched collinearly along the x-axis and based on CTA, RTA, KTA and KTP.

The nonlinear optical coefficients of KTP and its isomorphs are similar. Using a Maker-fringe method, Han and co-workers [5] obtained results (quoted here in the IEEE / ANSI standard piezoelectric reporting frame) indicating that d_{31} (RTA) ≈ 1.2 d_{31} (KTP), d_{32} (RTA) ≈ 0.5 d_{32} (KTP) and d_{33} (RTA) ≈ 1.4 d_{33} (KTP). The absolute values of the coefficients are also given but those supplied for KTP are substantially larger than the now accepted figures, suggesting that the relative magnitudes are of more value. Measurements by Cheng and co-workers [6], also made using the Maker-fringe method and subject to experimental uncertainties of ± 20 %, imply values of the nonlinear coefficients for RTA where d_{31} = 3.8 pm/V, d_{32} = 2.3 pm/V and d_{33} = 15.8 pm/V. A summary of these and other properties of RTA is given below in Table 5.1.

Table 5.1 Structural and optical properties of RTA

Property	*Value*	*Ref.*
Crystal class	Orthorhombic, point group $2mm$ space group $Pna2_1$	[5]
Unit cell parameters	a = 10.764Å, b = 13.243 Å, c = 6.669	[5]
Refractive index (λ = 1.064 μm)	n_x = 1.803, n_y = 1.809, n_z = 1.881, (positive biaxial)	[6]
Transmission	350 nm - 5.3 μm	[5, 8]
Damage threshold	400 MW / cm^2	[9]
Average nonlinear optical coefficients	$d_{15(31)}$ = 4.1 pm/V $d_{24(32)}$ = 1.7 pm/V d_{33} = 13.7 pm/V	[5, 6, 10, 11, 12]

5.3 RTA-based femtosecond optical parametric oscillator

Phase-matching and gain calculations

In common with KTP, the largest (phasematchable) nonlinear coefficient in RTA is d_{15} . Therefore, as expected, the variation of the effective nonlinear coefficient with angle (illustrated in Figure 5.3) is similar in behaviour to KTP. The propagation direction which maximises parametric gain is, similarly, parallel to the x-axis and non-critical phase-matching was chosen for the OPO crystal to avoid Poynting-vector walkoff and for the reasons outlined in Chapter 4.

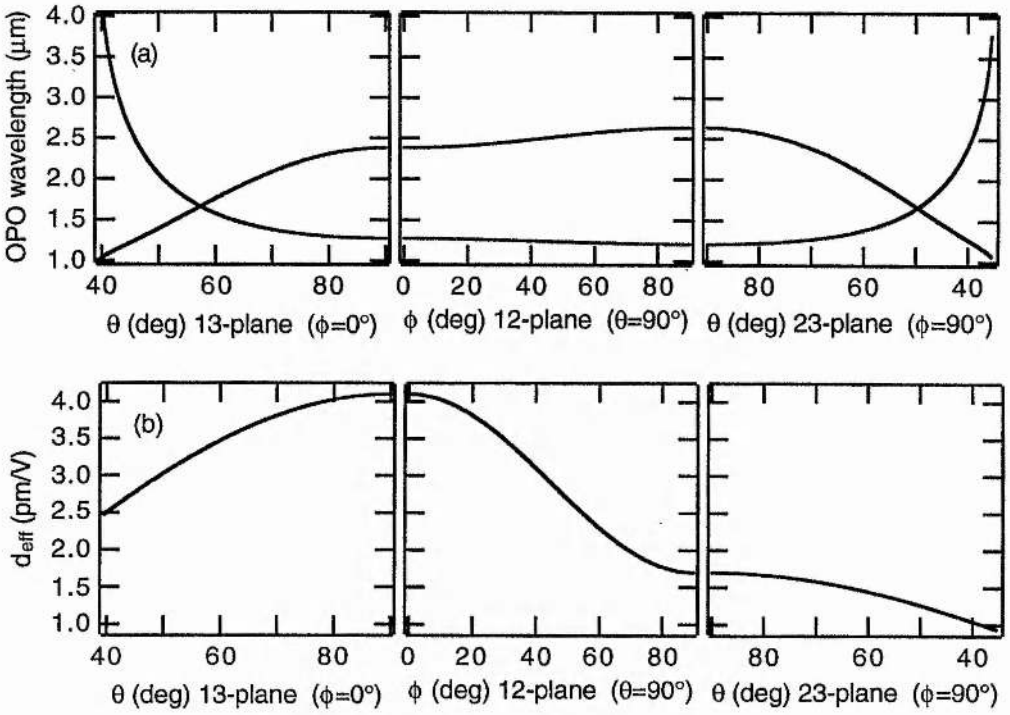

Figure 5.3 Phase-matching curves (a) and effective nonlinear coefficient (b) in the principal optical planes for a Type II parametric interaction in RTA with a pump wavelength of 830 nm. Refractive index data used in calculations are from Ref. [6].

The signal and idler wavelengths generated using pump tuning from 700 - 1000 nm along the x-axis cover 1.20 - 1.51 μm and 1.68 - 2.94 μm respectively. Phase-matching along the y-axis over the same pump wavelength range produces signal output from 1.09 - 1.47 μm and idler from 1.96 - 3.11 μm. The predicted pump tuning of the RTA OPO for phase-matching along the x and the y axes is shown in Figure 5.4.

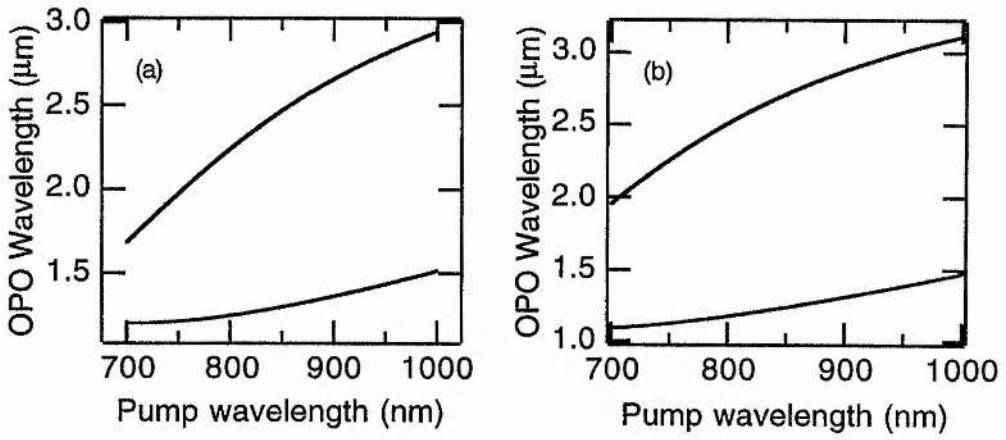

Figure 5.4 *Phase-matching wavelengths generated in RTA for pump tuning along the x (a) and the y (b) axes.*

Using the analysis presented in Chapter 3, the oscillation threshold can be estimated for the RTA parametric oscillator. The effective nonlinear coefficient for Type II parametric interaction along the x-axis is d_{15} = 4.1 pm/V and the corresponding average pump power threshold, calculated for a 1-mm thick crystal, is just 70 mW. As the measured threshold of the KTP oscillator described earlier was approximately 4 times the predicted value, a thickness of 2 mm was chosen for the RTA crystal to ensure sufficient gain.

At a pump wavelength of 830 nm, the signal phase-matching bandwidth of a 2-mm-thick RTA crystal cut for propagation along the x-axis is approximately 21 nm. This bandwidth is sufficient for the generation of transform-limited 85-fs-duration $\text{sech}^2(t)$ signal pulses. Group-velocity walkaway calculations at the same pump wavelength show that the signal leads the pump pulse by ≈ 132 fs/mm while the idler lags the pump by ≈ 110 fs/mm. Walkaway values of this magnitude might be expected to lower the gain by reducing the temporal overlap of the pulses. Nevertheless, walkaway may not dominate the gain process

because the substantial pump depletion expected in the RTA OPO may broaden the pulses enough to allow interaction over the full length of the crystal. Furthermore, the effect of walkaway itself may only be to broaden the signal and idler pulses rather than reduce the single-pass gain.

Table 5.2 Summary of the specifications of the OPO-RTA crystal at a pump wavelength of 830 nm

Parameter (λ_p = 830 nm)	*Value*
Phase-matching orientation	Collinear non-critical phase-matching for propagation // *x*-axis: *p* // *y*-axis, *s* // *y*-axis, *i* // *z*-axis
Dimensions	2 mm (*t*) x 3 mm (*w*) x 5 mm(*h*)
Signal and idler wavelengths	λ_s = 1.274 μm, λ_i = 2.381 μm
Anti-reflection coatings	T > 99.9 % @ λ = 1.274 μm T > 95 % @ λ = 830 nm
Effective nonlinear coefficient	d_{eff} = 4.1 pm/V
Signal phase-matching bandwidth	$\Delta\lambda_s$ = 21 nm
Group-velocity walkaway	*p-s* 132 fs/mm (*signal* leads) *p-i* 110 fs/mm (*idler* lags)

Our RTA crystal was supplied by *Crystal Associates Inc.* [13] and had an aperture of 3 mm (// *z*-axis) by 5 mm (// *y*-axis). The crystal faces were anti-reflection (AR) coated with a single quarter-wave layer of MgF_2 similar to that used in the KTP-OPO crystal. Maximum transmission (T > 99.9 %) centred at the signal phase-matching wavelength of 1274 nm was specified and high transmission (T > 95 %) at 830 nm was also obtained. As before, no coating requirement was

specified at the idler wavelength. A summary of the complete RTA crystal details is given in Table 5.2.

RTA femtosecond OPO without dispersion compensation

Since the first cw femtosecond OPO based on the KTP crystal was reported [14] other KTP isomorphs including KTA [15], CTA [16] and RTA [17] have been used successfully in similar parametric oscillators to produce femtosecond pulses in the 1 μm to 5 μm spectral region. The previously reported RTA femtosecond OPO [17] used only noncollinear critical phase-matching; the non-critical crystal geometry has, until now, not been demonstrated in an RTA parametric oscillator.

Without dispersion compensation the parametric oscillator was configured as a 3-mirror resonator (depicted in Fig. 5.5) using two curved mirrors (r = -100 mm) and one plane mirror. The mirrors used were highly-reflecting (HR) single-layer dielectric coatings centred at 1274 nm (R > 99.9 %) and had a high transmission (T > 95 %) at 830 nm. The pump light was focused into the crystal through one of the curved mirrors using a 50 mm focal length lens.

With a pump wavelength of 825 nm and the cavity configured with all HR mirrors oscillation was maintained for pump powers as low as 50 mW. Replacing the plane mirror with a 2.5 % output coupler increased the oscillation threshold to 140 mW. When a pump power of 880 mW was incident on the focusing lens the total output power in the signal branch at 1.27 μm was measured to be 185 mW. From conservation of energy the corresponding power in the idler at 2.4 μm is calculated to be 100 mW, implying a pump conversion efficiency in excess of 32 %.

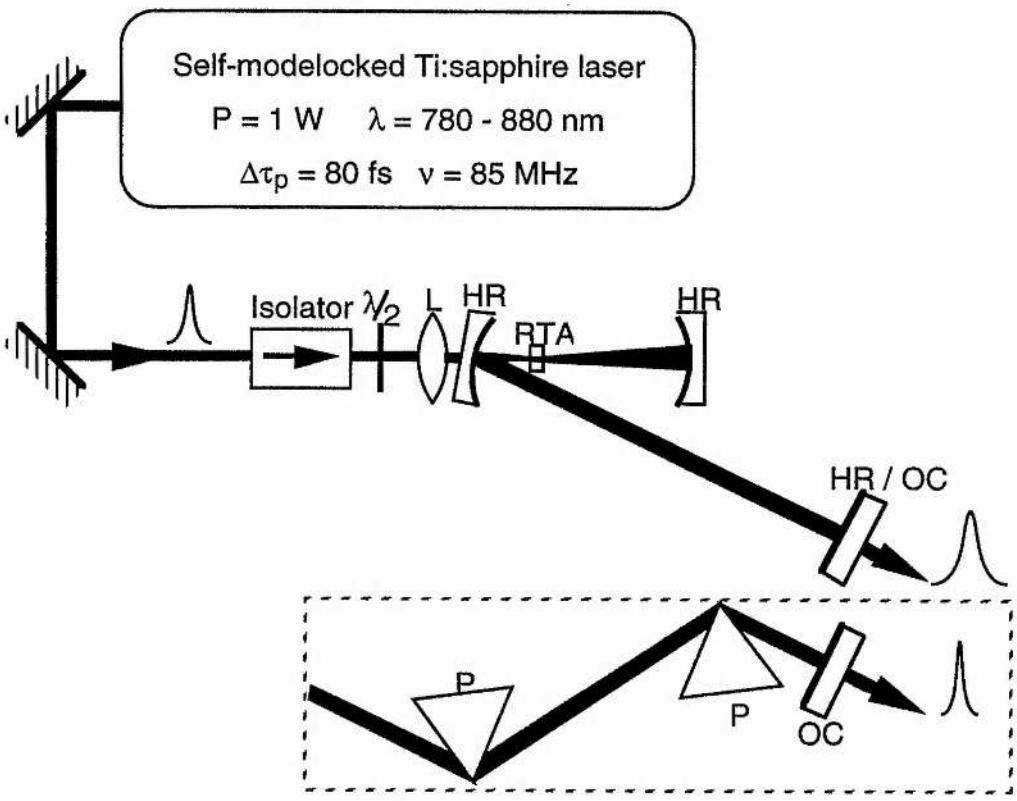

FIgure 5.5 *Cavity schematic of the RTA femtosecond OPO with (inset) and without dispersion compensation*

The intensity autocorrelation of the signal (see Fig. 5.6a.) implies a pulse duration of 980 fs. In the absence of group-velocity dispersion (GVD) compensation the signal pulses are highly chirped due to the substantial self-phase-modulation (SPM) in the RTA crystal. The broad pedestal of the interferometric autocorrelation (Fig. 5.6b) and the modulation in the power spectrum (Fig. 5.6c) are characteristic of SPM.

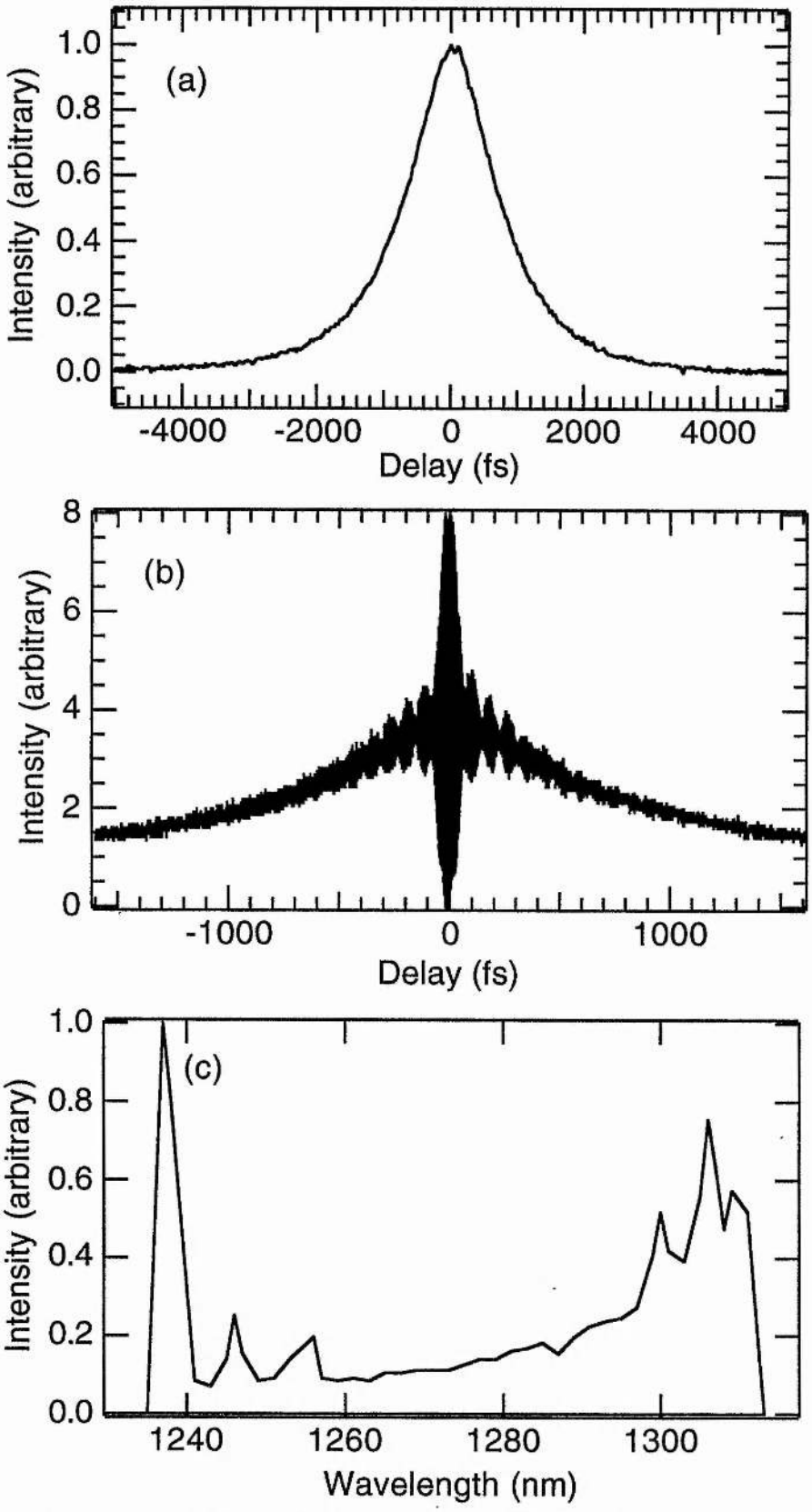

Figure 5.6 Intensity (a) and interferometric (b) autocorrelation profiles and spectrum (c) of the signal output from the uncompensated OPO.

When the results of the SPM model outlined in Chapter 4 are applied to the pulses from the RTA oscillator, it is clear that self-phase-modulation is particularly high in the uncompensated cavity. At least 24 minima can be counted in the interferometric autocorrelation although visibility is poorer further into the wings. This implies a peak nonlinear phase-shift of at least 12π radians. Unlike the results from the KTP oscillator, the modulation in the pulse spectrum predicted by the model can be clearly seen as periodic maxima separated by intervals of $\approx$ 10 nm. Beating between the strongest components in the spectrum at 1237 nm and 1307 nm is responsible for the 80-fs modulation which is observed in the autocorrelation.

RTA femtosecond OPO with dispersion compensation

The effects of dispersion and self-phase-modulation in the cavity were compensated for by the insertion of a pair of SF14 glass prisms with an apex spacing of 30 cm as illustrated in Fig. 5.5 (inset). With the plane mirror replaced by a 2.5 % output coupler the oscillation threshold for this configuration was still only 160 mW. The signal output power was reduced to 100 mW and the corresponding idler power was 55 mW for a pump power of 880 mW. This represents a total conversion efficiency of approximately 18 %. A typical interferometric autocorrelation of the signal output corresponding to a 76-fs duration pulse is shown in Figure 5.7a together with the corresponding spectral profile in Figure 5.7b. Assuming a $\mathrm{sech}^2(t)$ intensity profile, the time-bandwidth product calculated from these results is 0.32 implying that the signal pulses are transform-limited and chirp-free. Optimising the amount of intracavity glass produced the shortest pulses which were measured to have durations of 67 fs. Adjusting the prisms to produce positive values of net cavity dispersion resulted in a

pulse autocorrelation profile displaying a triple-peak structure consistent with the soliton generation discussed in detail in Chapter 4.

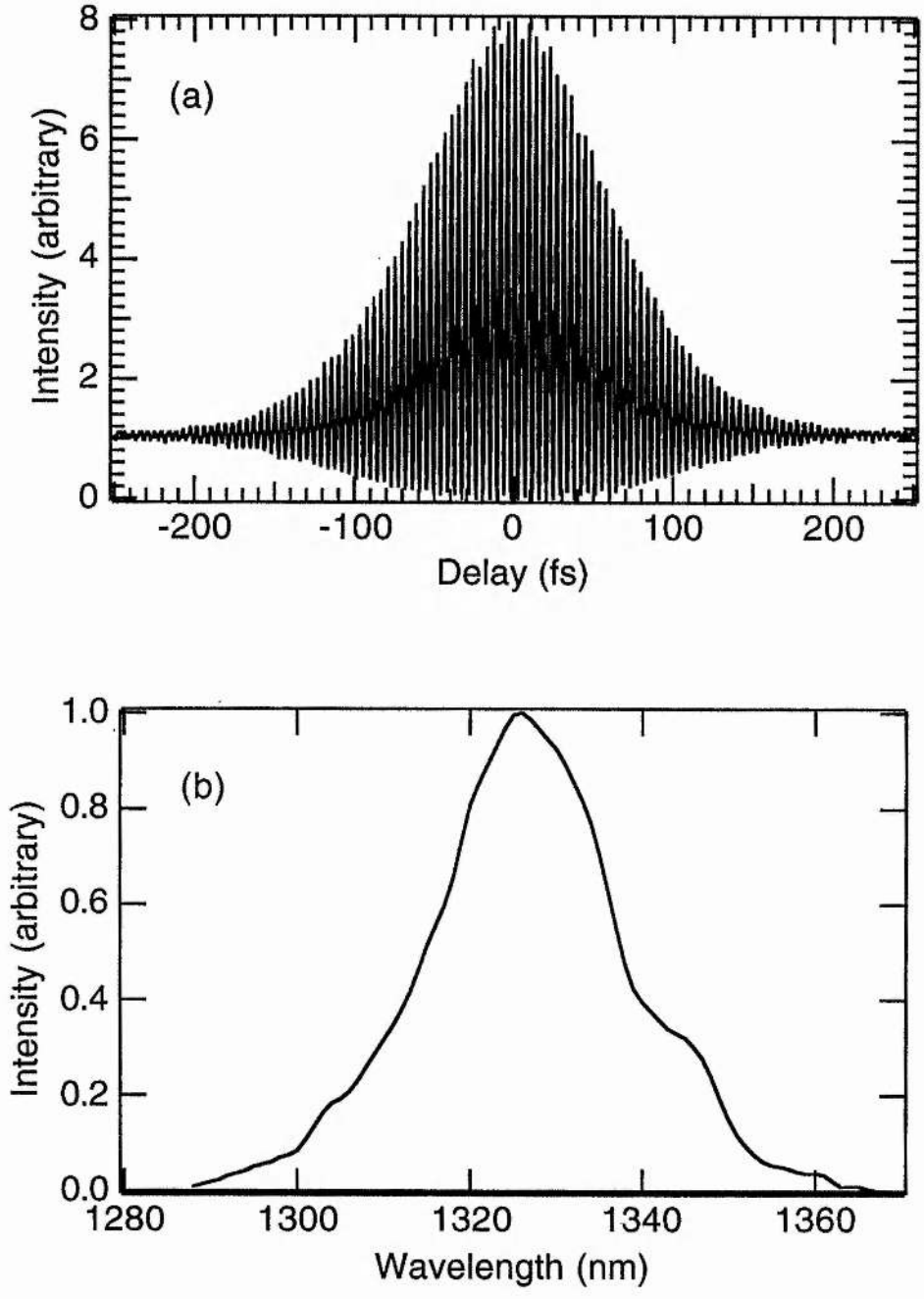

Figure 5.7 Interferometric autocorrelation (a) and corresponding spectrum (b) for the signal output pulses from the dispersion-compensated OPO.

Wavelength tuning of the RTA femtosecond OPO

Pump tuning of the signal from 1230 - 1340 nm and of the idler from 2100 - 2430 nm was achieved using pump wavelength tuning alone. Experimental tuning data together with theoretical curves derived from Sellemeier equations for RTA [6] are shown in Figure 5.8.

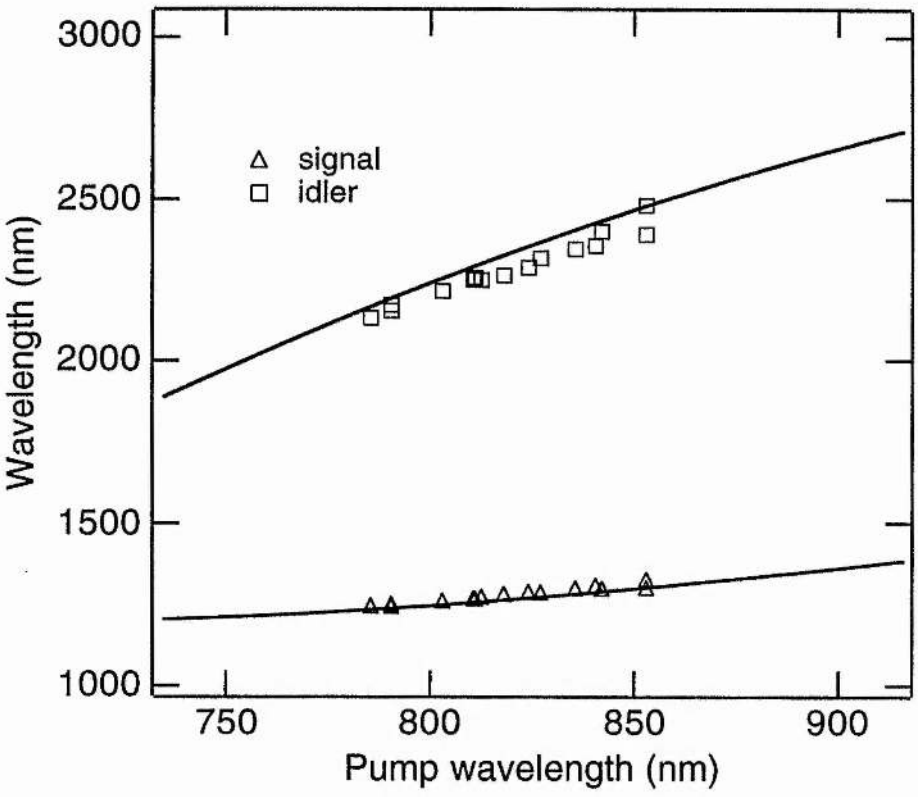

Figure 5.8 Signal wavelength data (triangles) and inferred idler data (squares) for pump wavelengths from 785 - 853 nm. The solid lines indicate the tuning predicted from Sellemeier equations for RTA.

The only adjustment required between each wavelength measurement was a change in cavity length to maintain synchronism between the OPO and the pump laser. Oscillation was observed over a cavity-length tolerance of 1.0 μm and the signal wavelength tuned by 27 nm across this range as the centre wavelength shifted to maintain synchronism with the pump laser. Shortening the cavity length caused a shift to longer

wavelengths similar to the behaviour of the KTP OPO. When pumped sufficiently above threshold the OPO was very stable with operation over several hours possible without requiring any change in cavity length.

In addition to the signal and idler outputs at 1.274 μm and 2.381 μm, a further six non-phase-matched processes were observed in the RTA crystal. Single-pass second-harmonic generation occurred for each of the pump, signal and idler waves giving outputs at 415 nm, 637 nm and 1190 nm. Sum-frequency mixing was also observed between the pump and the signal giving 503 nm and between the pump and idler to give 615 nm. Additionally, third-harmonic generation of the signal, giving 425 nm, was observed. The spectrum included as Fig. 5.9 shows the frequency-doubled signal at 639 nm and the pump-idler sum-frequency component at 615 nm measured for a signal wavelength of 1.278 μm. The 16 nm bandwidth of the output at 639 nm is consistent with pulses of 28 fs duration if they are assumed to be transform-limited with a $\mathrm{sech}^2(t)$ intensity profile but autocorrelation measurements would be necessary to confirm the exact pulse duration.

The average power generated by any of the non-phase-matched interactions was only a few microwatts. In particular, the pump-signal sum-mixing was significantly weaker than in the KTP counterpart.

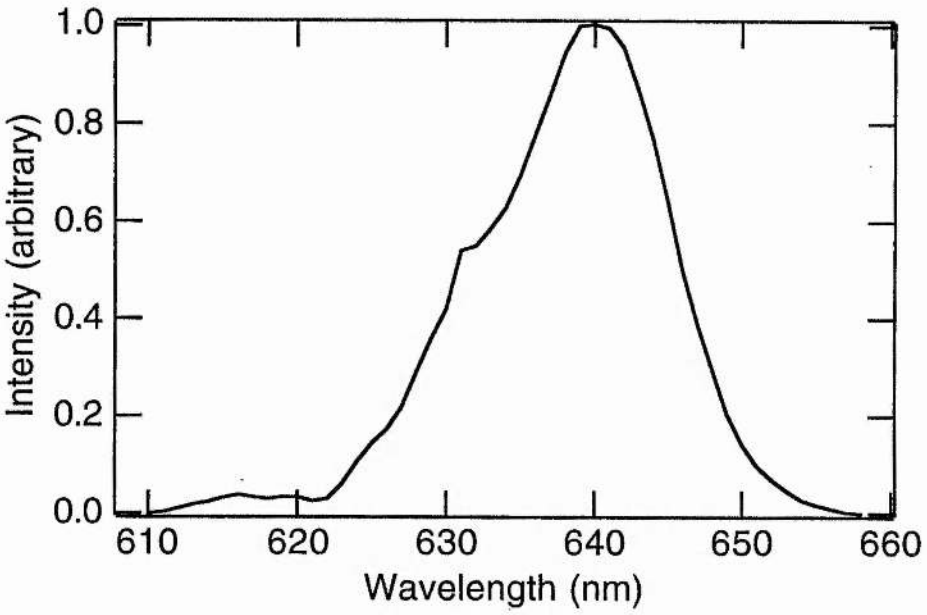

Figure 5.9 Spectrum of the frequency-doubled signal centred at 639 nm. The weak component at 615 nm corresponds to sum-frequency-mixing between the pump and the idler waves.

Compared with the KTP-based OPO, the low-threshold operation and the higher efficiencies measured in the RTA oscillator are not fully explained by the additional crystal length. The results obtained suggest that the nonlinear coefficients of RTA may have been underestimated. A comparison of nonlinear coefficients of KTP and RTA using a phase-matched measuring technique such as single-pass second-harmonic generation would be required to investigate this assertion properly.

The high intracavity powers and conversion efficiencies apparent in the OPO configuration described in this chapter imply that highly efficient intracavity frequency-doubling could be realised. In the following section the extension of the wavelength coverage of the RTA parametric oscillator into the visible region using intracavity second-harmonic generation is described.

5.3 Intracavity frequency-doubled RTA femtosecond OPO

For over a decade since its original demonstation, the colliding-pulse-modelocked (CPM) dye laser [18] remained the only source of high-repetition-rate femtosecond pulses in the visible. While frequency-doubling of the self-modelocked Ti:sapphire laser [19, 20] now offers a route to femtosecond pulse generation in the blue, the efficient production of high-repetition-rate pulses in the complementary green to red spectral regions is made possible only by intracavity doubling [21] or blue-pumping [22] of a femtosecond optical parametric oscillator. The most efficient femtosecond OPO generation in the visible to date has been achieved in an intracavity frequency-doubled system [21].

This section details the operation and configuration of an intracavity-frequency-doubled femtosecond optical parametric oscillator based on RTA. Using a Brewster-cut crystal of βBBO situated at a second intracavity focus, efficient single-pass, frequency-doubling of the signal into the red can be achieved. The characteristics of this system operated with and without intracavity dispersion compensation are compared and the design of the frequency-doubling arrangement is described in detail.

Intracavity-frequency doubling assembly

The doubling crystal used in the OPO was an uncoated 5 mm x 10 mm x 200-μm-thick section of β–BaB_2O_4 (βBBO) which was Brewster-cut for Type I second-harmonic generation ($o + o \rightarrow e$) at 1200 nm ($\theta = 21.2°$). Previous work involving intracavity doubling of CPM dye lasers with βBBO [23] demanded the use of ultrathin crystals ($t \sim 50$ μm) to achieve second-harmonic output pulses of durations shorter than the fundamental

pulses. The limiting factor was group velocity walkaway between the fundamental and the SHG light which, for dye laser wavelengths, was typically ≈ 400 fs/mm. For doubling of 1.3 μm, the walkaway values are around 30 fs/mm which allows longer crystals to be used and increases single-pass conversion efficiency. At Brewster incidence the path length inside the βBBO crystal used in the OPO was 230 μm so pulse broadening due to group velocity walkaway was restricted to ≈ 5 fs.

The crystal acceptance bandwidth may also broaden the frequency-doubled pulses. In βBBO, Type I second-harmonic phase-matching is efficient and has the advantage that Type I interactions generally have a much wider acceptance bandwidth than the equivalent Type II process.

The full-width acceptance bandwidth for the fundamental wave in a collinear SHG interaction can be derived using the method described in Chapter 3. If the fundamental radiation has a frequency of ω_1 and the frequency-doubled light ω_2, then the wavevector mismatch will be,

$$\Delta k = 2k_1 - k_2 \tag{1}$$

Using a Taylor-series expansion for $\partial\Delta k/\partial\lambda_1$, the full-width acceptance bandwidth ($-\pi/l < \Delta k < \pi/l$) for a crystal of length l can be written as,

$$\Delta\lambda = \frac{2\pi}{l}\left(\frac{4\pi}{\lambda_1}\frac{\partial n_1}{\partial\lambda_1} - \frac{2\pi}{\lambda_1}\frac{\partial n_2}{\partial\lambda_2}\right)^{-1} \tag{2}$$

The variation of the SHG acceptance bandwidth in the 1 - 2 μm wavelength region is illustrated, for a 230-μm-thick crystal of βBBO, in Figure 5.10 and is seen to maximise at a wavelength of around 1.5 μm. At the OPO signal wavelength of 1.274 μm, the acceptance bandwidth is approximately 300 nm which implies that the pulse duration of the frequency-doubled light should not be limited by the crystal bandwidth.

Furthermore, the OPO can therefore be tuned over a range of several hundred nanometres without changing the phase-matching angle of the βBBO crystal.

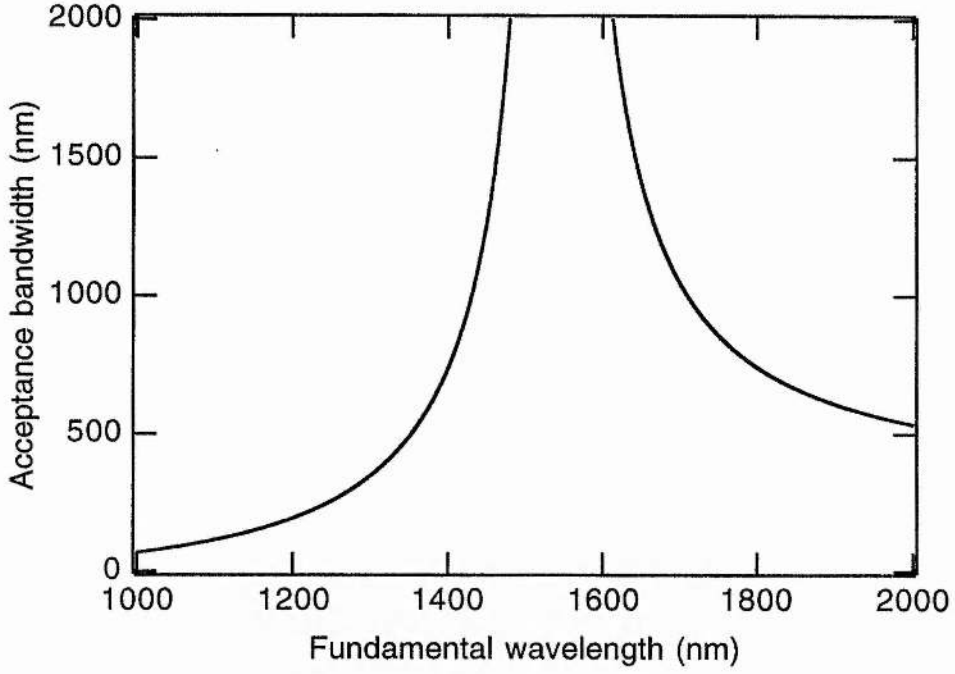

Figure 5.10 Wavelength dependence of the full-width spectral acceptance bandwidth of the fundamental wave for SHG using a 230-μm-thick βBBO crystal.

An estimation of the single-pass power conversion efficiency from the fundamental to the second-harmonic can be made using a Gaussian-wave analysis provided by Boyd and Kleinman [24]. Expressed in *esu* units the efficiency is given by,

$$\frac{P_2}{P_1} = \left(\frac{128\pi^2 \omega_1^2}{c^3 n_1^2 n_2} \right) d_{eff}^2 P_1 l k_1 h(\xi) . \qquad (3)$$

The effective nonlinear coefficient for Type I SHG in βBBO has been measured directly to be ≈ 2.0 pm/V [11] which, using the conversion given in Chapter 3, is equivalent to 9.5 x 10^{-9} esu. The focusing factor $h(\xi)$

is similar to that introduced earlier in the calculation of the power threshold for a parametric oscillator. Practical considerations limit the tightest focusing to a spot radius of ≈ 20 μm which, for a 230-μm-thick crystal, implies a value of $h \approx 0.06$. The average power conversion efficiency also depends on the the durations of the fundamental and second-harmonic pulses and is proportional to $\Delta\tau(2\omega) / \Delta\tau(\omega)$. If the average power of the fundamental is 2 W and is delivered as 100-fs-duration pulses at an 85 MHz repetition frequency, and the second-harmonic pulses have durations of 70 fs, then the conversion efficiency is calculated to be approximately 3.5 %. Efficiencies up to an order of magnitude higher would be expected for optimum focusing.

The crystal was mounted by its edges on a thin perspex holder using ordinary clear nail polish. The mount, illustrated in Figure 5.11, was designed to offer the maximum aperture for the transmitted light and was secured on top of a prism table which provided fine angular adjustment. This assembly was situated on two orthogonal translation stages which allowed the intracavity beam to be focused to any point on the crystal surface and the best part of the crystal to be selected. Once mounted, the correct orientation was determined using the output of the Ti:sapphire laser.

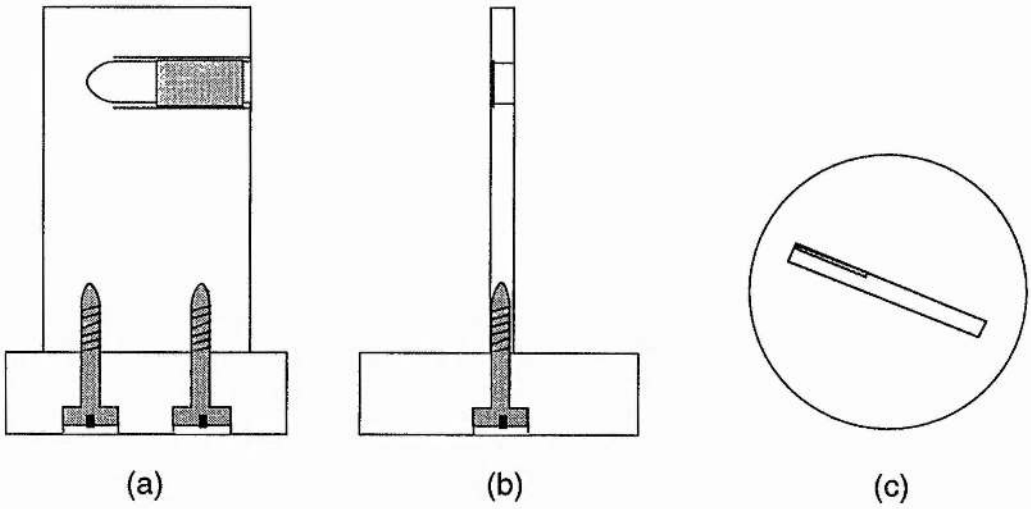

Figure 5.11 Side (a), end (b) and top (c) views of the perspex mount used to hold the βBBO crystal

Configuration and output characteristics of the frequency-doubled RTA optical parametric oscillator

As depicted by the schematic in Figure 5.12, the signal was resonant in a five-mirror standing-wave cavity comprising a plane mirror, two r = -100 mm curved mirrors, which formed the focus in the RTA crystal, and two r = -75 mm mirrors for the focus inside the βBBO crystal. With the exception of the plane 2.5 % signal output coupler (OC) all the mirrors were highly-reflecting (HR) single-layer dielectric coatings centred at 1274 nm (R > 99.9 %) and having high transmission (T > 95 %) at 830 nm.

The parametric oscillator was initially aligned without the doubling crystal present using the alignment techniques described previously. After external orientation, the βBBO crystal was then inserted into the OPO cavity. Once inserted, the crystal was easily adjusted to optimise the second-harmonic generation efficiency.

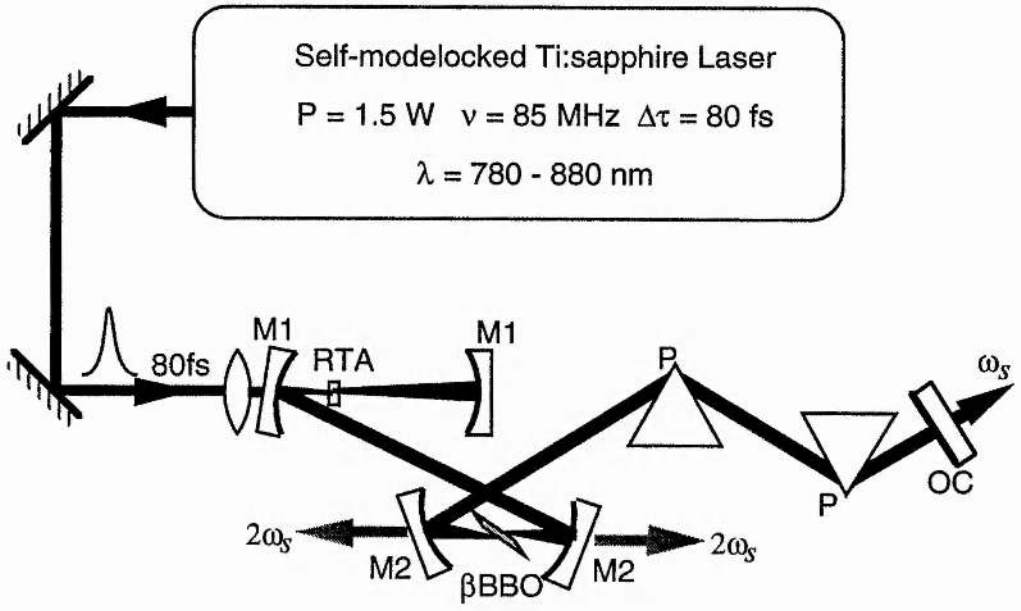

Figure 5.12 Cavity configuration of the intracavity-doubled RTA optical parametric oscillator.

The intracavity-doubled OPO was operated both with and without the dispersion-compensating prism sequence and is shown in Figure 5.12. Configured with all HR mirrors and without intracavity prisms as much as 135 mW was generated in the second harmonic when pumped with 880 mW. The light was coupled out from the cavity through the r = -75mm HR mirrors (T = 50 % @ 640 nm) in two diverging beams each containing approximately 25 % of the total power. The remaining light was lost through Fresnel reflections at the surface of the βBBO (~20 %) and transmission loss (~30 %) at two other HR mirrors. To couple the majority of the output into only two beams a dualband mirror coating centred at the signal wavelength and with T > 90 % at the second harmonic could be obtained. The strongest output beams were in the fundamental transverse mode with no signs of scattering in the βBBO crystal and were easily collimated using a 10 cm-focal-length lens. One beam was used as the input to an autocorrelator constructed using a 500-μm-thick crystal of βBBO and a UV-visible photomultiplier tube. In the absence of dispersion compensation the pulses were measured to have durations of

approximately 250 fs and the time-bandwidth product of ≈ 2.7 indicates the presence of substantial chirp. A typical interferometric autocorrelation and spectrum of the second harmonic output from the uncompensated OPO are reproduced in Figure 5.13.

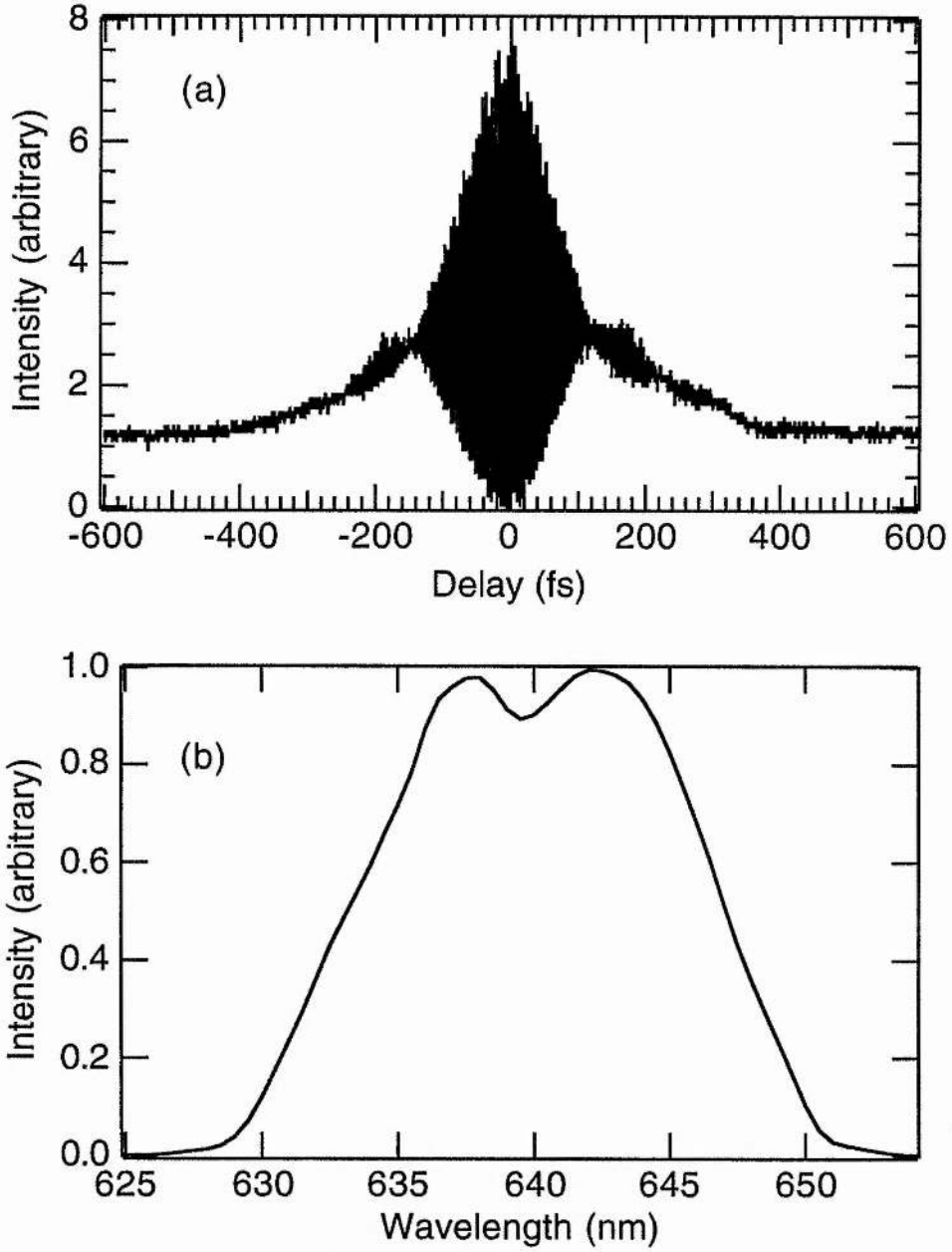

Figure 5.13 Interferometric autocorrelation profile (a) and corresponding spectral data (b) for the output second harmonic pulses from the OPO operated without dispersion compensation.

Inserting the 2.5 % signal output coupler allowed measurement of the fundamental signal pulse. The signal pulse was measured to have a duration of 390 fs and the corresponding pulse duration of the second harmonic was 265 fs. This signal pulse duration is shorter than that measured from the RTA OPO without the intracavity doubling arrangement because that configuration exhibited a threshold many times lower than the doubled OPO and pump depletion therefore contributes significantly to broadening the signal pulse.

With 1.1 W of pump power 100 mW was measured at 1.3 μm through the output coupler and simultaneously a total second harmonic power of 60 mW was produced. This corresponded to a single-pass conversion efficiency to the second harmonic of 0.75 %.

Dispersion compensation was necessary to reduce the output pulse durations of the second-harmonic and to remove chirp present on the pulses due to group velocity dispersion (GVD) and self-phase-modulation (SPM). Intracavity dispersion compensation was included by inserting a pair of SF14 glass prisms (apex separation 29 cm) into the OPO. Optimising the amount of intracavity glass resulted in the production of chirp-free second harmonic pulses as short as 59 fs and illustrated by the interferometric autocorrelation and corresponding spectrum contained in Fig. 5.14. The time-bandwidth product of 0.34 implies that the pulses are very close to the transform limit if a $\mathrm{sech}^2(t)$ intensity profile is assumed.

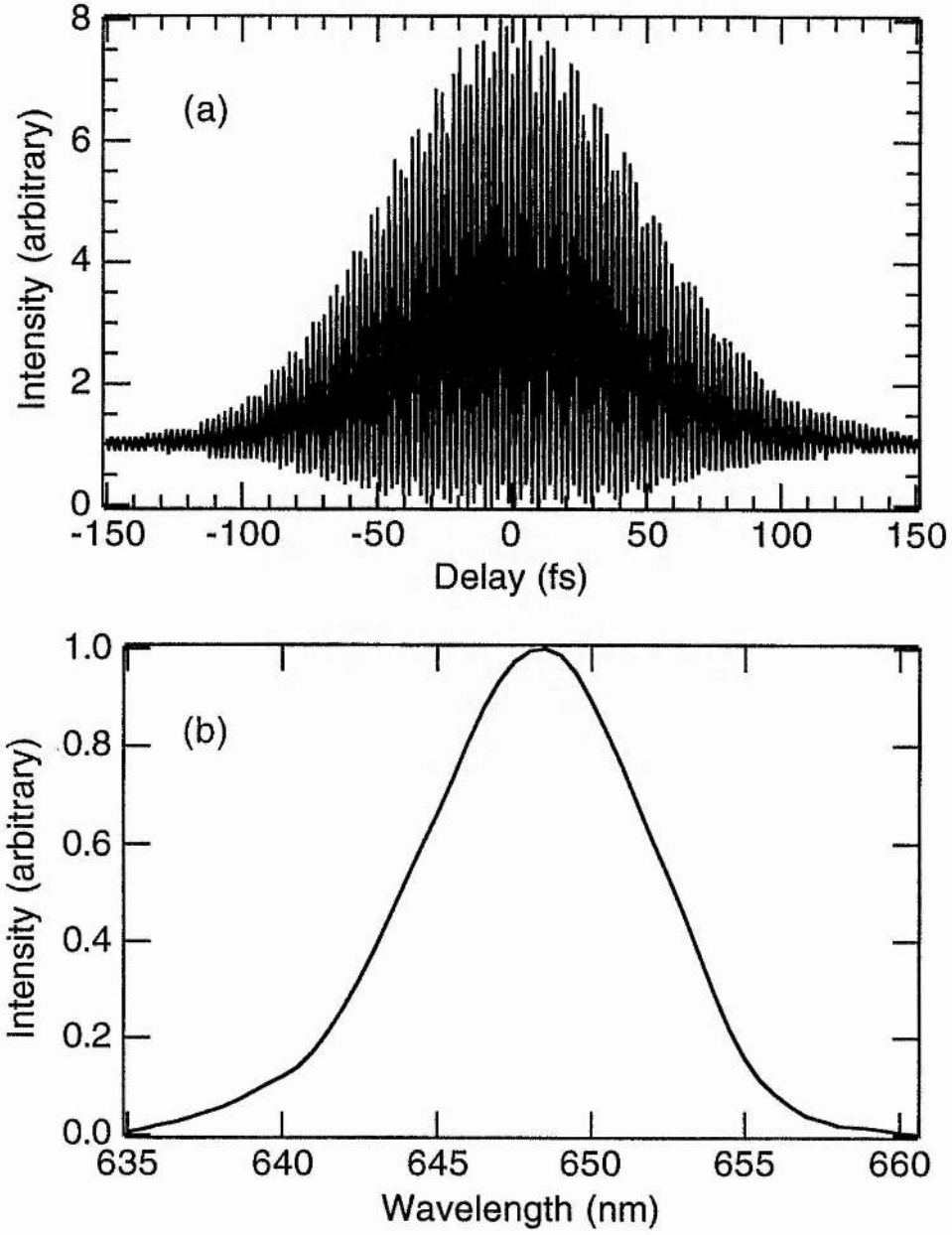

Figure 5.14 Interferometric autocorrelation (a) and spectrum (b) for the second harmonic output pulses from the dispersion-compensated OPO.

For a pump power of 1.1 W a total output power in the second harmonic of 170 mW was measured with over 40 mW in each of the strongest beams. The inclusion of the 2.5 % output coupler reduced the total second harmonic output to 135 mW while 55 mW of fundamental was coupled out of the cavity. The corresponding average intracavity

power was 2.2 W and implies a single pass conversion efficiency from the fundamental to the second harmonic of 3.1 % which is significantly higher than that measured in an intracavity-doubled KTP-based OPO [21]. The total amount of power coupled from the dispersion-compensated OPO either with HR mirrors or an output coupler was between 260 - 290 mW which represents a total extraction efficiency approaching 27 %. The photograph displayed as Figure 5.15 shows the dispersion-compensated intracavity-doubled RTA oscillator in operation and illustrates the amount of power contained in the visible output.

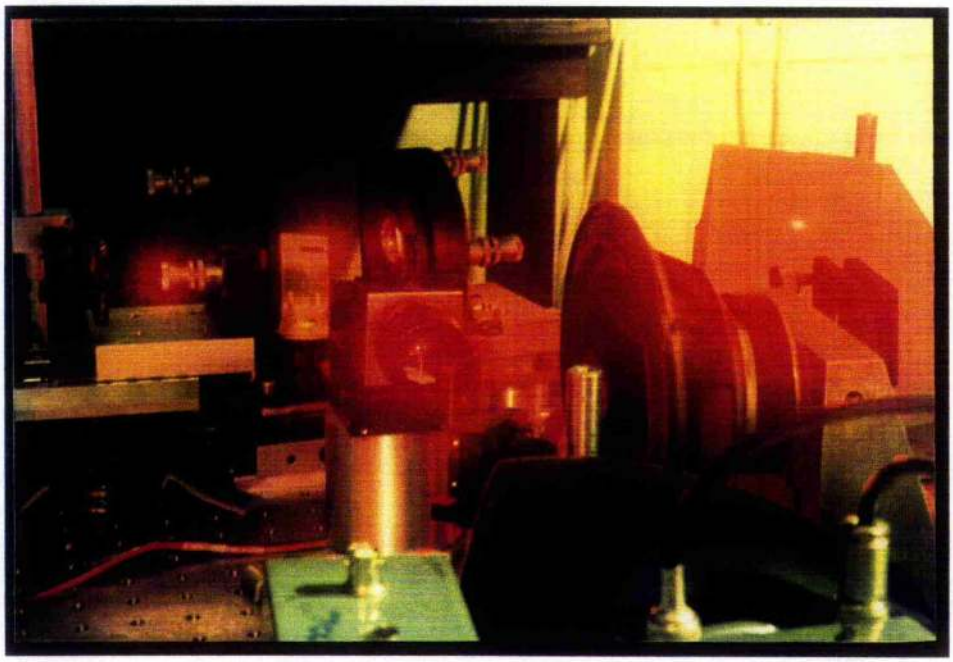

Figure 5.15 The intracavity-doubled RTA OPO in operation

When the OPO is optimally output coupled, the maximum available power (after signal output coupling) will be converted into the second-harmonic. The results presented above suggest a total signal output coupling of ≈ 8 % when losses through the output coupler and in the second-harmonic are considered. If a comparison is made with the

optimum coupling of a laser resonator [25], then the single-pass gain is given by,

$$g_o = \frac{(T_{opt} + L_i)^2}{L_i}, \tag{4}$$

where T_{opt} is the optimum output coupler transmission and L_i is the fractional resonator loss per roundtrip. The fractional losses for the OPO cavity can be estimated to be output coupling + 1 % = 3.5 % total. This implies a single-pass gain for the RTA crystal of 38 %. A similar calculation based on the results reported from an intracavity-doubled OPO using a 1.5-mm-thick KTP crystal [21] gives a single-pass gain of only 10 %. These figures are consistent with the threshold powers measured for the KTP and RTA oscillators and they clearly show the advantages of the RTA crystal.

Pump tuning of the frequency-doubled RTA OPO

Tuning of the OPO was achieved by varying the wavelength of the Ti:sapphire pump laser. Using only pump tuning, the fundamental output tuned from 1240 - 1320 nm and the second harmonic from 620 - 660 nm for Ti:sapphire pump wavelengths covering 780 - 880 nm. Experimental data are given in Fig. 5.16 together with theoretical curves derived from Sellemeier equations for RTA [6]. The only adjustment required between each measurement was a change in cavity length to maintain the OPO in synchronism with the pump laser. Oscillation occurred over a cavity-length tolerance of approximately 1.0 μm although optimum stability was observed within a smaller range of a few hundred nanometres. Altering the cavity length induced a corresponding change in the wavelength of the signal which modified the group transit time through the cavity elements and maintained synchronism with the pump laser. Tuning of

10 nm in the second harmonic and 20 nm in the fundamental was easily achieved by cavity length tuning alone. When pumped sufficiently above threshold the OPO was very stable with operation over several hours possible without requiring any change in cavity length.

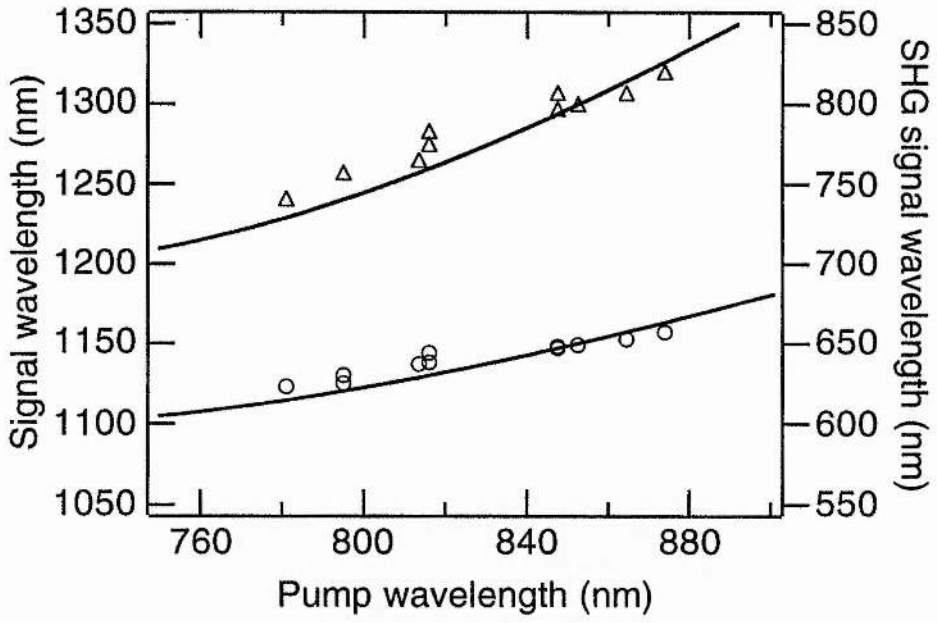

Figure 5.16 Experimental signal wavelength data (triangles) and second harmonic data (circles) for Ti:sapphire pump wavelengths from 780 - 880 nm. The solid lines indicate the tuning predicted from RTA Sellemeier data taken from ref. [6].

Amplitude noise measurements

Amplitude noise was measured for the Ti:sapphire pump laser and the second harmonic output of the OPO operated with and without dispersion compensation. The outputs of the pump laser and the OPO were measured separately using fast photodiodes and a slow-timebase oscilloscope. The oscillograms shown in Figure 5.16 were recorded with a sweep time of 0.1 s. The pump amplitude fluctuations (Figure 5.16a) are less than 1 % while the dispersion-compensated OPO (Figure 5.16b) shows approximately 5 % variations in intensity. Without the spectral control

introduced by the prism sequence the output of the uncompensated OPO (Figure 5.16c) is noisy showing intensity fluctuations of approximately 10 %.

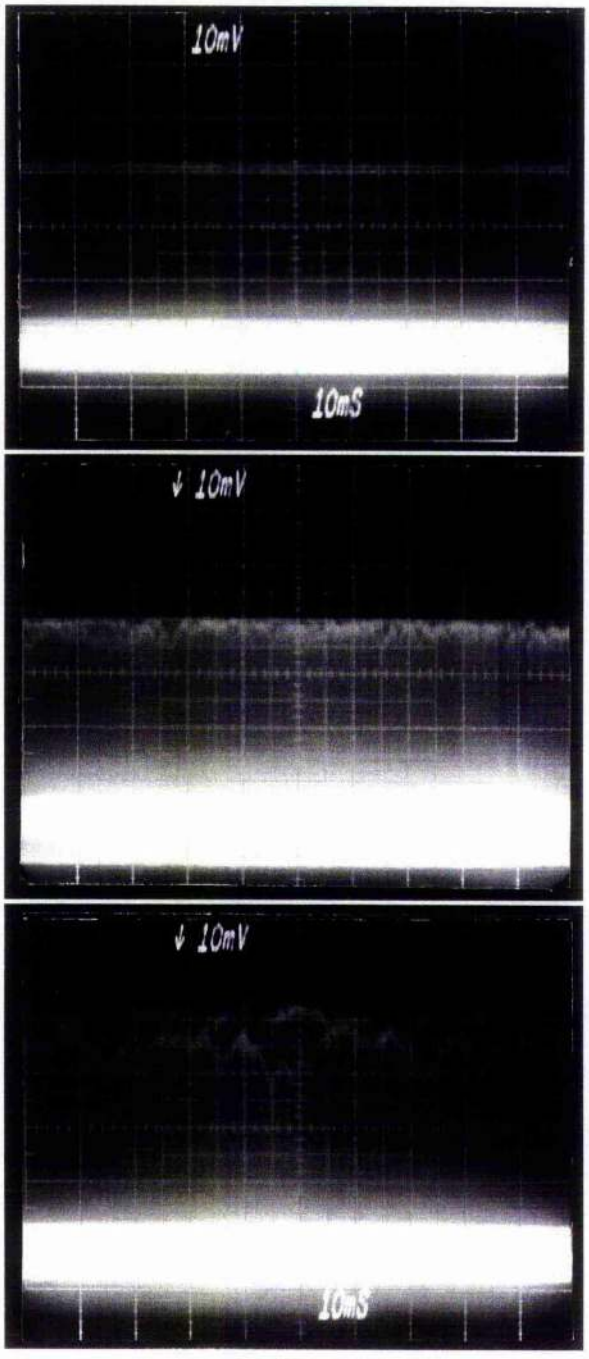

Figure 5.16 Oscillograms showing intensity fluctuations on the output of the Ti:sapphire pump laser (a) and on the second harmonic output of the OPO operated with (b) and without (c) dispersion compensation.

5.4 Conclusions

The high conversion efficiency of the intracavity-doubled RTA parametric oscillator together with its large potential tuning range make it an attractive method of producing tunable femtosecond pulses in both the visible and the infrared. The superior gain of RTA and direct access to the 1.3 μm wavelength in a non-critical phase-matching geometry offer clear advantages over KTP. With angle or pump tuning, the 1.5 μm region can also be reached and it is likely that the efficient operation achieved at 1.3 μm will be possible at longer wavelengths as well.

The visible and infrared output of the RTA and KTP oscillators described in this and the previous chapters complement the wavelengths available from the self-modelocked Ti:sapphire laser. Efficient and continuous wavelength coverage of femtosecond pulses from the visible to the infrared remains an important objective and the future of this work will rely on new nonlinear materials such as RTA which demonstrate high efficiency in optical parametric oscillator applications. Comparison of the peformance of the RTA and KTP oscillators shows that RTA is the preferable crystal for femtosecond parametric devices operating in the 1.0 - 1.5 μm spectral region.

Generation of ultrashort pulses in the visible was shown to be particularly efficient when an intracavity-doubling configuration was included in the RTA oscillator. The alternative approach to pulse generation in this region uses the fundamental output of a parametric oscillator pumped by the second-harmonic of a Ti:sapphire laser. Even with a powerful Ti:sapphire fundamental laser output of around 2 W, the second-harmonic pump light can only be produced with an efficiency of,

at best, 50 % and this has severe implications for the efficiency of the OPO system as a whole. Consequently, intracavity-doubled systems are always likely to be more efficient sources of visible pulses.

The concluding chapter in this thesis presents a discussion of possible research directions which may lead to parametric devices capable of generating femtosecond pulses throughout the visible and mid-infrared.

References

1. J. D. Bierlein and H. Vanherzeele, Appl. Phys. Lett. **54**, 783 (1989)

2. G. M. Loiacono, D. N. Loiacono, J. J. Zola, R. A. Stolzenberger, T. McGee and R. G. Norwood, Appl. Phys. Lett. **61**, 895 (1992)

3. G. M. Loiacono, D. N. Loiacono and R. A. Stolzenberger, J. Crys. Growth **131**, 323 (1993)

4. J. Y. Wang, Y. G. Liu, J. Q. Wei, L. P. Shi, and M. Wang, Z. Krist **191**, 231 (1990)

5. J. Han, Y. Liu, M. Wang and D. Nie, J. Crys. Growth **128**, 864 (1993)

6. L.-T. Cheng, L. K. Cheng and J. D. Bierlein, SPIE Proceedings, OE LASE Los Angeles (February 1993)

7. L. K. Cheng, L. T. Cheng, J. D. Bierlein and J. Parise, Appl. Phys. Lett. **64**, 1321 (1994)

8. R. A. Stolzenberger, D. N. Loiacono, J. Rottenberg, Paper CFF2 in: Conference on Lasers and Electro-Optics **8**, 415 (1994)

9. Preliminary data-sheet: "Potassium Titanyl Arsenates" from Crystal Associates, Inc., 15 Industrial Park, Waldwick, New Jersey 07463

10. K. Kato, IEEE J. Quant. Electron. **27**, 1137 (1991)

11. R. C. Eckardt, H. Masuda, Y. X. Fan and R. L. Byer, IEEE J. Quant. Electron. **26**, 922 (1990)

12. D. A. Roberts, IEEE J. Quant. Electron **28**, 2057 (1992)

13. *Crystal Associates, Inc.*, 15 Industrial Park, Waldwick, New Jersey 07463

14. D. C. Edelstein, E. S. Wachman and C. L. Tang, Appl. Phys. Lett. **54**, 1728 (1989)

15. P. E. Powers, S. Ramakrishna, C. L. Tang and L. K. Cheng, Opt. Lett. **18**, 1171 (1993)

16. P. E. Powers, C. L. Tang and L. K. Cheng, Opt. Lett. **19**, 37 (1994)

17. P. E. Powers, C. L. Tang and L. K. Cheng, Paper CWM4 in: Conference on Lasers and Electro-Optics **8**, 251 (1994)

18. R. L. Fork, B. I. Greene and C. V. Shank, Appl. Phys. Lett. **38**, 671 (1981)

19. D. E. Spence, P. N. Kean and W. Sibbett, Opt. Lett. **16**, 42 (1991)

20. R. J. Ellingson and C. L. Tang, Opt. Lett. **17**, 343 (1992)

21. R. J. Ellingson and C. L. Tang, Opt. Lett. **18**, 438 (1993)

22. T. J. Driscoll, G. M. Gale and F. Hache, Opt. Comm. **110**, 638 (1994)

References continued,

23. D. C. Edelstein, E. S. Wachman, L. K. Cheng, W. R. Bosenberg and C. L. Tang, Appl. Phys. Lett. **52**, 2211 (1988)

24. G. D. Boyd and D. A. Kleinman, J. Appl. Physics **39**, 3597 (1968)

25. A. Yariv, *Quantum Electronics*, Third Edition, ISBN 0-471-60997-8, p 195 (1988)

6.1 Review

The work presented in this thesis has described the operation, design and configuration of femtosecond optical parametric oscillators based on the materials $KTiOPO_4$ (KTP) and $RbTiOAsO_4$ (RTA) and pumped using a self-modelocked Ti:sapphire laser. By way of introduction, a review of the various conventional modelocked lasers producing femtosecond pulses in the visible and infrared has been presented. This was accompanied by a retrospective of the development of the singly-resonant femtosecond parametric oscillator from earlier Q-switched and doubly-resonant systems.

In Chapter 2, the performance, configuration and design of the self-modelocked Ti:sapphire laser used as the pump source for the optical parametric oscillators was described. In typical operation this laser produced a useful average power output of over 1 W in the form of 85-fs pulses completely free of any background cw-component or multiple pulsing effects. Continuous tuning of the laser from 780 - 880 nm was demonstrated and was only limited by the mirror set available. In an effort to formulate a reproducible alignment technique for the self-modelocked laser, an experimental investigation of the importance of the pump-induced thermal lens in the Ti:sapphire gain medium was carried out. A general alignment procedure resulting from this has been described which successfully optimised the modelocking performance of the laser at any pump power.

The factors critical to the design of a femtosecond optical parametric oscillator were discussed in Chapter 3 and implications of linear and nonlinear pulse-propagation effects were considered in depth. The calculations necessary to determine the choice of an appropriate nonlinear crystal were illustrated and pulse-shaping phenomena unique to femtosecond parametric oscillators were introduced.

The application of these principles in the construction and operation of a KTP-based optical parametric oscillator constituted the subject matter of Chapter 4. The experimental configuration of the oscillator was described both with and without intracavity dispersion compensation and a discussion of the alignment procedures and the choice of resonator optics was included. Optimum performance was achieved for pump and signal focused beam waists of ≈ 18 μm corresponding to average powers of up to 150 mW in the signal and of approximately 50 mW in the idler. The oscillation threshold of the basic oscillator was 230 mW and increased to approximately 300 mW with the addition of intracavity dispersion-compensating prisms. Without dispersion compensation, chirped signal output pulses were produced which had a duration-bandwidth product of ≈ 5. A numerical investigation showed that self-phase-modulation in the KTP crystal was most probably responsible for this chirp and implied a total phase shift across the pulse of as much as 5π radians. With extracavity compensation sufficient chirp was removed to produce pulses with durations of 90 fs although these pulses still did not approach the Fourier transform-limit.

The inclusion of intracavity dispersion compensation allowed 39-fs-duration pulses to be generated with average powers of up to 50 mW. This result, which we believe represents the shortest transform-limited pulses

to be reported from a femtosecond parametric oscillator, provided experimental evidence that pulses with durations much shorter than the pump pulse can be produced by this kind of parametric device. Tuning of the oscillator was achieved by tuning the pump laser wavelength and coverage from 1.12 - 1.25 μm in the signal wave and 2.5 - 3.0 μm in the idler was demonstrated. Cavity-length tuning was also observed and varied the centre-wavelength of the signal by up to 40 nm. Additional weak non-phasematched processes generated several visible outputs at 400 nm, 415 nm, 490 nm, 600 nm and 635 nm.

The stability of the system was investigated by measurements of the phase and amplitude noise of the signal output. Amplitude noise figures of 1 %, 4 % and 10 % were recorded for the pump and the dispersion-compensated and uncompensated outputs respectively. Phase-noise results from the dispersion-compensated oscillator were consistently better than the pump laser but without compensation the phase-noise was significantly higher. Although the improvement in phase noise shown by the compensated OPO can be understood qualitatively in the manner described in Chapter 2, a formal treatment of timing jitter in a synchronously-pumped oscillator (with or without gain storage) would be needed to give a more thorough understanding of this result.

Reduced-threshold operation of the system was obtained by feeding back the idler pulse in synchronism with the signal. Threshold reductions and output power increases of around 10 % were achieved but further improvement was limited by pulse group-velocity walkaway in the crystal. The attempt to operate a femtosecond parametric oscillator in a doubly-resonant configuration was always recognised to belong to the category of the "high-risk, high-dividend" experiment. The potential

rewards of a truly doubly-resonant system are sufficient to encourage a subsequent effort using thinner, higher-gain crystals or materials with more favourable walkaway parameters.

The behaviour of the system in the presence of variable positive group-velocity dispersion was studied and results indicating simultaneous solitonic and dispersive wave formation were obtained. The typical soliton period corresponded to ≈ 40 cavity roundtrips and this and other measurements were in good agreement with theory. The wide spectral bandwidth (≈ 200 nm) which accompanied solitonic behaviour may be useful in generating wavelengths inaccessible to pump or angle tuning.

In Chapter 5 the operation of a femtosecond optical parametric oscillator based on RTA was detailed. This oscillator was capable of low-threshold operation for pump powers as low as 50 mW and achieved conversion efficiencies exceeding 30 %. Without dispersion-compensation signal output pulses with durations of ≈ 1 ps and powers of 185 mW and ≈ 100 mW were generated in the signal and idler outputs respectively. The dispersion-compensated oscillator produced 100 mW in the signal output in the form of pulses with durations as short as 66 fs. Pump tuning was demonstrated from 1230 - 1340 nm in the signal from 2100 - 2430 nm in the idler.

The excellent performance demonstrated by the RTA-based device challenges the position of KTP as the "material of choice" for tunable femtosecond parametric pulse generation. This was further underlined by the impressive results from the intracavity frequency-doubled RTA-based oscillator. With the simple addition of a 200-μm-thick β-BBO crystal, transform-limited pulses tunable in the visible from 620 - 660 nm were

generated. Powers of up to 170 mW in the red were produced and total efficiencies of approximately 28 % were obtained. The output showed intensity fluctuations of around 5 % for a pump noise of approximately 1 %. Single-pass gain calculations derived from these frequency-doubling results and oscillation threshold measurements provide a strong indication that RTA has a larger nonlinear gain than KTP when used in a femtosecond optical parametric oscillator.

6.2 Future work

The versatility of the femtosecond optical parametric oscillator makes it an ideal system for simultaneously generating a number of synchronised pulse sequences at different wavelengths. By using intracavity and extracavity nonlinear frequency-conversion techniques, a range of femtosecond pulse sequences from the ultraviolet to the mid-infrared can be generated by one oscillator. The repetition frequency of each of the pulse sequences is identical and the timing-jitter is correspondingly low. The attractions of such a system in, for example, pump-probe applications are therefore clear and similar devices can be expected to find increasing uses as femtosecond parametric oscillators become more widespread. In this final section, the extensions of the wavelength coverage of the femtosecond optical parametric oscillator to the visible and to the mid-infrared will be discussed and the possibility of an all-solid-state femtosecond optical parametric oscillator is considered.

Femtosecond pulse generation in the 500 - 700 nm region

The wavelength coverage of the fundamental output of the Ti:sapphire laser (700 - 1000 nm) and its second-harmonic (350 -500 nm) leaves a wide spectral window in the visible from 500 - 700 nm which cannot be easily

accessed by conventional lasers. Dye lasers are capable of restricted tuning in this region but only at low average power. One possible method of efficiently generating visible pulses in this wavelength band is to use an intracavity sum-frequency-mixing scheme in a femtosecond optical parametric oscillator as illustrated in Figure 6.1.

The RTA-based system described in the previous chapter offers useful phasematching wavelengths for this proposal. With pump tuning from 700 - 1000 nm the pump-signal mixing wavelength would produce visible light from 442 - 602 nm. A similar device using CTA would generate wavelengths from 483 - 649 nm. The results of the frequency-doubling of the RTA oscillator suggest that between 20 - 30 mW of visible light could be produced with this method.

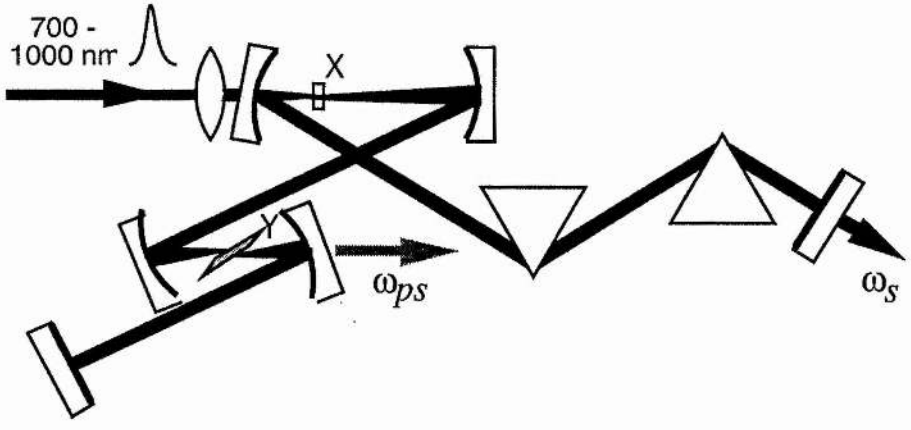

Figure 6.1 Cavity schematic of the proposed intracavity pump signal sum-frequency-mixing scheme. OPO crystal, X; mixing crystal, Y.

Femtosecond pulse generation in the 5 - 10 μm region

Difference-frequency mixing between the signal and idler outputs of a femtosecond optical parametric oscillator can produce widely tunable output in the mid-infrared if the signal and idler wavelengths are correctly chosen. Angle (or temperature) tuning allows the pump wavelength to

remain fixed and generally provides more rapid variation in the difference-frequency wave than pump wavelength tuning. For example, a typical CTA-based system would require an internal angle variation of only ≈ 5° for the signal-idler difference wave to tune from 5 - 10 μm. An intracavity mixing scheme similar to the arrangement depicted in Figure 6.1 would provide the best efficiency and average infrared powers of around 1 mW should be achievable. An intracavity scheme also has the advantage that the signal and idler pulses are already synchronised and do not need to be phased using individual optical delay lines.

All-solid-state femtosecond optical parametric oscillator

The low-threshold operation of the RTA-based system brings closer the reality of a completely solid-state widely-tunable infrared femtosecond source. Self-modelocked vibronic oscillators pumped either directly by high-brightness laser-diodes or by mini-lasers, although currently capable of producing only a few tens of mW, can be expected, before too long, to deliver output powers exceeding 100 mW. Coupled with a low-threshold parametric oscillator, these lasers constitute will solid-state femtosecond sources tunable over wide spectral regions in the visible and infrared. By this time, such lasers may perhaps have become as widespread as the ubiquitous Argon-ion laser.

Clearly the technology of femtosecond optical parametric oscillators is still in its infancy. New nonlinear materials offering low-threshold operation and varied tunability will continue to extend efficient femtosecond pulse generation to spectral regions otherwise difficult to access using conventional lasers.

Journal Publications

Characteristics of a noncritically phasematched Ti:sapphire pumped femtosecond optical parametric oscillator

J. M. Dudley, D. T. Reid, M. Ebrahimzadeh and W. Sibbett

Optics Communications **104**, pp 419 - 430 (1994)

Ti:sapphire pumped femtosecond optical parametric oscillator exhibiting soliton formation

D. T. Reid, J. M. Dudley, M. Ebrahimzadeh and W. Sibbett

Journal of Modern Optics **41**, pp 1231 - 1242 (1994)

Soliton formation in a femtosecond optical parametric oscillator

D. T. Reid, J. M. Dudley, M. Ebrahimzadeh and W. Sibbett

Optics Letters **19**, pp 825 - 827 (1994)

Non-critically phase-matched Ti:sapphire-pumped femtosecond optical parametric oscillator using $RbTiOAsO_4$

D. T. Reid, M. Ebrahimzadeh and W. Sibbett

Optics Letters **20** (1995)

Ti:sapphire-pumped femtosecond optical parametric oscillators based on $KTiOPO_4$ and $RTiOAsO_4$

D. T. Reid, M. Ebrahimzadeh and W. Sibbett

Applied Physics B. accepted (1995)

Efficient femtosecond pulse generation in the visible in a frequency doubled optical parametric oscillator based on $RbTiOAsO_4$

D. T. Reid, M. Ebrahimzadeh and W. Sibbett

Journal of the Optical Society of America B., submitted (1995)

Conference Publications

Noncritically phase-matched Ti:sapphire-pumped femtosecond optical parametric oscillator

D. T. Reid, J. M. Dudley, M. Ebrahimzadeh and W. Sibbett

Paper UPFr3 in: *European Quantum Electronics Conference '93*, **1**, pp 399 - 402 (1993)

Noncritically phase-matched Ti:sapphire-pumped femtosecond optical parametric oscillator

D. T. Reid, M. Ebrahimzadeh, J. M. Dudley and W. Sibbett

Paper 107 in: *Eleventh UK National Quantum Electronics Conference*, QE-11 (1993)

Noncritically phase-matched Ti:sapphire-pumped femtosecond optical parametric oscillator

M. Ebrahimzadeh, D. T. Reid, J. M. Dudley and W. Sibbett

International Symposium on Ultrafast Processes in Spectroscopy, Vilnius (1993)

Continuous-wave and femtosecond optical parametric oscillators of LBO and KTP pumped by tunable Ti:sapphire lasers

M. Ebrahimzadeh, D. T. Reid, F. G. Colville, W. Sibbett and M. H. Dunn

Institute of Physics Annual Congress pp 148 - 149 (1994)

Sub-40 fs pulse generation in a KTP-based optical parametric oscillator

D. T. Reid, J. M. Dudley, M. Ebrahimzadeh and W. Sibbett

Paper WC24 in: *Ultrafast Phenomena* **7**, pp 400 - 402 (1994)

Soliton formation in a femtosecond optical parametric oscillator

D. T. Reid, J. M. Dudley, M. Ebrahimzadeh and W. Sibbett

Paper CThI11 in: *Conference on lasers and Electro-Optics* **8**, pp 325 - 326 (1994)

Non-critically phase-matched Ti:sapphire-pumped optical parametric oscillator using $RbTiOAsO_4$.

D. T. Reid, M. Ebrahimzadeh and W. Sibbett

Postdeadline paper CPD 1.3 in: *European Conference on Lasers and Electro-Optics* (1994)

Acknowledgements

Special thanks are due to Professor Wilson Sibbett for his buoyant encouragement and supervision throughout the duration of the work presented in this thesis.

I am indebted to Dr John Dudley for his invaluable contributions to the early work on the femtosecond OPO and to Dr Majid Ebrahimzadeh for numerous helpful discussions and for heroic proof-reading of *Chapter 3* in this thesis.

A mention is also deserved by all the members of the *W-Squad* for cheerful assistance in and out of the lab, and to Emma - thanks for all the muffins.

Much of the hardware employed in the laboratory apparatus could not have been made to the necessary precision without the assistance of the members of the departmental technical workshop who deserve particular thanks for their many contributions. I am also grateful to Reg Gavine and Andy Barman for their patient tuition and supervision in the student machine workshop.

Financial support for the duration of this project was provided by the U. K. Engineering and Physical Sciences Research Council (EPSRC) to whom I am grateful for their sponsorship.

REPRINTED FROM:

OPTICS COMMUNICATIONS

Optics Communications 104 (1994) 419–430
North-Holland

Full length article

Characteristics of a noncritically phasematched Ti:sapphire pumped femtosecond optical parametric oscillator

J.M. Dudley, D.T. Reid, M. Ebrahimzadeh and W. Sibbett
J.F. Allen Research Laboratories, Department of Physics and Astronomy, University of St Andrews, St Andrews, Fife KY169SS Scotland, UK

Received 22 June 1993

NORTH-HOLLAND
AMSTERDAM – LONDON – NEW YORK – TOKYO

For 1994, volumes 103–111 (54 issues) have been announced. The subscription price for these volumes is available upon request from the publisher.

Subscriptions should be sent to the publisher, Elsevier Science B.V., Journals Department, P.O. Box 211, Amsterdam, The Netherlands, or to any subscription agent or bookseller. Claims for issues not received should be made within six months of publication. If not, they cannot be honoured free of charge.

US mailing notice - Optics Communications (ISSN 0030-4018) is published semi-monthly in 1994 by Elsevier Science (Molenwerf 1, 1000 AE Amsterdam, The Netherlands). The annual subscription price in the USA is US$ 2121.00 (valid in North, Central and South America only), including air speed delivery. Second class postage paid at Jamaica, NY 11431.

USA Postmasters: Send address changes to: Optics Communications Expediting, Inc., 200 Meacham Avenue, Elmont, NY 11003. Airfreight and mailing in the USA by Publication Expediting.

Published semi-monthly

Printed in The Netherlands

Optics Communications 104 (1994) 419–430
North-Holland

OPTICS
COMMUNICATIONS

Full length article

Characteristics of a noncritically phasematched Ti:sapphire pumped femtosecond optical parametric oscillator

J.M. Dudley, D.T. Reid, M. Ebrahimzadeh and W. Sibbett

J.F. Allen Research Laboratories, Department of Physics and Astronomy, University of St Andrews, St Andrews, Fife KY169SS Scotland, UK

Received 22 June 1993

The operating characteristics of a singly-resonant femtosecond optical parametric oscillator (OPO) based on a noncritically phasematched geometry in KTP are described. The parametric oscillator is synchronously pumped by a self-modelocked Ti:sapphire laser and is operated in a standing-wave cavity configuration. With extracavity dispersion compensation, chirped pulses of 90 fs are generated, whilst shorter transform-limited pulses of 40 fs are generated with intracavity dispersion compensation. A numerical model of the effects of self-phase-modulation in the OPO has been developed and gives results which are in good qualitative agreement with experiment. Experimental results are presented relating to non-phasematched processes in the OPO, and the implications for the development of a tunable femtosecond source in the blue spectral region are discussed. A characterisation of the amplitude and phase noise of the OPO has also been performed, and provides insight into the important physical processes governing the stability of OPO operation.

1. Introduction

The emergence of passive nonlinear modelocking techniques has had enormous impact on femtosecond laser technology and has opened the way for development of a new generation of ultrafast laser sources based on this concept [1]. Broadband solid-state gain media, most notably titanium-doped sapphire in a self-modelocked laser configuration, can now routinely provide pulses having durations less than 100 fs over an attractively wide tuning range in the near-infrared. Many applications, however, require tunable ultrashort pulses in regions of the optical spectrum not directly accessible by conventional modelocked lasers. The synchronously pumped optical parametric oscillator (OPO) has long been recognised as a complementary technique for the generation of tunable ultrashort pulses over extended spectral regions [2]. While material difficulties and a lack of suitable pump sources have hampered the development of parametric devices for many years, the recent emergence of novel nonlinear crystals and improved modelocked laser sources has renewed interest in OPO's as practical ultrafast optical sources. In particular, the recent development of OPO's pumped by self-modelocked Ti:sapphire lasers has resulted in the generation of high power femtosecond pulses having extended tunability in the near- and mid-infrared spectral regions. The first such femtosecond parametric oscillators reported were based on a critically phasematched geometry in KTP with a non-collinear pumping configuration. Pulses as short as 62 fs have been generated from a femtosecond OPO using extracavity dispersion compensation [3], while a similar cavity configuration using intracavity dispersion compensation has generated pulses as short as 57 fs [4]. More recent results have included a femtosecond parametric oscillator using KTP in a non-critical phasematching geometry [5], femtosecond OPO's based on other nonlinear materials KTA [6] and LBO [7] and a femtosecond OPO with intracavity second harmonic generation [8].

In this paper we report a detailed study of a singly-resonant Ti:sapphire-pumped femtosecond OPO based on KTP in a noncritically phasematched geometry, similar to that previously reported in reference [5]. The operation of the OPO has been stud-

ied in cavity configurations with and without dispersion compensation, and the output pulse characteristics, including measurements of the pulse autocorrelation and spectrum will be presented. Measurements of the OPO amplitude and phase noise characteristics in these different configurations have also been made and provide some additional insights into the physical processes that are especially relevant to femtosecond optical parametric oscillators. As well as studying the features of the resonant signal pulse, we have investigated in some detail a number of non-phase matched processes in the OPO and we consider their applicability in the generation of femtosecond pulses from the OPO in the visible as well as in the near- and mid-infrared spectral regions.

2. Experimental design

The pump source for the OPO is a regeneratively initiated, self-modelocked Ti:sapphire laser similar to that described in ref. [9], with dispersion compensation provided by a sequence of four intracavity prisms. The laser routinely delivers 1 W of average mode-locked power at 830 nm in sub-100 fs pulses at a repetition rate of 84.5 MHz. Figure 1 shows a typical interferometric autocorrelation and spectrum from the pump laser. The pulse duration deduced from the corresponding intensity autocorrelation (assuming a sech^2 pulse profile) is 90 fs and the spectral width is 8.5 nm. The corresponding duration–bandwidth product of 0.32 indicates that the pulses are close to the transform limit. The experimental OPO configurations that have been studied are shown in fig. 2. Figure 2a shows the OPO in its simplest form as a standing-wave, three-mirror, folded cavity formed by two concave high reflectors ($r=10$ cm) and a plane output coupler located on a precision translation stage for cavity length adjustment. The fold angle of the cavity is kept small (less than 1 degree) to eliminate the need for astigmatic compensation. The 1.5 mm long KTP crystal is positioned at the focus of the OPO resonator, and the pump laser beam is focused with a 7 cm focal length lens to a 15 μm spot radius inside the crystal through one of the concave mirrors. The OPO is collinearly pumped and the pump beam makes a single

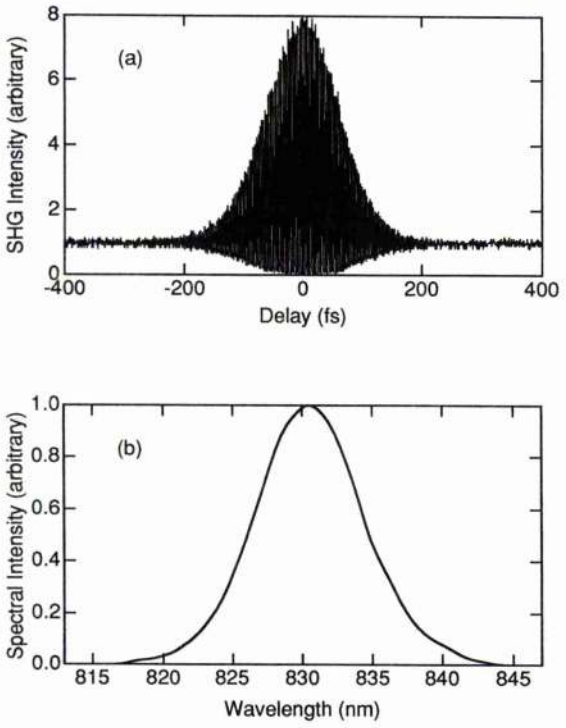

Fig. 1. Interferometric autocorrelation (a) and spectrum (b) of transform-limited pulses from the self-modelocked Ti:sapphire pump laser.

pass through the cavity. To avoid feedback, an optical isolator and a half-wave plate are included between the pump and the OPO. The hydrothermally grown KTP crystal has an antireflection-coating centred at 1180 nm on both faces. It is cut for noncritical type II interaction (e→eo) along the x-axis and the pump and the resonated signal wave have extraordinary polarisations along the y-axis. The nonresonant idler wave has ordinary polarisation along the z-axis. Tuning of the OPO is achieved either by rotation of the KTP crystal in the xy-plane or by changing the pump wavelength. The concave mirrors are highly reflecting ($R>99.7\%$) over 1.1–1.3 μm and highly transmitting ($T>95\%$) at the pump wavelength and the output coupler is 1.5% transmitting at the signal wavelength. The OPO has also been operated with both extracavity and intracavity dispersion compensation using pairs of SF14 prisms, and these arrangements are shown in figs. 2a and 2b, respectively.

Alignment of the femtosecond OPO is made difficult by the very low levels of single-pass parametric

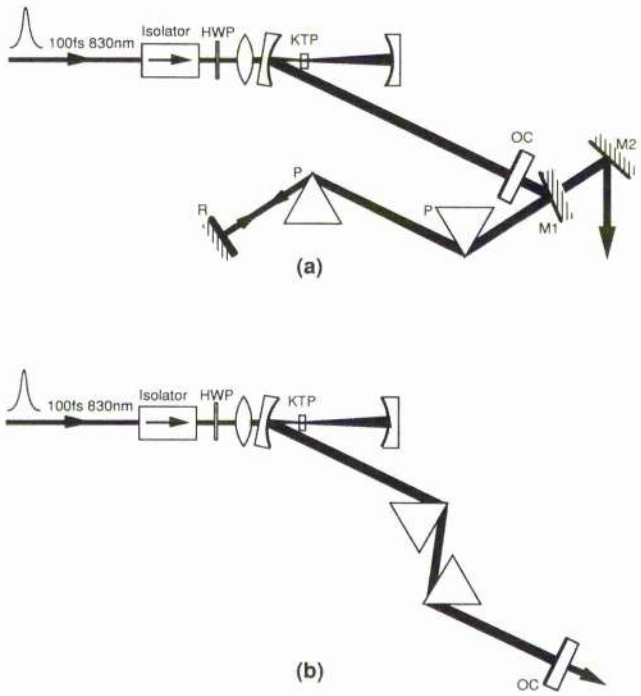

Fig. 2. Cavity configurations of the femtosecond OPO; with extracavity dispersion compensation (a) and with intracavity dispersion compensation (b).

fluorescence from the KTP crystal and the strict cavity length tolerances imposed by synchronous pumping. The previously reported technique used to align the femtosecond OPO [4] is based on the detection of the weak single pass fluorescence but requires the use of a low-noise, cooled detector. We use an alternative approach which does not require detection of parametric fluorescence but nonetheless provides a reliable technique for routine alignment. This technique exploits the collinear pumping geometry and the fact that the high peak power of the pump beam produces several mW of single pass second harmonic generation (SHG) blue light at 415 nm. The OPO (without dispersion compensation) shown in fig. 2a is aligned simply by monitoring and overlapping the reflections of the pump and the second harmonic beams from the crystal surfaces and the mirrors. Oscillation occurs when the OPO is brought into synchronism with the pump through fine cavity length adjustment. With the dispersion compensated cavity shown in fig. 2b, the alignment technique used is slightly different because the inclusion of intracavity prisms necessarily means that the pump, the single-pass second harmonic and the signal all follow different paths in the resonator. To facilitate alignment, the OPO without dispersion compensation is aligned as described above, and while oscillating, the apex of one prism is introduced into the cavity to refract some of the oscillating signal light while still allowing the OPO to be maintained above threshold. With this small amount of signal light now coupled out of the cavity, a second prism and an output coupler can be inserted and adjusted so that the signal light is retroreflected. At this stage the first prism is inserted further into the uncompensated OPO until oscillation is extinguished, and oscillation in the dispersion compensated cavity is observed when the OPO cavity is again brought into synchronism with the pump.

3. Results and discussion

Operating without dispersion compensation, the OPO oscillation threshold was measured as 300 mW of average pump power at the KTP crystal. With an increased pump power of 900 mW, the OPO output measured through the 1.5% output coupler was up to 135 mW in the signal beam, representing a signal extraction efficiency of 15%. The corresponding internal efficiency deduced from pump depletion measurements is greater than 50%. The remaining 35% of converted pump is divided among the idler, intracavity signal losses and other non-phasematched processes which will be discussed in more detail below. Because of the constraints imposed by the collimating and collecting optics, we have not yet been able to determine the total single-pass idler power extracted from the OPO cavity. From the ratio of the photon energies we expect, however, that an additional 50–100 mW is generated in the idler beam. The characteristics of the output pulses from the OPO are examined using an optical spectrum analyser and both intensity and interferometric autocorrelation techniques. The intensity autocorrelation measurement is used to measure the durations of the OPO pulses while the interferometric measurement provides information about the frequency chirp in the pulses. Results from the OPO without any dispersion compensation are shown in fig. 3. The pulse duration measured from the intensity autocorrelation reproduced in fig. 3a is 400 fs, but the shape of both

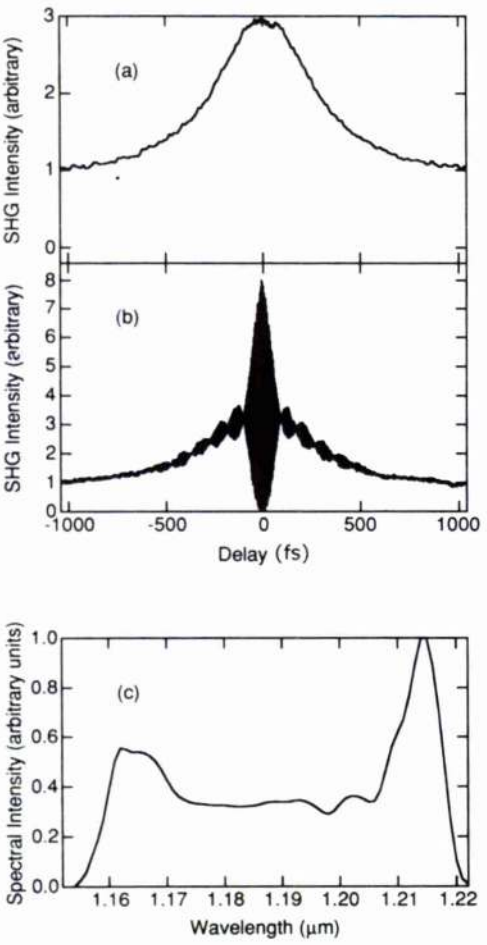

Fig. 3. Intensity (a) and interferometric (b) autocorrelation profiles and corresponding spectral data (c) for the output of the OPO without dispersion compensation.

the interferometric autocorrelation in fig. 3b and the spectrum in fig. 3c indicate that the pulses are highly chirped and the corresponding time–bandwidth product is around 5.

The chirp on these pulses arises primarily from self-phase-modulation (SPM) occurring in the focal region of the KTP crystal, and the observed pulse broadening from the pump to the signal is attributed to the combined effect of this SPM and group velocity dispersion (GVD) of the resonant signal pulse as it makes multiple passes within the OPO cavity. The temporal group velocity walkaway (GVW) between the pump pulse and the signal pulse in the KTP crystal will also contribute to this broadening effect. That significant SPM is expected in the OPO can be seen from a simple calculation of the peak nonlinear phase shift in the KTP crystal. A pulse centred at a wavelength λ and with maximum intensity I_0 propagating through a length L of material with nonlinear refractive index n_2 experiences a maximum nonlinear phase shift from SPM given by [10]

$$\phi_{\mathrm{MAX}} = \frac{2\pi}{\lambda} n_2 I_0 L \,. \tag{1}$$

With an output coupling of 1.5%, the average photon lifetime of the signal in the cavity is about 67 round trips. Taking n_2 for KTP to be 3.1×10^{-15} cm^2 W^{-1} [11], a net phase shift of π radians will be accumulated in the cavity lifetime with intracavity intensities of the order of 1 GW cm^{-2}. Typical intracavity intensities of the OPO are of the order of 10's of GW cm^{-2} so it is clear that significant SPM should be observed.

Although a detailed treatment of the effects of SPM and GVD in the OPO requires the numerical solution of the nonlinear Schrödinger equation, a simple model in which only SPM is included [12] can nonetheless be used to explain the essential features of the observed pulse characteristics. Consider a gaussian pulse with carrier frequency and intensity pulse duration (fwhm) $\Delta\tau$. The electric field amplitude is given by

$$E_0(t) = \exp(-2\ln 2 t^2/\Delta\tau^2)\exp(\mathrm{i}\omega_0 t) \,, \tag{2}$$

with corresponding intensity

$$I(t) = E_0^*(t)\, E_0(t) \,. \tag{3}$$

The effect of propagating through a material where SPM occurs is to introduce a nonlinear phase shift across the pulse so the resultant field envelope becomes

$$E(t) = E_0(t)\exp[\mathrm{i}\phi_{\mathrm{NL}}(t)] \,. \tag{4}$$

The nonlinear phase shift $\phi_{\mathrm{NL}}(t)$ is given by

$$\phi_{\mathrm{NL}}(t) = I(t)\,\phi_{\mathrm{MAX}} \,, \tag{5}$$

where the maximum phase shift ϕ_{MAX} given by eq. (1). Using this simple model, the effect of SPM on the initial pulse envelope can be calculated for a variety of different values of the maximum phase shift. It is then also possible to calculate [13] both the corresponding pulse spectrum and interferometric autocorrelation for comparison with experiment. The results of the modelling are shown in fig. 4 for a va-

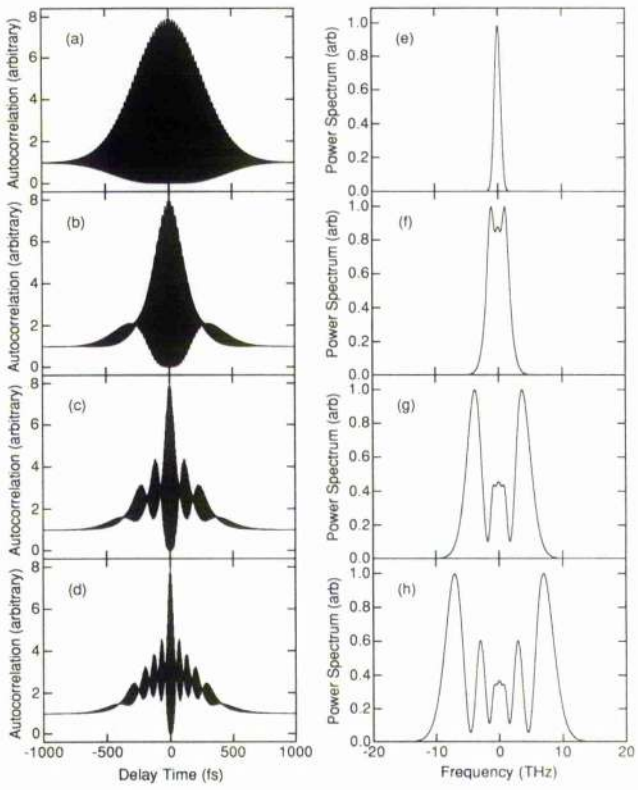

Fig. 4. Numerical results showing the effects of SPM on the interferometric autocorrelation and the spectrum of an initially unchirped gaussian pulse of fwhm 400 fs. For peak nonlinear phase shifts of 0, π, 3π and 5π, the interferometric autocorrelations are shown in (a), (b), (c) and (d), respectively, while the corresponding pulse spectra are shown in (e), (f), (g) and (h), respectively.

riety of different values of the maximum SPM phase shift using an initial gaussian pulse with intensity fwhm $\Delta\tau = 400$ fs. It is well known that the effect of SPM in the frequency domain is to introduce significant spectral broadening and the appearance of a twin-peaked structure in the power spectrum. In the time domain, although SPM on its own does not introduce any change in the shape of the pulse intensity envelope, the nonlinear phase shift on the pulse is manifested as a prominent modulation in the wings of the autocorrelation function. This modulation can be understood in physical terms as a beating between the various spectral components generated in the SPM process. It can be seen from the results of the modelling that the maximum phase shift can be estimated empirically from the number of visible minima in the interferometric autocorrelation function. For N minima, the phase shift (within a factor of $\pi/2$) is given approximately by $\phi_{MAX} \sim N\pi/2$.

Experimentally, although a prominent pedestal is observed on the OPO pulse autocorrelation at all levels of intracavity power, a strong modulation is only observed at intracavity power levels less than 20 GW cm^{-2}. This is to be expected because as the SPM phase shift increases with intracavity power, the modulation frequency will increase and be more difficult to resolve in the autocorrelation function. The results shown in fig. 3 were obtained with an estimated intracavity intensity in the KTP crystal of 5 GW cm^{-2} corresponding to a maximum phase shift, calculated using eq. (1), of $\phi_{MAX} = 16$ radians $= 5.1\pi$. This is in good agreement with the phase shift $\phi_{MAX} \sim 5\pi$ expected based on the observed number of 10 minima in the experimental autocorrelation function.

Several other features of the experimental results can be also explained with a simple qualitative consideration of the effects of SPM and GVD in the OPO cavity. The observed spectrum in fig. 3 is strongly asymmetric, unlike those predicted from the simple model, but it has been shown that asymmetric pulse spectra from SPM are generated when the propagating pulse is itself asymmetric [10]. It is possible that pump depletion in the KTP crystal will also lead to the generation of an asymmetric pulse from the OPO because the leading edge of the OPO pulse (generated by the undepleted pump) would be steeper than the trailing edge of the OPO pulse (generated by the depleted pump). The frequency shift due to SPM is known to red-shift the leading edge of the pulse and blue-shift the trailing edge and with this form of pulse asymmetry it would be expected that the pulse spectrum would contain more red-shifted components than blue-shifted components, in agreement with experimental observations. Note that the modulation of the autocorrelation function predicted by the simple SPM model is stronger than that which is experimentally observed. Furthermore, the model also predicts a deep spectral modulation which is not clearly observed in the experimental results. This loss of contrast suggests that there are additional field dephasing processes occurring in the OPO cavity, most likely arising from the effects of

GVD and GVW in the KTP crystal. It would, however, be necessary to use a more detailed model based on the nonlinear Schrödinger equation to study these effects more quantitatively.

The use of dispersion compensation external to the OPO cavity using a two-prism sequence in a double-pass configuration results in the compression of these chirped pulses, and with a separation of 90 cm between the prisms, pulses of 90 fs were obtained as shown in figs. 5a and 5b. The interferometric autocorrelation of these pulses still shows a residual pedestal, and this is attributed to uncompensated nonlinear chirp. The inability to completely compensate the chirp on the signal pulses from the OPO is a consequence of using extracavity dispersion compensation [13], which, although leading to a reduction in the pulse duration in the time domain, does not alter the shape or content of the spectrum. The temporally compressed pulses therefore still have durations well above the transform limit with a duration–bandwidth product around unity. In order to obtain transform-limited pulses it is necessary to use intracavity dispersion compensation. With an intracavity prism pair separation of 24 cm, the temporal and spectral characteristics of the output signal pulses from the OPO are reproduced in fig. 6. The duration of these pulses measured from the intensity autocorrelation in fig. 6a is 40 fs (assuming a sech^2 pulse profile), and the interferometric autocorrelation in figure 6(b) confirms that these pulses are essentially chirp-free. The spectral width from fig. 6c is 41 nm giving a duration–bandwidth product of 0.33 which is close to the Fourier transform limit. The average output power of the OPO with intracavity dispersion compensation is typically 50 mW with corresponding peak powers of ~15 kW. The reduction in OPO output power in the configuration with intracavity dispersion compensation is attributed to the insertion loss of the intracavity prism sequence. We believe that this loss has arisen through a slight im-

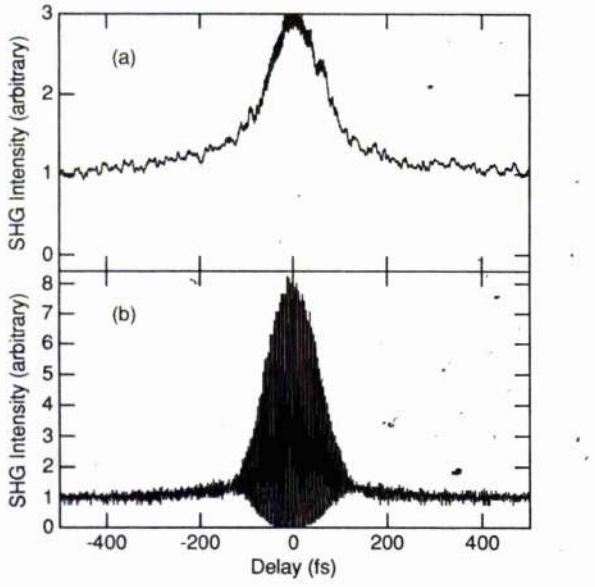

Fig. 5. Intensity (a) and interferometric (b) autocorrelation profiles of the pulses from the OPO with extracavity dispersion compensation.

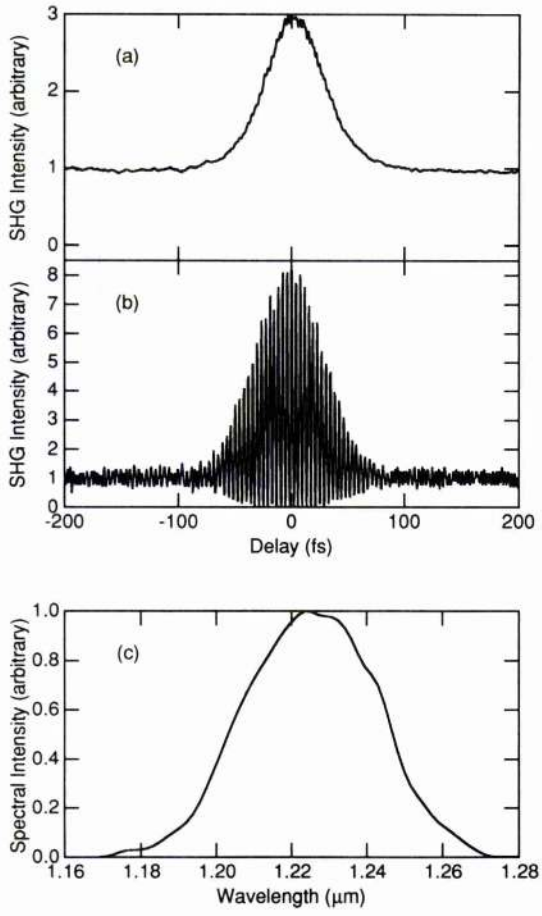

Fig. 6. Intensity (a) and interferometric (b) autocorrelation profiles and corresponding spectral data (c) for the output of the OPO with intracavity dispersion compensation.

perfection in the cut of the KTP crystal which causes the plane of the signal polarisation to be rotated away from the plane of the intracavity prism sequence. With optimisation of the crystal and prism orientation it should be possible to obtain powers of over 100 mW from the intracavity compensated OPO.

Previous theoretical studies [14] of OPO's in the picosecond regime have neglected the effects of SPM and GVD on the output pulse duration. In the femtosecond regime, however, the higher intracavity peak powers mean that these effects must be included in any comprehensive treatment [15]. The pulse duration from the OPO is determined by the balance between the SPM occurring in the KTP crystal and the GVD from the crystal and the intracavity prism sequence. We have studied these effects in more detail by measuring the pulse spectral and temporal characteristics as the amount of intracavity GVD in the OPO was varied by translating one of the SF14 prisms. Figure 7 shows the output pulse duration from the OPO as the amount of glass in the intracavity prism sequence was altered. For these experiments the spacing of the prisms was maintained constant at 24 cm. It is useful to convert the figure for the amount of intracavity glass to an equivalent value for GVD in fs^2 [12] and these results are also shown in fig. 7. Note that the point of zero GVD in the figure was normalised to the point of minimum pulse duration. It can be seen that for increasingly negative values of GVD, the pulse duration increases slowly. Furthermore, the pulses in this regime were observed to be free of chirp and to be transform-limited as shown in fig. 6. For increasingly positive values of GVD the measured pulse duration increase rapidly, and the pulses in this regime were observe to become increasingly chirped with the appearanc of a pedestal on the autocorrelation function and double peaked structure in the power spectrum These results are similar to those observed in pre vious studies of modelocked femtosecond laser [16,17], and are in good qualitative agreement wit the theoretical predictions [18] for the pulse evo lution in laser systems where the pulse formatio process depends on the balance between SPM an GVD.

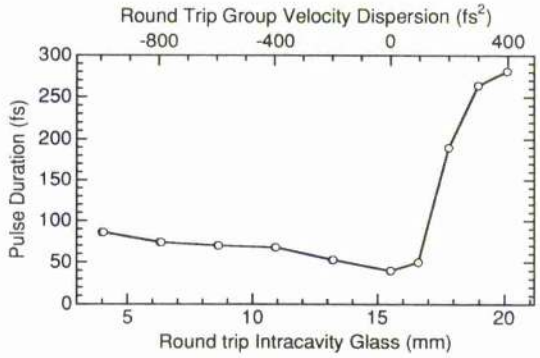

Fig. 7. Dependence of the pulse duration on the amount of intracavity glass introduced in the dispersion-compensated OPO. The upper axis indicates the equivalent GVD in fs^2 with the point of zero GVD normalised to the position of minimum pulse duration.

When adjusted correctly, the OPO produces trans form-limited pulses over the entire tuning range tha extends from 1.1 μm to 1.3 μm, limited by the re flectivity of the available mirrors and the particula cut of the KTP crystal that we have used. As the OP is tuned, the modification of the signal wavelengt changes the net cavity GVD such that a slight ad justment of the intracavity prism sequence is nec essary to recover the minimum pulse duration. Th output of the OPO over this tuning range was in th fundamental TEM_{00} mode, but higher-order trans verse modes were observed from the OPO if the fo cussing section of the OPO cavity was misaligned Indeed, the transverse modes of the OPO cavity an the pump Ti:sapphire cavity were observed to be in dependent of each other. With the Ti:sapphire lase adjusted to operate in a TEM_{10} mode it was still pos sible to obtain output from the OPO in a TEM_{0} mode although the transverse mode mismatch be tween the pump and the OPO cavities resulted in substantial reduction in gain. Optimum perform ance of the OPO required that both the pump an the OPO cavities were aligned for TEM_{00} operation

Although the primary output of the OPO is in th resonant signal beam, there is significant output i the non-resonant single-pass idler beam. In addition in both the OPO cavity configurations with an without intracavity dispersion compensation, w have observed five additional wavelengths arisin from non-phasematched processes in the KTP crys tal. Apart from the single-pass SHG of the pump ligh discussed earlier, we have observed both SHG an third harmonic generation (THG) of the resonan signal beam generating pulses at 600 nm and 400 nm respectively. We have also observed two sum-fre

quency-mixing (SFM) processes; SFM between the pump and the resonant signal generates pulses at 490 nm while SFM between the pump and the idler generates pulses at 635 nm. (These processes are summarised in table 1 for the OPO with intracavity dispersion compensation.) All of these processes are non-resonant because there is negligible feedback of the non-phasematched light from the mirrors used in the OPO cavity. It should be noted, however, that the light generated in SHG and THG of the resonant signal is emitted in both directions from the KTP crystal because of the standing wave nature of the OPO cavity. By contrast, the light generated from SFM involving the single-pass pump in the KTP crystal is emitted only in the same direction as the pump. The most prominent of these non-phasematched processes is that of sum-frequency-mixing between the resonant signal and the pump resulting in about 1 mW of blue light at 490 nm. We have measured the spectrum of this SFM light and the results for the OPO having intracavity dispersion compensation are shown in fig. 8. Although we have not yet been able to measure the pulse duration of this SFM light directly, the measured spectral width of 2.5 nm is consistent with pulses having duration around 100 fs. Whilst there has been recent theoretical interest [19] in studying OPO's containing an additional intracavity nonlinear crystal for SFM, the possibility of the same nonlinear crystal being used for simultaneous parametric generation and SFM has not yet been considered. If the efficiency of the intracavity SFM that we have observed could be increased, (with an appropriate choice of cavity mirrors for example), then it is possible that this could lead to the realisation of a tunable femtosecond source in the blue spectral region using only a single intracavity element.

Table 1
A summary of the different parametric processes observed in the intracavity dispersion compensated OPO. Each process is described in terms of a conservation of energy condition where ω_p, ω_s, ω_i refere to pump, signal and idler photon energies, respectively. The measured polarisations of each of the waves is also indicated where e and o refer to extraordinary and ordinary polarisations, respectively.

Wavelength λ (nm)	Description of nonlinear interaction		Average intracavity power
400	$\omega=\omega_s+\omega_s+\omega_s$	e+e+e→e	<1 μW
415	$\omega=\omega_p+\omega_p$	e+e→o	1 mW
490	$\omega=\omega_s+\omega_p$	e+e→e	1 mW
600	$\omega=\omega_s+\omega_s$	e+e→o	10 μW
635	$\omega=\omega_i+\omega_p$	e+e→e	<1 μW
1200	$\omega_s=\omega_p-\omega_i$	e+o→e	3.5 W
2690	$\omega_i=\omega_p-\omega_s$	e+o→o	30 mW

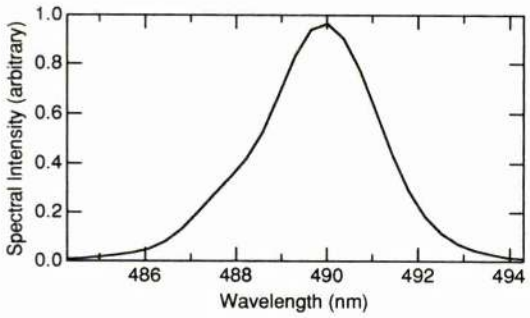

Fig. 8. Spectrum of the non-phasematched SFM light generated at 490 nm. The bandwidth of 2.5 nm corresponds to a lower limit on the pulse duration of approximately 100 fs.

In order to maintain parametric oscillation, the optical cavity length of the OPO must be matched to that of the pump Ti:sapphire laser with interferometric tolerances. Figure 9a shows the variation in signal output power as the cavity length of the intracavity dispersion compensated OPO is varied in sub-micron increments. This measured oscillation range of 0.8 μm depends on the exact OPO configuration, and as observed in reference [4], higher cavity length tolerances are observed if the OPO is operated further above threshold. It has been noted in ref. [20] that changing the cavity length of a synchronously pumped OPO introduces a shift in the resonant signal wavelength, and fig. 9b shows the variation of the resonant signal wavelength with cavity length observed in our OPO. This wavelength tuning occurs because cavity length detuning of the OPO introduces a loss in synchronism between the resonant signal and the pump pulses. To maintain synchronism (and optimise the gain in the OPO), the signal wavelength shifts, thereby adjusting the group velocity of the resonant signal such that the cavity roundtrip time is maintained constant. The exact nature of the cavity length tuning depends on the group velocity dispersion characteristics of the OPO. The results in fig. 9b were obtained with a net negative cavity GVD at the signal wavelength so that shorter OPO cavity lengths are compensated by

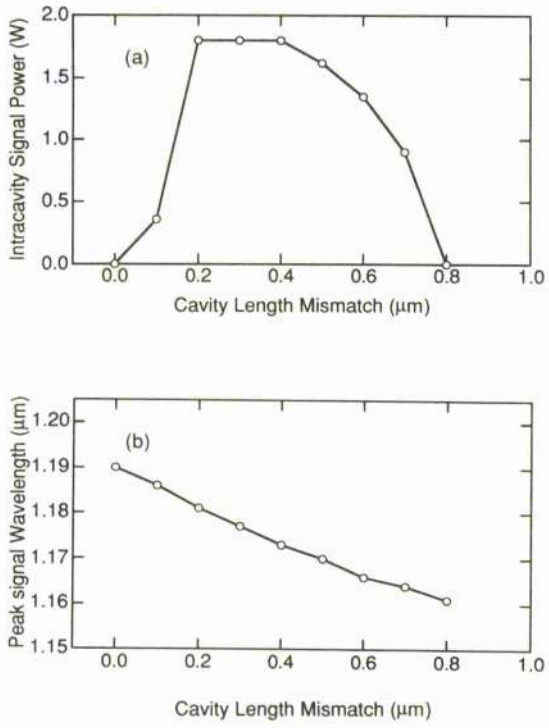

Fig. 9. Dependence on cavity length of the power (a) and the wavelength (b) of the signal pulses in the intracavity dispersion-compensated OPO.

a shift to longer wavelengths with corresponding slower group velocities.

Despite stringent alignment conditions, we have observed that the OPO is a remarkably robust device, providing a stable source of sub-100 fs pulses for several hours at a time without any form of active stabilisation. Typical recorded oscillograms showing the stability of the Ti:sapphire and the OPO outputs are included in fig. 10. The amplitude noise of the pump Ti:sapphire laser (fig. 10a) was measured to be approximately 1%, consistent with results which have been reported previously [21]. The output of the OPO without dispersion compensation (fig. 10b) is quite unstable with intensity fluctuations of over 10%, but the addition of intracavity dispersion compensation (fig. 10c) substantially improves the OPO amplitude noise to approximately 4%. Considering the nonlinear nature of the parametric generation process, it is to be expected that the amplitude noise of the OPO would be an exaggeration of that of the pump source. The improvement in the OPO stability with the addition of intracavity dispersion compen-

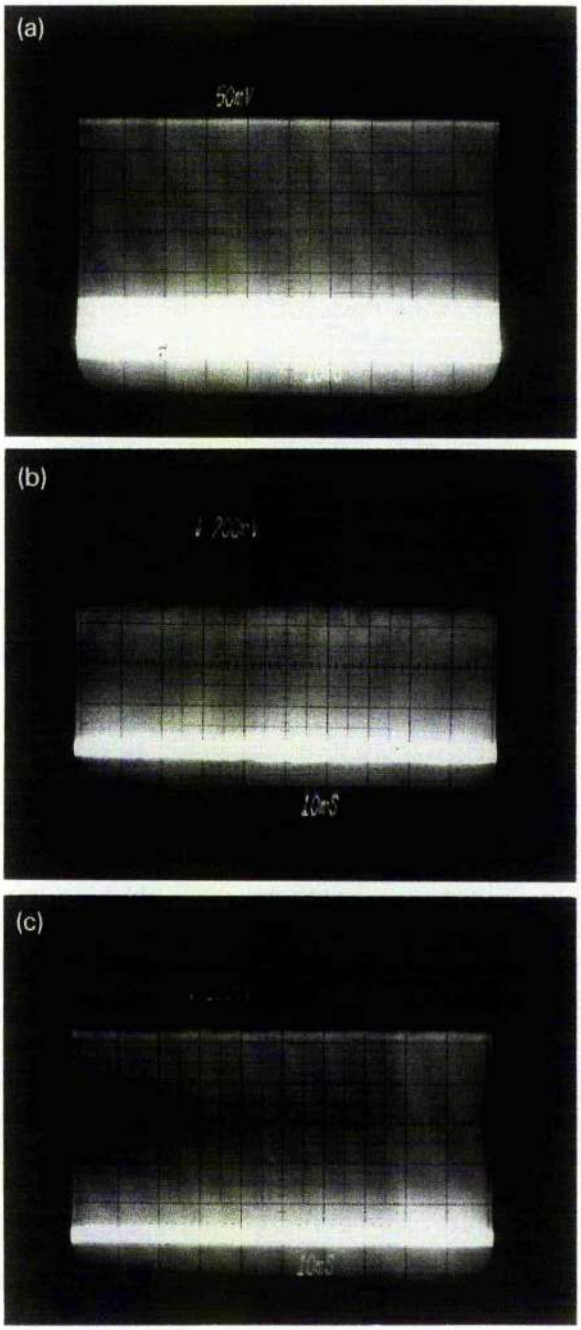

Fig. 10. Oscillograms showing the amplitude noise of the self modelocked Ti:sapphire pump laser (a), the OPO with no dispersion compensation (b) and the OPO with intracavity dispersion compensation (c). The timebase is 10 ms/division in each case.

sation can be attributed to the additional spectral control introduced by the intracavity prism sequence. Both experimental and theoretical studie

[17,22] have indicated that inadequate spectral control in femtosecond lasers where SPM and GVD are significant can lead to a relatively unstable output, and it is likely that similar considerations apply to the stability of the femtosecond OPO. It should be noted that although drifts in the OPO cavity length of the order of a micron will eventually cause oscillation to cease, the OPO maintains oscillation in the presence of sub-micron cavity length fluctuations. As discussed above, however, these length fluctuations will introduce a slight shift in the resonant signal wavelength. From fig. 9b, it can be seen that cavity length fluctuations of 0.1 μm introduce a corresponding peak wavelength shift in the signal of 3.8 nm, but since this wavelength shift occurs within a total bandwidth of the order of 40 nm there is little significant modification to the pulse structure in the time domain. It is possible that these wavelength variations are associated with a slight increase in amplitude instability in the OPO, but active cavity length stabilisation of the OPO [1] can be used to compensate for this. Such a scheme is presently being evaluated in our system, but all the results presented in this paper were obtained without any stabilisation.

Measurements have also been made of the relative phase noise of the pump laser and the OPO operating both with and without intracavity dispersion compensation. The phase noise measurement techniques have been described elsewhere [23] and the results are summarised in table 2 in terms of the relative rms timing jitter in a particular frequency band [24]. The phase noise data for the pump Ti:sapphire laser are in good agreement with those previously reported [9], but it is of more relevance in the present context to compare the phase noise of the OPO with that of the pump laser. The relative phase noise between the pump laser and the OPO can be readily compared by considering the rms timing jitter in the frequency band 50–500 Hz. The measured phase noise in this frequency band corresponds to timing jitter fluctuations on millisecond timescales and provides an important indicator of long term phase noise stability. It can be seen from table 2 that the phase noise of the OPO operated without dispersion compensation is significantly worse than that of the pump laser. This result is consistent with the large intensity fluctuations observed from the OPO in this configuration, and this increased phase noise is again likely to be attributable to an absence of spectral control in the OPO.

When the parametric oscillator is operated with intracavity dispersion compensation, the phase noise results are perhaps rather surprising. Although the amplitude noise of the OPO in this configuration was measured to be slightly worse than that of the pump laser, the results shown in table 2 indicate that the phase noise characteristics are significantly improved. In order to interpret this result it is necessary to consider the various factors that contribute to the phase noise of the pump laser and the OPO. Phase noise characteristics of the self-modelocked Ti:sapphire have been studied extensively experimentally [9, 25] and a recent theoretical analysis [26] has provided further insight into the processes influencing the laser phase noise. The major source of low frequency phase noise in the Ti:sapphire laser is from amplitude fluctuations in the argon-ion pump laser occurring at 50 Hz, 100 Hz, etc., corresponding to inadequate smoothing in its power supply unit. These fluctuations couple into the self-modelocked

Table 2
Measured phase noise characteristics of the pump Ti:sapphire laser and the OPO operated with and without intracavity dispersion compensation. The rms timing jitter is shown for the specified frequency bands. Note that the level of instrumental noise meant that it was only possible to obtain an upper limit on the phase noise measurements in the highest frequency band (5–50 kHz).

Frequency band	Cavity Configuration		
	Pump Ti:sapphire laser	OPO without dispersion compensation	OPO with intracavity dispersion compensation
50–500 Hz	12.0 ps	41.8 ps	3.6 ps
500 Hz–5 kHz	1.7 ps	2.4 ps	0.70 ps
5–50 kHz	<0.62 ps	<1.4 ps	<1.0 ps

Ti:sapphire laser and increase the laser timing jitter by causing bulk refractive index changes in the Ti:sapphire crystal, as well as variations in the gain and the spontaneous emission background during laser operation.

The factors determining the phase noise of the OPO, however, are somewhat different. The OPO is a synchronously pumped device, with the OPO pulse repetition frequency determined by the repetition frequency of the pump Ti:sapphire laser pulses and not by the OPO cavity length. As shown above in fig. 9, oscillation occurs over a 0.8 μm range of cavity length, but the OPO repetition frequency was observed to remain fixed at that of the pump laser over this range. The effect of cavity length detuning between the pump and the OPO is manifested as a wavelength shift in the OPO, not as a difference in the cavity repetition frequencies. It might therefore be expected that any timing jitter in the pump laser would be followed by identical jitter in the OPO. However, the coupling between timing fluctuations in the pump laser and the OPO is reduced by effects such as group velocity walkaway and the finite buildup time of oscillation in the OPO. Furthermore, unlike a laser, the parametric generation process is instantaneous, without any buildup of population inversion in the crystal over long timescales. Consequently, there is no appreciable spontaneous emission background in the OPO which would introduce additional timing jitter. It is therefore reasonable to conclude that if the OPO is operated in a configuration with intracavity dispersion compensation such that factors such as SPM and GVD are adequately controlled, then the phase noise of the OPO could indeed be reduced below that of the pump laser.

It should be stressed that this discussion has been of a basic and qualitative nature and clearly much further work is needed before a quantitative basis can be established for these observations. On the basis of the above results however, it is clear that an indepth and complementary theoretical modelling of the phase noise characteristics of the OPO is now justified. The differences between the phase noise characteristics of the pump laser and the OPO appear to have their origin in the distinctive features of the optical parametric oscillator as compared with the laser, and any phase noise investigation would have to take due account of this. Features such as the wide OPO bandwidth, group velocity walkaway effects, pump depletion and the finite oscillation buildup time for the OPO would all need to be included in a proper analysis.

Our experimental results are consistent with the qualitative considerations discussed above. Significantly, these observations also imply that whilst active stabilisation of the OPO cavity length improves the amplitude noise by improving the wavelength stability, it may not directly reduce the OPO phase noise. The OPO amplitude and phase noise characteristics appear to be quite independent of each other, and improvements of the OPO phase noise characteristics will need to involve simultaneously frequency referencing both the pump Ti:sapphire laser and the OPO to a low phase noise external oscillator. Experiments to implement this phase noise stabilisation scheme are currently being implemented and in conjunction with amplitude stabilisation, this should lead to a highly stable output from the OPO and considerably increase its utility as a practical femtosecond device.

4. Conclusions

In this paper we have presented a characterisation of a femtosecond Ti:sapphire laser pumped optical parametric oscillator. Operated in a configuration without any dispersion compensation, the OPO produces highly chirped pulses, and an analysis of the chirp on these pulses has provided insight into the importance of SPM in an OPO. With intracavity dispersion compensation, the OPO has produced transform-limited 40 fs pulses over an extended tuning range from 1.1 to 1.3 μm in the near-infrared, but the observation of other non-phasematched processes in the OPO has also suggested the possibility of its exploitation as a tunable femtosecond source in the visible spectral region. The stability of the OPO has been studied, and most significantly, with intracavity dispersion compensation, the phase noise of the OPO has been observed to be better than the pump self-modelocked Ti:sapphire laser. This has enabled us to identify several operational factors of the femtosecond OPO that are worthy of further investigation. Despite the relatively complex nature of

a synchronously pumped femtosecond OPO, our studies have demonstrated that it is a very versatile and reliable source of tunable femtosecond radiation. Ongoing improvements to the cavity design and the use of other nonlinear materials should further increase its applicability in the study of ultrafast phenomena in new and important spectral regions.

Acknowledgements

Overall funding for this research was provided by the UK Science and Engineering Research Council (SERC). One of us (DTR) gratefully acknowledges financial support through a SERC PhD studentship. M. Ebrahimzadeh is grateful to the Royal Society for the provision of a University Research Fellowship.

References

[1] Special Issue on Ultrafast Optics and Electronics, IEEE J. Quantum Electron. 28 (1992).
[2] K. Burneika, M. Ignatavicius, V. Kabelka, A. Piskarskas and A. Stabinis, IEEE J. Quantum Electron. 8 (1972) 574.
[3] Q. Fu, G. Mak and H.M. van Driel, Optics Lett. 17 (1992) 1006.
[4] W.S. Pelouch, P.E. Powers and C.L. Tang, Optics Lett. 17 (1992) 1070.
[5] A. Nebel, C. Fallnich and R. Beigang, paper JWB5, in: Conference on Lasers and Electro-Optics 1993, Vol 11, OSA Technical Digest Series (1993) p. 282.
[6] P.E. Powers, W.S. Pelouch, S. Ramakrishna, C.L. Tang and K.L. Cheng, paper CThK2, in; Conference on Lasers and Electro-Optics 1993, Vol 11, OSA Technical Digest Series (1993) p. 432.
[7] J.D. Kafka, M.L. Watts and J.W. Pieterse, Paper CPD32, in: Conference on Lasers and Electro-Optics 1993, Postdeadline Summary (1993) p. 68.
[8] R.J. Ellingson and C.L. Tang, Optics Lett. 18 (1993) 438.
[9] D.E. Spence, J.M. Evans, W.E. Sleat and W. Sibbett, Optics Lett. 16 (1991) 1762.
[10] R.H. Stolen and C. Lin, Phys. Rev. A 17 (1978) 1448.
[11] M. Sheik-Bahae, D.C. Hutchings, D.J. Hagan and E.W. van Stryland, IEEE J. Quantum Electron. 27 296 (1991).
[12] See for example G.P Agrawal, Nonlinear fiber optics (Academic, New York, 1989).
[13] J-C.M. Diels, J.J. Fontaine, I. McMichael and F. Simoni, Appl. Optics 24 (1985) 1270.
[14] E.C. Cheung and J.M. Liu, J. Opt. Soc. Am. B 8 (1991) 1491.
[15] J.A. Moon, IEEE J. Quantum Electron. 29 (1993) 265.
[16] A. Finch, G. Chen, W. Sleat and W. Sibbett, J. Modern Optics 35 (1988) 345.
[17] H. Avramopoulos, P.M.W. French, G.H.C. New, M.M. Opalinska, J.R. Taylor and J.A.R. Williams, Optics Comm. 76 (1990) 229.
[18] H.A. Haus, J.G. Fujimoto and E.P. Ippen, J. Opt. Soc. Am. B 8 (1991) 2068.
[19] G.T. Moore and K. Koch, IEEE J. Quantum Electron. 29 (1993) 961.
[20] D.C. Edelstein, E.C. Wachman and C.L. Tang, Appl. Phys. Lett. 54 (1989) 1728.
[21] J.D. Kafka, M.L. Watts and J-W.J. Pieterse, IEEE J. Quantum Electron. 28 (1992) 2151.
[22] W.L. Nighan, T. Gong and P.M. Fauchet, IEEE J. Quantum Electron. 25 (1989) 2476.
[23] D. Walker, D.W. Crust, W.E. Sleat and W. Sibbett, IEEE J. Quantum Electron. 28 (1992) 289.
[24] D. von der Linde, Appl. Phys. B 39 (1986) 201.
[25] J. Son, J.V. Rudd and J.F. Whitaker, Optics Lett. 17 (1992) 733.
[26] H.A. Haus, IEEE J. Quantum Electron. 29 (1993) 983.

JOURNAL OF MODERN OPTICS, 1994, VOL. 41, NO. 6, 1231–1242

Ti : sapphire pumped femtosecond optical parametric oscillator exhibiting soliton formation

D. T. REID, J. M. DUDLEY, M. EBRAHIMZADEH and W. SIBBETT

J. F. Allen Research Laboratories, Department of Physics and Astronomy, University of St Andrews, Fife KY16 9SS, Scotland.

(*Received 21 September 1993; revision received 26 October 1993*)

Abstract. The configuration and operation of a singly resonant Ti : sapphire pumped optical parametric oscillator (OPO) based on KTP is discussed. Cavity arrangements with and without dispersion compensation are described and the generation of sub-40 fs transform-limited pulses is highlighted. Evidence for soliton pulse formation in the OPO is presented and good quantitative agreement with existing theory is implied. Results of amplitude and phase noise measurements of the OPO are given and compared with those of the pump laser. Generation of pulses at several visible wavelengths by non-phase-matched processes is also briefly discussed.

1. Introduction

Since the first optical pulses of duration less than 100 fs from a visible dye laser were reported [1] the spectral regions accessible to femtosecond pulses have been substantially expanded. Self-mode-locking of vibronic lasers, notably Ti : sapphire [2] and Cr : LiSAF [3], together with the coupled-cavity mode-locking of colour-centre lasers [4] has made available pulses of sub-100 fs durations over extended regions in the near-infrared. Femtosecond pulses having tunability in the near to mid-infrared with high peak powers are in particular demand for general applications in time domain spectroscopy [5] and the study of semiconductor dynamics in particular [6]. The emergence of new nonlinear materials such as KTP [7] and KTA [8] which combine high damage thresholds with large nonlinear coefficients offers an efficient means of generating femtosecond pulses in wavelength regions not directly available from conventional lasers. The first c.w. femtosecond optical parametric oscillator (OPO) to be reported [9] used KTP in a critically phase-matched geometry and was intracavity pumped by a colliding-pulse mode-locked (CPM) dye laser. More recently attention has turned to extracavity pumped femtosecond OPOs using self-mode-locked Ti : sapphire lasers [10–12].

In this paper we report results obtained from a singly resonant Ti : sapphire pumped femtosecond OPO based on KTP in a non-critically phase-matched geometry. The OPO has been operated in cavity configurations with and without dispersion compensation and the temporal and spectral output pulse characteristics have been investigated. From these experimental data, evidence is presented in support of solitonic pulse shaping in the OPO and this suggestion is related to theory. Measurements of the OPO amplitude and phase noise have also been taken for different cavity arrangements and these provide further insights into the dynamics of the femtosecond parametric oscillator. In addition we report behaviour unique to the femtosecond OPO including several non-phase-matched parametric processes and cavity length dependent tuning effects.

0950-0340/94 $10·00

2. Experimental configuration

A regeneratively-initiated self-mode-locked Ti : sapphire laser similar to that described in [13] was used as the pump source for the OPO. Operated at a centre wavelength of 830 nm the laser routinely provided sub-100 fs pulses at average powers in excess of 1 W and a repetition frequency of 85 MHz. A cavity schematic of the laser and a typical interferometric autocorrelation of its output are included as figure 1. The pulse duration corresponding to the autocorrelation shown is 85 fs (sech^2 pulse profile assumed) which together with the measured spectral width of 9 nm indicates that the pulses are near to the transform limit.

Cavity arrangements used for the OPO are depicted in figure 2. The basic three-mirror, standing-wave resonator consists of two concave high reflectors ($r = 10$ cm) and a plane output coupler. The cavity fold angle is minimized to reduce astigmatism and the cavity length is synchronous with that of the pump laser. Pump light is focused using a 75 mm focal length lens to a 15 μm spot radius inside the KTP crystal through one of the curved mirrors. The hydrothermally grown KTP crystal is 1·5 mm thick and is antireflection coated on both faces for a centre wavelength of 1180 nm. It is cut for non-critical Type II interaction ($e \rightarrow eo$) along the x axis with the signal and pump polarized parallel to the y axis and the non-resonant idler polarized parallel to the z axis. Tuning of the OPO is achieved by changing the pump wavelength or by rotating the crystal in the xy plane. The curved mirrors are highly reflecting ($R > 99{\cdot}7\%$) for the wavelengths 1·1–1·3 μm and are highly transmitting ($T > 95\%$) at the pump wavelength and the output coupler is 1·5% transmitting at the signal wavelength. Intracavity dispersion compensation is achieved using a pair of SF14 prisms as shown in figure 2 (*b*).

3. Results and discussion

3.1. *Optical parametric oscillator without dispersion compensation*

With a pump power of 1 W and in the absence of dispersion compensation the parametric oscillator produced up to 150 mW in the signal beam. The corresponding

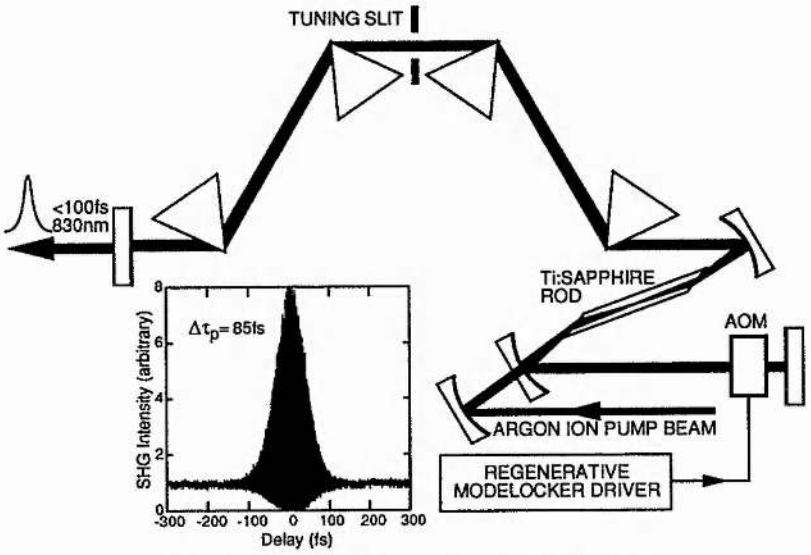

Figure 1. Cavity configuration of the regeneratively-initiated self-mode-locked Ti : sapphire laser and typical interferometric autocorrelation of the output pulses produced (inset).

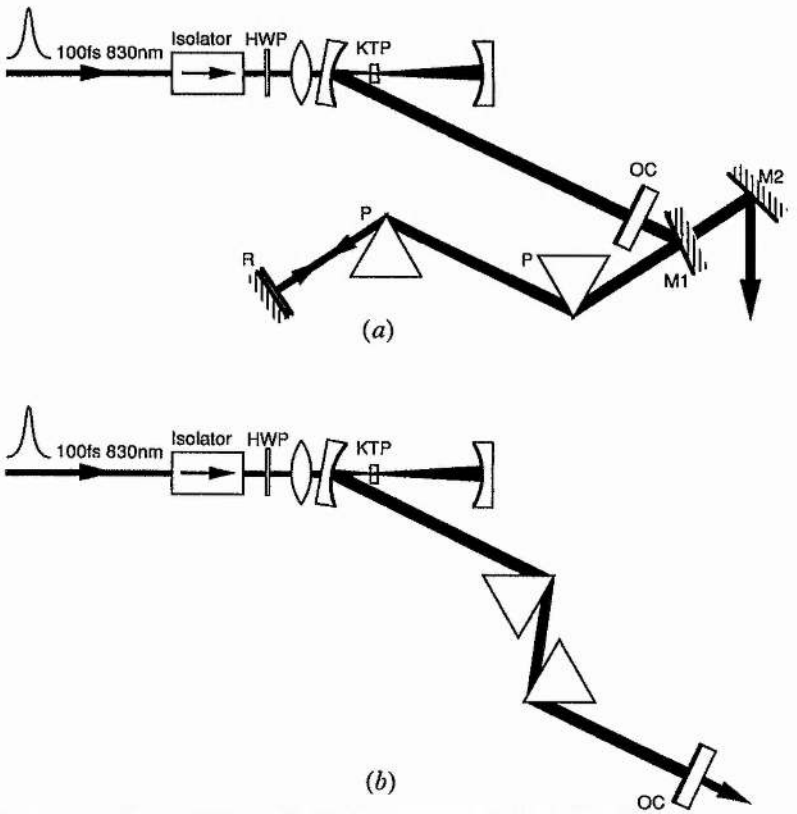

Figure 2. Cavity configurations of the femtosecond OPO; with extracavity dispersion compensation (*a*) and with intracavity dispersion compensation (*b*).

oscillation threshold was measured to be 300 mW of average power at the KTP crystal. Difficulties of collection and collimation prevented the power in the idler beam from being determined directly but from the ratio of photon energies we expect 50–100 mW to be generated. The OPO output was observed to be in a TEM_{00} mode and was essentially independent of the pump mode. Intensity and interferometric autocorrelation techniques were used to measure pulse durations and to obtain information about frequency chirp in the pulses. An optical spectrum analyser was used to monitor the spectral composition of the pulses.

Results from the OPO when operated without any dispersion compensation are reproduced in figure 3. The measured intensity autocorrelation (figure 3 (*a*)) implies a pulse duration of 400 fs. The interferometric autocorrelation (figure 3 (*b*)) and the pulse spectrum (figure 3 (*c*)) indicate that the pulses are highly chirped and the corresponding duration-bandwidth product is around five. Self-phase-modulation (SPM) occurring at the focus within the KTP crystal gives rise to this frequency chirp and the observed spectrum having a twin-peaked structure is characteristic of the SPM effect. The combination of self-phase modulated spectral broadening and intracavity group velocity dispersion (GVD) broadens the resonant signal pulses to a duration much longer than the original pump pulse. Extracavity dispersion compensation of these pulses has been implemented using a pair of SF14 prisms separated by 90 cm and used in a double-pass configuration as depicted in figure 2 (*a*). Intensity and interferometric autocorrelations of the pulses after optimal extracavity dispersion compensation are included as figure 4. The pulse duration deduced from the intensity autocorrelation of figure 4 (*a*) is 90 fs but the residual

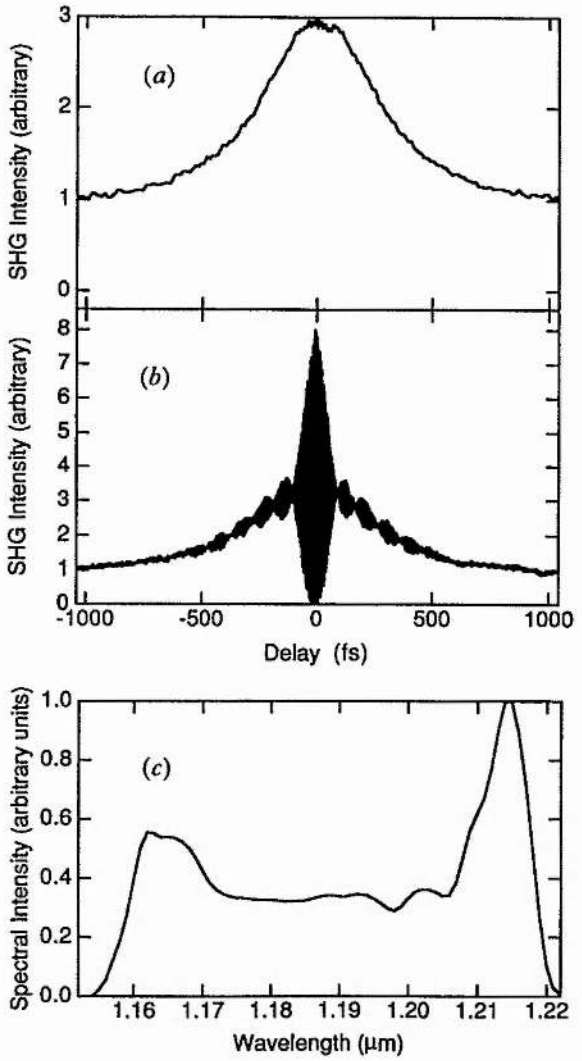

Figure 3. Intensity (*a*) and interferometric (*b*) autocorrelation profiles and corresponding spectral data (*c*) for the output of the OPO without dispersion compensation.

pedestal on the interferometric autocorrelation in figure 4 (*b*) indicates that some uncompensated nonlinear chirp still remains. The inability to completely remove the chirp on the signal pulses is a limitation of this scheme for extracavity dispersion compensation [14].

3.2. *Parametric oscillator having intracavity dispersion compensation*

To obtain the shortest pulses from the parametric oscillator it is necessary to fully utilize the increased bandwidth produced by self-phase modulation in the crystal. Intracavity dispersion compensation permits the chirp introduced on to the pulse in a single pass of the cavity to be removed before it becomes large enough to dominate the kinetics of pulse evolution in the OPO. By using a pair of intracavity SF14 prisms having an apex separation of 24 cm it was possible to routinely recover transform-limited pulses having sub-40 fs durations. Representative temporal and spectral characteristics of the output signal pulses are reproduced in figure 5. The duration of

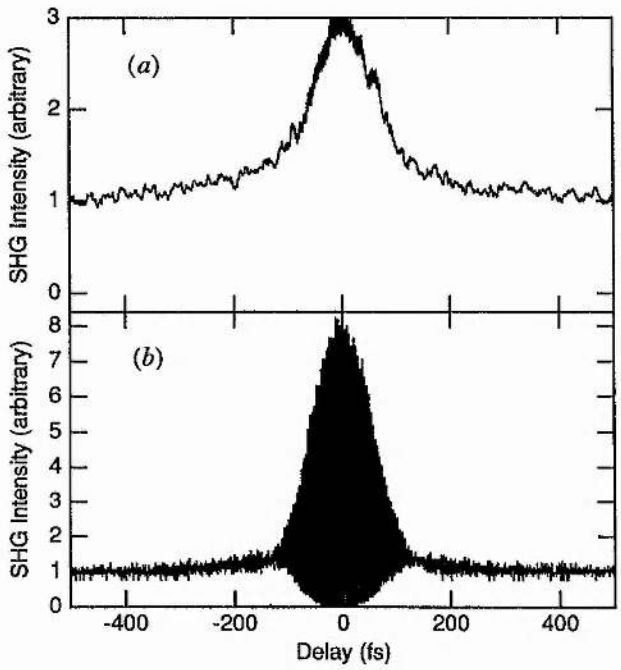

Figure 4. Intensity (*a*) and interferometric (*b*) autocorrelation profiles of the pulses from the OPO with extracavity dispersion compensation.

these pulses measured from the intensity autocorrelation in figure 5 (*a*) is 39 fs. Inspection of the interferometric autocorrelation in figure 5 (*b*) and the pulse spectrum in figure 5 (*c*) reveals that the pulses are chirp free and their duration-bandwidth product of 0·33 (sech^2 profile assumed) is close to the Fourier transform limit. The average output power from the intracavity dispersion compensated OPO is typically 50 mW, corresponding to peak output powers of ~15 kW. A small increase in the oscillation threshold to 350 mW was observed due to the inclusion of the prism pair. Optimization of the prism orientation should make it possible to achieve output powers and thresholds approaching those of the uncompensated OPO.

The intracavity peak power of the dispersion compensated OPO is close to 1 MW and is therefore capable of generating directly observable sequences of pulses in the visible via non-phase-matched processes that would normally be too inefficient to be observed through parametric oscillation. We have observed a total of five non-phase-matched interactions in addition to the production of the signal and idler pulse sequences and these are listed in table 1. The strongest processes involve sum-frequency mixing between the single-pass signal and the pump light to generate blue light at 490 nm and single-pass frequency doubling of the pump light producing a wavelength of 415 nm. The other processes observed are the second and third harmonic generation of the signal which generate pulses at 600 nm and 400 nm respectively and sum-frequency mixing between the single-pass idler and the pump light that produces light at 635 nm. The spectral bandwidths of the light generated at 490 nm and 600 nm are sufficient to support pulses of sub-100 fs duration. The addition of a second intracavity nonlinear crystal cut for efficient sum-frequency mixing or second harmonic generation could thus lead to the development of a femtosecond source having substantial tunability over the visible spectrum.

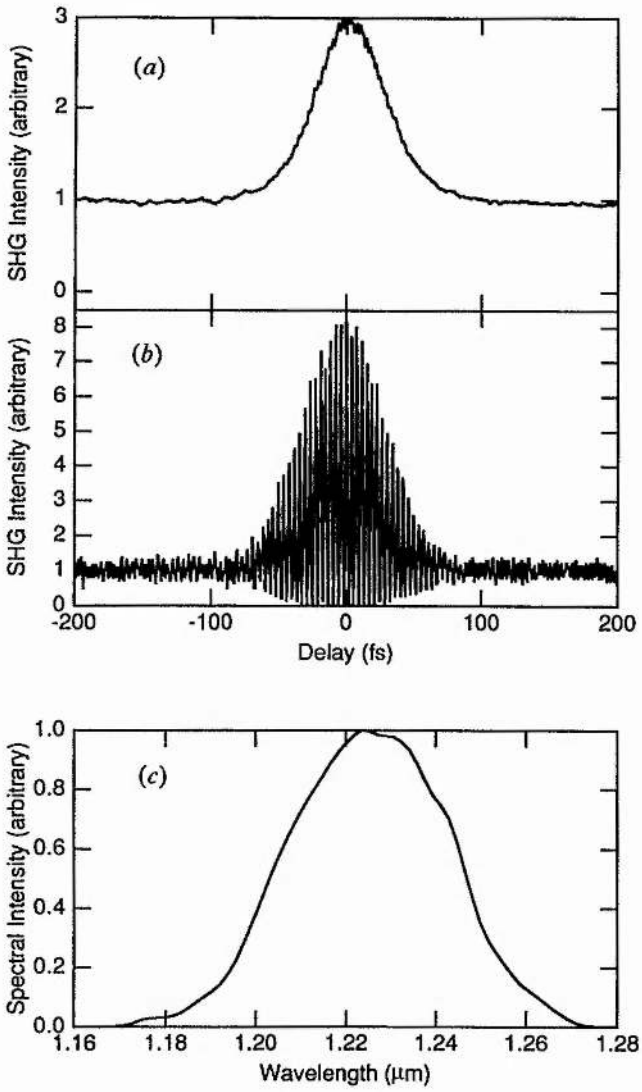

Figure 5. Intensity (*a*) and interferometric (*b*) autocorrelation profiles and corresponding spectral data (*c*) for the output of the OPO with intracavity dispersion compensation.

Table 1. A summary of the different parametric processes observed in the intracavity dispersion compensated OPO. Each process is described in terms of a conservation of energy condition where ω_p, ω_s, ω_i refer to pump, signal and idler photon energies respectively. The measured polarizations of each of the waves are also indicated where *e* and *o* refer to extraordinary and ordinary polarizations respectively.

Wavelength λ (nm)	Description of nonlinear interaction		Average intracavity power
400	$\omega=\omega_s+\omega_s+\omega_s$	$e+e+e\rightarrow e$	$<1\,\mu W$
415	$\omega=\omega_p+\omega_p$	$e+e\rightarrow o$	1 mW
490	$\omega=\omega_s+\omega_p$	$e+e\rightarrow e$	1 mW
600	$\omega=\omega_s+\omega_s$	$e+e\rightarrow o$	$10\,\mu W$
635	$\omega=\omega_i+\omega_p$	$e+e\rightarrow e$	$<1\,\mu W$
1200	$\omega_s=\omega_p-\omega_i$	$e+o\rightarrow e$	3·5 W
2690	$\omega_i=\omega_p-\omega_s$	$e+o\rightarrow o$	30 mW

3.3. *Solitonic pulse shaping in the optical parametric oscillator*

Solitonic behaviour in a femtosecond laser was first reported in a CPM dye laser at 620 nm when amplitude modulation of the output pulse wavetrain at the soliton frequency was observed [15]. Subsequent results also obtained from such a passively mode-locked dye laser were interpreted on the basis of simultaneous formation of solitons and dispersive waves [16] and the splitting of the pulse spectrum into dispersive and solitonic components was consistent with theoretical predictions [17].

During this work an amplitude modulation at a frequency of 2 MHz has been observed on the output of the OPO which can be attributed to periodic soliton break-up and restoration. This explanation is supported by a supplementary observation of spectral splitting when the OPO is operated with low values of positive cavity dispersion. The spectral and temporal characteristics of the output of the OPO have been investigated as a function of the amount of intracavity GVD through translating one of the SF14 prisms. Pulse spectra and corresponding autocorrelations were recorded for a wide range of positive cavity dispersion values and pulse durations were found to vary with dispersion as shown in figure 6. The point of zero dispersion has been normalized to the maximum amount of intracavity glass that allowed the formation of transform-limited pulses. We have found that a small increase in positive cavity dispersion to $+100\,fs^2$ results in the generation of a second spectral component at a wavelength which is 70 nm longer than the original. The maximum wavelength shift occurs for a cavity dispersion of $+700\,fs^2$ where the two spectral components are separated by 70 nm and the peak wavelength is displaced by 70 nm from the position occupied at zero cavity dispersion. Further increases in the cavity dispersion ultimately lead to the formation of pulses having the same duration and spectrum as the uncompensated OPO. These results are summarized in figure 7.

It is clearly evident that there is a maximum wavelength which can be produced by the OPO above which the output spontaneously shifts to longer wavelengths. For the OPO this wavelength appears to be around 1·32 μm and separates the dispersive

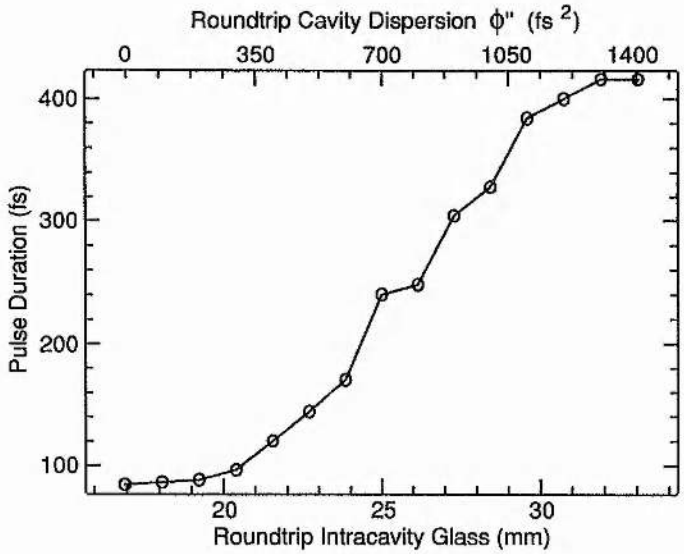

Figure 6. Dependence of the pulse duration on the amount of intracavity glass introduced in the intracavity dispersion compensated OPO. The upper axis indicates the equivalent cavity dispersion in fs^2 with the point of zero dispersion normalized to the maximum amount of intracavity glass that allowed the formation of transform-limited pulses.

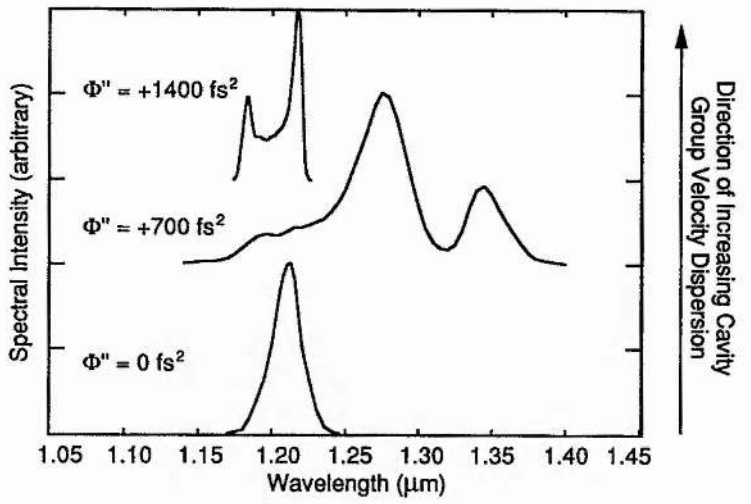

Figure 7. Spectral data for the output of the intracavity dispersion compensated OPO operated with positive cavity dispersion.

component of the pulse from the solitonic component. By identifying this critical wavelength with the zero dispersion point of the fibre model proposed by Wai *et al.* [17] we can apply the analysis of this model to our results.

The model, which was developed for fibres at 1·3 μm, presents a condition necessary for soliton propagation in terms of the wavelength shift, $\Delta\lambda$, observed towards the anomalous regime:

$$\Delta\lambda > \frac{6\,(\text{nm})\,(\text{ps})}{\Delta\tau_p}.$$

In our OPO, the pulse duration of 240 fs observed at the position of maximum wavelength shift sets a lower limit of 25 nm for $\Delta\lambda$ at this point. At the point where longer wavelength generation became evident pulses of duration 88 fs were monitored and this would require $\Delta\lambda > 68$ nm for soliton propagation. This is close to the 80 nm shift measured experimentally.

A further prediction of the model is that the solitonic and dispersive components of the spectrum are found to be displaced by different amounts from the critical frequency. The dispersive part is expected to experience 1·7 times the displacement of the soliton. The results in figure 7 show a ratio of the displacements of frequency in the dispersive wave to that of the soliton of 1·6 which is again in good agreement with the model.

Our observation of a periodic intensity variation in the pulse train can be related to dispersion using an expression derived by Salin *et al.* [15] which gives the soliton frequency f_o as a function of the cavity dispersion ϕ'':

$$f_o = \frac{2\phi''}{0{\cdot}322\pi\Delta\tau_p^2 T}.$$

When this formula is applied for parameters at the position of maximum wavelength shift where $\Delta\tau_p = 240$ fs, $\phi'' = 700$ fs^2 and the cavity repetition period $T = 11{\cdot}8$ ns the predicted soliton frequency is 2·0 MHz, in excellent agreement with experiment. It is interesting to note that the number of cavity roundtrips corresponding to the soliton period, $N_o = (1/f_o T) \sim 40$, is close to the average number of 70 roundtrips accumulated by a signal pulse before extinction through cavity losses.

3.4. *Phase and amplitude noise measurements*

We have observed that the femtosecond OPO is an extremely robust device requiring no alignment on a day to day basis except for minor cavity length adjustment. Oscillation persists for several hours at a time without any form of active stabilization. The amplitude noise present on the outputs of both the parametric oscillator and the pump laser has been measured and typical oscillograms are shown in figure 8. Although intensity fluctuations on the Ti : sapphire pump laser are less

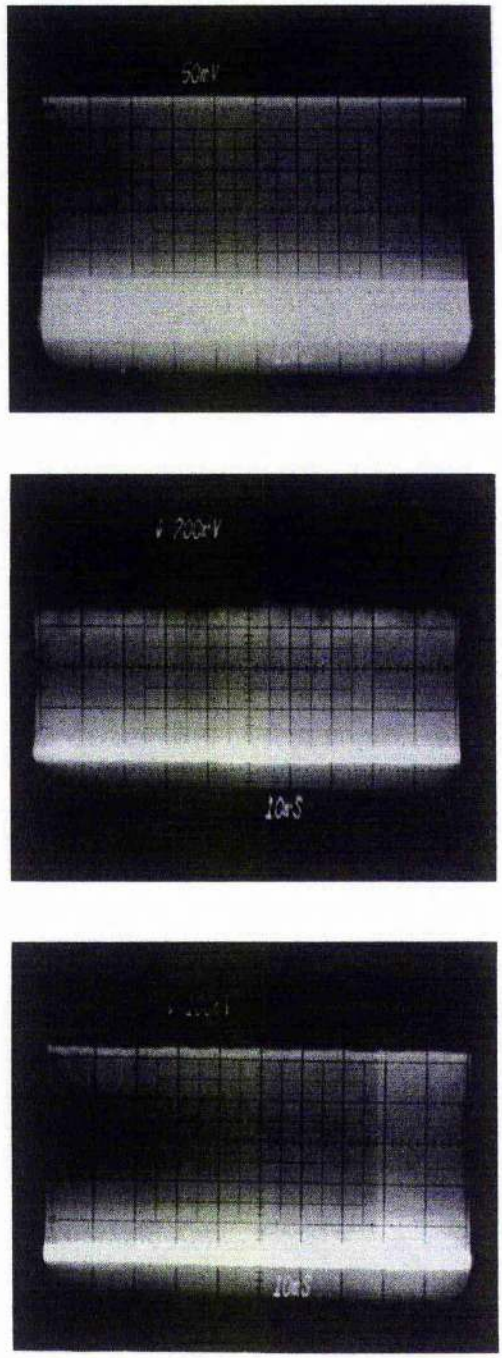

(*a*)

(*b*)

(*c*)

Figure 8. Oscillograms showing the amplitude noise of the self-mode-locked Ti : sapphire pump laser (*a*), the OPO without dispersion compensation (*b*) and the OPO with intracavity dispersion compensation (*c*). The timebase is 10 ms/division in each case.

than 1%, in the absence of dispersion compensation the output of the OPO is relatively noisy, exhibiting amplitude fluctuations of around 10%. The addition of dispersion compensation and the associated increase in spectral control reduces this figure to around 4%. The amplitude noise figures measured for the OPO should be expected to exceed those of the pump laser given the nonlinear nature of the parametric amplification process. Amplitude locking can be implemented to reduce the intensity fluctuations present on the OPO output. The original technique used exploited the shift in output pulse wavelength arising from a change in cavity length [18]. Wavelength tuning of this kind occurs when a cavity length change results in a loss of synchronism with the pump laser. In response the centre wavelength of the resonant signal pulse shifts and the ensuing change in group velocity delay in the KTP crystal brings the OPO back into synchronism with the pump laser and maximizes gain. Cavity length tuning in the dispersion-compensated OPO is shown in figure 9. The variation of wavelength with cavity length is linear and corresponds to a rate of 35 nm μm^{-1}. Oscillation is observed to occur within a cavity length adjustment of 0·8 μm but higher cavity tolerances are observed if the OPO is operated further above threshold [12].

Using techniques described elsewhere [19, 20], measurements were also made of the phase noise in the output of the OPO and typical results are listed together with the phase noise of the pump laser in table 2. The phase noise performance in the 50–500 Hz frequency range provides the most useful comparison between the OPO

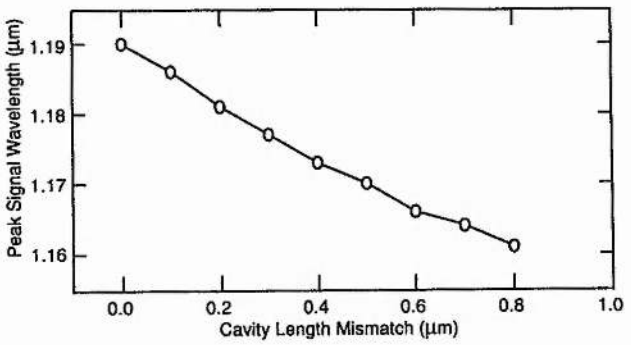

Figure 9. Cavity length dependence of the signal pulse wavelength in the intracavity dispersion compensated OPO.

Table 2. Measured phase noise characteristics of the Ti : sapphire pump laser and the OPO operated with and without intracavity dispersion compensation. The r.m.s. timing jitter is shown for the specified frequency bands. Note that the level of instrumental noise meant that it was only possible to obtain an upper limit on the phase noise measurements in the highest frequency band (5–50 kHz).

	Cavity configuration		
Frequency band	Ti : sapphire pump laser	OPO without dispersion compensation	OPO with intracavity dispersion compensation
50–500 Hz	12·0 ps	41·8 ps	3·6 ps
500 Hz–5 kHz	1·7 ps	2·4 ps	0·70 ps
5–50 kHz	<0·62 ps	<1·4 ps	<1·0 ps

and the pump laser because this frequency band corresponds to timing jitter fluctuations on millisecond timescales and provides a good indicator of longer term pulse stability. In the absence of dispersion compensation the phase noise of the OPO is considerably worse than that of the pump laser. This observation is consistent with the large intensity fluctuations apparent in this configuration and is attributed to the lack of spectral control in the cavity. The results when the OPO is operated with dispersion compensation are perhaps unexpected since the phase noise characteristics measured in this configuration are consistently better than those of the pump laser. The improvement in phase noise can be attributed to a combination of synchronous pumping and the lack of a population lifetime in the parametric process. Timing jitter present on the pump laser will not couple efficiently into the OPO since any mismatch in arrival time between the pump and signal pulses at the nonlinear crystal will result in reduced gain and cannot be transferred to the amplified signal pulse. Phase noise in the OPO can, however, exceed that of the pump laser when the resonant signal pulse has a duration much greater than the pump pulse. In this situation the arrival time of the pump pulse at the crystal is less critical and timing jitter in the pump pulse sequence will be communicated to the signal pulse.

Our observations suggest that the amplitude and phase noise in the OPO are independent of each other. Thus control of the OPO cavity length by active stabilization, although improving the amplitude noise characteristics, may not therefore serve to directly improve the phase noise.

4. Conclusions

In this paper we have reported results obtained from a Ti : sapphire pumped femtosecond optical parametric oscillator. In the absence of dispersion compensation the output pulses are highly chirped and the pulse spectrum is asymmetric due to uncompensated self-phase modulation in the KTP crystal. The addition of intracavity dispersion compensation allows transform-limited pulses with sub-40 fsec durations to be produced. Solitonic behaviour in the OPO has been recorded and found to be in good quantitative agreement with existing theory. The stability of the OPO has been studied and its phase noise has been shown to be consistently less than that of the pump laser. Several non-phase-matched processes occurring in the OPO have been reported and their implications for a visible femtosecond source considered. With new materials and improvements to cavity design the femtosecond OPO will represent an extremely attractive source of ultrashort pulses having tunability in the visible to mid-infrared spectral regions.

Acknowledgments

Overall funding for this research was provided by the UK Science and Engineering Research Council (SERC). One of us (D. T. R.) gratefully acknowledges financial support through a SERC PhD studentship. M. Ebrahimzadeh is grateful to the Royal Society of London for the provision of a University Research Fellowship.

References

[1] Fork, R. L., Greene, B. I., and Shank, C. V., 1981, *Appl. Phys. Lett.*, **38**, 671.

[2] Spence, D. E., Kean, P. N., and Sibbett, W., 1990, *Digest of Conference on Lasers and Electro-Optics* (Washington D.C.: Optical Society of America), paper CPDP10; 1991, *Optics Letters*, **16**, 42.

[3] EVANS, J. M., SPENCE, D. E., SIBBETT, W., CHAI, B. H. T., and MILLER, A., 1992, *Optics Lett.*, **17**, 1447.
[4] KEAN, P. N., GRANT, R. S., ZHU, X., CRUST, D. W., BURNS, D., and SIBBETT, 1988, *Digest of Conference on Lasers and Electro-Optics* (Washington D.C.: Optical Society of America), paper PD-7.
[5] See for example JEDJU, T. M., ROTHBERG, L., and LABRIE, A., 1988, *Optics Lett.*, **13**, 961.
[6] IPPEN, E. P., 1993, *Technical Digest of the Eleventh UK National Quantum Electronics Conference* (Belfast: Institute of Physics), paper 119.
[7] ZUMSTEG, F. C., BIERLEIN, J. D., and BRIER, T. D., 1976, *J. App. Phys.*, **47**, 4980.
[8] BIERLEIN, J. D., VANHERZEELE, H., and BALLMAN, A. A., 1989, *Appl. Phys. Lett.*, **54**, 783.
[9] EDELSTEIN, D. C., WACHMAN, E. S., and TANG, C. L., 1989, *Appl. Phys. Lett.*, **54**, 1728.
[10] PELOUCH, W. S., POWERS, P. E., and TANG, C. L., 1992, *Technical Digest*, CLEO '92, paper CPD14-1/27.
[11] FU, Q., MAK, G., and VAN DRIEL, H. M., 1992, *Optics Lett.*, **17**, 1006.
[12] PELOUCH, W. S., POWERS, P. E., and TANG, C. L., 1992, *Optics Lett.*, **17**, 1070.
[13] SPENCE, D. E., EVANS, J. M., SLEAT, W. E., and SIBBETT, 1991, *Optics Lett.*, **16**, 1762.
[14] DIELS, J.-C. M., FONTAINE, J. J., MCMICHAEL, I., and SIMONI, F., 1985, *Appl. Optics*, **24**, 1270.
[15] SALIN, F., GRANGIER, P., ROGER, G., and BRUN, A., 1986, *Phys. Rev. Lett.*, **56**, 1132.
[16] WISE, F. W., WALMSLEY, I. A., and TANG, C. L., 1988, *Optics Lett.*, **13**, 129.
[17] WAI, P. K. A., MENYUK, C. R., CHEN, H. H., and LEE, Y. C., 1987, *Optics Lett.*, **12**, 628.
[18] WACHMAN, E. S., EDELSTEIN, D. C., and TANG, C. L., 1990, *Optics Lett.*, **15**, 136.
[19] WALKER, D. R., CRUST, D. W., SLEAT, W. E., and SIBBETT, W., 1992, *IEEE J. quant. Electron.*, **28**, 289.
[20] VON DER LINDE, D., 1986, *Appl. Phys.* B, **39**, 201.

Soliton formation in a femtosecond optical parametric oscillator

D. T. Reid, J. M. Dudley, M. Ebrahimzadeh, and W. Sibbett

J. F. Allen Research Laboratories, Department of Physics and Astronomy, University of St. Andrews, Fife KY16 9SS, Scotland, UK

Received December 20, 1993

We report evidence for soliton formation in a Ti:sapphire-laser-pumped femtosecond optical parametric oscillator. Appropriate conditions of dispersion are discussed, and temporal and spectral measurements of the output pulses are presented. Quantitative agreement with existing theory is implied.

Soliton formation in a femtosecond laser was first reported in a colliding-pulse mode-locked dye laser operating at 620 nm when $N = 3$ solitons were observed.[1] Such results were consistent with theoretical predictions for dispersive optical fibers, which showed that pulses capable of propagating without dispersive broadening could exist when an appropriate balance between self-phase modulation and group-velocity dispersion (GVD) was established.[2] Soliton formation in a mode-locked laser can be expected to manifest itself in both the temporal and the spectral characteristics of the laser output. Pulse breakup and restoration at the soliton frequency have been observed as an amplitude modulation of the mode-locked pulse sequence.[1] In addition, the simultaneous production of solitonic and dispersive waves displaces the pulse spectrum toward the region of anomalous GVD, and spectral splitting around the point of zero dispersion has been reported.[3]

The necessary conditions for soliton formation that combine sufficient self-phase modulation with variable GVD can be achieved in a femtosecond optical parametric oscillator (OPO). We have demonstrated behavior that is characteristic of soliton formation in a Ti:sapphire-laser-pumped, dispersion-compensated parametric oscillator. Based on a 1.5-mm-thick crystal of KTP cut for noncritical type II ($o \rightarrow oe$) phase matching along the x axis, our OPO is capable of producing transform-limited sub-40-fs pulses. When the OPO is pumped at 830 nm with sub-100-fs pulses and 700-mW average power, its intracavity peak power approaches 1 MW when the resonator is configured with two single-stack broadband high-reflectivity ($R > 99.7\%$) mirrors of center wavelength 1180 nm and a 1% output coupler.[4] In normal operation substantial self-phase modulation is experienced by a pulse in the nonlinear crystal, and the GVD is compensated by a pair of intracavity SF14 prisms of 24-cm apex separation, which permits transform-limited pulses to be produced. When the intracavity GVD is made slightly positive the spectrum of the pulse splits and shifts toward longer wavelengths. This behavior is accompanied by a periodic amplitude modulation on the pulse sequence at a frequency in the 0.5–2.2-MHz range.

We have investigated the spectral and tempor characteristics of the output of the femtosecond OP as a function of the amount of intracavity GVD by a justing one of the SF14 prisms. Pulse spectra ar corresponding autocorrelations were recorded for range of positive cavity dispersion values, and th pulse duration was observed to vary with dispersio as shown in Fig. 1. The point of zero dispersion ha been normalized to the maximum amount of intr cavity glass that allowed the formation of transfor limited pulses. The pulse spectrum at zero GVD depicted in curve (a) of Fig. 2. Increasing the pos tive cavity dispersion by a small amount to +100 f resulted in the generation of a second spectral co ponent at a wavelength that is 80 nm longer than th original, as shown in curve (b) of Fig. 2. The ma imum wavelength shift shown in curve (c) of Fig. occurred for a cavity dispersion of +700 fs^2. Th two spectral components produced were separated b 70 nm, and the peak wavelength was displaced b 70 nm from that at zero cavity dispersion. An add

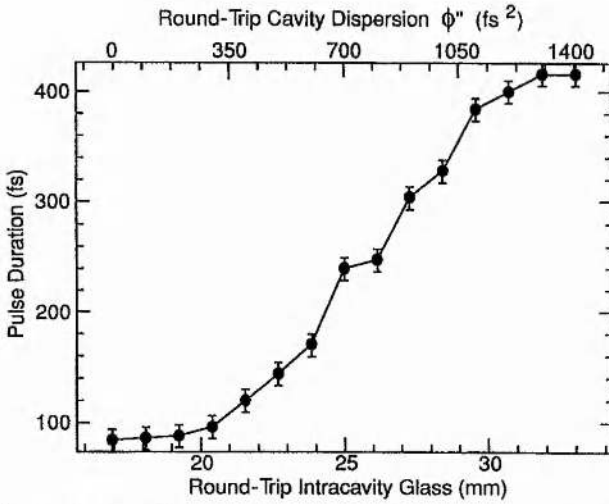

Fig. 1. Dependence of the pulse duration on t amount of intracavity glass introduced in t dispersion-compensated OPO. The upper axis indicat the equivalent cavity dispersion with the point zero dispersion normalized to the maximum amou of intracavity glass that allowed the formation transform-limited pulses.

0146-9592/94/110825-03$6.00/0

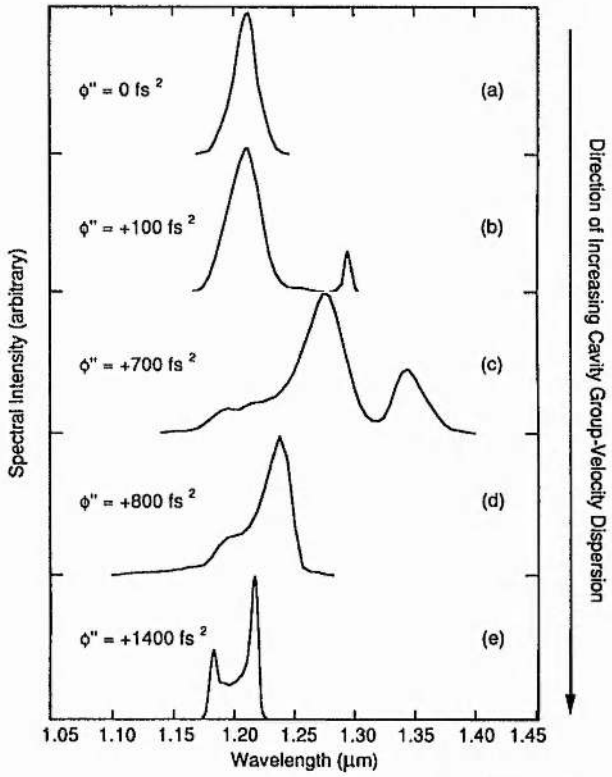

Fig. 2. Spectral data for the output of the dispersion-compensated OPO operated with positive cavity dispersion.

tional increase of 100 fs² in the dispersion inhibited longer-wavelength generation, and the corresponding spectrum is shown in curve (d) of Fig. 2. Further increases in the cavity dispersion led ultimately to the formation of pulses having the spectrum shown in curve (e) of Fig. 2, which is characteristic of the OPO when it is operated in the absence of any dispersion compensation.

It has been observed that there is a maximum operating wavelength for the OPO above which the output spontaneously shifts to longer wavelengths. For the particular configuration of the OPO that we have used this wavelength is near 1320 nm, where the dispersive component of the pulse separates from the solitonic component. The spectral splitting that we observe was predicted by Wai *et al.*,[5] who used a model developed for pulse propagation in optical fibers at 1300 nm. By identifying the critical wavelength of the OPO with the zero dispersion point of the fiber model, we can quantitatively relate our experimental data to the theory.

In the model a condition necessary for soliton propagation is presented in terms of the wavelength shift, $\Delta\lambda$, toward the anomalous regime, requiring that

$$\Delta\lambda > 6\ (\mathrm{nm\,ps})/\Delta\tau_p\,,$$

where $\Delta\tau_p$ is the duration of the soliton pulse in picoseconds. In our OPO the pulse duration of 240 fs observed at the position of maximum wavelength shift sets a lower limit of 25 nm for $\Delta\lambda$ for this condition. At the point where longer-wavelength generation became evident, pulses of 88-fs duration were monitored, and this would require $\Delta\lambda > 68$ nm for soliton propagation. This is close to the 80-nm shift measured experimentally.

A further prediction of the model is that the solitonic and dispersive components of the spectrum will be displaced by different amounts from the critical frequency. The dispersive part is expected to experience 1.7 times the spectral displacement of the soliton. The spectrum of curve (c) of Fig. 2 displays a ratio of the displacement of frequency in the dispersive wave to that of the soliton of 1.6, which is again in good agreement with the model.

In the configuration described above we observed that the rf spectrum of the output of the OPO exhibited strong sidebands at 2.0 MHz. This observation of a periodic intensity variation in the pulse train can be related to dispersion by an equation derived by Salin *et al.*,[1] which gives the soliton frequency f_0 as a function of the cavity dispersion ϕ'' and the cavity round-trip period T:

$$f_0 = 2\phi''/0.322\pi\Delta\tau_p{}^2T\,.$$

By application of this formula under the conditions of maximum wavelength shift, where $\Delta\tau_p = 240$ fs, $\phi'' = 700$ fs², and the cavity period is 11.8 ns, the predicted soliton frequency of 2.0 MHz agrees closely with experimental observation. This frequency, which corresponds to approximately 40 cavity round trips, is considerably higher than the tens of kilohertz (i.e., several thousand round trips) observed in colliding-pulse mode-locked dye lasers.[1,3] The difference arises because the KTP crystal used in the OPO contributed substantially higher phase modulation and dispersion during each cavity round trip than the jets used in dye lasers.

The observation, at a wavelength of 1180 nm and an intracavity dispersion of 320 fs², of a triple-peaked intensity autocorrelation profile (see Fig. 3) is consistent with the properties of an $N = 3$ soliton.[1,6] In the absence of equipment permitting direct measurement of pulse shape evolution within the soliton period, we are, however, unable to establish with certainty the order of the solitons generated in the OPO. An oscillogram showing the accompanying intensity modulation of the output of the OPO is given in Fig. 4. The modulation frequency of 550 kHz implies a pulse

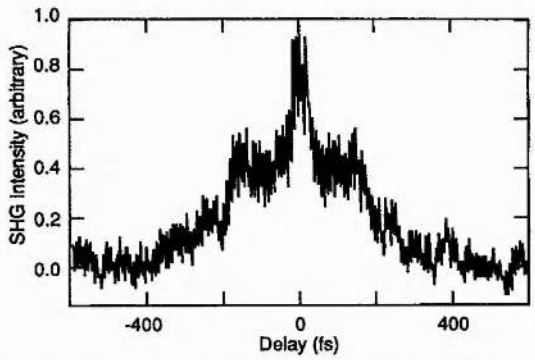

Fig. 3. Intensity autocorrelation profile of the output of the OPO at a wavelength of 1180 nm exhibiting the threefold splitting that is characteristic of a solitonic pulse. SHG, second-harmonic generation.

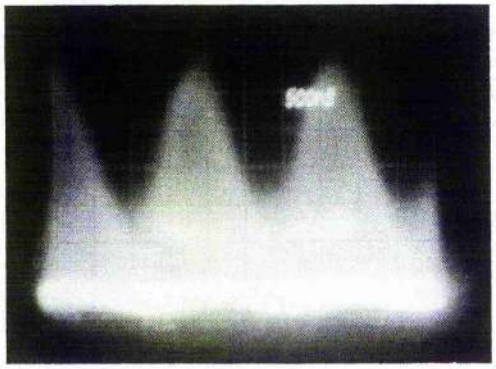

Fig. 4. Oscillogram showing intensity modulation of the output pulse sequence from the OPO.

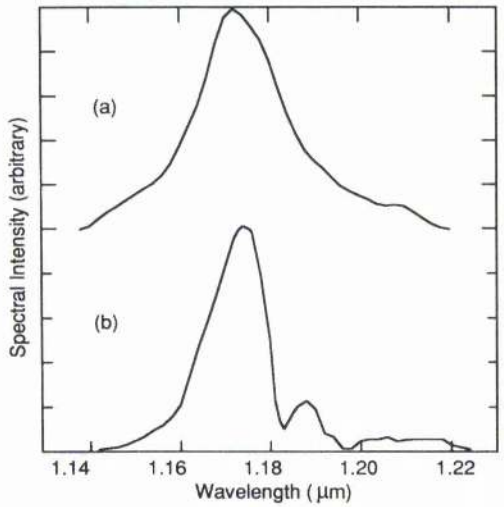

Fig. 5. Optical spectra of the OPO without an intracavity aperture [curve (a)] and with a long-wavelength-pass aperture [curve (b)].

duration of near 300 fs under the corresponding dispersive conditions. The autocorrelation profile presented contains information covering approximately 10,000 cavity round trips and is therefore an average over many soliton periods. In contrast to the experience of soliton production in colliding-pulse mode-locked dye lasers, the OPO showed a large degree of instability, and the character of the autocorrelation profile changed rapidly between solitonic and dispersive modes. We attribute this behavior to a combination of the sensitivity of the soliton formation to wavelength and fluctuations in the OPO center wavelength that result from small changes in cavity length.[7]

The pulse spectrum corresponding to the autocorrelation of Fig. 3, shown in curve (a) of Fig. 5, did not exhibit the spectral spliting observed at longer wavelengths. We inserted an intracavity aperture into the shorter-wavelength edge of the dispersed beam to test whether the solitonic component of the spectrum was embedded in a strong dispersive component. The effect of the aperture was to discriminate against shorter-wavelength production, and the resulting spectrum is shown in curve (b) of Fig. 5. This double-peaked spectrum exhibits a critical wavelength of 1183 nm in this configuration, and the ratio of the displacement of frequency in the dispersive wave to that of the soliton is 1.8, which is consistent with the results taken at longer wavelengths. Autocorrelation profiles obtained with the aperture in place were similar to that shown in Fig. 3.

In conclusion, we have observed the formation of solitons in a femtosecond optical parametric oscillator when appropriate conditions of dispersion and self-phase modulation are satisfied. Good quantitative agreement with theory derived from the nonlinear Schrödinger equation is implied. Time-resolved pulse measurements within the soliton period would establish with certainty the exact soliton order, but time-averaged autocorrelation measurements presented here are consistent with third-order soliton behavior.

Overall funding for this research was provided by the UK Science and Engineering Research Council (SERC). D. T. Reid gratefully acknowledges financial support through a SERC Ph.D. studentship. M. Ebrahimzadeh gratefully acknowledges the support of the Royal Society in the form of a University Research Fellowship.

References

1. F. Salin, P. Grangier, G. Roger, and A. Burn, Phys. Rev. Lett. **56,** 1132 (1986).
2. A Hasegawa and F. Tappert, Appl. Phys. Lett. **23,** 142 (1973).
3. F. W. Wise, I. A. Walmsley, and C. L. Tang, Opt. Lett. **13,** 129 (1988).
4. J. M. Dudley, D. T. Reid, M. Ebrahimzadeh, and W. Sibbett, Opt. Commun. **104,** 419 (1994).
5. P. K. A. Wai, C. R. Menyuk, H. H. Chen, and Y. C. Lee, Opt. Lett. **12,** 628 (1987).
6. L. F. Mollenauer, R. H. Stolen, and J. P. Gordon, Phys. Rev. Lett. **45,** 1095 (1980).
7. D. C. Edelstein, E. S. Wachman, and C. L. Tang, Appl. Phys. Lett. **54,** 1728 (1989).